Characterisation of Hardened Cements Incorporating Simulant Intermediate Level Waste

James Andrew Rickerby

Submitted in accordance with the requirement for the degree of
Doctor of Philosophy

The University of Leeds

Faculty of Engineering – School of Civil Engineering
Institute of Resilient Infrastructure

January 2015

Acknowledgements

I am grateful to the Nuclear Decommissioning Authority for funding this project, presenting me with the valuable opportunity to continue my studies.

I would like to thank my primary supervisor Prof. Ian G. Richardson for his supervision, guidance and support throughout my PhD research.

I would also like to thank all those people involved with this project and who provided me with required training, feedback and support which made this project possible: Dr Leon Black, Dr Steve Williams, Dr Shuangxin Li and Dr Rae Taylor. Additional thanks is due to the staff in LEMAS for their valuable help and training in electron microscopy especially Mr Mike Ward for his insights. I would also like to thank Dr D.C. Apperley and his staff at Durham University's EPSRC-funded NMR service for the collection of ^{29}Si and ^{27}Al NMR spectra.

I would like to extend my thanks to all my colleagues for their discussions, friendship and support along this journey, in particular; Mark, Shanshan, Sharlly, Rae, Sam, Julia and Josh. Your continued encouragement and company throughout this process has been a pleasure. I would also like to additionally thank all the civil engineering staff who gave me support particularly our materials technicians Les and Becky.

Thank you to my mum, dad and sister for their continued support and encouragement over the last 4 years, you've helped me whenever possible and I can never thank you enough. To my girlfriend Amanda thank you for putting up with me over the last few years, your patience has been incredible and I've always had a cheering face to come home to.

A special thank you is reserved for my dad, without you these years would have been much harder and more stressful. Your incredible support and advice has helped guide me throughout this process; no matter how many spectra, plots or images we discuss you have never complained and you will always be an inspiration to me.

Abstract

Blended cement grouts are used in the UK for the encapsulation of various intermediate level nuclear wastes (ILW). To ensure the long term confidence in the durability of these grouts detailed knowledge of the exact nature of the hardened cement and its interaction with the waste material is essential. This PhD project aims to characterise various aged blended cement grouts utilised in the encapsulation of radioactive wastes. The grouts have been modified by the incorporation of simulant wastes produced to allow comparison with current in-service waste formulations. The grouts were analysed using a multi-technique approach to assess the reactions which have occurred within the cement matrix and their significance for successful encapsulation of the waste.

The samples underwent investigation after long-term storage using a variety of techniques including thermal analysis, X-ray diffraction, electron microscopy and nuclear magnetic resonance spectroscopy. This suite of techniques allowed for the identification of various crystalline and amorphous phases produced during the hydration process and thereafter. Comparison was then made with similar samples containing no simulant waste to contrast the findings and possible effects upon the cement matrix and understand the implications for long-term storage.

The blended cement samples showed a varying level of modification due to the inclusion of the simulant wastes. It was shown a major controlling factor was the relative solubility of the waste-form. A magnesium corrosion based simulant showed very little reaction in cement matrix, however aluminium based simulants typically displayed a wide range of reactions. Waste carbonate systems also displayed a high level of reaction, with the formation of new phases causing the destabilisation of AFt and encapsulation of the carbonate waste within AFm. The requirement for detailed characterisation of the C-S-H phase was confirmed with substantial changes being observed for samples containing waste flocs. Analysis of this phase proposed a high degree of substitution into the silicate chain lengths with the likely incorporation of additional metal cations into the structure via charge balancing.

It was found all samples showed characteristics supporting the potential successful physical encapsulation of radioactive wastes. In addition to this various chemical immobilisation process have been studied, confirmed or proposed.

Contents

List of Tables

List of Figures

List of Abbreviations and Symbols

A - Aluminium Oxide (Al_2O_3)

AFm - Alumino/Ferric- mono phase variable composition

AFt - Alumino/Ferric- tri phase (Ettringite)

Al[IV] - Tetrahedrally coordinated aluminium

Al[V] - Pentahedral coordinated aluminium

Al[VI] - Octahedrally coordinated aluminium

BFS - Blast furnace slag

BSE - Backscattered electron

BSI - Backscattered electron imaging

β-C_2S - β Polymorph phase of Dicalcium silicate (Ca_2SiO_4, Belite)

C_3A - Tricalcium aluminate phases ($Ca_3Al_2O_6$)

C_4AF - Calcium aluminate ferrite phases ($Ca_4Al_xFe_{2-x}O_5$)

C_2S - Dicalcium silicate phases (Ca_2SiO_4, Belite)

C_3S - Tricalcium silicate phases (Ca_3SiO_5, Alite)

CC - Calcium Carbonate ($CaCO_3$)

CH - Calcium Hydroxide ($Ca(OH)_2$)

C-S-H - Calcium silicate hydrate

DTA - Differential thermal analysis

EDX - Energy dispersive X-ray analysis

EGA - Evolved gas analysis

F - Iron oxide (Fe_2O_3)

GDF - Geological disposal facility

GGBS - Ground granulated blast furnace slag

H - Water

ILW - Intermediate level waste

Ip - Calcium silicate hydrate inner product

MAS NMR - Magic spinning angle solid-state nuclear magnetic resonance

MCL - Mean aluminosilicate chain length

NMR - Nuclear magnetic resonance

NRVB - Nirex reference vault backfill material

Op - Calcium silicate hydrate outer product

OPC - Ordinary portland cement

PC - Portland cement

PFA - Pulverised fuel ash

S - Silicate (SiO_2)

SEM - Scanning electron microscopy

STA - Simultaneous thermal analysis

T/CH - Tobermorite/Calcium hydroxide viewpoint for C-S-H nanostructural model

T/J - Tobermorite/Jennite viewpoint for C-S-H nanostructural model

TEM - Transmission electron microscopy

TG - Thermogravimetric analysis

w/b - waste/binder (cement) ratio

XRD - X-ray diffraction

Chapter 1 : Introduction

1.1 Context of study

Radioactive wastes are produced throughout the world via many mechanisms and in a wide variety of forms. Due to their nature, the management of these wastes involves their containment and confinement rather than dilution and prospective release. The objective of radioactive waste management is to contain the waste and isolate it from the immediate environment. Radioactive waste management therefore consists of collecting the waste, processing into a stable form and interim storage prior to its final disposal in surface or geological repositories [1].

The future public acceptance of new nuclear generating capacity relies upon confidence in the safe and efficient management of the resultant wastes. It is therefore fundamental that current waste management technologies can be demonstrated to effectively and safely manage the current waste portfolio in existence.

This project is part of the NDA supported Diamond university research programme into the decommissioning, immobilisation and management of nuclear wastes for disposal; with particular interest into legacy wastes, contamination migration and material performance. A number of management systems and processes have been established to respond to the hazardous nature of radioactive wastes and consequences of any potential release into the environment.

After the desirable options of waste minimisation and recycling have been exhausted, waste immobilisation and containment becomes the next management process. Immobilisation reduces the potential for migration or dispersion on containments including radionuclides [2]. The IAEA [3] defines immobilisation as the conversion of a waste into a wasteform by solidification, embedding or encapsulation. Immobilisation of waste is achieved by its chemical incorporation into the structure of a suitable matrix so it is captured and unable to escape. Encapsulation of waste is achieved by physically surrounding it in materials so it is isolated and its radionuclides are retained [2].

One primary form of management for various radioactive waste streams is containment and subsequent encapsulation or immobilisation within cement grout, prior to interim and proposed long-term storage within a suitable geological disposal facility [4]. The grouts currently used in the UK for the encapsulation of intermediate level nuclear wastes (ILW) involve formulations of ordinary Portland cement blended with high levels of cement replacement materials such as blast furnace slag (BFS) and pulverised fuel ash (PFA). However several alternative mix compositions are being actively developed [5, 6]. This study investigates the long term incorporation and potential chemical immobilisation of several simulant ILW waste-forms within their relevant cement encapsulation grouts.

1.2 Research motivation

Due to the varied legacy waste portfolio currently in storage and awaiting treatment it is vital to ensure confidence in our capacity to apply current technologies to its treatment. This project enhances current knowledge into the effective treatment and stability of the resultant wasteforms, this is done by addressing current weaknesses in the existing experimental literature.

Considerable research activity has been targeted at confidently modelling the long-term performance and stability of nuclear waste-forms, nevertheless it is foreseen there could be significant limitations into the material characterisation work completed with regards to cemented waste-forms. One such limitation is the inadequate characterisation of the primary binding phase for cement C-S-H, this is due to the techniques relied upon in previous research particularly x-ray diffraction and scanning electron microscopy. These techniques have limited value in characterising C-S-H due to its amorphous nature and fine scale morphology, structure and potentially intermixed phases. This difficulty in accurately characterising the amorphous phases present with these cemented waste-forms has led to levels of speculation on their exact nature; removing or reducing this level of speculation is essential for confident long term predictions on stability.

1.3 Research objectives

This research aims to improve current knowledge into the characterisation of a range of cemented intermediate level nuclear wastes. To do this a number of material characterisation techniques have been applied to various simulant cementitious waste-forms which are based upon industry systems.

The primary aim is to increase the understanding into the exact nature of these studied simulant waste-forms and the potential level of interaction between the cementitious grout materials and the additional simulant wastes. To understand these processes is seen as integral to producing accurate predictions into long-term performance and stability of the waste-form. To accomplish this improved estimations of the micro-structural evolution and hydrated phase assemblages are required to enable higher levels of confidence into their effective management.

The outcome of the stated aim will be improved insights into the effectiveness of the studied waste treatment processes and the associated stability of the waste form after extended storage.

1.4 Experimental scope

The proposed study objectives outlined in section 1.3 have been addressed using a multi-technique experimental approach. Characterisation of the grouts composition and phase distributions was completed by backscattered electron (BSE) imaging of polished sections; additionally analytical transmission electron microscopy of ion-thinned sample allowed for finer scale analysis of resultant compositions and morphologies of identified phases.

Bulk analysis techniques were used to provide additional capabilities aside from electron microscopy; powder x-ray diffraction was used for the identification of present crystalline phases within the studied waste grouts. Furthermore, thermal analysis with evolved gas analysis allowed for the quantification of amorphous phases alongside crystalline and gave the added capability of estimation of the potential quantities of phases within a sample. At the commencement of the project it was anticipated solid-state nuclear magnetic resonance spectroscopy (NMR) would be used extensively in selected systems. This was to provide information on the nature of alumino-silicate ions within the C-S-H phase. Unfortunately due to equipment problems this was not possible for the majority of samples in the study; however ^{29}Si and ^{27}Al NMR spectras were collected at the EPSRC UK National Solid-state NMR service at Durham University to allow for estimations into the nature of the C-S-H phase.

1.5 Outline of thesis

In Chapter 2, a fundamental literature review is presented. This review covers the chemical composition of Portland cement and the relevant hydration stages, additionally various proposed structural models for the C-S-H phase and its natural mineral analogues are discussed and compared. Separate sections are included for the compositions, hydration and microstructures of the primary supplementary cementitious materials used within the blended cements studied in this project. A final section gives a detailed industrial context into the use of cement encapsulation for radioactive waste management; the review includes waste classifications, a description of waste forms, cement backfill material and alternative encapsulation systems.

Chapter 3 provides descriptions of the materials studied in this project; with discussions into the simulant wastes, encapsulation grouts and mixing procedures. General explanations are provided into the experimental techniques which is followed by a detailed description into the relevant experimental procedures used.

Chapters 4 to 8 include the related experimental results and discussions for the encapsulated simulant waste grouts. Each chapter includes an introduction, the bulk analysis and electron microscopy results and a conclusion into the effects of the simulant waste.

Chapter 9 provides a summary of the main conclusions discussed in chapters 4 to 8, additionally it includes a section into potential future works and considerations.

Chapter 2 : Literature Review

2.1 Introduction

The use of cements as a primary encapsulation medium for various nuclear waste streams is well established in the UK. However, the potential micro and nano-structural effects caused by the inclusion of these waste streams within their respective encapsulation matrices is often poorly understood due to insufficient characterisation. To determine the possible effects and to allow for long-term confidence of waste-form stability, in-detail characterisation of the C-S-H phase and the additional hydrated products is necessary. This literature review discusses the basic hydration mechanisms for OPC and supplementary cementitious materials; whilst also detailing various structural models produced to describe C-S-H. Additionally the review examines the current use of cementation in radioactive waste encapsulation, their classifications and the various industry produced waste-forms which are studied within this project.

2.1 Ordinary Portland cement (OPC)

Portland cement is the mostly commonly produced cement type in general use worldwide, it forms the basis of the majority of mixes used in construction. Portland cement is made by heating a mixture of limestone or chalk (the source of CaO) and clay or shale (the source of SiO_2, Al_2O_3 and Fe_2O_3) to a temperature of around 1450˚C. Upon heating a level of fusion occurs and the materials combine to form a hardened clinker. Calcium sulfate dihydrate (gypsum) is added to the clinker which is then ground to form cement.

2.1.1 Composition of OPC

OPC clinker commonly contains four principal phases alite (C_3S), belite (C_2S), aluminate (C_3A) and a ferrite phase (C_4AF); additional minor phases will also be present such as sulfates and various oxides. Alite is seen as the most important single constituent of normal Portland cements and it typically constitutes over 50% of the clinker, it reacts relatively quickly with water and contributes the majority of strength. Alite is an impure form of tricalcium silicate which has been modified in its structure and composition by the inclusion of foreign ions such as Mg^{2+} , Al^{3+} and Fe^{3+}. The second most common compound in cement clinker is belite which typically makes up to 30% of the material. Again belite is an impure compound of C_2S modified by ionic subsitutions, belite is normally found in its beta polymorph in cement clinkers and is commonly denoted as β-C_2S in cement notation. During hydration belite reacts more slowly than alite, contributing little to early strength development. However the effective hydration of belite is key to long-term later strength development after the 28 day period, after one year the reported strengths of pure hydrated alite and belite are very comparable [7].

The primary aluminate phase in OPC normally constitutes up to 10% of the clinker mix. It's typical composition is based upon C_3A, however similarly to the earlier reported phases it is often heavily modified by foreign ions. Aluminate is well known to rapidly react with water causing unwanted rapid 'flash' setting. To mitigate a controlling agent is introduced into the OPC mix, typically calcium sulfate (gypsum). The ferrite phase (C_4AF) is a tetra-calcium aluminoferrite compound which again can be modified by ionic substitutions and by its Al/Fe ratio. It reactivity is much lower than the aluminate phase and can be highly variable depending upon its internal composition, it is suggested that ferrite phase can initially react fairly rapidly with the reaction slowing over time [7].

2.1.2 Hydration of OPC to form C-S-H

As the cement clinker consists of multiphase solids each phase has a specific reaction with water creating a range of hydration products. The solid phases formed in the hydration of pure cement systems consist principally of calcium hydroxide, also known as portlandite, and a gel-like phase of a calcium silicate hydrate termed C-S-H. In the hydration reaction the alumina and ferrite phases react with the water, calcium and sulfate to form the products AFt (ettringite) and AFm. Calcium silicate hydrate (C-S-H) is the most important of these hydration products and the hyphens signify that its composition is highly variable. The nature of C-S-H can be affected by factors such as the cement's starting composition, water: cement or water: binder ratio and temperature.

2.1.2.1 Early age hydration

The definition of 'early' stage hydration used in this context is related to the first 24 hours of the hydration reaction. When water is added to the cement the ionic species begin to dissolve and a gel layer will form around the cement grains as the major phases of the cement react. These chemical reactions start the associated heat evolution found in the hydration of cement, with the main contribution coming from the hydration of aluminate. At this stage some aluminate and ferrite react with calcium sulphate to form an amorphous alumina silica-rich gel on the surface of the grains (Figure 2-1 Scrivener cited by Taylor [7]). Ettringite in small 'rods' then start to form across the surface of these grains as a product of C_3A with available calcium sulphate via the following reaction:

$$C_3A + 3CSH_2 + 26H \rightarrow C_6AS_3H_{32}\ (Ettringite)$$

During this early stage of hydration the level of dissolution is rapid, the heat evolution soon decreases due to saturation of Ca ions; at this point $Ca(OH)_2$ and C-S-H are starting to form due to the hydration of C_3S.

$$2C_3S + 7H \rightarrow C_3S_2H_4$$

The above equation shows the reaction of C_3S and the resulting C-S-H formed does not have an exact composition so the given $C_3S_2H_4$ is an approximation. Inside one day the C-S-H formed in the early hydration stages has formed a layer of 'outer product' (Op) on the arrangement of ettringite rods. In this middle stage it was reported by Scrivener that C-S-H began forming on the inside of the 'shell' formed from the outer product with additional production of C-S-H outer product. Scrivener also reported a secondary formation of ettringite by secondary hydration of the aluminate phase after 18 hours forming a small heat evolution peak.

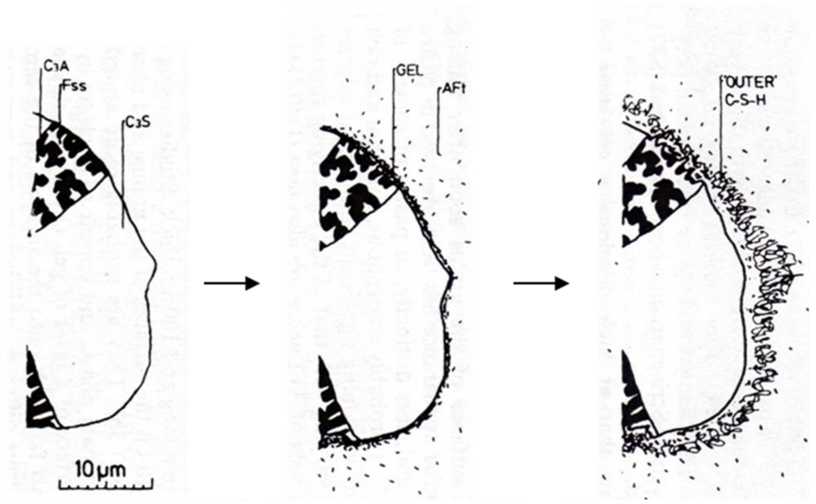

A) Unhydrated

Section of poly-mineralic grain

B) 10 minutes

Some C_3A reacts with calcium sulphate in solution. Amorphous, aluminate rich gel forms on the surface and short AFt rods nucleate at edge of gel and in solution.

C) 10 hours

Reaction of C_3S to produce 'outer' product C-S-H on AFt rods leaving 1µm between grain surface and hydrated shell

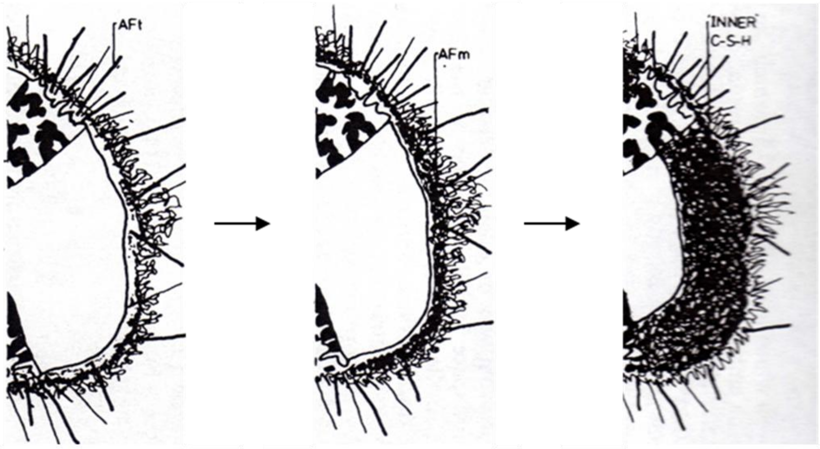

D) 18 hours

Secondary hydration of C_3A producing long rods of AFt. C-S-H 'inner' product starts to form on inside of shell from continuing hydration of C_3S.

E) 1-3 days

C_3A reacts with any AFt inside the shell forming hexagonal plates of AFm. Continuing formation of 'inner' product reduces separation of anhydrous grain and hydrated shell.

F) 14 days

Sufficient 'inner' C-S-H has formed to fill in the space between grain and shell. The 'outer' C-S-H has become more fibrous.

Figure 2-1: Development of microstructure during the hydration of Portland cement, adapted from Scrivener cited in Taylor [7]

2.1.2.2 Late age hydration

At the later stages of hydration after one day the formation of AFm phase monosulfate is observed inside the original shell as a result of C_3S and C_3A reacting with destabilised ettringite. The slow continued hydration of in-shell ettringite results in C-S-H deposition between the remaining anhydrous material and the shell until no anhydrous material remains and the grain is fully reacted. The heat evolution of the system continues to reduce. It is also during these later stages that the reaction of belite takes place in a hydration reaction similar to alite but with a greatly reduced level of heat evolution. During this continual reaction, the outer C-S-H will continue to be formed from available reaction products provided there is still water available for hydration. The formation of this outer C-S-H into the available pore spaces results in a differing morphology from the denser 'inner-shell' C-S-H. Outer-product C-S-H will often appear more porous and less compact in nature.

2.1.3 Basic morphology of C-S-H

As mentioned in the preceding sections during the hydration of cement to C-S-H there is a formation of inner (Ip) and outer (Op) products. These references to the formed microstructure were first used by Taplin [8]. The convention denotes the difference between those products which lie within the original boundaries of the clinker particles (inner products), and those which lie outside (outer products) and various authors have followed in using this concept. Evidence of the usefulness and validity of this convention can be seen from high resolution electron microscopy which shows the difference between the products [9]. As briefly discussed in 2.1.2.2 it has been shown when C-S-H is formed in larger pore spaces as outer product (Op) can have a 'coarse fibrillar' morphology, whilst inner product (Ip) displays a 'fine fibrillar' compact structure [10].

2.2 Structural models for C-S-H

2.2.1 Natural mineral analogues

There are number of crystalline minerals which are reportedly similar to the composition of C-S-H and a list of the related calcium silicate hydrates and calcium aluminosilicate hydrate phases has been published [11]. Many of these minerals are of particular interest due to their ability to help model the extremely variable and poorly ordered C-S-H phase which acts as the binder in cement.

2.2.1.1 Tobermorite

Tobermorite is a naturally occurring calcium silicate hydrate mineral, its layered structure is often classified by its interlayer basal spacings of 0.9nm, 1.1nm and 1.4nm [12, 13]. This interlayer spacing relates to the degree of hydration in the tobermorite which is affected by heating. Thus 1.1nm tobermorite is formed from 1.4nm tobermorite [14] by the loss of interlayer water via heating and 0.9nm tobermorite is created from further heating at higher temperatures. The structure of tobermorite consists of a central Ca-O 'sheet' which has silicate chains linked on both sides, the silicate chains are kinked with a three tetrahedron periodicity and are often called dreierketten chains [11]. This description is backed by a detailed determination of 1.4nm tobermorite crystal structure by Bonaccorsi et al [15]. This study concluded that its structure is made up of co-ordinated Ca cations flanked by wollastonite-like (dreierketten) chains, the inter-space between the complex layers contained additional Ca cations and H_2O molecules.

2.2.1.2 Jennite

Jennite is also a naturally occurring calcium silicate hydrate mineral which forms in the general composition $Ca_9Si_6H_{11}$ the crystal structure of jennite is discussed fully by Bonaccorsi et al [16]; structurally it is similar to tobermorite with Ca-O layers and silicate chains. However the structure of jennite presents with half the quantity of silicate chains, resulting in a higher Ca/Si ratio than tobermorite (1.5 for the $Ca_9Si_6H_{11}$ composition) [11], the reduced number of silicate chains are replaced by hydroxyl ions. Similarly to tobermorite, jennite loses water upon heating, at 70-90˚C the interlayer spacing decreases due to uni-dimensional lattice shrinkage resulting in the formation of meta-jennite ($C_9S_6H_7$)[7]. The reduction in the interlayer basal spacing from this structural transition upon heating is reported as being 1.05nm for jennite and 0.87nm for meta-jennite [17].

2.2.2 Taylor’s

Taylor’s model for C-S-H [18] is an extension on the layered structural models outlined by Feldman and Sereda [19] displayed in figure 2-2 or the modification proposed by Daimon et al [20]. The model is based upon elements of both 1.4nm tobermorite and imperfect jennite structures which were originally considered to form separate layers in a similar manner to that displayed by figure 2-2.

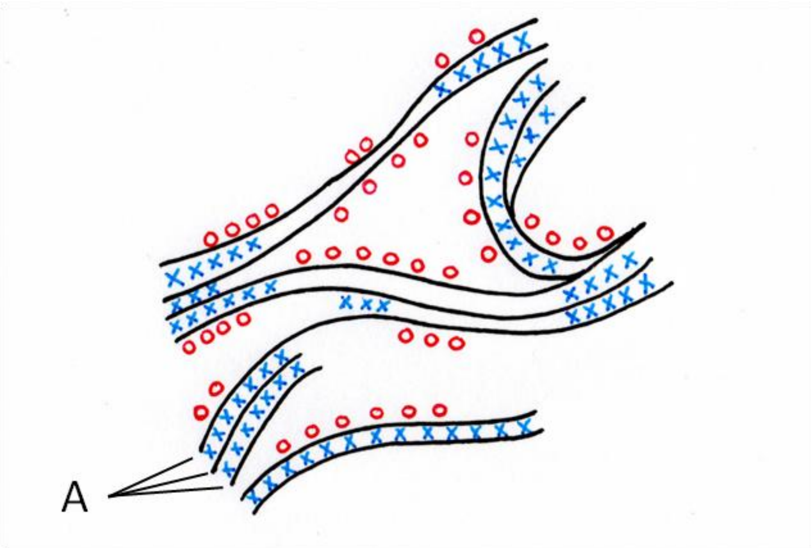

Figure 2-2: Feldman-Sereda model for the C-S-H gel nanostructure. Interlayer water is indicated by (×), physically adsorbed water indicated by (○), A - Tobermorite sheets, figure is adapted from [19].

Later studies and refinements to the model [21] however suggested that the tobermorite and jennite regions could be poorly defined potentially merging together within individual layers. The resultant T/J structure is highly disordered consisting of structurally imperfect jennite and levels of 1.4nm tobermorite altered by the loss of bridging tetrahedra. In the model many of the silicate tetrahedra are missing from the chains in both structures and this is particularly pronounced in the tobermorite. It was further theorised that in cement pastes some AFm phases may occur as individual layers intimately mixed with those of the calcium silicate hydrates within the C-S-H gels.

Taylor (1986) describes the silicate chains repeating in dreierketten form with three silicon tetrahedrals. Two of the three tetrahedra share O atoms with the Ca-O layer of paired tetrahedrals, the third does not and is referred to as a bridging tetrahedron (Figure 2-3). An additional consideration in Taylor's later paper (1993) was the inclusion of Al^{3+} ions replacing the Si^{4+} in the bridging tetrahedra sites which was anticipated as a possibility in earlier work. The proposal of Al^{3+} substitution for Si^{4+} within the bridging sites was backed up by the observation of an increase in Al^{3+} with a decrease in the Ca/Si ratio.

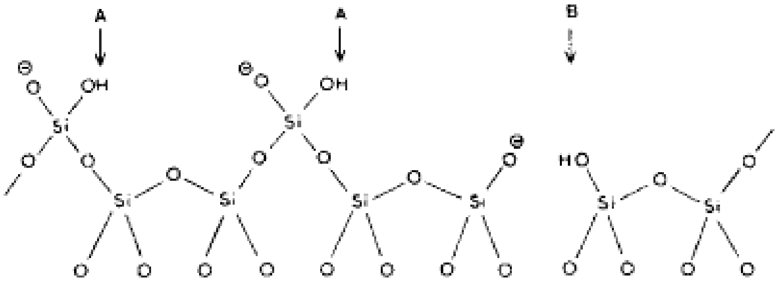

Figure 2-3: Silicate anion chain of the type present in jennite and 1.4nm tobermorite, consists of paired (bottom row) and bridging (top row) tetrahedral, suggested modification of a missing tetrahedron is shown at B [18].

Taylor continues that in theory both 1.4nm tobermorite and jennite silicate chains are infinitely long with the structure shown above . If some or all of the bridging tetrahedra were missing then finite chains containing 2, 5, 8,. . . ., 3n-1 tetrahedra would result. This omission agrees with the experimental evidence and accounts for the difference in Ca/Si ratio when compared to that of tobermorite or jennite when both are modified by omissions of bridging tetrahedra. It is also stated by Taylor that in both 1.4 nm tobermorite and jennite, if there is an omission of a tetrahedron then one of the broken ends of the chain will carry a H^+ as shown by A in figure 2-3. This would leave the net charge unchanged so the omission of a tetrahedron will not require any change in the amount of interlayer Ca.

Based on the above assumptions Taylor (1986) calculated the Ca/Si ratio at chain lengths moving from dimers to infinite lengths to be 2.25 - 1.5 for jennite and 1.25 - 0.83 for tobermorite (Figure 2-4). Taylor suggests that tobermorite will be the first to nucleate as material of lower Ca/Si ratio is formed, next to form could be a mixture of tobermorite and jennite dimers with Ca/Si ratios of 1.25 and 2.25. Later formations then appear as jennite pentamers, jennite-type material with this number of anions would have a Ca/Si ratio of 1.8 which is substantiated in his 1993 paper with NMR evidence.

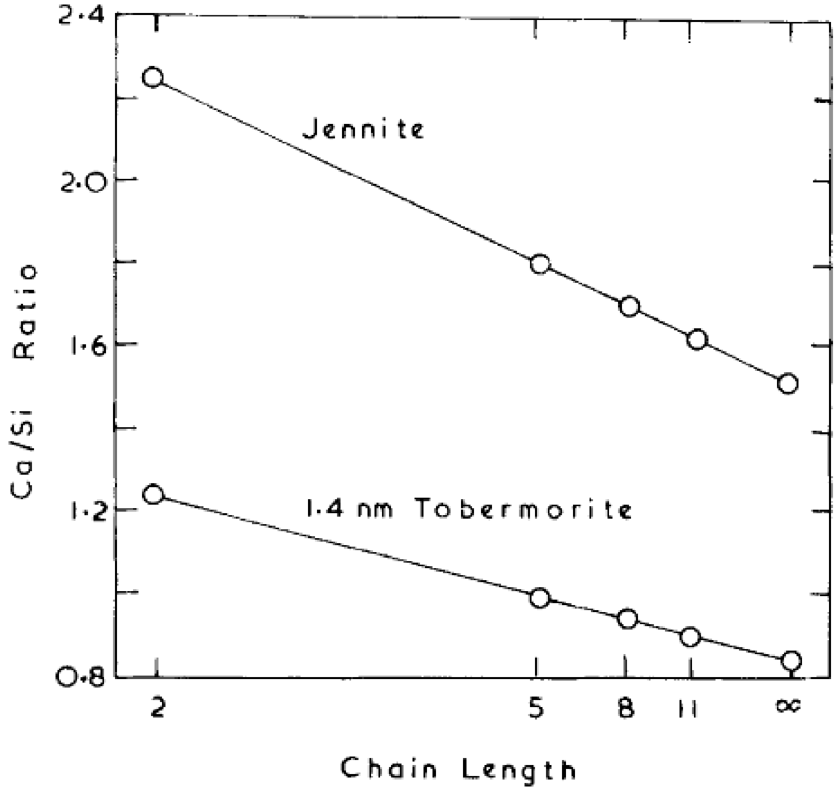

Figure 2-4: Calculated Ca/Si ratio against a function of chain length for jennite and 1.4nm tobermorite modified by omission of bridging tetrahedra [18].

2.2.3 Cong and Kirkpatrick

The model outlined by Cong and Kirkpatrick [22] lies within the concept that the structure of C-S-H is layered in a similar manner to that displayed by natural occurring tobermorite and jennite calcium silicate minerals. A tobermorite based structural model was proposed for C-S-H where individual layers have the structural characteristics of the 1.4nm tobermorite but contain significant levels of disorder. As with tobermorite mineral structures an interlayer spacing with Ca^{2+} ions and H_2O molecules was agreed in-between the structural layers which vary between the two cases displayed in figure 2-5. The first structure labelled a) is linked to an almost perfect tobermorite layer which has been distorted by the removal of some bridging tetrahedra. The secondary layered structure is highly distorted, containing mostly dimers due to the absence of many bridging tetrahedra. In this secondary layer the remaining tetrahedra are tilted, rotated and displaced relative to the CaO layers as shown in figure 2-5. It was suggested by Cong and Kirkpatrick that the two differing layers may merge into or occur simultaneously within a single layer, either by stacking together or being present within different areas of a sample. The relative disorder created by potential stacking and inherent structural disorder described within the layers would account for the diversity observed amongst C-S-H samples. Additionally it was proposed that the presence of $Ca(OH)_2$ layers may also occur within any stacking sequences in cement pastes, thereby further increasing the possible disorder and Ca/Si ratios.

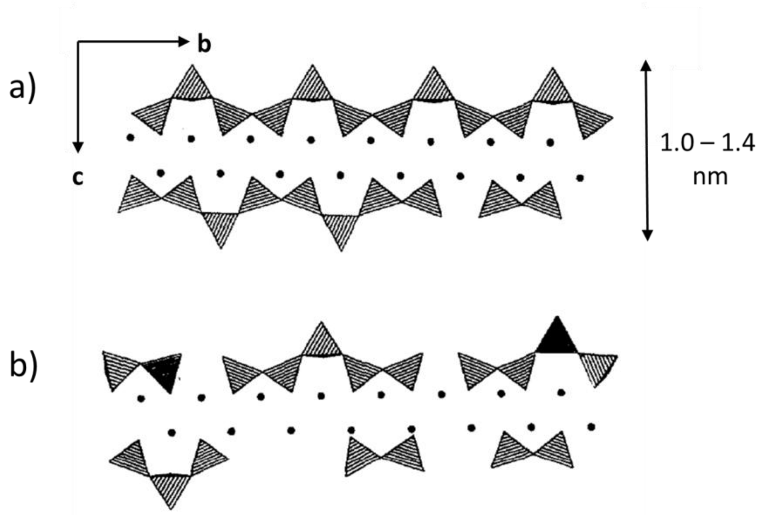

Figure 2-5: Proposed defect-tobermorite structural model for C-S-H, showing dreierketten and central CaO layers (filled circles). The interlayer Ca^{2+}, OH^- groups, and H_2O molecules are omitted. The layer on top (a) represents a relatively perfect 1.4nm tobermorite layer with a small number of bridging tetrahedral removed and relatively long structural chains. The bottom layer (b) represents a distorted layer, with individual tetrahedral and entire chains maybe tilted, rotated or displaced along the b axis. Most bridging tetrahedra are missing, resulting in many dimers and the loss of entire segments of silicate chains, reproduced from [22].

2.2.4 Chen et al

Chen et al investigated the relationships between the aqueous solubility and the chemical structure of calcium silicate hydrate formed using varied preparation methods using ^{29}Si MAS NMR spectroscopy and charge balance calculations. The study concluded the observed solubility differences arise from systemic variation in the Ca/Si ratio, silicate structure and Ca-OH content. Based on this observed evidence the solubility curves were interpreted as representing metastable phases whose structures ranged from purely tobermorite-like to largely jennite-like in nature [23].

2.2.5 Richardson and Groves

The Richardson and Groves ‘general’ model was proposed on the basis of extensive experimental results obtained from TEM-EDX analysis of varied hydrated cement samples used in conjunction with NMR. The model outlines C-S-H as based upon a highly disordered dreierkette structure derived from 1.4nm tobermorite. The layers contain varying levels of $Ca(OH)_2$ and finite silicate chains which obey the 3n-1 observation for bridging tetrahedra discussed earlier for Taylor’s model [18, 24, 25].

$$\left[Ca_{2n}H_W Si_{(3n-1)}O_{(9n-2)}\right].(OH)_{w+n(y-2)}Ca_{\frac{n.y}{2}}.mH_2O$$

Equation 2-1: General model for the structure and composition of C-S-H [25]

The model can be classified as either a model like Taylor’s with the structural perspective of both tobermorite and jennite structural units (T/J) or as a solid solution model with the structural units of tobermorite and calcium hydroxide (T/CH). A major point of the model is that both T/J and T/CH structural viewpoints can be used to account for compositional and structural data for the C-S-H in cement pastes [26].

Refinements to the general model [24] shown in equation 2-1 were made to allow for the addition of various trace elements into the structural model. This accounted for the observed experimental evidence and is referred to as R in the modified equations 2-2 and 2-3 for the T/J and T/CH viewpoints respectively, alongside the charge balancing interlayer ions (I^{C+}). The models therefore allow for the substitution of Al^{3+} ions into the bridging tetrahedral sites previous occupied by Si^{4+} ions, with the substitution into the dreierkette chains reducing the Ca/Si ratio and increasing the overall mean chain lengths (MCL) as the substitution increases.

$$[Ca_{2n}H_w(Si_{1-a}R_a^{[4]})_{(3n-1)}O_{(9n-2)}]I^{c+}_{\frac{a}{c}(3n-1)}.(OH)_{w+n(y-2)}.Ca_{\frac{n.y}{2}}.mH_2O$$

Equation 2-2: T/J viewpoint [26]

$$Ca_XH_{(6n-2X)}(Si_{1-a}R_a^{[4]})_{(3n-1)}O_{(9n-2)}.I^{C+}_{\frac{a}{c}(3n-1)}.zCa(OH)_2.mH_2O$$

Equation 2-3: T/CH viewpoint [26]

Where:

- n = number of units
- (3n-1) = the mean length of the silicate chain units
- w = amount of hydroxyl water
- $R^{[4]}$ = Trivalent cation (Usually Al^{3+} other cations i.e. Fe^{3+} possible)
- I^{c+}= is the interlayer ion (Ca^{2+})
- z = value for $Ca(OH)_2$ in one unit
- m = number of bound water molecules

The use of the above described models allows for the determination of Si/Ca and Al/Ca ratios for the possible T/CH and T/J units with the variable levels of protonation and aluminium substitution into the available bridging sites. This can be plotted as shown in figure 2-6 and compared to the results from compositional TEM-EDX analysis of the sample. Additional information for the mean silicate chain lengths and % bridging tetrahedra can be obtained from NMR evidence and used in conjunction with TEM-EDX to determine the structural composition of the C-S-H phase.

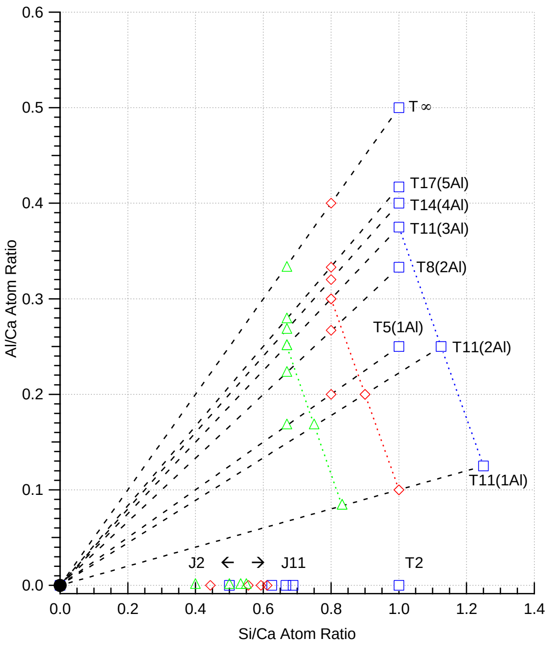

Figure 2-6: Si/Ca against Al/Ca atom ratio plot of the compositions of tobermorite (T) and jennite (J) based structural units with different levels of protonation of the silicate chains: the minimum (△; w/n=0), intermediate (◇; w/n=1) and maximum (□; w/n=2). The additional points included represent tobermorite-based units with chain lengths of 2, 5, 8, 11, 14, 17 and ∞. The black dashed lines join points for structural units of the same chain length but different degrees of protonation to CH.

The possible limits of the structural models for both the jennite and 1.4nm tobermorite are dictated by the levels of possible protonation in the silicate chains (w/n) , the maximum (2), intermediate (1) and minimum (0) levels are fully discussed in [26] and displayed in figure2-6. The model differs from Taylor's in that it provides a greater flexibility in composition with a maximum Ca/Si ratio of 2.5 for a jennite dimer and a minimum of 0.67 which is for an infinite length tobermorite as shown in figure 2-7. Additional flexibility in this model is provided by freely variable approach to the hydroxyl water content of the C-S-H which was constricted in Taylor’s model. One assumption made by the general model is that silicate chains are not linked by Si-O bridges in a similar manner to tobermorites. This is justified by the fact silicate tetrahedra linked to (Q^3 and Q^4) groups were not detected by ^{29}Si NMR, with only end (Q^1) and mid-chain (Q^2) units detected in the C-S-H gel [25].

The use of the modified models outlined in equations 2-2 and 2-3 allows for several experimental observations to be explained. Increasing levels of substitution into a fixed chain length will reduce the Si/Ca ratio whilst increased levels of polymerisation will allow for increased substitution. When considering the C-S-H composition for slag: OPC blends or other pozzolanic materials the more highly polymerised nature of the C-S-H phases was illustrated by increasing R:Ca ratios and associated decrease in the Ca:Si ratio, showing the models compatibility with experimental data [24].

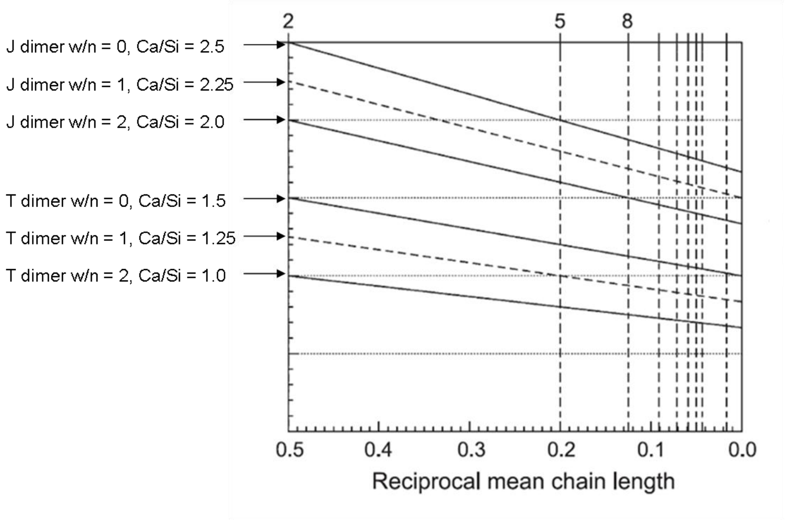

Figure 2-7: Ca/Si ratio and mean silicate chain lengths for T/J and T/CH structural models with possible protonations, adapted from [26].

2.2.6 Grutzeck

The proposed model by Grutzeck et al [27] suggested that formed C-S-H evolves via a phase separation from a rapidly formed and therefore initially 'active' C-S-H that has a sorosilicate structure and a high level of calcium activity. During the later separation the early stage active C-S-H converts to a mixture of tobermorite-like phases and a less soluble and 'inactive' sorosilicate-like phase; a representation of this is shown in figure 2-7.

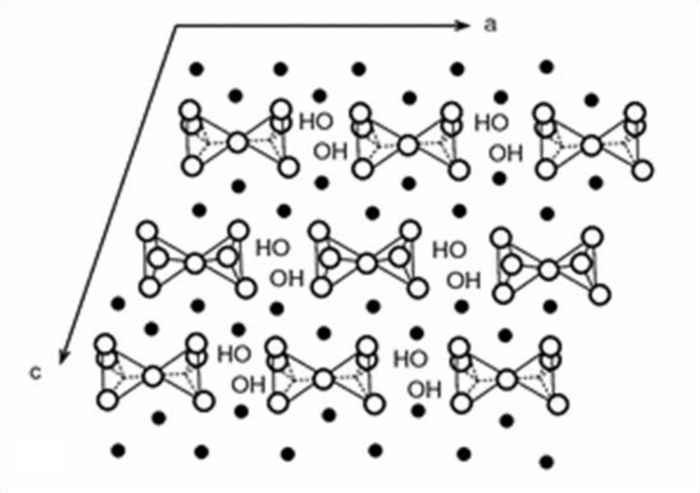

Figure 2-8: Fully stoichiometric sorosilicate-like structure for C-S-H (Ca/Si=2.0), reproduced from [27].

The sorosilicate-like C-S-H is not a layered structure as discussed for several of the previous models and natural mineral analogues for C-S-H, instead it is comprised of dimeric $(Si_2O_7)^{6-}$ ions which are linked to CaO octahedrally co-ordinated chains. It is also stated that the produced mature cement paste sample would contain a mixture of dimer and dreierketten chains; with the dimeric C-S-H forming soon after setting being meta-stable in their own right. Certain issues appear with this model including a satisfactory explanation for the substitution of aluminium into the C-S-H structure, which has been observed to occur in the tetrahedral co-ordination sites [28].

2.2.7 Nonat and Lecoq

Nonat and Lecoq proposed a model based upon tobermorite containing two C-S-H phases with differing $Ca(OH)_2$ concentrations [29]. The model differs from that suggested by Taylor or Cong and Kirkpatrick by not requiring a disordered structure with no Jennite-like regions present, therefore the calcium in the main plane would not-ordinate to OH^-. To allow for high Ca/Si values the model proposes the interlayer sites are occupied by Ca^{2+} ions which are charge balanced by OH^- in interlayer positions. Additionally missing bridging tetrahedra would allow for two further OH^- sites; these would charge balance and allow for the accommodation of one $Ca(OH)_2$ unit into the structure.

2.2.8 Jennings

Jennings' proposed a colloid model for the structure of C-S-H based upon experimental data on the surface area, density and water contents of hydrated phases; this was referred to as the colloid model I (CM-1) [30, 31]. The model describes globules of C-S-H clusters which pack together into two densities, named high density (HD) C-S-H and low density (LD) C-S-H which corresponds to the inner and outer products discussed earlier. The model treated C-S-H as a gelled colloid or a granular material rather than as a porous continuous material; the use of this packing model provided a basis for the later modelling of C-S-H via nanoindentation measurements [32]. The colloid model II (CM-2) made several refinements to CM-1, the globules were modified to include aspects of structural layers such as that presented by Feldman-Sereda (Figure 2-1). In CM-2 the concept of LD and HD C-S-H is still applicable due to the density of globules but the water maybe present in several locations. At the nanoscale the water either adsorbed onto the surface of calcium-silicate sheets, within the globules in nanopores or interlayer spaces or in the inter-globule spaces.

The colloid C-S-H model places emphasis in the scale range of approximately 1-100nm, placing its applicability into the meso/macrostructure of hydrated cement. Jennings' [33] does state however that below this scale the layer structure approach seems valid.

2.2.9 Pellenq

The model proposed by Pellenq et al [34] disregards the previous layered structural models based upon structurally imperfect 1.4nm tobermorite and jennite mineral analogues due to their incompatible densities and Ca/Si ratios to measured values [35].

The authors propose a new molecular model based upon a bottom-up atomic simulation approach where the chemical specificity of the system is seen as the overriding constraint. To produce the computational model, cells of CaO and SiO_2 were constructed with an interlayer spacing corresponding to 1.1nm tobermorite. Interlayer calcium ions were added to the model to maintain electroneutrality within the structure, SiO_2 groups in the silica tetrahedra where then removed as guided by NMR results. The level of adsorbed water will relate to the measured required density for the C-S-H model, as increases in adsorbed water will increase density. This measured density can also be controlled however by slight increases or reductions in the interlayer spacing. The reported overall chemical composition of the computational model of hydrated C-S-H was found to be $(CaO)_{1.65}(SiO_2)(H_2O)_{1.75}$ which was reported to be in reasonable agreement with the groups neutron scattering experiments [35].

2.2.10 Conclusions

In summary, eight proposed structural models for C-S-H have been discussed in this literature review and summaries of their conclusions presented. The use of Richardson and Groves' model in this study is preferred due to its ability to explain a wide range of findings, including the models outlined by Cong and Kirkpatrick, Chen et al and Nonat and Lecoq. The model described by Taylor can be viewed as a special case scenario of the Richardson and Groves' model. It includes a mix of tobermorite and jennite - like structures but in more structurally rigid formations than that allowed by Richardson and Groves', particularly in regards to the addition of tetrahedrally co-ordinated bridging sites.

Grutzeck's sorosilicate model describes a cement paste containing a mixture of dimer and dreierketten chain lengths after hydration. It does not however explain in detail the formation of these dreierketten chains. Additionally the model does not explain the observed experimental evidence for aluminium ions being accommodated within tetrahedrally co-ordinated bridging sites.

Jennings colloid model primarily considers its applicability to the meso/macrostructural properties of cement gels, the author has stated that below these scales a layer structure approach may be valid. Due to the experimental approach and focus on the cement microstructure used in this study direct comparison to the Richardson and Groves' model is more applicable. Similarly the experimental evidence collated does not allow for an easy direct comparison to the Pellenq model. This is particularly true for waste immobilisation matrices due to the reduced experimental data to confirm Pellenq's model.

2.3 Supplementary cementitious materials

2.3.1 Blast furnace slag (BFS)

Blast-furnace slags are formed during the manufacture of iron from iron ore. Slag forms between the temperatures of 1400˚C and 1600˚C and the slag rises to the surface of the melt and is tapped off. If the molten slag is fast cooled a vitreous Ca-Al-Mg silicate glass will form [36]. Once this glassy product is ground into a powder it has reasonable cementitious properties as it is latently hydraulic and is often known as GGBS (ground granulated blast furnace slag). Usually since the latent hydraulic reaction it produces solely is very slow, an alkaline activator is used normally OPC or free lime however additional activators have also been used [37-40].

In common with many industrial products the composition of BFS varies upon the industrial source. However the main components have been summarised as: lime (30-50%), silica (28-38%), alumina (8-24%), magnesia (1-18%), sulphur (1-2.5%) and ferrous and manganese oxides (1-3%) with other trace levels of titanium oxide and alkalis (Na_2O, K_2O)[41]. The use of slag-cement blends results in potentially higher strengths, lower heat of hydration, lower permeability and improved durability particularly to sulphate attack [42].

2.3.1.1 Hydration reactivity

Blast furnace slag displays slower hydration kinetics which results in a lower degree of hydration for composite cements containing significant fractions of slag. However due to resultant changes in composition and phase assemblage the performance of slag cements can surpass that of neat cement systems at later ages [43, 44]. It has been shown that the reactivity of slag-cement blends depends upon several factors including curing temperature, water/binder ratio and level of slag replacement [45] Additionally the slag chemistry itself should also be considered when estimating the potential degree of hydration.

2.3.1.2 Hydration of BFS/OPC systems

The hydration of slag cements generally produces comparable hydration products to neat cement pastes, C-S-H is formed as the primary binding phase with a potentially altered chemical composition due to the composition of the slag. The formation of ettringite and AFm phases within slag cements is seen to be related to the relative aluminate, sulfate and carbonate contents; the inclusion of one or more of these phases should be considered when accounting for the mineralogy of slag blended systems [46]. One additional hydration product expected in slag-cement blends is the a hydrotalcite-like phase associated with the reacted slap inner product. The quantity of this phase is therefore related to the proportion of slag included in the mix [47] and its initial magnesium content. It has also been observed that the measured levels of CH in slag-cement blends are greatly reduced, this is due to the consumption of CH in the activation of slag particles resulting in additional C-S-H production [47, 48].The chemical composition of the slag has been shown to have a measured effect upon the resultant composition of the formed hydrated phases and thus the performance of the hardened cements [43, 49].

2.3.1.3 Microstructure of BFS/OPC systems

Taylor [4] describes the microstructure of slag cement pastes as 'essentially similar to those of pure Portland cement paste, apart from the lower CH content.' Richardson and Cabrera

[50] using a TEM study showed that the Op and Ip in slag pastes can be differentiated, they also showed the morphology of the Op C-S-H changes from fibrillar to a foil-like morphology as the slag content is increased. Richardson and Groves [51] also showed the presence of AFm phases within the Op C-S-H explaining the reported Al/Ca ratios. The effect of increasing levels of slag upon C-S-H composition has been extensively investigated with a C-S-H of a reduced Ca/Si and higher Al/Si atomic ratio usually being formed [8, 51-55]. An example of the Op C-S-H morphology displayed by a high replacement slag cement system is shown in Figure 2-9.

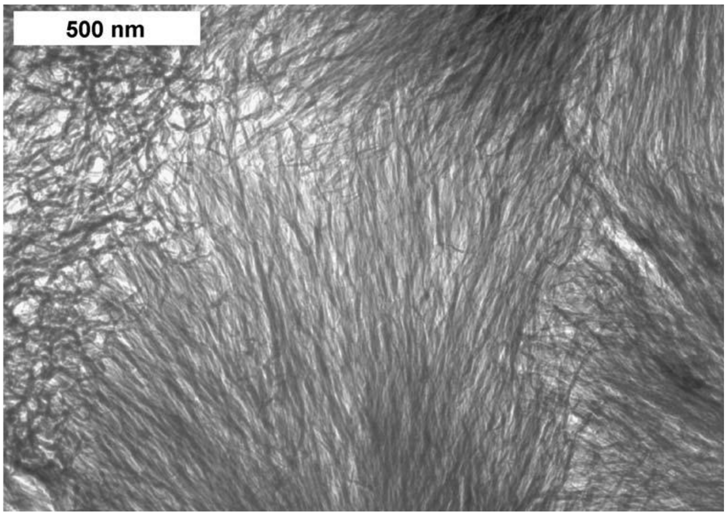

Figure 2-9: TEM micrograph showing Op C-S-H present in a OPC-75% GGBS paste at 14 months reproduced from Richardson [26]

2.3.2 Pulverised fuel ash

Fly ash is defined as being a 'fine powder of mainly spherical glass particles having pozzolanic properties which shall consist essentially of reactive silicon dioxide (SiO_2) and aluminium oxide (Al_2O_3), the remainder being iron (III) oxide (Fe_2O_3) and other oxides. PFA can be obtained by electrostatic or mechanical precipitation of dust-like particles from the flue gases of power station furnaces fired with pulverised bituminous or other hard coal.' [56]

Fly ash is a pozzolanic material rather than a latent hydraulic material and the impact of this is discussed below in section 2.3.2.1. Fly ashes are further divided depending on their production into either class C or class F subgroups. Class C ashes contain levels of calcium oxide (CaO) or free lime which gives them cementitous properties in addition to pozzolanic. Class F ashes contain predominately siliceous and aluminous materials which are not cementitously reactive but are pozzolans.

The composition, chemistry and affect on hydration of fly ashes are linked to the source of coal and the type of combustion technology used in the burning process. As mentioned above in the definition of fly ash significant levels of SiO_2, Al_2O_3 and Fe_2O_3 along with potentially smaller levels of CaO depending on the class are present in the material. In general fly ashes are considered to be composed of relatively few mineral phases; clays, pyrite, quartz and some calcium, iron and magnesium carbonates [57]. Studies using SEM imaging and analysis show the presence of crystalline quartz (SiO_2) and mullite ($Al_6Si_2O_{13}$) alongside smaller levels of hematite (Fe_2O_3) and magnetite (Fe_3O_4) within the glassy structure of the PFA [58]. The same study showed the mean particle size from SEM studies for the fly ash was 10-12 µm while the chemical compositions of the fly ashes studied is shown below in table 2-1.

Fly Ash	SiO_2	Al_2O_3	Fe_2O_3	CaO	MgO	Na_2O	K_2O	SO_3	LOI
FF	44.6	25.0	11.8	3.39	1.67	0.38	3.47	0.62	3.16
WB	47.74	25.96	9.10	1.67	1.33	1.35	3.43	0.84	5.84

(LOI= Loss on ignition)

Table 2-1: Phase composition of two PFA's studied by Halse el al [58]

2.3.2.1 Hydration reactivity

As mentioned above PFA is a pozzolanic material not a hydraulic material and consequently PFA will not rapidly hydrate upon exposure to water as cement clinker does. For the PFA to react, the Si-O-Si links have to be broken and the silica dissolved. In order for this to occur the pH of the alkaline environment which exists within cement must reach 13.2 [59]. This will only happen once a level of hydration has occurred with the OPC in the mix. This means the PFA is always delayed in its reaction when compared to the OPC. The delay is advantageous in respect to using PFA within a cement encapsulation material for nuclear wastes due to the reduction in the heat evolution exotherm associated with pure OPC mixes [60], this has been demonstrated experimentally and using simulation models [61].

2.3.2.2 Hydration of PFA/OPC systems

When PFA is involved in the hydration reaction alongside OPC the cement clinker material reacts first as described in section 2.3.2.1, the resultant CH formation increases the pH to the necessary levels for PFA reaction [62]. The initiation of this pozzolanic reaction has been reported at varying periods ranging from days to over a week after initial hydration [63, 64]. However the addition of fly ash has been shown to potentially have an effect upon the early silicate and aluminate reactions involving the OPC within the first two days of hydration [65].

2.3.2.3 Microstructure of PFA/OPC systems

Generally the microstructure of PFA blended cements have been reported to be similar in nature to C_3S and OPC based systems [66]; the primary difference being the reduction in visible CH crystals due to their consumption via the pozzolanic reaction. Examination of PFA/OPC samples has displayed the expected normal cement hydrate products C-S-H, AFt, AFm and CH in lower quantities [67, 68], iron-containing phases, hydrogarnet and hydrotalcite have also been reported however [66, 69]. When a fly ash particle activates, it forms a dense reaction rim of C-S-H which surrounds the edge of the particle. Inside this rim radial fibrils of C-S-H form often alongside a lower density inner product which characterises a fully reacted fly ash particle. Many of the crystalline phases associated with the PFA remain generally un-reacted during the hydration process and can be observed intact within the microstructure, this is particularly applicable to mullite and hematite formations. The reported Ca/Si and Al/Si atomic ratios for the C-S-H phase in PFA/OPC systems suggests a decreased level of calcium and increased levels of silicon and aluminium when compared to neat OPC cements [47, 70]. This is reported to result in an increase in polymerisation of the C-S-H silicate chains [68]. Additional levels of other elements have also been reported to exist in the outer product C-S-H such as potassium and other cations [66].

2.4 Use of cementation in radioactive waste encapsulation

The nuclear sector like most industrial processes produces waste. However the principal wastes produced apart from the actual spent nuclear fuel are widely varied solids, liquids or gases which have become contaminated through contact with radioactive substances. Wilson [71] described the object of radioactive waste management as:

(a) To concentrate the radioactive material as far as possible in a small volume that can be isolated indefinitely from human contact.

(b) Where streams such as the water from fuel storage ponds are too bulky for anything but release into the environment, to remove from them all radioactivity or harmful material that poses a significant risk.

The closure of the nuclear fuel cycle and safe disposal of radioactive wastes is fundamental for the effective use of nuclear power in the future. Without this dimension of safe disposal the use of nuclear energy as a future 'clean' source of power can be discounted.

2.4.1 Classification of radioactive wastes

Radioactive waste in the UK is classified as High Level Waste (HLW), Intermediate Level Waste (ILW) or Low Level Waste (LLW) according to its level of radioactivity. Generally HLW is heat releasing waste which contains products directly linked with the irradiated fuel. LLW produces virtually no heat and near surface disposal of LLW contains no hazards, ILW has too high levels of heat evolution to be classed as LLW [71]. Further definitions for high, intermediate and low level wastes are outlined in table 2-3.

Radioactive Wastes
High-Level Wastes (HLW): Wastes from the reprocessing of irradiated fuel which generate heat and will be vitrified. These contain over 95% of all the radioactivity in wastes from the generation of electricity by nuclear power.
Intermediate-Level Wastes (ILW): Wastes with radioactivity exceeding the boundaries for low-level wastes, but of a lower activity and heat output than high-level wastes.
Low-Level Wates (LLW): Waste with radioactivity not exceeding 4GBq/tonne alpha activity or 12 GBq/tonne beta/gamma activity, other than those acceptable for disposal with household refuse. These wastes do not normally require radiation shielding.

Table 2-2: Radioactive waste definitions [72]

The total volume of radioactive waste from all sources in the UK from the 1st April 2010 is shown below in Table 2-3.

	HLW(ii)	ILW(iii)	LLW(iv,v)	Total
Volume (m^3)(i)	1,020	287,000	4,430,000	4,720,000
Mass (tonnes)	2,700	300,000	4,700,000	5,000,000

(i) For HLW conditioned volume and mass are reported. Quantities of ILW and LLW are for untreated or partly treated waste, apart from conditioned waste streams (/C identifier) where the conditioned volume and mass are reported. Convention for reporting waste volumes given in chapter 2.4.4 of referenced report.

(ii)HLW conditioned volume and mass reduced to account for exports of HLW

(iii) ILW includes 8,690m^3 of waste expected to become LLW as a result of decontamination or decay storage.

(iv) LLW includes 3,060,000m^3 of VLLW and a further 239,00m^3 of mixed VLLW/LLW

(v) LLW includes 14,860m^3 held at the LLWR, as well as 16,800m^3 previously disposed of at Dounreay to be retrieved and repeacked as LLW. It does not include waste already disposed in trenches and Vault 8 at the LLWR.

Table 2-3: Wastes at 1st April 2010 and estimated for future arisings volumes and masses [73]

This study focuses upon various ILW waste streams generated during the nuclear fuel cycle; unfortunately many fuel cycle wastes often known as historic or legacy wastes are poorly characterised and stored under conditions which are far from ideal [74]. They can comprise a wide range of materials including fuel cladding, fuel elements and equipment. As many wastes were stored underwater long term degradation has occurred resulting in the formation of sludges and supernatant liquids.

Most of the waste streams investigated are related to the treatment of legacy waste streams in the NDA's portfolio and are produced via one or more of the chemical separation technologies listed [75]:

- Solvent extraction
- Ion-exchange
- Precipitation
- Dissolution
- Solvent leaching
- Filtration and/or membrane processes
- Combustion and/or degradation processes.

2.4.2 OPC and blended cement grouts for encapsulation of ILW

In the UK cementation is seen as the preferred encapsulation medium for a wide range of nuclear waste streams; cements have many attributes which make them highly suitable for consideration as the encapsulation medium for various radioactive wastes including ILW's. The following advantages were outlined by Sharp et al (2005) [76]:

- Easily available and relatively inexpensive
- Can be used as a fluid grout
- Durability
- Can act as a barrier to diffusion of ions
- They maintain a high pH which will decrease radionuclide solubility
- Can incorporate many ions into solid solution
- Provide radiation shielding that is not degraded by radiation
- Can have a very low liquid and gas permeability in a hardened state
- Are tolerant to a wide array of wasteforms
- Can be modified to suit a particular purpose through selection of appropriate constituents

- Relatively easily process in a remotely operated plant environment

Typically the immobilisation process consists of mixing the cement powders into a stainless steel drum of waste using a sacrificial mild steel paddle which remains after mixing. After the resulting matrix grout has hardened sufficiently the remaining ullage is filled with a PFA/OPC capping grout. The produced drum is then lidded and placed in an engineered storage area for final disposal [77].

The major formulations of cement grouts for the encapsulation of ILW involve composite cements with relatively high levels of supplementary cementitous materials (SCM's) when compared to cements used in the construction industry. This is due to the expected high thermal gradients potentially created within a 500L drum if conventional primarily OPC based grouts are used, the resultant internal stress produced would potentially cause cracking of the wasteform and structural instability [76, 78]. The mass addition of pozzolanic or latently hydraulic materials as SCM's reduces the thermal gradient created during OPC hydration leading to an uncompromised wasteform. The following cement composite formulations are currently being used by the industry to treat ILW [79]:

- 9:1 BFS:OPC
- 3:1 BFS:OPC
- 3:1 PFA:OPC
- 5:4 PFA:OPC

2.4.3 Description of cemented ILW wasteforms

A wide variety of ILW wastes are, or are proposed to be encapsulated by in-drum mixing in cements as described in section 2.4.2. Some of the wide array of waste streams under investigation is discussed in this chapter along with their treatment.

2.4.3.1 Metallic corrosion sludges

Sludges containing metallic corrosion products may arise from the conditioning of pond water used to store spent fuel or from the storage of historic metallic wastes. These sludges can contain a variety of metallic corrosion products such as $Mg(OH)_2$, $Al(OH)_3$ and $Fe(OH)_2$, additional organic matter and inorganic debris could also be present in service [77].

Magnesium based sludges resulting from the storage of spent Magnox fuel rods in storage ponds have been investigated using an inactive simulant produced from corroded metals; this investigation determined the simulant sludge contained mainly brucite and artinite ($Mg_2CO_3(OH)_2.3H_2O$)[80]. Additional work has also been completed on liquor and sludge samples taken from legacy fuel pond storage facilities at Sellafield. This study again showed the expected presence of brucite as a corrosion product and an Mg-hydrocarbonate phase linked to artinite; there was also indications of hydrotalcite phases formed via Al substitution during storage ($Mg_6Al_2(CO_3)(OH)_{16}.4H_2O$) [81].

Sludges containing metallic wastes as described above are normally treated using composite cements based around a BFS:OPC formulation. A number of published studies have investigated the possible effects of encapsulating reactive metals within these systems. However these studies are primarily focused upon corrosion of metals within the encapsulation matrix and the resultant products not the encapsulation of actual metal corrosion products. In these studies it was demonstrated that achieving the desired product stability is dependent upon controlling the magnox metal corrosion using cement grouts with a lower water content [82]. Encapsulation of aluminium in a BFS composite cement was found to produce a corrosion zone consisting of bayerite ($Al(OH)_3$) and stratlingite ($2CaO.Al_2O_3.SiO_2.8H_2O$); whilst magnesium encapsulation produced the expected brucite ($Mg(OH)_2$) layer [83]. In both cases the hydration of the bulk cement matrix was not overly affected by the corrosion of these metals.

Some work has been completed looking at the effects of simulated $Mg(OH)_2$ slurries representing corrosion products within composite cement matrices [84]. Simulant magnesium hydroxide sludges were prepared using distilled water and NaOH before being mixed into three composite cement matrices formulations used by industry. Collier et al (2010) concluded there was little reaction between the simulant sludges and any of the composite cements during hydration. Phases identified included C-S-H, unreacted brucite and a small level of a hydrotalcite type phase containing magnesium. Due to this the authors concluded the $Mg(OH)_2$ was successfully physically encapsulated within the matrix rather than any form of chemical immobilisation.

The reason for this relative stability was discussed by Collier et al [84] and Utton and Godfrey [77]. When considering the potential formation of new phases the relative solubilities of the hydroxide, sulphate and carbonate phases of the concerned reaction metal and calcium are important.

Anion/Cation	Ca^{2+}	Mg^{2+}	Fe^{2+}	Al^{3+}
OH^-	0.185	0.0009	0.00015	Insoluble
CO_3^{2-}	0.0014	0.0106	0.0067	--
SO_4^{2-}	0.209	26	Slightly soluble	31.3

Table 2-4: Solubility of hydroxide, carbonate and sulphate compounds for Ca, Mg, Fe and Al g/100cc at ambient temperature [85] reproduced in Utton and Godfrey (2010).

As table 2-4 shows the hydroxide phase is the least soluble for Mg, Fe and Al whilst for Ca the carbonate phase is the least soluble. This would mean for example Mg $(OH)_2$ is unlikely react and form $MgCO_3$ or $MgSO_4$ in preference to $Mg(OH)_2$ if exposed to common cement degradation mechanisms.

Due to the solubilities shown above Utton and Godfrey (2010) summarised that Al and Fe hydroxide sludges may potentially react with cement hydration products but are likely to remain in their hydroxide forms. The main consideration they raised however was the potential weakness an $Al(OH)_3$ containing wasteform could have to sulphate attack and the formation of ettringite due to the availability of aluminate ions.

2.4.3.2 Inorganic process sludges

Inorganic process sludges arise from pond storage and the reprocessing of spent fuel, generally they are described as being inorganic and unreactive. However one exception to this are wastes containing $BaCO_3$ which are encapsulated in a BFS:OPC grout [77].

$BaCO_3$ slurries are produced during nuclear fuel reprocessing at the Thermal Oxide Reprocessing Plant (THORP) at Sellafield. During processing the uranium oxide fuel is dissolved in nitric acid releases gases including $^{14}CO_2$ and ^{14}CO, these gases are passed through a caustic scrubber forming sodium carbonate. This solution is treated with $Ba(NO_3)_2$ which precipitates $Ba^{14}CO_3$, the final waste slurry contains 20-30 wt% $Ba^{14}CO_3$ precipitate which is then encapsulated in a 9:1 BFS:OPC system [86, 87].

Studies carried out on simulated $BaCO_3$ slurry in OPC and BFS:OPC matrices by Utton et al [86] indicated $BaCO_3$ significantly reacted with available SO_4^{2-} ions forming $BaSO_4$ with the freed CO_3^{2-} ions forming monocarboaluminate and potentially hydrotalcite. Further evidence for the uptake of sulfates via the addition of $BaCO_3$ has been reported; in one study $BaCO_3$ was added to decompose ettringite and stabilise sulphates via the formation of barite ($BaSO_4$) with the aim to mitigate against sulphate attack [88]. Both studies suggest the reactivity of $BaCO_3$ is determined by the relevant sulphate content within the cement system. Utton et al [86] concluded that the presence of $BaCO_3$ enhanced the hydration of BFS and the monocarboaluminate phase was stable effectively encapsulating the ^{14}C. The addition of large quantities of $BaSO_4$ into OPC cement systems has also been investigated and concluded $BaSO_4$ can successfully be included in mixes with a potential increase in reported $CaCO_3$ [89].

2.4.3.3 Flocs

Iron hydroxide flocs are produced from the treatment of liquids generated during the reprocessing of fuels typically in the Enhanced Actinide Removal Plant (EARP) at Sellafield [77]. EARP is a two stage process; firstly the ferric floc is formed by the addition of sodium hydroxide to acidic iron bearing waste streams, and secondly the precipitate is filtered using crossflow ultrafiltration [90]. Despite this ultrafiltration method Hildred (2000) reported a practical maximum solids content from EARP as 10 – 20 wt% due to viscosity limits for the plant equipment. This is important as the minimum cement to floc ratio achievable is limited by the amount of water which is within the floc. The resultant flocs provide sorption of radioactive elements whilst in situ within the effluent before subsequently being encapsulated in composite cements. However it has been demonstrated that flocs must be pre-treated prior to their encapsulation using slaked lime ($Ca(OH)_2$), the pre- treatment is reported to prevent subsequent cracking of the wasteform during curing [91].

Collier et al [92] investigated the reaction between the slaked lime and simulant ferric floc during the pre-treatment process. This work showed the floc reacts to form an amorphous hydrated calcium ferrite, additionally $CaCO_3$ from the carbonation of $Ca(OH)_2$ contributed to the formation of a crystalline iron hydroxyl carbonate phase ($Fe_6(OH)_{12}(CO_3)$). The study concluded that the pre-treatment allowed a pozzolanic reaction to occur between the PFA and $Ca(OH)_2$ during the cement matrix's hydration. This increased the amount of produced C-S-H resulting in a stronger stable wasteform [92].

Once the pre-treated simulant flocs have been encapsulated in a PFA:OPC composite cement it was reported that none of the crystalline phases detected during pre-treatment were detected after 90 days; with a new iron substituted silicate hydrogarnet observed $Ca_3Al,Fe(SiO_4)(OH)_8$ [91]. In a later more detailed study [93] Collier et al suggested that the iron in the floc reacted by substituting into and adsorbing onto the C-S-H phase formed during hydration in a similar manner to that described by Faucon et al [94]. This assumption was supported by EDS analysis showing iron was intimately mixed with hydration products and indications from TGA suggesting two C-S-H types, the second containing iron substituting within the silicate chains resulting in a more stable hydrate [93]. The results are interesting as they suggest there is a level of chemical and physical encapsulation involved in the immobilisation of flocs; this situation was well summarised by Milestone [5] who explained the distinction between immobilisation and encapsulation can become unclear.

2.4.4 Alternative encapsulation systems

As outlined by Milestone [5] to achieve successful encapsulation of the wide array of legacy wastes in the UK a range of cement systems with differing chemistries maybe required. One potential alternative is an acid-base cement system, based on mixing calcium aluminate cement (CAC) with acidic phosphate solutions [95]. Swift et al [96] looked at using phosphate modified CAC for the encapsulation of problematic radioactive wastes such as reactive metals due to their low pH. The study stated a sodium polyphosphate modified CAC developed the required strengths and had potential as an alternative encapsulation matrix; this work as was later expanded into comparative studies of aluminium corrosion within CAC and OPC systems [97].

Alkali-activated systems and geopolymers have also been touted as potential effective encapsulation systems [98, 99]. Fernandez-Jimenez et al [100] proposed the incorporation of Cs into the aluminosilicate gel of an alkaline activated fly ash matrix; Shi et al [101] has also demonstrated reduced leachability of contaminants from a alkali-activated cement when compared to a hardened Portland cement. Encapsulation of problematic metal alloys with metakaolin and Na-based geopolymers was investigated by Rooses et al [102, 103]; in these studies it was suggested that geopolymers were a suitable binder for Mg-Zr alloy encapsulation with respect to magnesium corrosion resistance. The use of metakaolin based geopolymers was further studied to immobilise Cs by Berger et al [104], the authors stated that geopolymers may be considered as alternative waste encapsulation materials. It was discussed however that the required efficiencies would only be realised with additional understanding of the reactions behind geopolymerisation.

Modifications to the blended Portland cement grouts have also been proposed by several authors [105, 106] using near neutral salts as additives to the composite cement powders. The addition of anhydrite and gypsum resulted in an increase in ettringite and reduction in corrosion and rate of hydrogen generation.

2.4.5 Cementitious backfill material

The phased geological repository concept (PGRC) was developed by Nirex for the long term management of long lived lower level radioactive wastes in the UK which were produced either during operation or subsequent decommissioning and clean-up of sites [107].

The PGRC is seen as a generic concept consisting of multiple barriers to the release of radionuclides, including physical immobilisation and chemical conditioning by a cement-based backfill material to reduce the mobility of many radionuclides [108, 109]. An outline of the containment phases in the PGRC including the cement-based backfill for chemical conditioning is shown in figure 2-10.

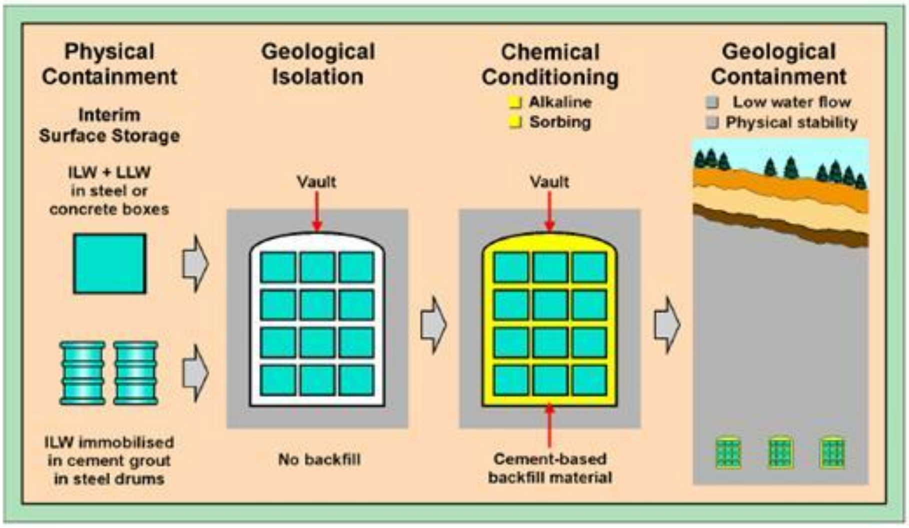

Figure 2-10: The Nirex Multi-barrier Repository Concept [105]

In the repository this chemical conditioning is one of the final steps of operation via 'backfilling of the repository at a time determined by future generations' [107]. This cement based backfilling would entail the use of Nirex Reference Vault Backfill (NRVB), a specially formulated cement grout that would be flooded into the vault to surround the isolated waste packages. The NRVB is an important barrier in the disposal concept and is designed to complement the cementitious encapsulation matrices discussed earlier for immobilisation of various waste streams. The materials primary purpose however was to condition inflowing groundwater to a high pH limiting the solubility of actinides and transition metals. A description of the essential and desirable characteristics of NRVB is shown below in Tables (2-5 and 2-6) [110].

Essential Requirements of a Vault Backfill

- Long term pore water must be maintained ay pH 10.5 or greater to provide chemical retention of radionuclides in the repository near field
- Cube strengths of not less than 1.5 MPa at 7 days and not less than 4.0 MPa at 28 days are required to provide adequate support for the placement of successive waste package and backfilling layers.
- A cube strength limit of 10 MPa at any age up to 50 years to assist grout removal should there be a future need to retrieve backfilled waste.
- Workability must be suitable for flow without vibration into a horizontal space 5m x 3m x 75mm high, which maybe typical under-package space.
- The mix must be suitable for pumping along a horizontal pipeline at most 250m in length.
- Bleeding/settlement must not exceed 2% to reduce the possibility of under-package void formation and surfaces of weakness in the backfill.

Table 2-5: Essential Requirements of a Vault Backfill [108]

Desirable Characteristics of a Vault Backfill

- Act as a chemical barrier to migration of long-lived radionuclides by providing:
  a) high pH to inhibit solubility
  b) good sorption capacity
- Sufficiently permeable to promote homogeneous aqueous chemistry and to enable gas transport
- Inhibit corrosion of steel packages
- Relatively low heat of hydration
- The use of cement additives (e.g. organic polymers), which might compromise the cement performance as a chemical barrier of the engineering properties, should be avoided.
- Mineral composition should be sufficiently durable to provide long term chemical conditioning of repository porewater.
- Possess well-understood mineral characteristics, which can be predicted during the repository evolution.
- Use materials which can be reasonably assured in terms of quality and quantity during repository operational period. Suitable for placement by remote methods in

waste vaults.

- Self-levelling and compacting and able to provide a firm level base for placement of further packages.
- Suitable for easy excavation to allow retrieval of waste packages if that was required.
- Relatively inexpensive to produce.

Table 2-6: Desirable Characteristics of a Vault Backfill [108]

Nirex completed various laboratory tests on the bulk mixing, performance and emplacement of NRVB against the above criteria, these studies were supported by detailed investigations of the physical chemistry and thermal properties of the material [111]. After these investigations the Nirex Reference Vault Backfill (NRVB) has been defined with one cubic metre containing [110]:

Ordinary Portland cement (OPC)	450 kg	(26%)
Limestone flour (Calcite)	170 kg	(10%)
Hydrated Lime (Calcium Hydroxide)	495 kg	(29%)
Water	615 kg	(35%)

Most work on NRVB has focussed upon the chemical containment potential of the material particularly solubility limitation created by the high pH conditions and sorption of any potential radionuclides due to NRVB's high active surface area [112-115].

Relatively little published academic work is available on the hydration and resultant composition of the NRVB material. McCarther et al [116] studied the short-term hydration and drying response of NRVB using electrical conductance and gravimetric measurements conducted at varied temperatures and humidities. The author found an increasing ambient temperature lead to an expected reduction in setting time and increased rate of hydration. It was also noted the drying rate of NRVB didn't follow a classical two stage process reflecting the change in state of the grout as it hydrates, this again would be expected as cement hydration products are formed during the time scale studied from initial mixing up to 7 days hydration. In a later paper [117] using the same techniques McCarther et al discussed how the early hydration of NRVB can be divided into three regions resulting from bleed effects attributed to the setting processes and increases in rigidity of the grout which coincided with a maximum internal temperature. In these closed cell experiments a surface zone setting gradient was proposed in the near surface 15-20 mm indicating a slow increase in rigidity due to increasing water content from bleed effects. At depths >30 mm electrical conductance decreased at a faster rate which was attributed to a more rapid increase in pore structure development due to hydration of the constituent materials. Butcher et al [118] led a study into leached NRVB samples which included a level of microstructural analysis; unleached samples showed a level of portlandite and C-S-H present once subjected to leaching however no portlandite was identified.

Collier et al [119] led an industry study into the interaction between NRVB and the main cementitious matrix grouts BFS:OPC and PFA:OPC, with samples cast singularly or in contact with NRVB at varying curing temperatures. The report characterised the interface regions and bulk materials after one year of curing looking at their constituents and microstructure using SEM EDX and XRD. The main phases found in the hardened NRVB material were portlandite, calcite and C-S-H. The recommendation from this report was to examine the materials further using TEM and thermal analysis techniques to investigate the nature of the formed C-S-H phase.

2.5 Conclusions from Literature Review

The literature review has shown a significant amount of work has been completed on intermediate nuclear waste streams within blended cement grouts. However, the often limited scope of the investigations with regards to the selected experimental techniques fails to address adequately the potential for possible ion incorporation into and modification of the C-S-H phase. An example of this limitation is observed in investigations into the treatment of flocs by Collier et al [91] who stated 'could this partly be an iron incorporated C-S-H?' during their conclusions. The experimental techniques discussed in Chapter 3 will attempt to push our knowledge beyond the use of XRD and SEM to analyse waste containing grouts. This will be accomplished by detailed analysis of the C-S-H phase which is responsible for much of the physical and chemical immobilisation in cements [77]. Samples will then be compared to the Richardson and Groves' structural model for C-S-H to guide insights into any modification due to the simulant waste inclusion.

The reviewed literature does include a wide range of studied samples, however, the majority do not contain results from aged cement pastes over one year after curing. This is of interest due to the known potential for cement phases to alter with time rather than reaching an unchanging 'steady state'. When considering the long-term storage of these waste forms it seems sensible to characterise 'aged' samples where possible for greater satisfaction into their inherent stability.

Limited amounts of microstructural characterisation and data has been collected on NRVB grout samples, due to a greater focus being placed upon the optimisation of the chemical containment potential of the material. Additional work therefore is required into the hydrated composition of NRVB and the effects of varied curing conditions. It is anticipated this will be addressed during this study and will build on the current knowledge of NRVBs sorption and chemical containment capability.

Chapter 3 : Experimental

3.1 Materials

The samples used in this study were provided by the National Nuclear Laboratory and by Magnox Ltd at the request of the NDA. The known mixture designs of the NRVB, PFA/OPC and BFS/OPC samples are given below along with the waste: binder ratios (w/b) when known. Many of the samples studied are from long term storage and originate from previous industry research carried out over the past two decades.

Sample IDM	Formulation of encapsulate	Composition	w/b[*]	Waste System
97-118	3:1 BFS:OPC	75% BFS, 25% OPC	1.10	Al-based slurry[◇]
97-120	3:1 BFS:OPC	75% BFS, 25% OPC	1.10	$Mg(OH)_2$ slurry[◇]
93-07	9:1 BFS:OPC	90% BFS, 10% OPC	0.33[◆]	$BaCO_3$ slurry
93-12	5:4 PFA:OPC	55.5% PFA, 45.5% OPC	1.125	Fe - Floc[◇]
91-13	5:4 PFA:OPC	55.5% PFA, 45.5% OPC	1.125	Fe - Floc[◇]
93-001	5:4 PFA:OPC	55.5% PFA, 45.5% OPC	1.125	Al - Floc[◇]
NRVB	OPC:CH:CC	40% OPC, 24% CH, 15%CC	N/A	N/A

[*] w/b : waste to binder ratio (binder is classed as BFS:OPC or PFA:OPC blends) calculated by mass.

[◆] Estimated from literature on similar samples

[◇] Sample preparation included pre-treament with lime prior to encapsulation

Table 3-1: Sample formulations studied in this investigation

For the successful encapsulation of the waste-forms within a sound solidified monolith the systems invariably underwent levels of pre-treatment before addition and mixing with their relevant cement powders. Details for the pre-treatment and preparation processes are given below in the following sections.

3.1.1 Magnox Ltd sample preparation

Mixes 97/118 and 97/120 were produced to assess the effects of sludges arising from corrosion products on candidate cement formulation envelops. They were designed to inform predictions of the short and long term evolution of the products formed when the sludges are solidified for onsite interim storage and eventual disposal. The sludge's were represented by inactive simulants comprising of aluminium/ferric floc and magnesium hydroxide, both samples were produced in 1997 and are described below:

- 97/118 is Al/Fe floc pre-treated with 10% Limbux lime - 3:1 BFS/OPC; waste/cement = 1.10

- 97/120 is Magnox sludge pre-treated with 10% Limbux lime - 3:1 BFS/OPC; waste/cement = 1.10

The waste/cement ratio was calculated assuming the waste to be Al/Fe floc or waste dry solids + mix water or a combination of both. Cement is classed as blends of BFS/OPC. Lime is not included in calculating the waste/cement ratio.

The Magnox sludge simulant was prepared with magnesium hydroxide which was supplied by Pennine Darlington Magnesia Ltd as a dry powder (trade grade PH9). The simplified aluminium hydroxide/ferric hydroxide or alumino/ferric floc material containing silicates was defined on the below composition:

Based on waste sampling data the average dry solids contents was approx 7.6 wt% with a typical chemical composition of [120]:
Silicates 24.7 wt%
Aluminium hydroxide 64.7 wt%
Iron hydroxide 3.9 wt%

Table 3-2: Average chemical composition of dry solids in simulant waste 97/118

The cementitious powders used in this programme of work were a Portland cement class 42.5N, formerly ordinary Portland cement (OPC) supplied by Castle Cement Ltd. Ground granulated blast furnance slag (BFS) supplied by Frodingham Ltd in bulk to British Standard specifications [121].

Mixes were prepared by water being added to the dry simulant materials with the cement powder added to the slurry or Al/Fe floc within 2 minutes. Mixing was continued for 10 minutes on the 20 litre mixes and 20 minutes on 60 litre scale mixes to obtain a homogeneous product; certain variations to this procedure were dependent on the pre-treatment processes.

3.1.2 NDA/NNL Samples

The samples provided from the NDA and NNL focused upon the ferric and alumino flocs produced during treatment of radioactive liquid effluent as part of the Enhanced Actinide Removal Plant (EARP). The composition of flocs is seen as being variable due to differing conditions during their manufacture, additionally the flocs are known to age during storage [91, 122].

The ferric and alumino hydroxide flocs studied in this work are inactive simulants representing the in service flocs ; work characterising the floc preparation was completed by Collier et al [92]. Flocs were pre-treated with $Ca(OH)_2$ at 10%wt to allow for successful encapsulation into the cemented waste-form, without pre-treatment cracking will occur during hydration. The reported main phase formed by this pre-treatment was an X-ray amorphous hydrated calcium ferrite with an estimated composition of $2CaO.2Fe_2O_3.12H_2O$ alongside small amounts of calcite, $Ca_6Fe_2(SO_4)_3(OH)_{12}.26H_2O$ and $Fe_6(OH)_{12}(CO_3)$ [92].

Additionally sample IDM 93-07 was sent from the NDA batch which consisted of a barium carbonate slurry encapsulated in a very high level replacement BFS:OPC composite grout. As discussed in chapter 2; $BaCO_3$ slurry containing radioactive ^{14}C is produced during waste treatment of spent oxide fuel. The slurry in service has been shown to include significant levels of soluble salts such as sodium nitrate [87], however for estimation of the effects of $BaCO_3$ 30wt% of pure grade $BaCO_3$ is commonly added to create simulant samples. The $BaCO_3$ powder is added to a 9:1 BFS:OPC system with a water to solid ratio designed to mimic that of a slurry added to cement powders as would be the case in service.

These samples were taken from full scale (500 litre) non active waste-cement development products produced in the early 1990's. Sellafield flocs are encapsulated in a 5:4 PFA:OPC system, pre-blended cement powders are mixed with the floc at a ratio of 1:1. As previously discussed flocs are pre-treated prior to encapsualtion with $Ca(OH)_2$. The full scale development products were cured in normal operating conditions. Cores were later removed from the full scale products in 2003, bagged in polythene sleeves and stored in a laboratory environment since 2003. In 2011 a number of these cores approximately 50mm in diameter were provided for this study, subsequently they were resealed and stored at 20˚c. The samples provided by the NNL via the NDA were described as follows:

- Sample Ref 6 IDM 93/07 - $BaCO_3$ in BFS:OPC from the Waste Encapsulation Plant
- Sample Ref IDM 91/13 Waste Packaging and Encapsulation Plant (WPEP) - Iron Hydroxide Floc with PFA:OPC
- Sample Ref IDM 93/12 WPEP - Iron Hydroxide Floc with PFA:OPC
- Sample Ref 93/001 - $Al(OH)_3$ Floc with PFA:OPC for WPEP

3.1.3 NRVB Samples

100-200ml specimens of NRVB grout were prepared and a low shear mixer was used for the initial mix. The grout was then mixed for 5 minutes at 6000rpm with a high shear mixer and finally mixed for 1 hour with a low shear mixer. The NRVB grout mixture was added to pots and cured for 7 days and left to cure at several temperatures (ambient, 35˚c and 80˚c).

Sample were subsequently placed within HDPE bottle (250ml) and heat sealed with lengths of 500 gauge polythene tubing, with care taken to minimise the amount of air enclosed within the specimens. The bottles were then placed inside lined steel cans and immersed in water. The integrity of the sample cans was confirmed using a weighing programme after 1 month and 1 year.

After 1 year of hydrothermal storage the samples were removed from the sealed storage cans, visually inspected and removed from their curing pots. The samples were then sliced into quarters using a masonry saw before subsequent analysis and storage in sealed plastic bags with the air expelled. A selection of these quartered samples cured at ranging temperatures was then provided to the University of Leeds for this study.

3.2 Introduction to Thermal Analysis

Thermal analysis refers to a suite of techniques where a material's properties and/or reaction products are measured as a function of temperature. The term encompasses many techniques including thermogravimetry (TG), differential thermal analysis (DTA), differential scanning calorimetry (DSC) and evolved gas analysis (EGA)[123].

DTA involves heating the sample of interest (S) and an inert reference (R) under identical conditions whilst recording any temperature difference between the sample and reference. This differential temperature is then plotted against time or temperature and changes in the sample which lead to the adsorption or evolution of heat can be detected relative to the inert reference; a schematic representation of this is shown in figure 3-1. The convention when plotting DTA is that energy evolved by a transition or reaction is positive and an endothermic process, where heat is absorbed by the sample (for example during the melting of a metal) is negative. By determining the nature and temperature of observed peaks DTA can be used to obtain useful qualitative and quantitative analysis of a sample [123]. In contrast TG is a measure of the weight change of the sample as the temperature increases or decreases. This will occur as the phases decompose and gases are released. The TG data from OPC shown in figure 3-2 clearly illustrates the power of the technique in identifying physical changes within a material with temperature. Commonly both techniques are used together as a combined analysis which is normally referred to as simultaneous thermal analysis (STA).

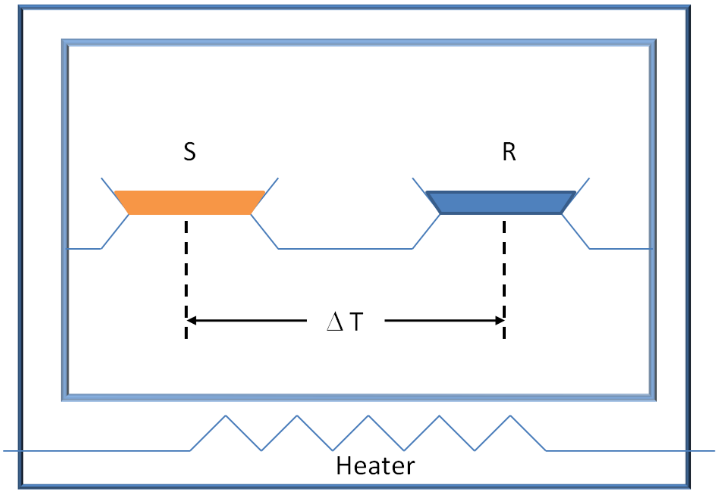

Figure 3-1: Schematic diagram of a DTA cell

The combined techniques of TG and DTA are frequently used in cement science to quantify the composition of phases within pastes. The primary reactions that occur during the heating of a cement paste sample are summarised below [124] :

- 30 - 105 ˚C: the evaporable water and a part of bound water, all evaporable water assumed lost at 120 ˚C.
- 110 - 170 ˚C: decomposition of gypsum, ettringite and the loss of water from some carboaluminate hydrates [125].
- 180 - 300 ˚C: loss of bound water from decomposition of the C-S-H and carboaluminate hydrates.
- 400 - 550 ˚C: dehydroxylation of portlandite (calcium hydroxide).
- 700 - 900 ˚C: decarbonation of calcium carbonate.

The resultant thermogram of a cement paste after a combined TG and DTA experiment is shown below in figure 3-2. In a typical OPC based cement paste such as this the most observable reactions are for the dehydroxylation of the portlandite (CH) phase and release of carbon dioxide from calcium carbonate.

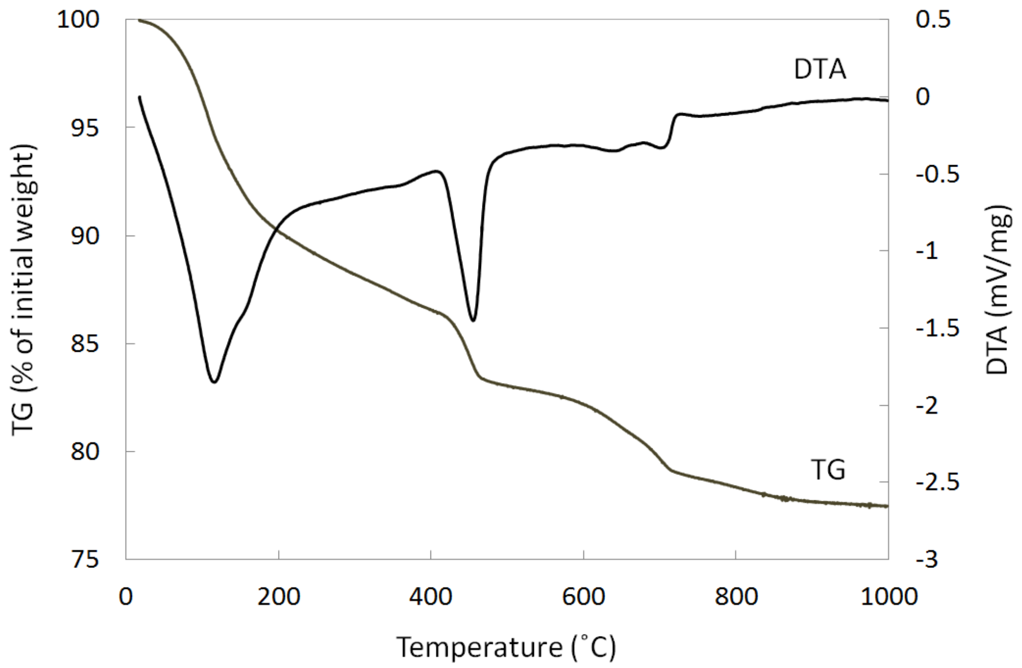

Figure 3-2: DTA/TG thermogram of a 28 day OPC cement paste

As shown in figure 3-2 the TG and data is used to quantify the amounts of portlandite (CH), calcium carbonate within the cement pastes. This is useful to assess the level of pozzolanic reactions using supplementary cementitous materials or level of carbonation in a sample [126-128]. To enhance the available data from thermal analysis evolved gas analysis (EGA) was used in conjunction with the aforementioned techniques to identify the gases generated as a function of the measured temperature.

3.2.1 Experimental Procedure

STA was performed using a Stanton-Redcroft STA 1000, the samples were crushed and ground into a fine powder in a agate mortar and pestle. Approximately 15-18 mg of powdered sample was placed into a platinum crucible in the STA apparatus. The samples were heated from 20-1000˚C at a heating rate of 20˚C/min; this was done in a constant flow of nitrogen at a rate of 58 ml/min. When available EGA analysis using a basic mass spectrometer (Cirrus Mass Spectrometer, MKS Spectra) was carried out, the DTA was connected via a heated capillary tube and acts as the ionic source. The evolved gases forced into the mass analyser by a vacuum inducing turbo pump, the resultant signal is amplified and provides a mass spectrum plotted as a function of time or temperature.

Once completed the TG curve with the % weight loss plotted against temperature was used to estimate the amount of CH and calcium carbonate present in the sample where relevant. The determination of the amounts of these phases is displayed below in equations 3-1 and

3-2. As discussed the dehydration of calcium hydroxide (CH) occurs in the temperature range of 400-550˚C. A major peak observed in figure 3-2 can be described as a percentage of calcium hydroxide present by the following:

$$Ca(OH)_2 \rightarrow CaO + H_2O \;\; (400 - 550°C)$$

As dehydration of one mole of water (18 gmol^{-1}) results from one mole of $Ca(OH)_2$ (74 gmol^{-1}) therefore when *y* is the % mass loss from 400-550˚C:

$$Percentage\ of\ CH = \left(\frac{74}{18}\right) y$$

Equation 3-1: Calculation of CH%

Similarly the percentage of calcium carbonate (CC) present at 600-800˚C can be determined by:

$$CaCO_3 \rightarrow CaO + CO_2$$

As decomposition of one mole of CO_2 (44 gmol^{-1}) results from one mole of $CaCO_3$ (100 gmol^{-1}) therefore when *x* is the % mass loss from 600-800˚C.

$$Percentage\ of\ CC = \left(\frac{100}{44}\right) x$$

Equation 3-2: Calculation of Calcium Carbonate %

3.3 Introduction to X-ray diffraction

XRD was used to identify the presence of crystalline phase(s) within the solidified products. This technique consists of directing X-rays at the sample and because crystals are symmetrical arrays of atoms containing rows and planes of high atomic density, they are able to act as a 3-D diffraction grating. When X-rays interact with a solid, elastic scattering of X-ray photons occurs in any direction. When atoms spaced at regular intervals are irradiated the scattered radiation undergoes constructive interference which results in well-defined X-rays leaving the sample at various angles which give rise to diffraction peaks which are a 'finger-print' of the crystalline phases present in the probed volume. This constructive interference can only occur under highly restrictive conditions defined mathematically by Bragg’s law, as shown below [129].

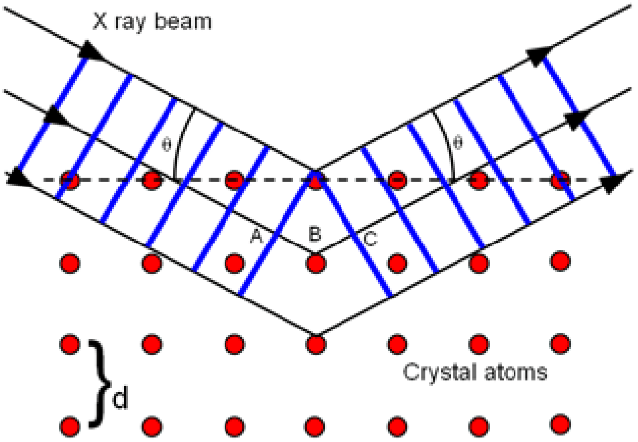

Figure 3-3: Bragg's Law [130] where AB and BC is the additional distance travelled if incident beams are to continue travelling adjacent and parallel. Since nλ=AB+BC and BC= d sin θ and BC=CD this equates to nλ=2BC which gives Bragg's law as defined below.

Bragg’s Law is defined as:

$$n \lambda = 2d \sin \theta$$

Where n is an integer, λ is the wavelength of the X-ray beam, and d is the interplanar spacing in angstroms and θ is the angle of incidence in degrees.

By measuring the scattering angle and the intensity of peaks it is possible to identify the various phases present in the sample. Figure 3-4 shows a diffraction spectrum where the 2θ position of the individual peaks are indicative of the material, in this case calcite. Therefore by matching the recorded positions and intensities of the peaks with those of known crystalline phases, it is possible to characterise the phases present in the sample material. The proportion of a given phase can be estimated by comparing the percentage of a phase as shown by XRD with the percentage in the total sample of the same phase. The percentage content in the total sample may be determined by alternative characterisation techniques or by adding a known quantity of crystalline material (e.g. Al_2O_3) to the sample.

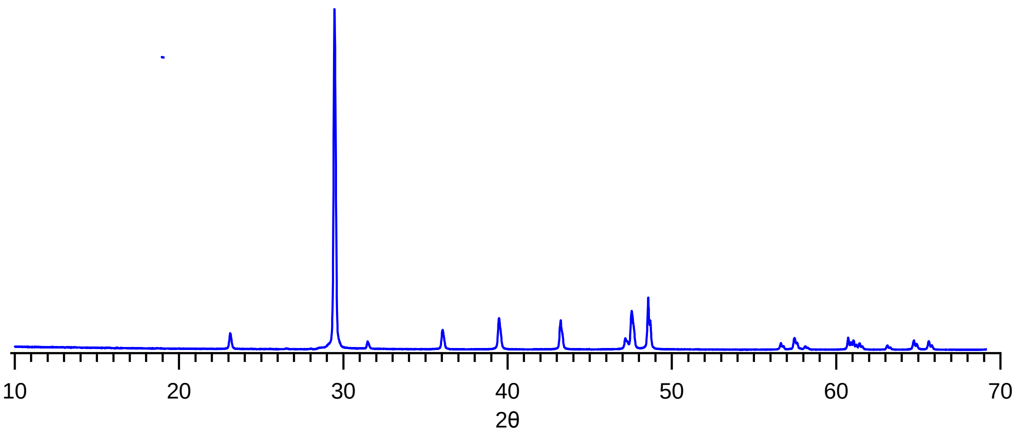

Figure 3-4: Experimental XRD spectra of calcite

Within cement samples XRD is an important technique as each crystalline phase will produce a unique diffraction pattern which can be identified. From this data additional information on a minerals structural state can be asserted. This is significant ,especially if new phases are being formed within the studied systems [131].

3.3.1 XRD experimental procedure

The XRD measurements were performed using a Bruker D2 phaser diffractometer with a lynxeye detector, operated with Cu Kα radiation at 10mA and 30kV. Samples for XRD were freshly sliced from the provided cores and then crushed and ground into a fine powder in an agate mortar and pestle. Samples were backfilled into the sample holders to reduce preferential orientation and mounted onto a spinning stage set at a rotation of 2 turns a second. The samples were run on a continuous scan mode over the range of 5 - 65˚ 2θ with a step size of 0.024˚ (2424 steps) and an acquisition time of 5 seconds. Samples were additionally run containing a 10%wt internal standard of corundum (Al_2O_3) under the same conditions; this was to allow calibration of peak positions with the known standard.

The resultant XRD patterns were collected and analysed with peak listings, phase identification and matching completed with Pan'alytical's X'Pert Highscore software with attached databases from the International Centre for Diffraction Data (PDF-4). Additional analysis of the samples diffraction properties was completed using Crystaldiffract and Crystalmaker software (CrystalMaker Software Ltd). This software allowed for the modification and comparison of crystal phases from databases with the measured experimental results.

3.4 Introduction to Solid-State MAS NMR

Nuclear magnetic resonance (NMR) has proven to be a powerful and versatile spectroscopy tool. The phenomenon of nuclear spin and its relative isolation from its surroundings makes it an ideal non-interfering probe of the electronic environment [132].

The basic principles of NMR are based upon the physical spinning of the nucleus of a certain selected chemical element. Investigated nuclei must have spin properties to be used in NMR (eg ^{13}C, ^{27}Al , ^{29}Si). When nuclei with a nonzero spin property are placed within a strong magnetic field an energy transfer is possible producing a spilt of energy levels known as the Zeeman interaction [133] and is displayed graphically for a proton with spin I=1/2 in figure 3-5. The energy transition and absorption or emission of photons corresponds to a radio frequency which can be measured and yield an NMR spectrum for the nucleus under investigation.

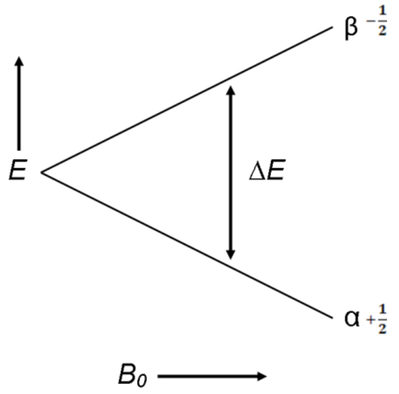

Figure 3-5: Energy level diagram for spin with $I = \frac{1}{2}$ in a magnetic field B_0 [134] (α=high level energy, β=low level energy)

In summary the nonzero spin nucleus is placed in a strong external magnetic field and the resulting spilt of energy levels of the nucleus will depend on the different local structural environments. The nucleus is then perturbed by an applied pulse of radiofrequency radiation which will induce electronic transitions. The perturbation to the nucleus is then removed returning it to its initial state which will absorb or emit a photon, the frequency of which is measured as a reported chemical shift (δ)[133].

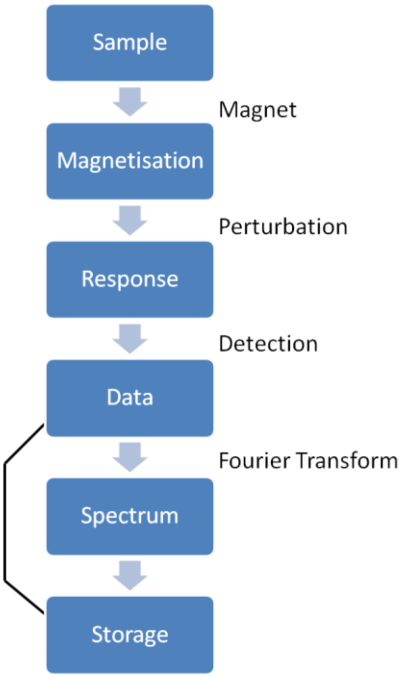

Figure 3-6: A conceptual block diagram of the pulsed Fourier transform NMR experiment [134]

The adoption of NMR to materials in solid form has developed at a slower rate than its solution-state counterpart. This is primarily due to the produced broad peaks created by a number of interactions notably the dipolar and quadrupolar interactions and spin - spin relaxation which can generally be ignored in solutions [132]. Additionally the second major difference between NMR in solids and solutions is generated by the chemical shift anisotropy (CSA). This chemical shift is produced by electrons shielding the nucleus from the applied magnetic field, due to this chemical shifts can take on directional properties [134]. To overcome this the solid sample can be spun at the magic spinning angle (MAS) at high speed (10-15kHz), in solids the dipolar coupling and CSA contain an angular dependence of the form $3\cos^2\theta$-1. As when θ= 54˚47', $3\cos^2\theta$-1 will =0 this angle therefore is referred to as the magic spinning angle. By spinning the sample at this angle to the axis of the applied magnetic field it will reduce the potential observed line broadening in solid-state samples.

NMR has proved very useful in probing the atomic environments of cement pastes, this is primarily due to the fact that NMR has no limitation to crystalline phases. Additionally NMR is capable of monitoring changes to the structural order over time and show the development of hydrated phases. Most solid-state NMR studies have been based around the study of ^{27}Al MAS and ^{29}Si MAS NMR; this reflects both the importance of these elements in cement science and the natural abundance of these elements allows for their acquisition to be experimentally viable [135, 136]

3.4.1 MAS NMR experimental procedure

The ^{29}Si NMR spectra collected at Leeds University were acquired from a Varian Infinity Plus 300 MHz spectrometer equipped with Chemagnetics style MAS probes and 7.1T magnet, the instrument was referenced to a belite (C_2S) sample with a known peak at -71.3ppm. Samples were sliced from the supplied cores and then crushed and ground into a fine powder which was packed into a 6mm zirconium spinning rotor. The examination of the sample was operated with a spinning speed of 6500Hz, pulse delay of 2s, pulse width of 4.0µs and an acquisition time of 20ms over approximately 32 hours.

The quantitative information from the ^{29}Si MAS NMR relating to the structural order of the sample included the mean aluminosilicate chain length (MCL), Al/Si ratio, percentage of silicate type and estimation of hydrated material. These were obtained through the deconvolution of NMR spectra using Igor Pro 6.0 software (Wavemetrics) utilising a user made procedure. The spectra were fitted with the initial setting of a baseline to a cubic multinomial function and the parameters (intensity, peak shift, shape and width) were then fitted to the experimental spectrum. The integrated areas below each of these fitted curves was then used to produce the structural order data discussed previously.

Due to issues with the NMR facilities at Leeds additional solid-state ^{29}Si NMR spectra for the samples were obtained at the EPSRC UK National Solid-state NMR service at Durham University. Samples were run as direct excitation experiments on a Varian VNMRS 400 spectrometer using neat tetramethylsilane as a reference standard. The samples were loaded into a 6mm rotor spun at 6800Hz with a pulse delay of 5s, pulse width of 6.2µs and an acquisition time of 30ms for on average over 1000 repetitions.

All solid-state ^{27}Al NMR spectra for the samples were obtained at the EPSRC UK National Solid-state NMR service at Durham University. Samples were again ran as direct excitation experiments on the same spectrometer using 1M aqueous $Al(NO_3)_3$ as the reference standard. The samples were loaded into a 4mm rotor spun at 14000Hz with a pulse day of 0.2s, pulse width of 1.0µs and an acquisition time of 10ms for on average 7000 repetitions.

3.5 Introduction to Transmission Electron Microscopy (TEM)

To understand a materials behaviour and to facilitate the design of new or improved materials it is necessary to characterise both composition and microstructure at the highest levels of resolution possible. Transmission electron microscopy (TEM) is an established method for the characterisation of materials and provides the capability for physical and chemical analysis [137]. The use of TEM in cement science and characterisation was reviewed by Richardson (2002) which outlined the historical context of microscopy in this field and the possibilities of TEM imaging and X-ray analysis [138]. The mentioned review discusses the various studies which have utilised TEM-EDX to examine the microstructure of cements and specifically calcium silicate hydrates [10, 139-141].

The basic layout of a typical transmission electron microscope is shown in figure 3-7, the electron gun is situated at the top of the column which is kept under vacuum. The resultant electron beam is focused by one or more condenser lenses (C_1 & C_2) often with variable apertures onto the specimen which sits in a holder inserted via an airlock. The objective lens (*O*) sits below the sample above an intermediate lens (*I*) both of these lenses also have variable apertures, the projector lens *P* then forms the final image onto the fluorescent screen; below this screen a film, plate or digital camera sits enabling images to be saved [130]. The theoretical limit of TEM resolution is limited primarily by the aberrations of the objective lens the main aberrations (Chromatic, spherical and axial) therefore should be minimised; to accomplish this a routine alignment procedure is followed when using the TEM prior to sample examination [142].

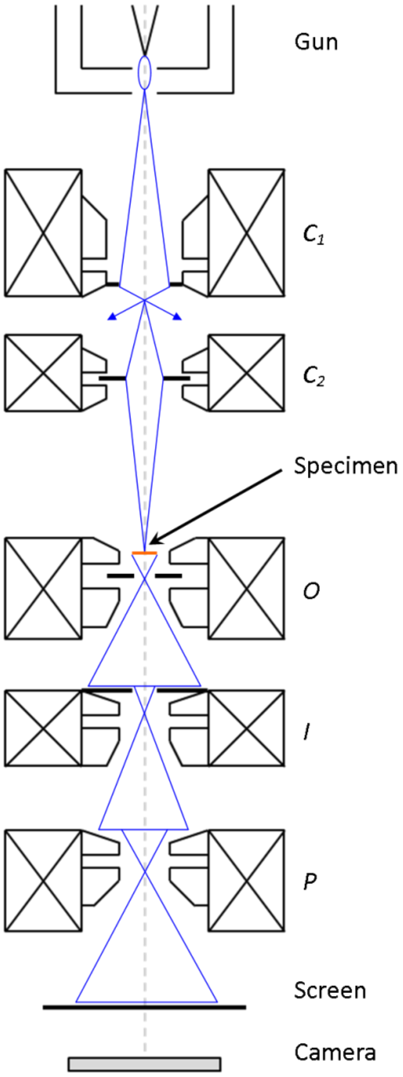

Figure 3-7: Schematic representation of the layout of the main TEM components figure adapted from Bowen and Hall [130]

One primary disadvantage of TEM analysis is the potentially higher levels of difficulty in producing electron transparent samples which can lead to extensive preparation techniques depending on the application; a review of preparation techniques for thin films and bulk samples is discussed by Bowen and Hall [130]. Additionally a level of care and attention must be exercised by the observer during sample examination to reduce the potential for damage due to beam exposure. This can be reduced by utilisation of the lowest possible magnifications for general viewing [138] and by simply minimising the exposure and 'idle' time in sensitive areas. Rößler et al [143] discussed the examination of C-S-H structure using TEM and proposed an electron dose of 6.4×10^{3} e Å^{-2} at room temperature above which its crystalline structure is degraded leaving only an amorphous diffraction pattern.

3.5.1 TEM Experimental Procedure

The samples were sectioned and then cut into thin 1mm slices using a low speed saw (ISOMET) using a diamond edged wavering blade, the slices were then dried at 50˚C after cutting. Samples were then flatted using a 600 micron SiC paper and attached to a glass slide by cyanoacrylate glue. Once attached the slice was thinned by hand to about 30µm thick or until the samples were sufficiently thin enough to be able to read text though it with the aid of a light box. The samples were thinned using 600, 1200 and 2400 micron SiC papers whilst being constantly checked for uniform thinning or grit damage. Once thinned sufficiently the slice and glass slide was immersed in acetone to allow the thinned sample to be removed, once removed copper TEM slot grids were glued to both sides of the sample using epoxy. After this the sample was checked under an optical microscope and then transferred to an ion beam miller (Fischione Model 1010 low angle miller) for thinning for TEM observation. The conditions used for milling were 4kV, 3mA at a milling angle of 15˚ with constant rotation using argon gas, during milling the sample was cooled using liquid nitrogen to avoid heat damage and kept at vacuum. Once milled satisfactorily with a hole in the centre the samples were coated with approximately 2nm of carbon (Agar Turbo Carbon Coater with film thickness monitor) and then stored in vacuum desiccators until observation. Samples were produced ready for observation to reduce the amount of required storage time and possible atmospheric affects upon the thinned samples.

The samples were examined in a FEI Tecnai TF20 FEGTEM with a LaB_6 filament operated at 200kV. The TEM was equipped with an Oxford Instruments 80mm X-Max SDD detector and associated INCA EDX system and software for elemental analysis. Imaging of the microstructure used a Gatan Orius CCD camera. Whilst studying the microstructure of the samples a maximum basic magnification of 10000x was used with higher magnifications only utilised when a site of interest was found. EDX analysis of the sample was performed at 17500x unless additional magnification was required to analyse 'pure' phases adequately. Acquisition time for EDX was limited to 45s and performed at spot size 6. Prior to EDX analysis the selected area electron diffraction (SAED) aperture was inserted and diffraction mode used to check the analysis area (often C-S-H) for intermixed crystalline phases such as calcium hydroxide. Due to the interest in additionally formed phases in the cements hydration, potentially due to the simulant waste addition, intermixed phase analyses where not discarded; however the data points were removed from pure phase composition estimations later. Micrograph imaging was performed at 6500x - 27500x magnification with the exposure time user controlled via software to reduce possible beam damage.

3.6 Introduction to Scanning Electron Microscopy (SEM)

In scanning electron microscopy (SEM) a controlled beam of electrons usually generated by thermionic emission from a heated tungsten filament is directed at the specimen. When the incident beam of electrons hits the specimen the electrons are either scattered or adsorbed producing various signals including secondary electrons (SE), backscattered electrons (BSE), X-rays and auger electrons.

The most commonly used signals on the SEM for imaging are secondary and backscattered electrons. Secondary electron images (SEI) are useful for surface and fracture imaging of microstructure phases due to the high resolution possible. This high resolution is due to the majority of the SE signal being generated from a region only a little larger than the diameter of the incident beam; therefore SE has the smallest sampling volume giving better spatial resolution than other signals [144]. SEM SEI imaging has been used extensively to the study of fracture surfaces of cement providing useful information on the microstructure of cement and morphologies of various phases [138]. Backscattered electron (BSE) imaging offers compositional contrast based images based upon the relative atomic number of the elements images; phases of the greatest mean atomic number appear brightest on the image [145]. Successful BSE imaging relies upon minimizing topographical variations on the sample surface to represent phases accurately [146]. Figure 3-8 shows a basic schematic of the generation areas of secondary and backscattered electrons in SEM analysis.

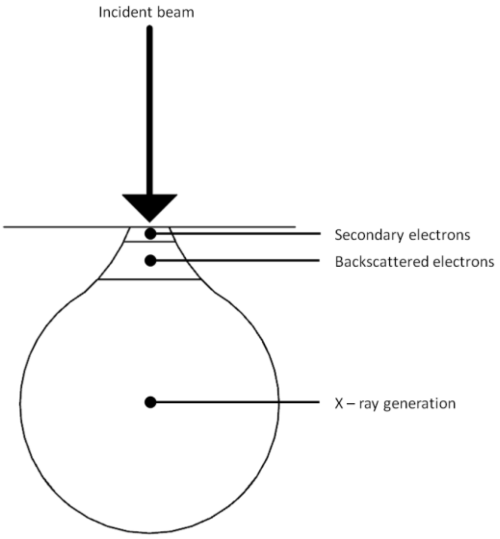

Figure 3-8: Schematic of the interaction volume created in the SEM

Energy dispersive X-ray analysis (EDX) is used to help characterise the chemistry of phases found during SEM BSE imaging. The method is based upon the generation of characteristic X-rays in the atoms of the specimen by the incident beam electrons as shown in figure 3-9. When the incident electron hits an atom it can cause an inner shell ionization. This results in an empty space which is subsequently filled by an electron transition from a higher energy state, the resultant freed energy is ejected in the form of an X-ray. The energy of the ejected X-ray is characteristic for the element from which they originate and so allow you to gain data on the elements present within the specimen [147].

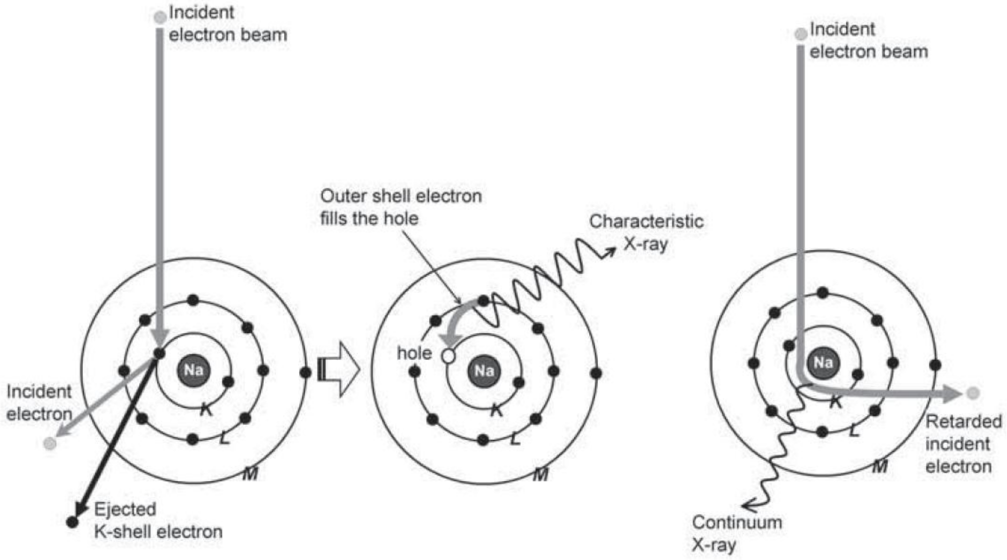

Figure 3-9: Generation of characteristic and continuum X-rays in atoms of the specimen by incident electrons [147]

Certain considerations must be made when using SEM EDX analysis; since the X-ray generation volume in a bulk specimen is estimated at 1-2µm^3 compositional analyses of hardened cements will often correspond to a mixture of different phases [138]. The actual size of the interaction volume as illustrated in figure 3-8 will depend upon the examined specimens' physical properties (density, composition) and the operating conditions of the microscope (accelerating voltage, probe diameter) [148]. Wong and Buenfield applied a Monte Carlo technique to simulate the interaction within a cement material; the authors estimated that the maximum penetration depth was 1.5µm at 10KeV and 5.0µm at 20KeV with a hemispherical interaction volume [148].

3.6.2 SEM sample preparation

For SEM analysis approximately 5mm slices of the cement grout were cut from the segmented cores using a low speed cut off saw (Buehler Isomet) equipped with a diamond edged wavering blade. After cutting samples were simply dried in a 35˚C oven and if required stored in a desiccator before further preparation. Samples were then flattened on one surface using 1200µm SiC paper before being vacuum impregnated using a low viscosity cold setting embedding resin (Struers Epofix), mixed according to the manufacturers guidelines. Samples were cured at 40˚C for 24 hours to set then demoulded and precision cut to remove excess resin for the polishing procedure. The grinding and polishing of the samples was accomplished on Struers RotoPol units equipped with PdM force-20 and 30 units. The samples were ground down using 600, 1200 and 2400 µm SiC papers until uniformly smooth; due to the varied sample compositions grinding times and pressures varied, additionally Struers Kemet lubricant was used during the process. After grinding and the removal of excess resin the samples were polished using 6, 3, 1 and 1/4 µm diamond paste cloths. Polishing continued until the visible scratches from the SiC papers were removed; during the whole process the samples were regularly checked using optical microscopy to avoid over polishing until no excess resin was remaining. When ready for SEM examination an electron conductive coating was applied to prevent charging on the examined surface; carbon was applied primarily due to its ease of use and low atomic number which reduces potential absorption of emitted X-rays. After coating conductive copper taping was applied across the edges of the sample again to reduce potential charging.

Samples were examined using a Jeol 5800LV SEM equipped with Oxford Instruments Aztec Energy EDX system and a Philips XL30 FEGSEM equipped with a Bruker Quantax EDS system for BSE imaging and EDX analysis. Additional secondary electron imaging utilised a Philips XL30 ESEM which had low vacuum capabilities for fracture surface imaging. Typical operating procedures for SEM analysis included a maximum operating voltage of 20kV with a typical voltage of 15kV used for EDX analysis, working distance was approximately 10mm and acquisition times for EDX analyses were at least 30 seconds.

Chapter 4 : Results and discussion of NRVB grout

4.1 Introduction

The NRVB samples were cast by the NNL during a study to increase the understanding of interactions between NRVB and the primary cementitious grouts used for the encapsulation of nuclear wastes. The samples were cured at ambient, 35˚C and 80˚C for at least one year before removal and storage in sealed bags in laboratory conditions.

As discussed in section 2.4.5 relatively little published academic work is available on the hydration of NRVB or characterisation of the resultant composition. Most work focuses upon the chemical containment potential of the material [111-113] and potential carbonation kinetics [149]. Due to the high constituent level of limestone flour as part of the NRVB grout mix (10%wt) the majority of the results from this study are therefore discussed with reference to the extensive literature on the addition of calcium carbonate to OPC systems and the resultant phases formed [46, 150-157]. It is expected the NRVB material will perform within the model outlined by Matschei et al [46], with the observed formation of AFm phases within the matrix in addition to C-S-H.

4.2 XRD

The main crystalline phases present in the grout cured under ambient conditions were portlandite, calcite and a carbonate containing AFm phase identified as monocarboaluminate (see Figure 4-1). Small peaks were also identified for ettringite (AFt), C-S-H and a hydrotalcite phase (Ht).

The presence of large crystalline peaks for CH and calcite are expected due to the original constituents of the NRVB grout being both hydrated lime (29%wt) and calcite-based limestone flour (10%wt) along with OPC (26%wt). The noticeable formation of monocarboaluminate (Mc) is also expected with Mc known to be relatively stable and can exist in the presence of calcite [46, 150, 152, 153]. Damidot et al [150] showed that with increasing carbonate availability firstly hemicarboaluminate (Hc) and then monocarboaluminate are formed. No Hc (10.8° 2θ) was identified by XRD for the NRVB samples as shown in Figure 4-1. These findings are in accordance with the modelling calculations of Matschei et al [46], which stated ‘AFt, monocarboaluminate, calcite and portlandite will be observed as an important stable phase assemblage in limestone-blended cements’. Matschei et al [8] also showed that Hc would not remain stable at 25°C in the presence of excess calcite as shown in Figure 4-2 thus explaining its absence in the NRVB grouts. In all NRVB samples AFt (9.1° 2θ) was found in small quantities, suggesting that in the presence of limestone that the stabilisation of Mc indirectly stabilises ettringite [153] and therefore carbonates; monocarbonate not monosulphate is the stable AFm phase at ambient temperatures. A small reflection at around 32.2˚ 2θ was attributed to unreacted clinker phases (C_3S, C_2S) this was present in all samples but especially prevalent at 80˚C.

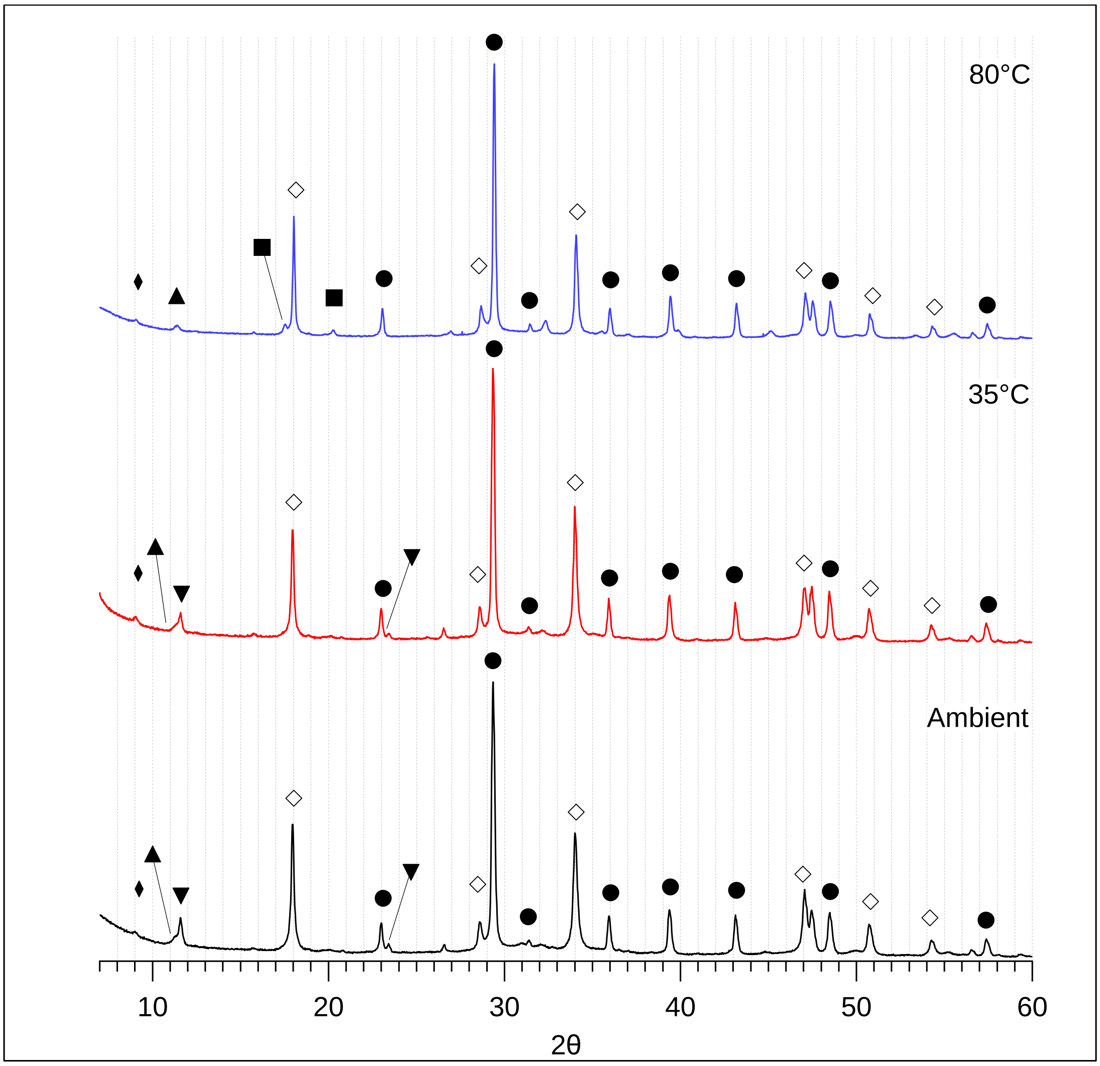

Figure 4-1: XRD trace of NRVB samples. Data are plotted using same intensity scales. ● - Calcite, ◇- Portlandite, ▼ - Monocarboaluminate (Mc), ♦ - Ettringite (AFt), ■ - Hydrogarnet (HG), ▲ - Hydrotalcite (Ht).

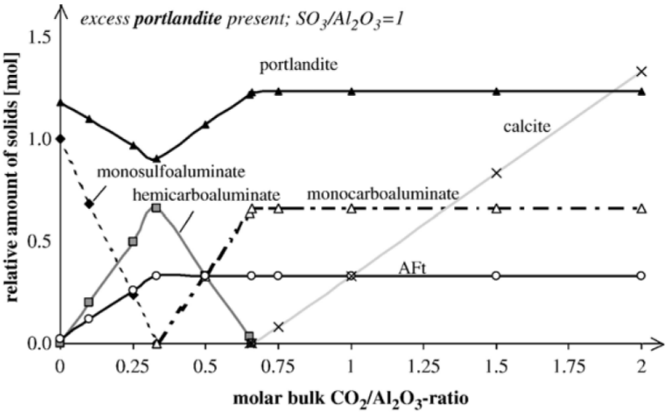

Figure 4-2: Relative amount of hydrate phases of a hydrated model mixture consisting of 1 mol C_3A, 1.25 mol portlandite and with a fixed initial sulphate ratio (SO_3/Al_2O_3 = 1) showing phase development and its dependence on changing carbonate ratios (CO_2/Al_2O_3) at 25°C, Matschei et al [46].

The primary difference for the higher temperature (80°C) sample is the absence of the Mc peak (11.7° 2θ) as shown in figure 4-3 indicating that the Mc phase is not stable at this curing temperature. The stability of the Mc phase under temperature changes was investigated by Matschei et al [154] with Mc remaining stable and unchanged at temperatures ≤70°C. However Mc is reported to decompose to a mixture of C_3AH_6 and $CaCO_3$ at temperatures ≥90°C. Fentiman [158] reported the peak area of Mc to reduce at higher curing temperatures up to 70°C in a calcium aluminate cement with $CaCO_3$. Utton et al [86] formed Mc during the encapsulation of $BaCO_3$ and reported the presence of Mc in both an OPC and BFS: OPC matrix, the phase was stable at ambient conditions but unstable in the OPC matrix at 60°C forming a hydrogarnet phase and additional $CaCO_3$. In the mentioned study it was interesting to note in the 9:1 BFS:OPC the Mc phase was stable at 60°C probably due to the higher Al content in this system.

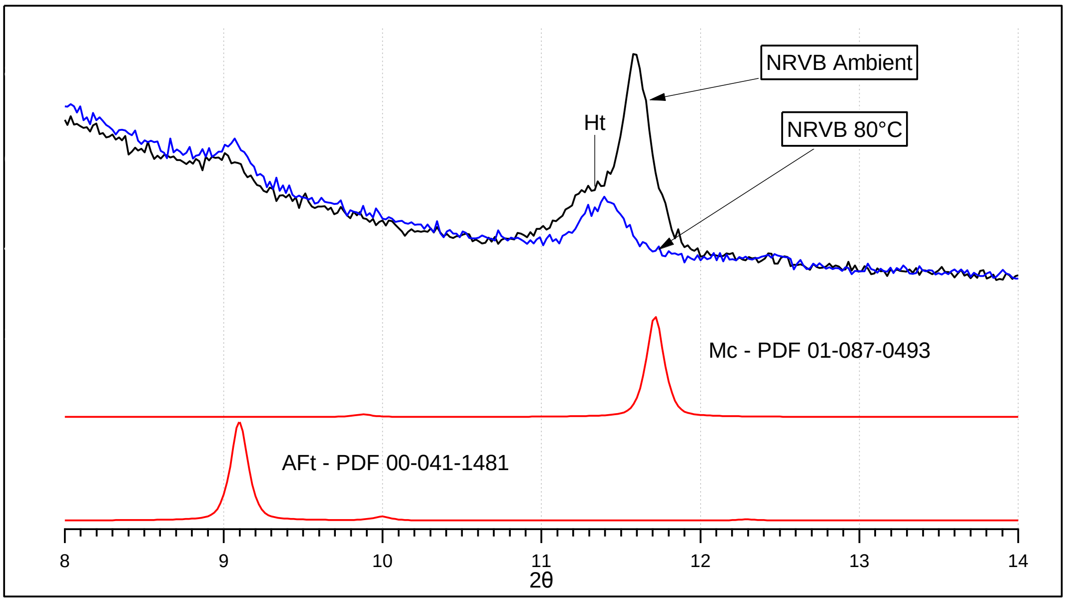

Figure 4-3: Comparative low angle XRD traces for ambient and 80°C cured NRVB sample; Relevant AFt and AFm phases shown. Mc – Monocarboaluminate ($Ca_4Al_2(CO_3)(OH)_{12}.5H_2O$), AFt – Ettringite, Ht - Hydrotalcite

To assess if there had been a decomposition of Mc in the 80°C system it was important to identify the associated reported decomposition products as described in [86, 154, 158]. Figure 4-4 below shows an identified hydrogarnet phase (C_3AH_6) found in the elevated temperature sample, this phase matches that predicted by Matschei et al [154] to result from the decomposition of Mc at around 85°C.

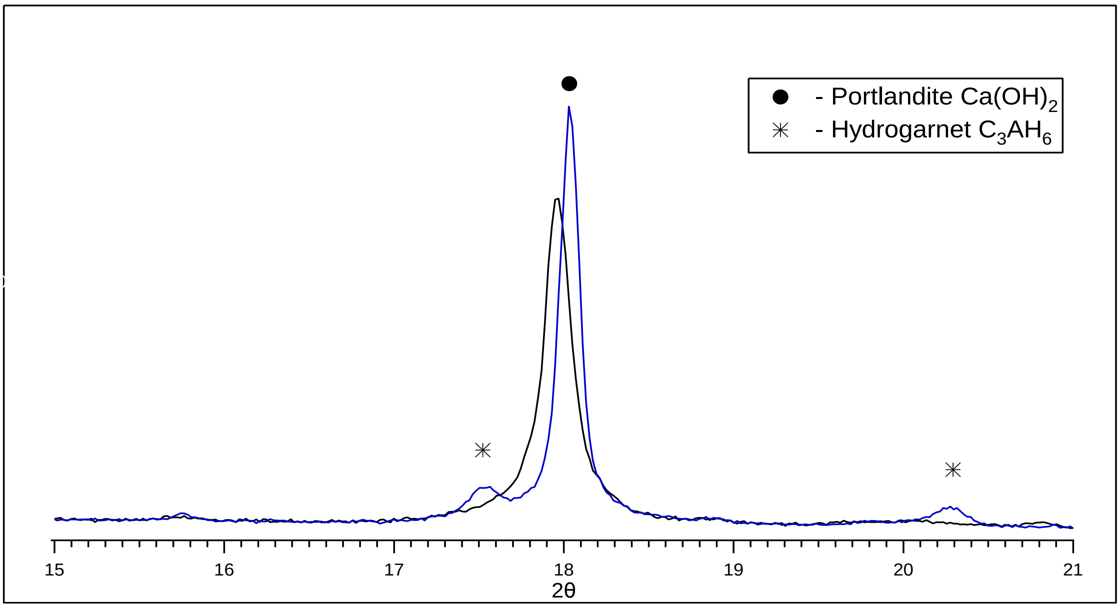

Figure 4-4: XRD trace showing two small peaks associated with C_3AH_6 for the 80°C sample

The second expected decomposition phase from Mc is additional calcite formed from CO_3^{2-} released during the formation of $BaSO_4$, however due to the large quantities of unreacted calcite in the sample as shown in Figure 4-1 it is difficult to correctly assess a small calcite content increase by XRD. There was however an increase in peak intensity for the ambient to 80°C cured sample (29.4° 2θ) showing potentially an increase in quantity or crystallinity of the $CaCO_3$ phase. However it should be noted an increase in CH intensity and content was also seen. This potential increase in calcite content was further investigated using thermal analysis as shown below. Few changes were found between the ambient and 35˚C samples in terms of identified phases with Mc still stable at this temperature along with the presence of ettringite, the hydrogarnet peaks for the katoite (C_3AH_6) were not identified in the 35˚C sample.

4.3 Thermal Analysis

Simultaneous thermal analysis confirmed the presence of portlandite and calcite in the NRVB samples in line with the XRD results presented in 4-1. The relevant STA data trace for the ambient NRVB sample is shown in Figure 4-5, the TGA measurement for the ambient sample confirms the presence of an AFm phase at around 150°C which has been attributed to Mc [153, 157]. Note that the weight loss at 150°C is not present in the 80°C sample agreeing with the XRD data that the Mc phase has decomposed at the higher curing temperature. The associated evolved gas analysis (EGA) in Figure 4-6 shows the mass trace for water (mass 18) and carbon dioxide (mass 44) in the ambient sample, the associated losses for $Ca(OH)_2$ and $CaCO_3$ were observed alongside the decompositions seen for AFt, C-S-H and Mc which closely match the DTA trace in Figure 4-5.

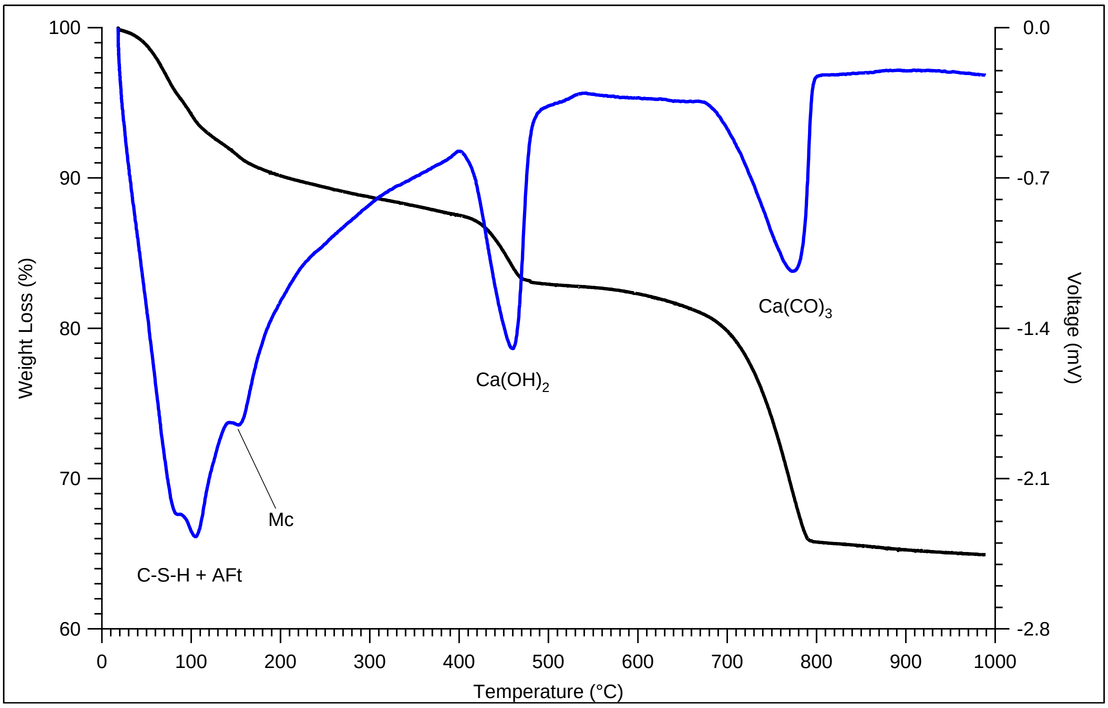

Figure 4-5: STA trace for NRVB sample cured at ambient conditions; AFt – Ettringite, Mc – Monocarboaluminate AFm phase

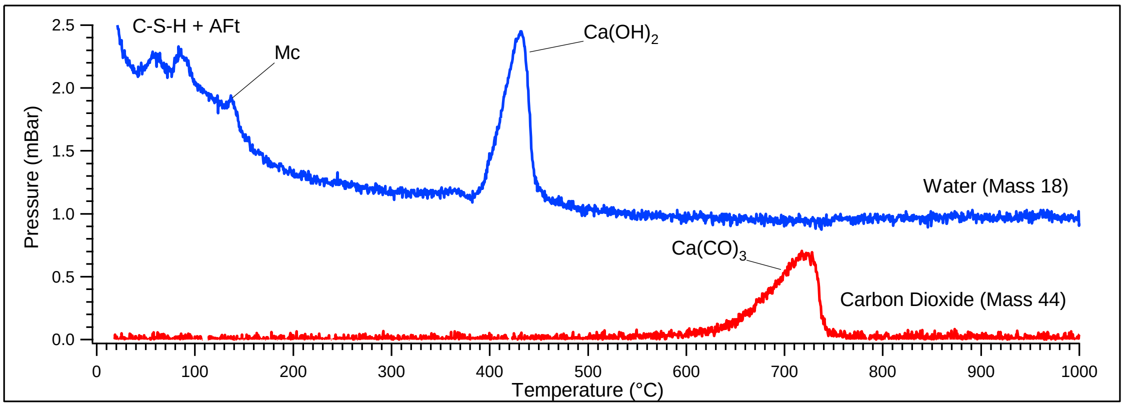

Figure 4-6: Associated mass spectrometer trace for NRVB sample cured at ambient conditions.

The STA traces for the sample cured at 80˚C can be seen in Figure 4-7, the higher temperature cured sample had a lower unbound water content than the ambient sample but showed the characteristic mass losses related to the decomposition of $Ca(OH)_2$ and $CaCO_3$. The decomposition loss for monocarboaluminate at 150˚C was not present for the 80˚C cured sample showing its instability at this higher temperature. Additionally the doublet decomposition associated with C-S-H and the AFt phase isn't resolved in the 80˚C sample as was shown at the ambient temperature. A small mass loss at around 300˚C has been attributed to the potential hydrogarnet phase seen by XRD, this decomposition temperature is consistent with work on a synthetic Al - katoite hydrogarnet (C_3AH_6) by Dilnesa et al [159].

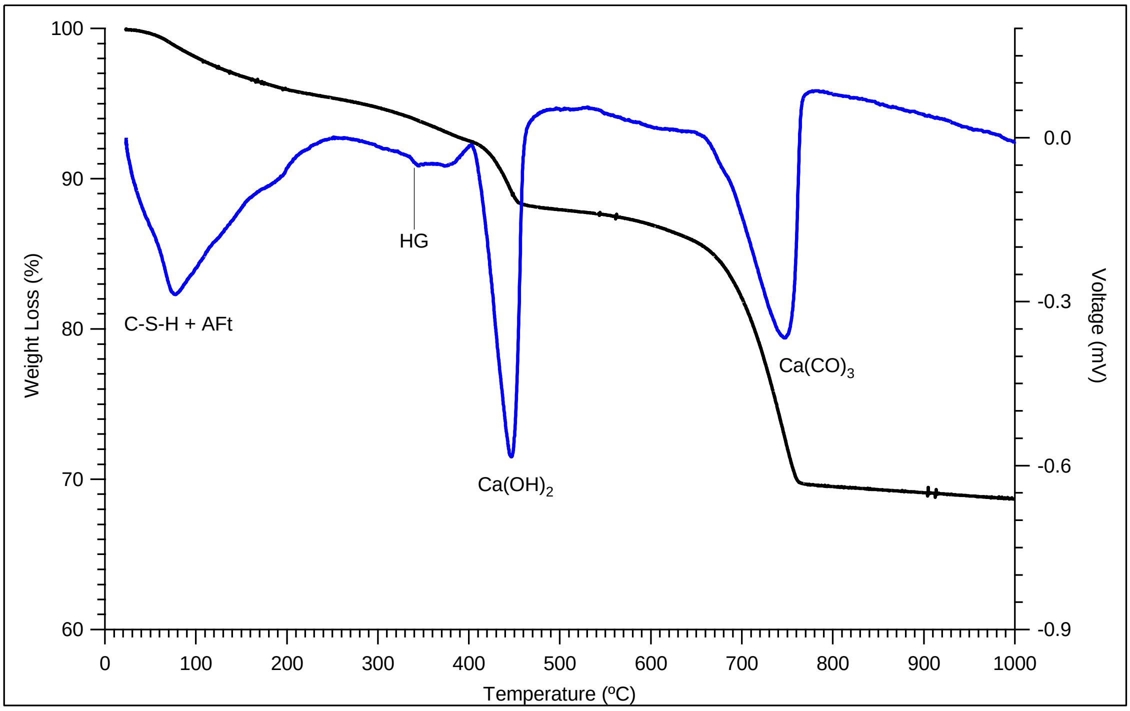

Figure 4-7: STA trace for NRVB sample cured at 80˚C ; AFt – Ettringite, HG – Hydrogarnet (Al-Katoite C_3AH_6)

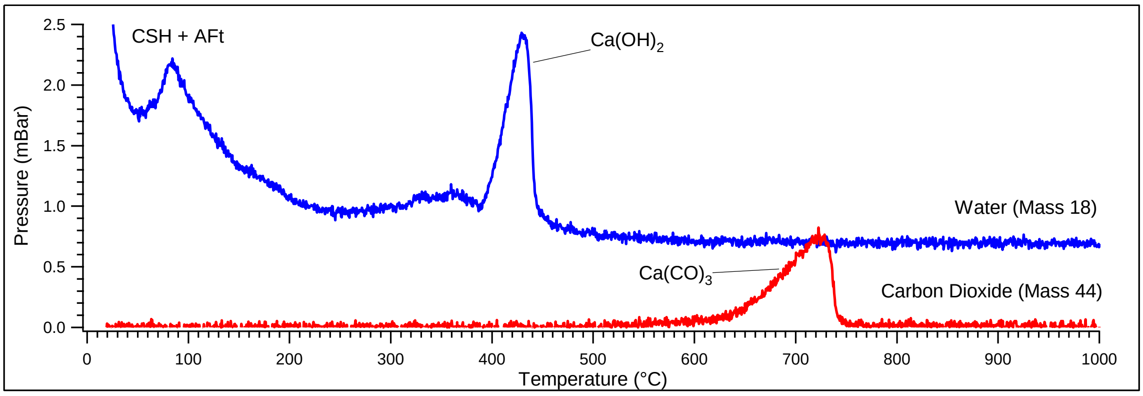

Figure 4-8: Associated mass spectrometer trace for NRVB sample cured at ambient 80˚C.

The 35˚C cured NRVB sample performed similarly to the ambient cured sample with near identical TG traces for unbound water, $Ca(OH)_2$ decomposition and $CaCO_3$ content; these contents are shown in table 4-1. The mass loss and associated water loss by EGA for monocarboaluminate was present at 150˚C; however this was less prominent than that found at ambient temperatures using the same techniques. Like the sample cured under ambient conditions there was a doublet decomposition loss for C-S-H + AFt which changed for the higher temperature sample.

Sample Cure	$Ca(OH)_2$ content (%)	$CaCO_3$ content (%)
NRVB Ambient	15.2	36.4
NRVB 35˚C	16.0	36.8
NRVB 80˚C	13.2	38.4

Table 4-1: Calcium hydroxide and calcium carbonate contents calculated by TGA

All the calculated contents for $Ca(OH)_2$ and $CaCO_3$ in the NRVB samples showed a reduction in CH content by weight when compared to the original composition of the NRVB mixture (29% wt). The $CaCO_3$ content of all three samples was greatly increased by approximately 25% wt from an original composition of 10% wt of limestone flour. This relates to a consumption of CH to $CaCO_3$ primarily due to the carbonation of the original unreacted hydrated lime in the mix in addition to the potential carbonation of CH produced from the hydration of the OPC. This production of $CaCO_3$ and decomposition of $Ca(OH)_2$ was most noticeable in the 80˚C sample which showed the lowest levels of remaining CH and highest levels of carbonation.

The carbonation of NRVB material was not unexpected due to the original starting constituents. As mentioned in section 2.4.5 a benefit of carbonation for the geological disposal concept would be the absorption of radioactive ^{14}C contained with CO_2 generated from degradation of certain waste components [112]. Sun [149] studied the carbonation kinetics of NRVB and identified that the various stages of carbonation were controlled by the openness of the pores in the NRVB material. This presents initially as a rapid stage controlled by the diffusion rate of CO_2 followed by a slow final stage as the decalcification of C-S-H releases Ca^{2+} for further carbonation. The TG/DTA data from Sun [149] shows a carbonated specimen carbonated for 102 hrs under pressure. Weight loss from decomposition of $CaCO_3$ was increased with no $Ca(OH)_2$ present after accelerated carbonation. The 'fresh' NRVB trace was comparable to the samples from this study however the percentage weight losses were not calculated. Industry – based investigations into the carbonation of NRVB has shown the carbonation kinetics depend greatly upon the water saturation. In partially saturated material the carbonation kinetics are parabolic with a well-defined K value, in more saturated material (+90% RH) the carbonation kinetics cannot be described by a simple parabolic rate equation and the rate is considerably slower than at a lower humidity. The reasons for this may be linked to microstructural changes after extensive carbonation of the material in addition to the slower diffusion rates present when the material is saturated [160, 161].

4.4 SEM-EDX

The relevant microstructures for the NRVB grouts cured at each temperature are shown in Fig 4-9 a) - f). The BSE imaging of the samples shows a microstructure dominated by the presence of unreacted $CaCO_3$ particles as shown by the lack of any hydration rims, smaller $CaCO_3$ particles are seemingly acting as nucleation sites surrounded by C-S-H.

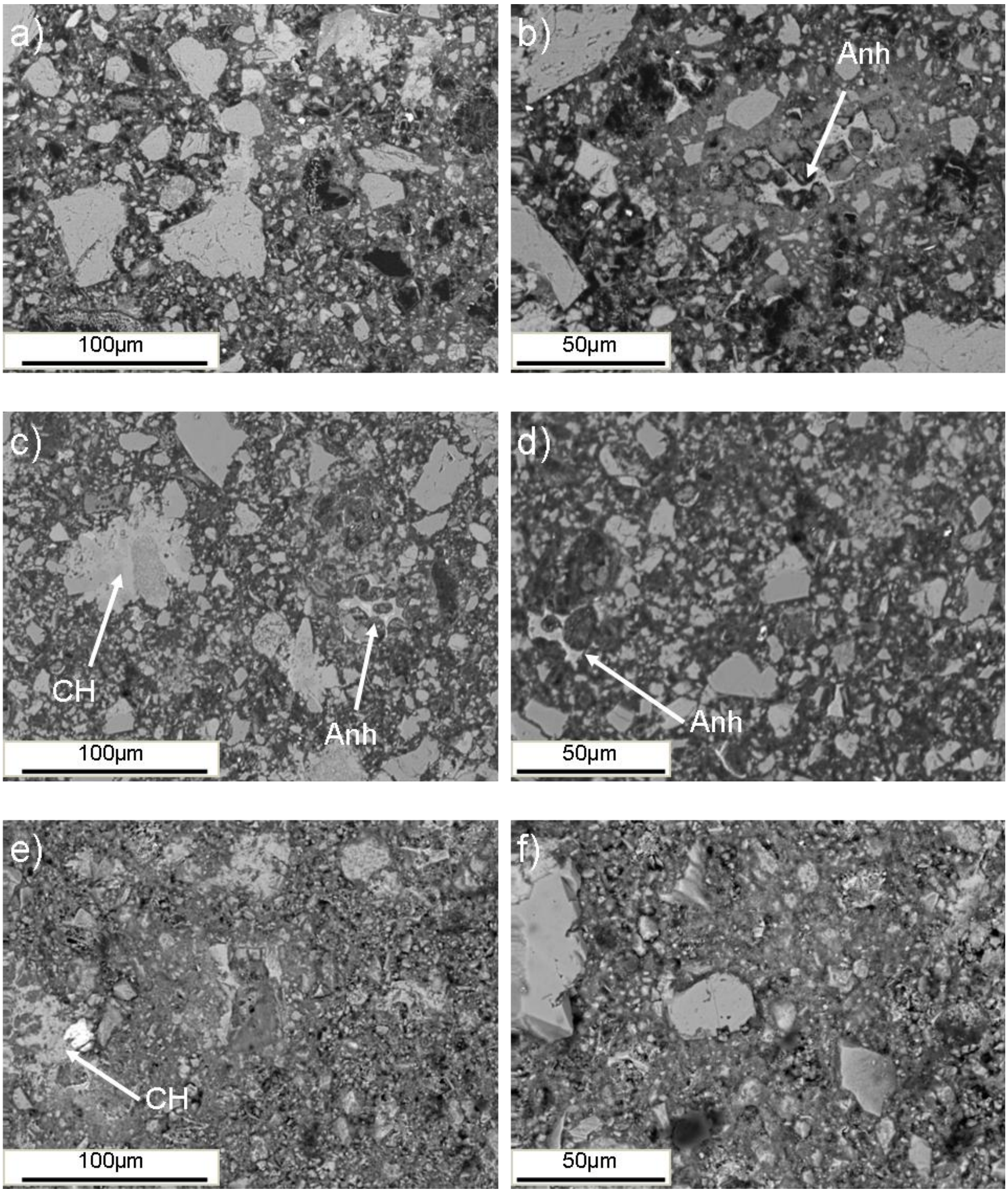

Figure 4-9: SEM BSE images for the NRVB grouts; Ambient cure (a - b), 35˚C cure (c - d), 80˚C cure (e -f). CH = Calcium Hydroxide, Anh = anhydrous material.

The effect of finely ground limestone accelerating cement hydration due to additional surface area for nucleation and growth of hydration products is known [153, 162]. As shown in figure 4-9 a large quantity of portlandite (marked CH) remains within the microstructure often in close relation to larger unreacted limestone particles, this agrees with the observed TG and XRD traces discussed earlier. The large quantities of limestone and portlandite are found in all of the NRVB samples for each curing temperature with the content percentages best calculated by TGA.

Anhydrous clinker material was observed at all temperatures in the samples, particularly unreacted belite (C_2S) and calcium aluminoferrite phase (C_4AF) shown in figure 4-10 and labelled as anhydrous (Anh) on figure 4-9. This is also shown in elemental mapping of a 35˚C sample in figure 4-11. Unreacted alite (C_3S) was not commonly observed in the samples leading to the suggestion that the early - age hydration of alite is not greatly hindered in the NRVB samples. Indeed it has been reported finely ground limestone should accelerate the hydration of C_3S [163].

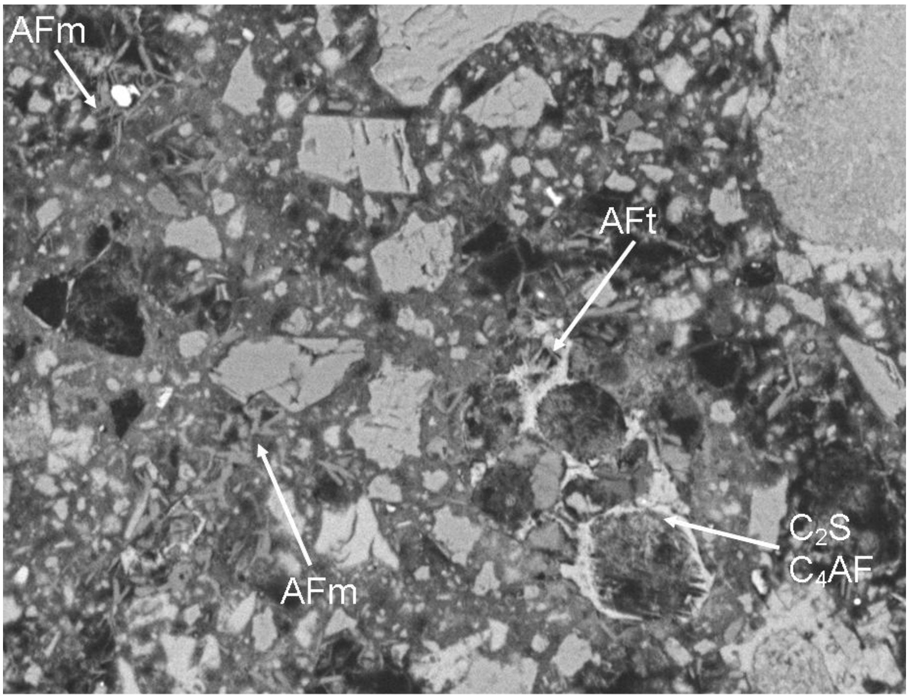

Figure 4-10: BSE Image of NRVB ambient sample showing higher density C-S-H surrounding partially reacted clinker with associated AFm and Aft hydrate phases formed locally (x1000).

In the BSE images variations in C-S-H grey scale can be seen which relate to changes in the density of C-S-H formed. For example figure 4-10 shows an area of denser C-S-H surrounding a partially hydrated clinker particle with the C_3S hydrated leaving unreacted

C_2S, C_4AF and AFt. In this area of denser formed C-S-H, limestone particles can be seen incorporated along with the presence of substantial amounts of an AFm phase, this was confirmed by EDX analysis to be monocarboaluminate with smaller amounts of AFt. The presence of unreacted clinker particles and potential Ip C-S-H was indicated by the use of elemental mapping as the OPC was the primary source of Al and Si within the system. Whilst Si is present in varying concentrations throughout the paste within the C-S-H, Al and other elements such as Mg and Fe are more likely to remain within the local environment of the hydrated PC particle within Ip [164]. In the BSE images this should correspond to the lighter greyscale in BSE imaging of Ip C-S-H, due to the higher atomic mass of contained elements or potentially show an increase in calcium content within the C-S-H phase [145, 165]. EDX analysis of distinct Ip and Op C-S-H phases was found to be difficult due to the fine intermixing of limestone particles, unreacted clinker phases and portlandite. Atomic ratios for all three curing temperatures were plotted to visualise trend lines corresponding to intermixing phases with C-S-H as shown in figure 4-11.

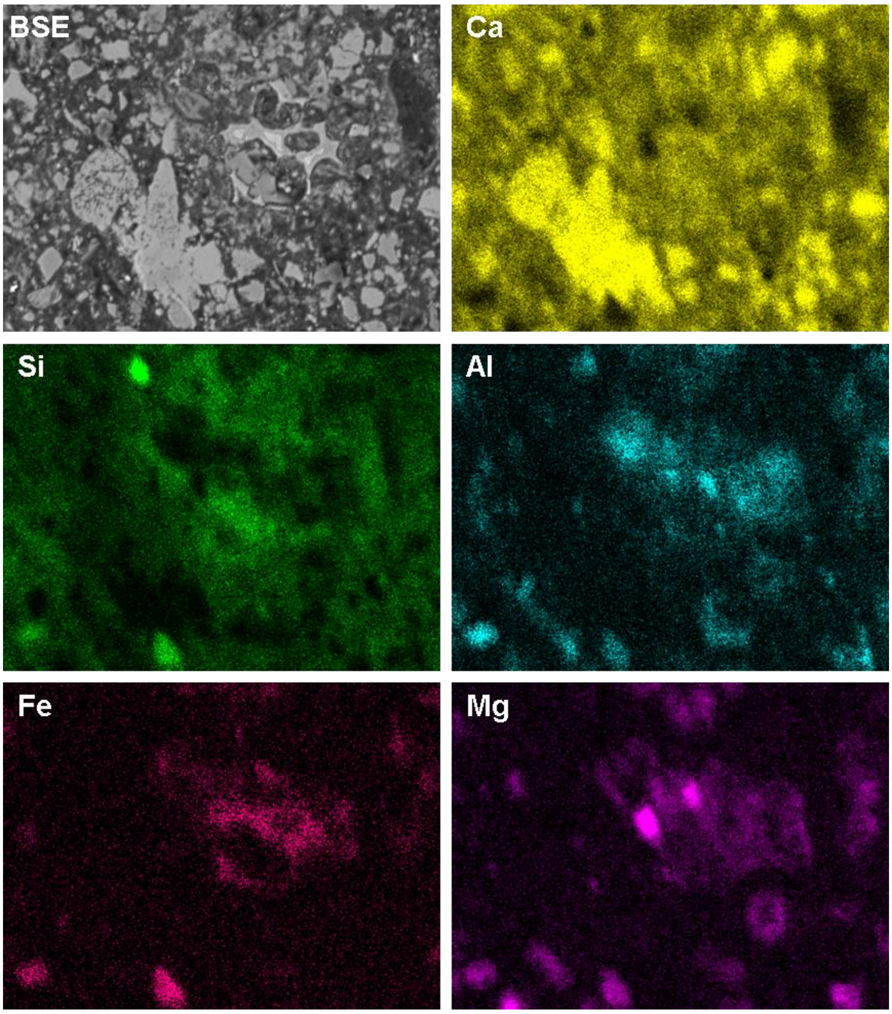

Figure 4-11: Elemental mapping for NRVB 35˚C showing presence of CH and unreacted C_2S and C_4AF.

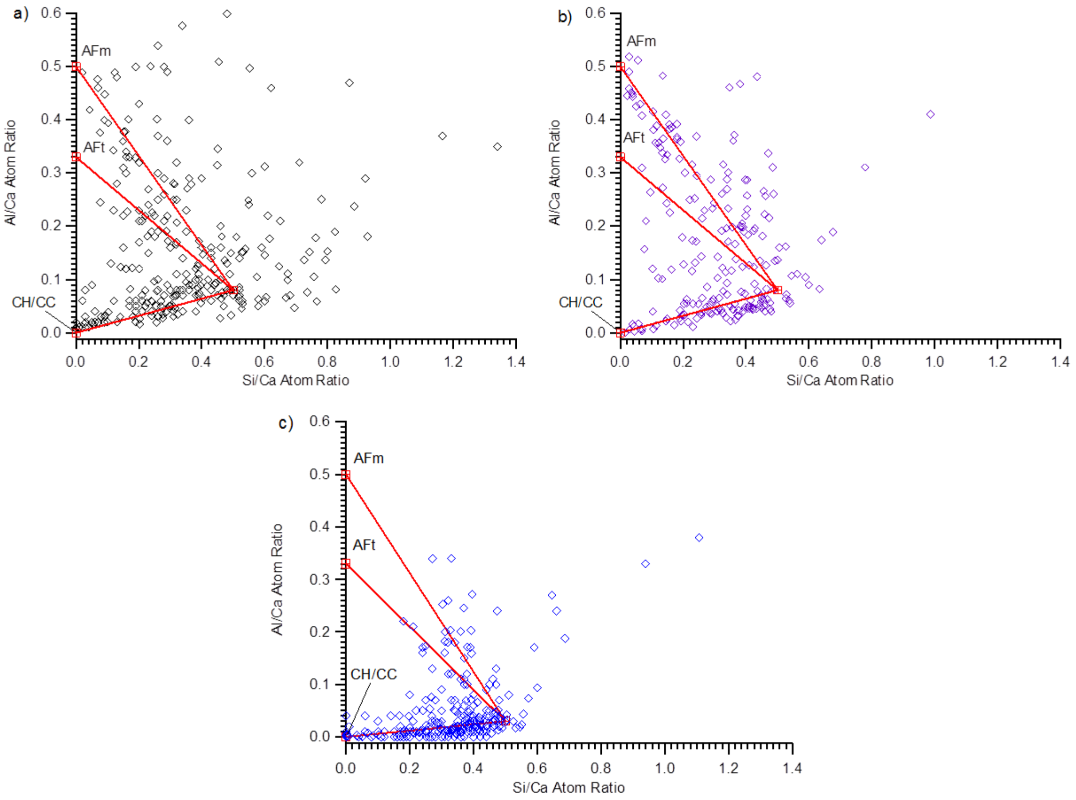

Figure 4-12: SEM EDX from the NRVB samples a) Ambient cure, b) 35˚C cure and c) 80°C cure; tie lines shown for detected intermixed phases.

Atomic ratio plots of Si/Ca against Al/Ca from SEM-EDX with trend lines for additional intermixed phases are shown in Figure 4-12. The analyses clearly show an intermixing of C-S-H with a pure calcium phase which can be assumed to be either of the primary crystalline phases identifed by XRD (portlandite or calcite). SEM-EDX also showed the intermixing of C-S-H with an aluminate hydrate phase; to identify this phase trend lines for a pure AFm and AFt phase have been displayed with their respective Al/Ca ratios (0.50, 0.33).

The results for the ambient and 35˚C cured samples show a similar trend towards AFm and AFt phases being present within the binding matrix. The 80˚C sample didn't show a strong response for a AFm phase when compared to the lower temperatures, however it did show a potential trend for the presence of AFt and a Al - substitued hydrogarnet phase containing both Al and Si. These results match well with the previously reported XRD results for the samples cured at lower temperatures, showing greater trend responses for AFm at lower temperatures and potential AFt responses for all samples. To assess the composition of the aluminate hydrate phases the S/Ca and (Al+Fe)/Ca ratios were plotted in figure 4-13, all the samples showed evidence of a monocarbonate phase (Mc) due to the low S/Ca ratio . The 80˚C sample showed the best response for an AFt phase despite this phase appearing on all XRD traces, however the XRD response was small and BSI showed it occured close to partially reacted clinker which was avoided by SEM-EDX. The amount of Mc suggested by EDX for the high temperature sample is less than suggested for lower temperatures.

The average Ca/Si ratios for the C-S-H phase from SEM-EDX in the NRVB samples are not displayed due to the level of intermixing and high standard deviation of the results when calculated. More accurate ratios for the C-S-H phase are discussed in section 4.5 using the TEM-EDX method. The trend for ambient and 35˚C samples in figure 4-12 suggested a very similar Ca/Si ratio with a level of Al incorporation within the C-S-H. The 80˚C sample showed a difference in Al content for the potential C-S-H cluster due to a reduced Al/Ca ratio compared to the lower temperature cured samples. The measured Si/Ca atom ratio seemed to be roughly similar to the lower temperature samples with the maximum potential Ca/Si ratio from EDX being around 2.0 when measured by the SEM.

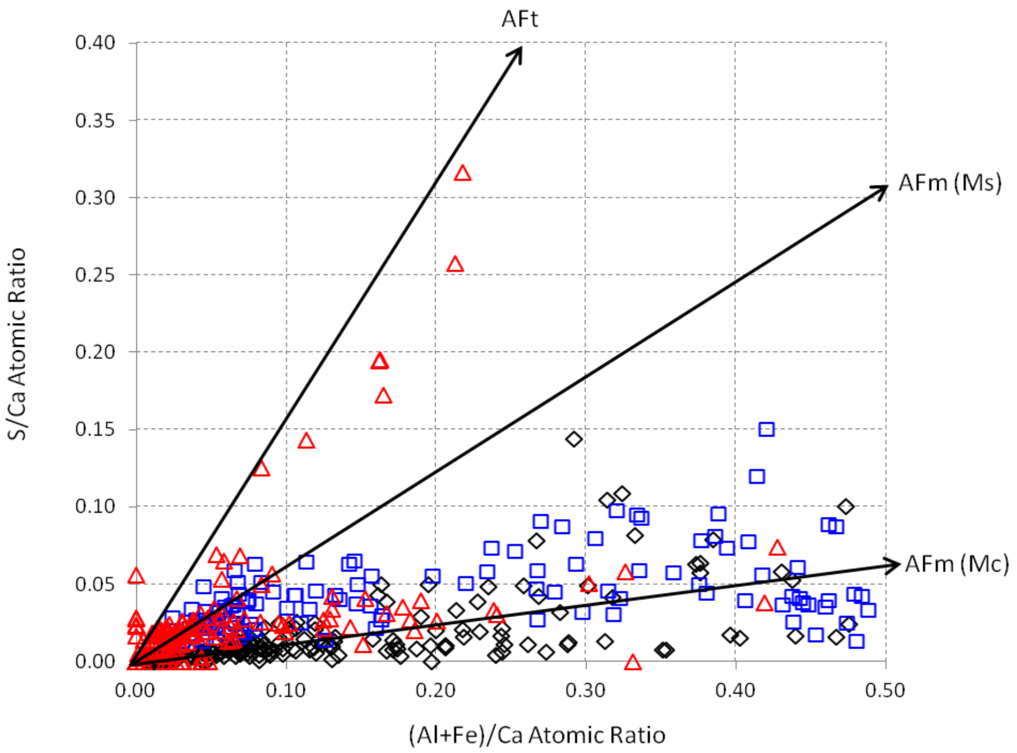

Figure 4-13: (Al+Fe)/Ca against S/Ca Atomic Ratio plot showing composition of aluminate phases by SEM-EDX; Ambient (◇), 35˚C (□), 80˚C (△).

4.5 TEM-EDX

Transmission electron microscopy on ion beam thinned sections was used to investigate the microstructure of the NRVB grouts cured at various temperatures. The microstructure consisted of very homogeneous amorphous C-S-H which presented a coarse fibrillar morphology outer product (Op), C-S-H bridges the open gaps found within the paste as shown in figures 4-14 to 4-16. The morphology of the Op C-S-H is similar to that described for the fibrillar outer products in tricalcium silicate (C_3S) paste investigated by Groves et al [166], and that of a 330 day old C_3S paste by Jennings et al [140]. Inner product (Ip) C-S-H tended to show a coarse foil - like morphology however only very small areas of Ip were observed in the TEM and this was identified by the presence of Mg responses within it which are known to be present in Ip for OPC pastes [167].

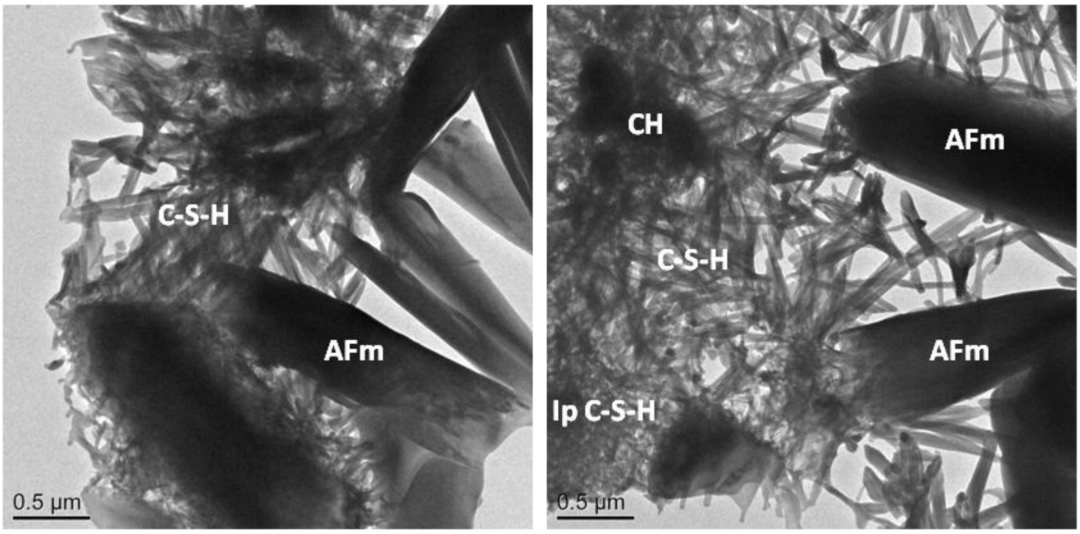

Figure 4-14: TEM micrographs of ambient NRVB showing AFm Mc phase.

At ambient temperature the presence of AFm crystals was identified intermixed with C-S-H hydration products consistent with the XRD data. This was confirmed by point EDX analysis as shown in figure 4-18. AFt was not observed by EDX analysis in the TEM, however this was not unexpected due to its relatively instability under TEM analysis [167] and weak response from XRD. In some areas there was a suggestion that microcrystalline calcite was intermixed within the coarse fibrillar C-S-H similar to observations on carbonate deposition in Op discussed by Groves et al [168]. The samples cured at 35˚C show similar results as for the ambient paste sample, AFm again was observed in the microstructure formed within the Op C-S-H. In more open spaced areas the nature of the Op C-S-H was again very coarse and fibrillar as shown on the left of figure 4-15.

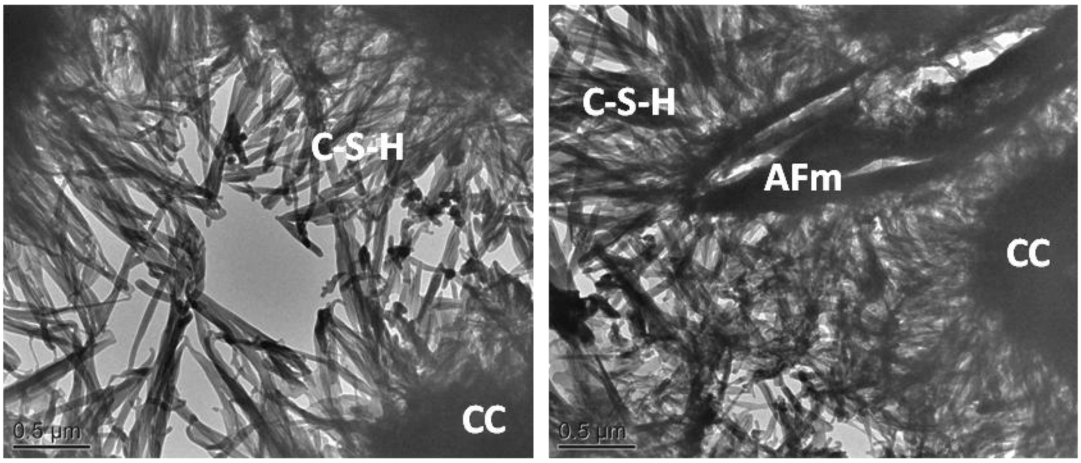

Figure 4-15: TEM micrographs of 35˚C NRVB showing C-S-H, AFm and fine calcium carbonate particles

In areas close to fine calcium carbonate particles identified by selected area electron diffraction (SAED), a more compact but still essentially fibrillar Op C-S-H is found. This is shown in figures 4-15 and 4-16 and agrees with the idea that fine calcium carbonate particles will act as nucleation sites for the growth of C-S-H during hydration. The continuing presence of calcium carbonate and calcium hydroxide phases within the TEM samples at all temperatures matches with the XRD data of the pastes. The CH phases are assumed to be mainly from the initial mix rather than hydrated from the OPC due to their differing appearance from that in studies of ion milled OPC pastes [167].

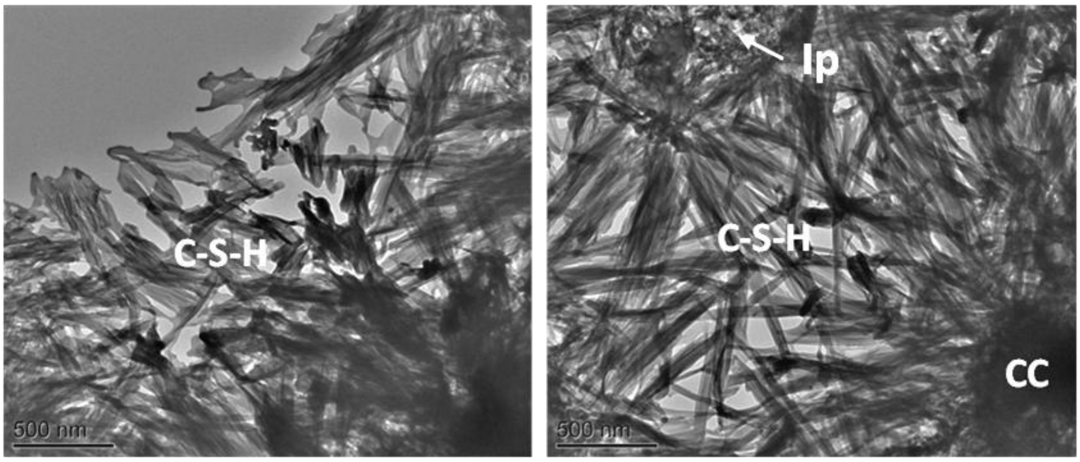

Figure 4-16: TEM micrograph of 80˚C NRVB showing Op C-S-H

The sample cured at elevated temperature showed a more compact fibrillar - like Op C-S-H, again there was evidence for calcium carbonate particles acting as nucleation sites for the C-S-H phase. No AFm phases were found during TEM studies of the 80˚C sample which agrees with previous experimental evidence that this phase is reduced at elevated temperatures.

To summarise the TEM observations the outer product C-S-H present in the NRVB pastes has a fibrillar morphology which can be likened to the outer product found in hardened C_3S, β -C_2S and OPC pastes [26, 140]. In open pore spaces such as that shown in figure 4-14 and 4-15 the fibrils of C-S-H have formed with a high length to width ratio which was described by Richardson [26, 138] as being of a coarse fibrillar nature. In the TEM images fibrils of C-S-H can also be seen in more compact spaces often near hydrated phases or nucleation sites. In this case the C-S-H takes on a more fine fibrillar and directional appearance. Figure 4-17 shows an enlargement of the two different morphologies showing how the finer fibrillar morphology seems to suggest several layers of fibrils, whist the coarse morphology seems to have a different length to width ratio in comparison. Richardson [10] described this morphology as being a function of the space constraint with the Op forming in a more space efficient manner with a directional aspect in smaller spaces. This comparison with model C_3S and β-C_2S pastes is sensible as the C-S-H present in hardened OPC pastes are compositionally similar [10], except with the addition of small levels of Al which has been detected by SEM and TEM.

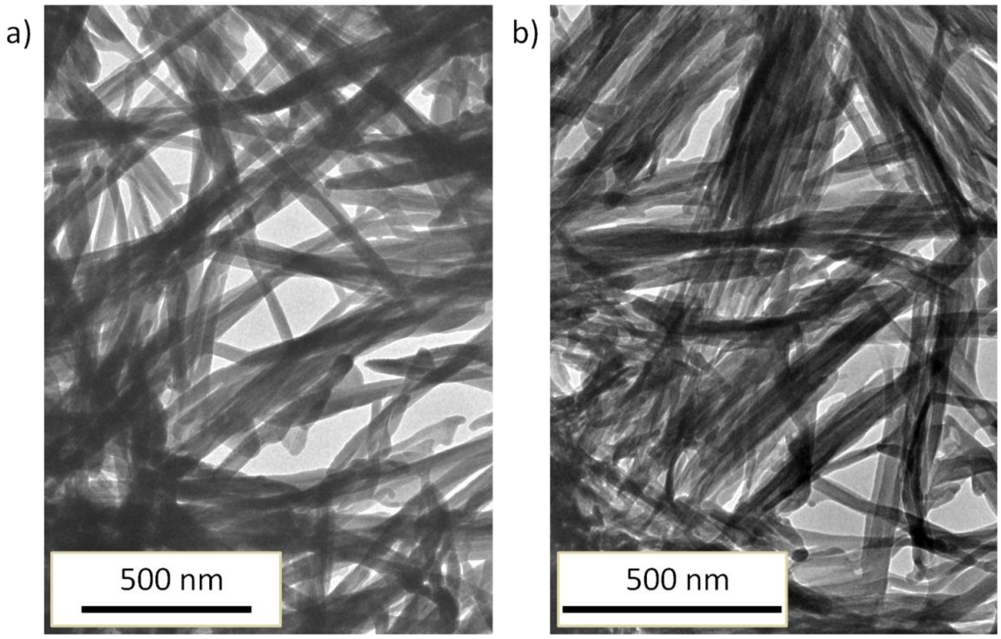

Figure 4-17: Comparison of observed coarse (a) and finer fibrillar (b) Op C-S-H morphology in NRVB samples

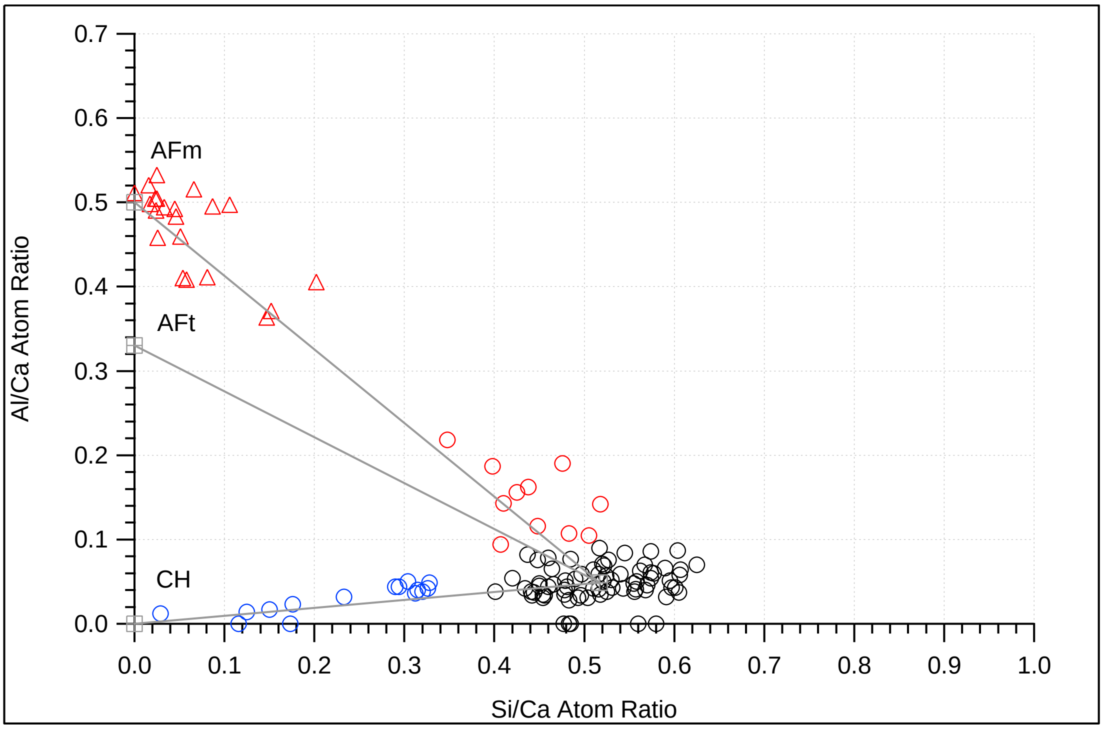

Figure 4-18: NRVB Ambient, Si/Ca against Al/Ca atom ratio plot of TEM-EDX analyses of AFm (△), Op (○), Op + AFm (○), Op/CH (○).

The overall TEM-EDX results for the ambient NRVB sample is shown in figure 4-18 with the same trend lines as used for the SEM-EDX analysis, intermixing phases are shown and only the identified Op values where used in the calculations. This analysis confirmed the identification of AFm phases within the cement matrix for the lower temperature samples and close scale intermixing of C-S-H with 'pure' calcium phases (calcite or CH) being present in all samples.

Detailed investigation of the Si/Ca and Al/Ca ratios found in the three samples is shown in figure 4-19 with the relevant mean atomic ratios presented in table 4-2. All three samples show a high Ca/Si ratio which is consistent and similar to those found for C_3S and neat OPC mixes [10, 167]. The mean values for the Ca/Si ratio varies with curing temperature, with an increased spread in data observed for samples produced under ambient conditions. In the literature the effect of temperature regarding variations in Ca/Si ratio are conflicting [169] and depend on whether Ip or Op are being analysed. It is generally agreed that high temperature curing results in denser hydration Ip rims resulting in a coarser porosity and increase of mean pore radii [165, 170, 171]. From figure 4-19 it can be seen that the actual range of Si/Ca compositions remains relevantly similar despite the temperature changes in curing. Figure 4-19 also shows there seems to be a definite minimum value to the

Ca/Si ratio of Op C-S-H is these samples (Ca/Si $_{min}$ =1.59) whilst the maximum value for the Ca/Si ratio was (Ca/Si $_{max}$ = 2.50, 1.95, 2.14) respectively for ambient, 35˚C and 80˚C samples. It seems however from figure 4-19 that the Ca/Si ratio seems not to be greatly affected by the increase in curing temperature for these NRVB samples , this agrees with the findings of Lothenbach et al [172] and Escalante García and Sharp [169]. It should be noted however that the Ca/Si $_{max}$ for the ambient sample (2.50) is very high. This suggests that the TEM analysis may include responses from an additional Ca phase, since the centre of the ambient C-S-H cluster suggests a median Ca/Si value of 1.92.

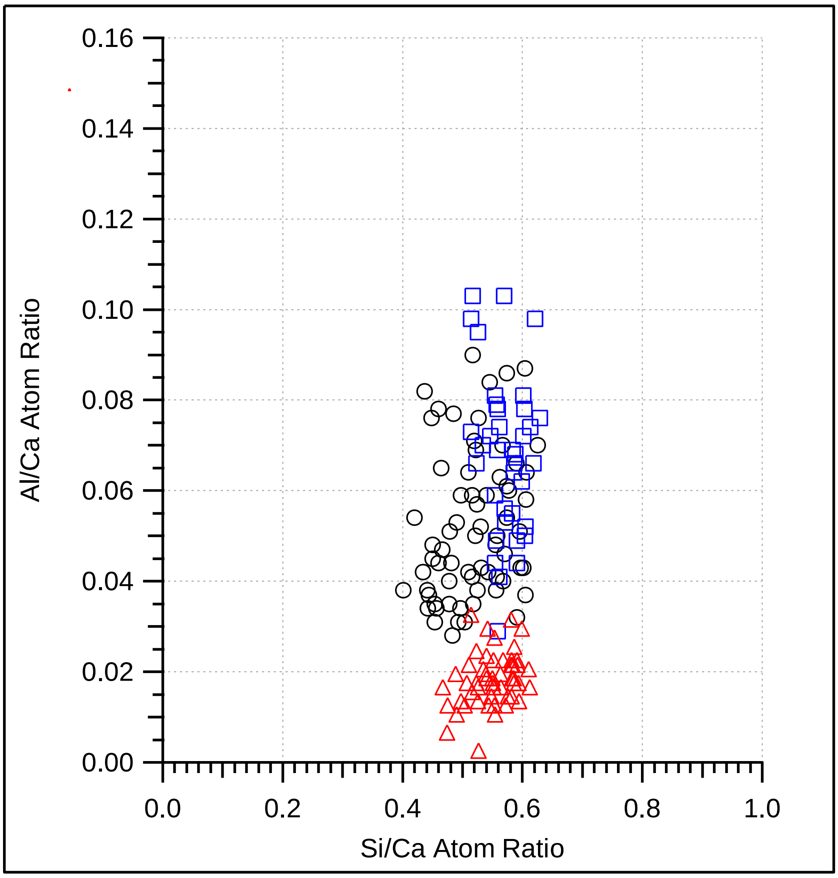

Figure 4-19: Si/Ca against Al/Ca atom ratio plot of TEM-EDX analyses of Op C-S-H present in NRVB samples; Ambient (○), 35˚C (□), 80˚C (△).

The Al/Ca ratio for all samples is < 0.1 as expected for a sample related to neat OPC. The most noticeable observation from the change in temperature for these samples is the decrease in Al/Ca ratio as the curing temperature is increased to 80˚C. Similar reductions in Al/Ca ratio has reported previously [169, 172] along with a potential increase in the mean S/Ca ratio by Garcia and Sharp [31] and Lothenbach et al [34]. These changes in Al content are likely linked to a reduction in available Al due to the known increase in Ip density caused by higher temperature curing [173, 174]. The aluminium is at higher temperatures more likely to be incorporated in the denser Ip C-S-H rather than the Op, partly due to the reduced diffusion into the Op. Additionally a reduced degree of hydration has been observed for the ferrite phase (C_4AF) in cements cured at higher temperatures [170], which would reduce the long - term availability of Al.

Sample		Ca/Si		Ca/(Al+Si)		Al/Si	
	N❖	Mean	SD	Mean	SD	Mean	SD
Ambient	67	1.96	0.21	1.78	0.20	0.10	0.03
35˚C	37	1.75	0.10	1.64	0.09	0.07	0.02
80˚C	52	1.83	0.13	1.77	0.13	0.03	0.01

❖N = Number of EDX analysis

Table 4-2: Atomic ratios of Op C-S-H in NRVB samples obtained by TEM-EDX

4.5.1 Nanostructural model for C-S-H

The applicability of the TEM-EDX data has been discussed in relation to the tobermorite-jennite (T/J) and tobermorite - 'solid solution' calcium hydroxide (T/CH) approaches for the nanostructure of C-S-H proposed by Richardson and Groves [24, 26, 175].

The polymerisation sequence of C-S-H formed during the early stage hydration of C_3S or neat PC has been shown by solid-state NMR to mostly consist of dimeric silicate units [176, 177]. The subsequent later age C-S-H consists of higher polymeric species mainly linear pentamer and octamer leading to the 2, 5, 8. . . (3n-1) chain length sequence. However with long - term ageing it has been suggested that dimer's will remain in substantial quantities [178, 179]. Additionally NMR has shown that in systems with significant Al substitution for Si within the C-S-H phase the (3n-1) chain length sequence remains applicable as the Si^{4+} in the bridging tetrahedra sites are replaced with Al^{3+} [180-183].

For the described (3n-1) structural chain lengths the associated Ca/Si ratios were calculated using equation (4-1) for structural units without any potential Al substitution; equation (4-2) was used for structural units with the incorporation of Al assuming full saturation of the available bridging sites (n-1) with Al^{3+}. In equations (4-1 & 4-2) *y* relates to the relative degree of protonation (w/n), the limits to which are shown graphically in figure (4-20) and explained by Richardson [26], *a* relates to the Al/Si ratio which can be expressed as: $0 \le a \le (n-1)/(3n-1)$. As mentioned full saturation is plotted unless otherwise stated.

$$Ca/Si = \frac{n(4+y)}{2(3n-1)}$$

Equation 4-1: Calculation for Ca/Si of a chain length *n* with no Al substitution present from Richardson [23]

$$Ca/Si = \frac{n(4+y)}{2(1-a)(3n-1)}$$

Equation 4-2: Calculation for Ca/Si of a chain length *n* with full Al saturation from Richardson [23]

$$Al/Si = \frac{a}{1-a}$$

Equation 4-3: Calculation for Al/Si ratio

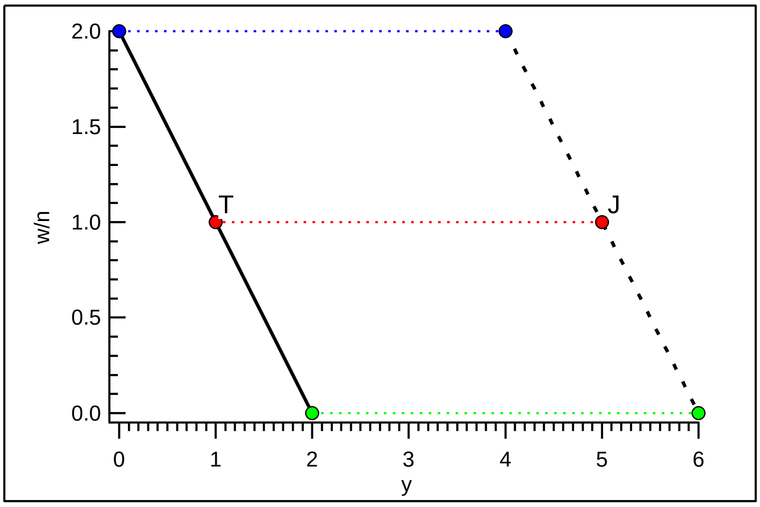

Figure 4-20: The combinations of the degree of protonation w/n and y possible in formula X, Taylor's [184] tobermorite-based structural units occur at T and jennite at J, reproduced from [26].

The resultant calculated atom ratios were plotted for fully protonated, half protonated and unprotonated tobermorite and jennite units. The experimental data for Si/Ca and Al/Ca was then plotted to assess which is the most appropriate structural arrangement to fit the TEM-EDX data. This can give an insight to the likely dreierkette chain structure according to Richardson and Groves' structural model for C-S-H.

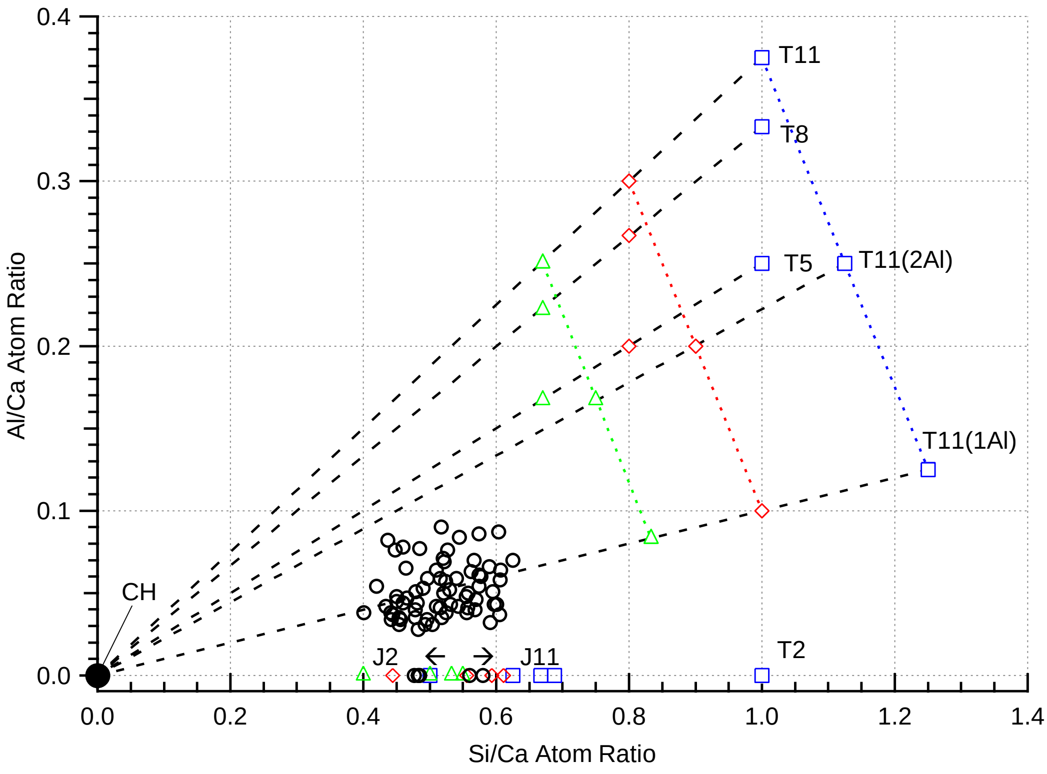

Figure 4-21: Si/Ca against Al/Ca atom ratio plot of TEM-EDX analyses of Op (○) C-S-H present in Ambient cured NRVB. The additional symbols represent the compositions of tobermorite (T) and jennite (J) based structural units with different levels of protonation of the silicate chains: the minimum (△; w/n=0), intermediate (◇; w/n=1) and maximum (□; w/n=2). The additional points included represent tobermorite-based units with chain lengths of 2, 5, 8, 11. All units are assumed to be saturated with Al where possible. (ie all the occupied bridging sites are occupied by Al rather than Si). The only exception is for units with 11 tetrahedral chain length, as additionally to those saturated with Al (T11) those with only one or two of the three possible bridging sites are also shown labelled as (T11(1Al) and (T11(2Al) respectively. The black dashed lines join points for structural units of the same chain length but different degrees of protonation to CH. T11 units with the same protonation but differing Al content are joined by coloured dashed lines.

Examination of the ambient TEM-EDX data in figure 4-21 indicates only some of the analyses definitely fall inside the possible limits for the T/CH structural model. Those that do are situated with a lower Al/Ca ratio than that represented by a chain length of 5 (T5) suggesting a level of substitution of Al below the full saturation level plotted in figure 4.21 (T8, T11 etc). This is expected as the level of Al in these examined systems is much reduced from that seen in blended cements. Therefore an aluminosilicate chain length of below 8 with partial substitution of 1 Al bridging site is proposed to explain the analyses which fall best within the T/CH model. The mean aluminosilicate chain length (MCL) for a OPC paste which has been shown to be microstructurally similar has been reported as 5.6 [53] so the proposed chain length would seem sensible. As only some of the analyses are explained by the T/CH model the remaining data has been evaluated against the T/J approach as shown in figure 4-22.

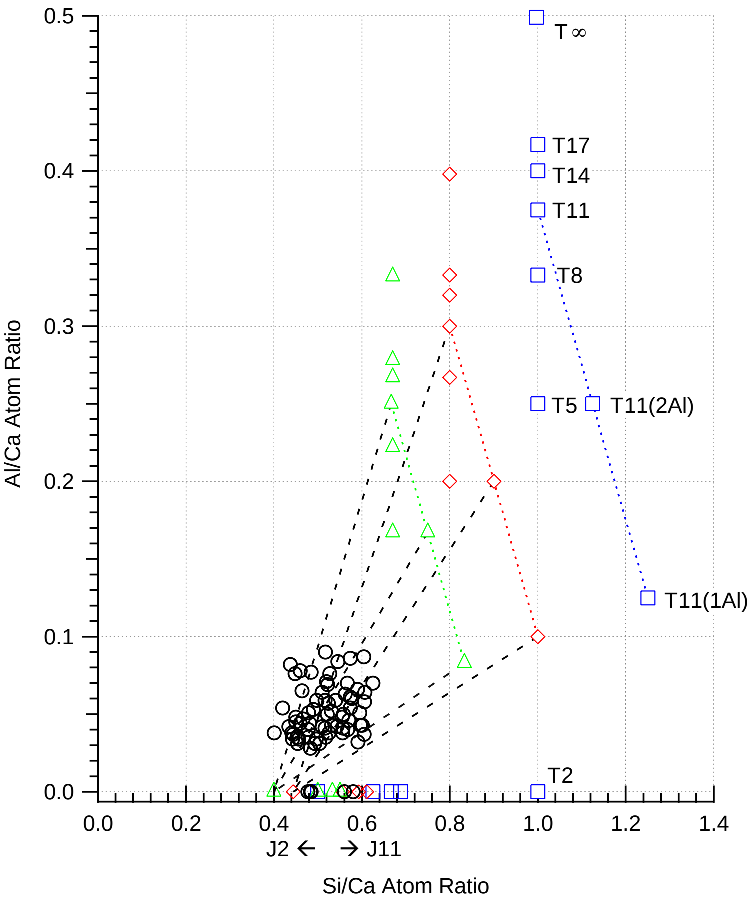

Figure 4-22: As Fig 4-21 except black dashed lines now join points for T11 structural units with the points representing jennite-based dimer of the same protonation. Op (○) C-S-H.

As shown in figure 4-22 the T/J model does fit the remaining number of analyses with the represented tie-lines on figure 4-22 relating to jennite-based dimer units, as it is known a large amount of dimer remains even after long - term hydration of neat PC pastes [26]. The TEM-EDX analyses displayed agree with this conclusion that a large amount of short J-based units remain within the C-S-H. Additionally present are a level of longer chain length T-type structures which contain the required tetrahedral Al^{3+} by substitution to explain the experimentally found Al/Ca atomic ratios.

The 35˚C sample analyses are shown in figures 4-23 and 4-24 for the T/CH and T/J structural viewpoints respectively. As with the ambient sample a percentage of the data analyses with higher Al/Ca ratio can be explained by the T/CH model if partial substitution of the T-type structure is allowed along with previously reported chain lengths for neat OPC pastes.

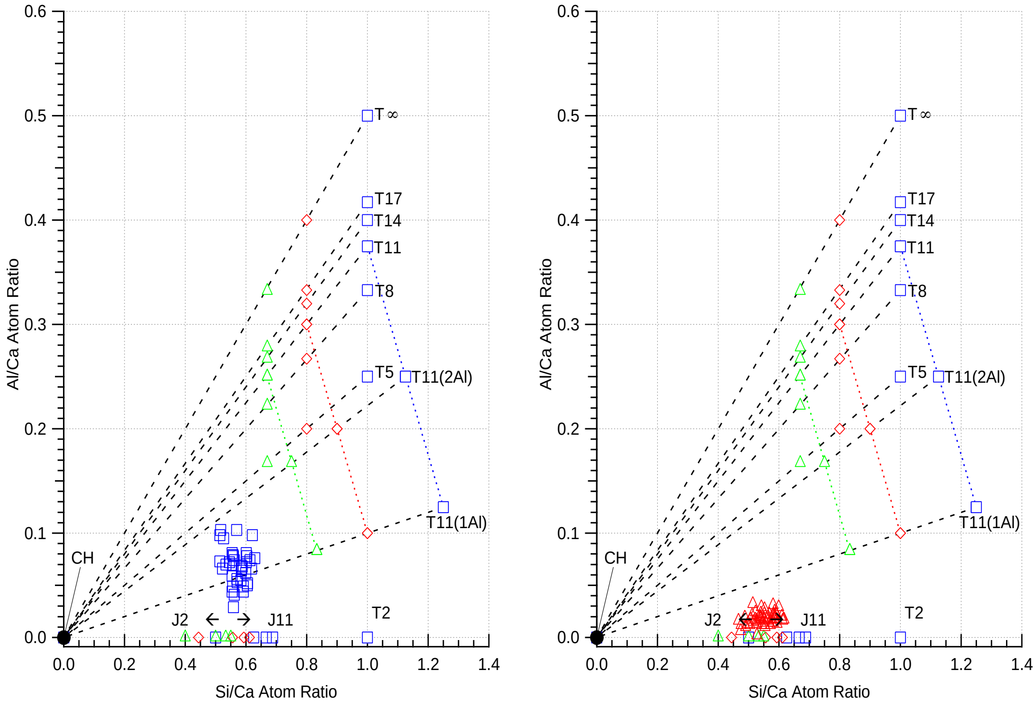

Figure 4-23: As Fig 4-21 except TEM-EDX analyses of Op C-S-H present in 35˚C (□) and 80˚C (△) cured samples.

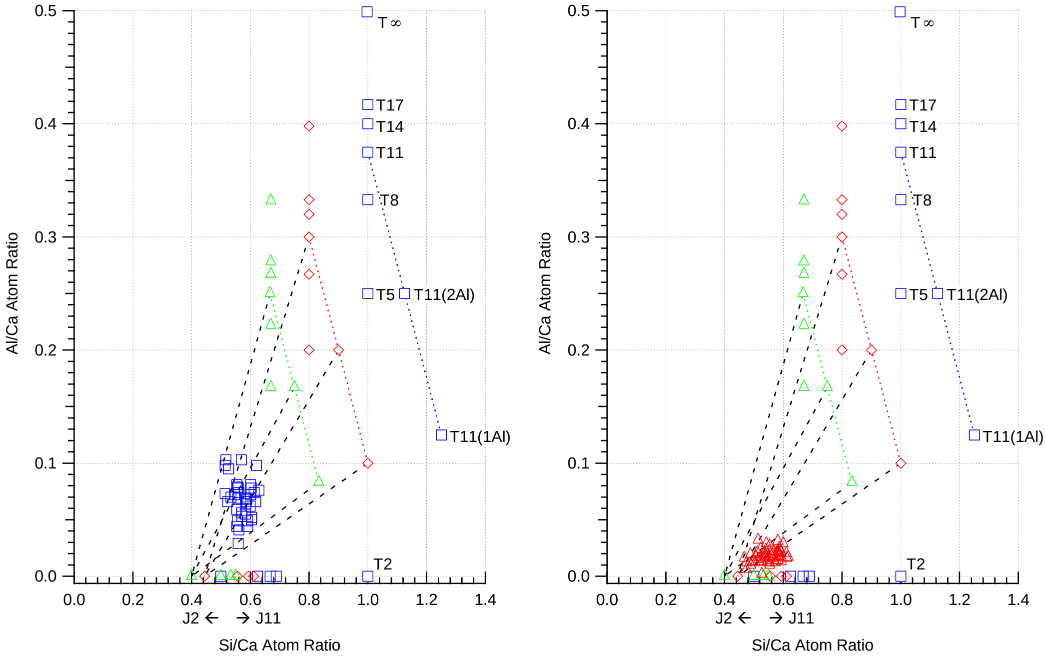

Figure 4-24: As Fig 4-21 except black dashed lines now join points for T11 structural units with the points representing jennite-based dimer of the same protonation. TEM-EDX analyses of Op C-S-H present in 35˚C (□) and 80˚C (△) cured samples.

The T/J approach for the 35˚C analyses show a tighter grouping of data points relating to narrowing of the possible J-type chain lengths in the C-S-H. The data also indicates a possible increase in the J-type chain length on average when compared to an ambient sample suggesting an increase in polymerisation in the J-type structure. However the tie lines do indicate a substantial quantity of dimer will still remain within the C-S-H phase at 35˚C. Similarity to the ambient sample, the J-type structure will coexist alongside a level of longer chain length T-type structures which contain the required tetrahedral Al^{3+} to explain the experimental data points.

The 80˚C cured sample has a much lower Al/Ca ratio when compared to the lower temperature samples. Due to this the analysis points do not fit into the T/CH model in figure 4-23 for structural units with either full or partial substitution of Al, with even very long chain lengths (T17 +) substituted with 1Al forming a tie line above the maximum Al/Ca ratio suggested by a T/CH model. The 80˚C analyses are better explained by the T/J model with the analyses showing a tight grouping suggesting an increased J-type chain length away from dimer to the pentamer and octamer form. The data is then explained by a small inclusion of T-type structures to account for the small level of Al incorporation. Tie lines in figure 4-22 propose that the T-type maybe of a longer chain sequence with low saturation (T11(1Al)) rather than lower amounts of smaller chain lengths fully saturated by Al^{3+}. However mean chain length (MCL) cannot be confidently proposed without supporting quantitative ^{29}Si NMR evidence.

4.6 NMR

Solid-state NMR spectra for the NRVB samples were obtained at the EPSRC UK National Solid-state NMR service at Durham University for comparison with ^{29}Si and ^{27}Al NMR spectra of neat PC and C_3S pastes.

4.6.1 ^{29}Si MAS NMR

The ^{29}Si MAS NMR spectra for the NRVB samples are shown in figure 4-25 and have been annotated with 3 initial peaks relating to anhydrous material and the hydrated phases Q^1 and Q^2. The small peak relating to anhydrous material is found with a chemical shift of ≈71.8ppm and is referred to as Q^0. The reason anhydrous material (Anh) has been used as a marker in Figure 4-25 is that the small response could be due to two responses; either unreacted alite with a broad peak centered around -73 ppm or β-belite which represents as a single resonance at -71.3 ppm [136, 185]. Q^1 denotes chain end group tetrahedra with the characteristic chemical shift observed at -79 ppm, Q^2 denotes mid chain groups in which both adjacent tetrahedra are occupied by Si with a shift observed at -85 ppm.

The observed spectra for the NRVB samples all show essentially two responses related to Q^1 and Q^2 and they closely resemble the spectra found for C_3S pastes [176, 177, 186] at later stages of hydration.

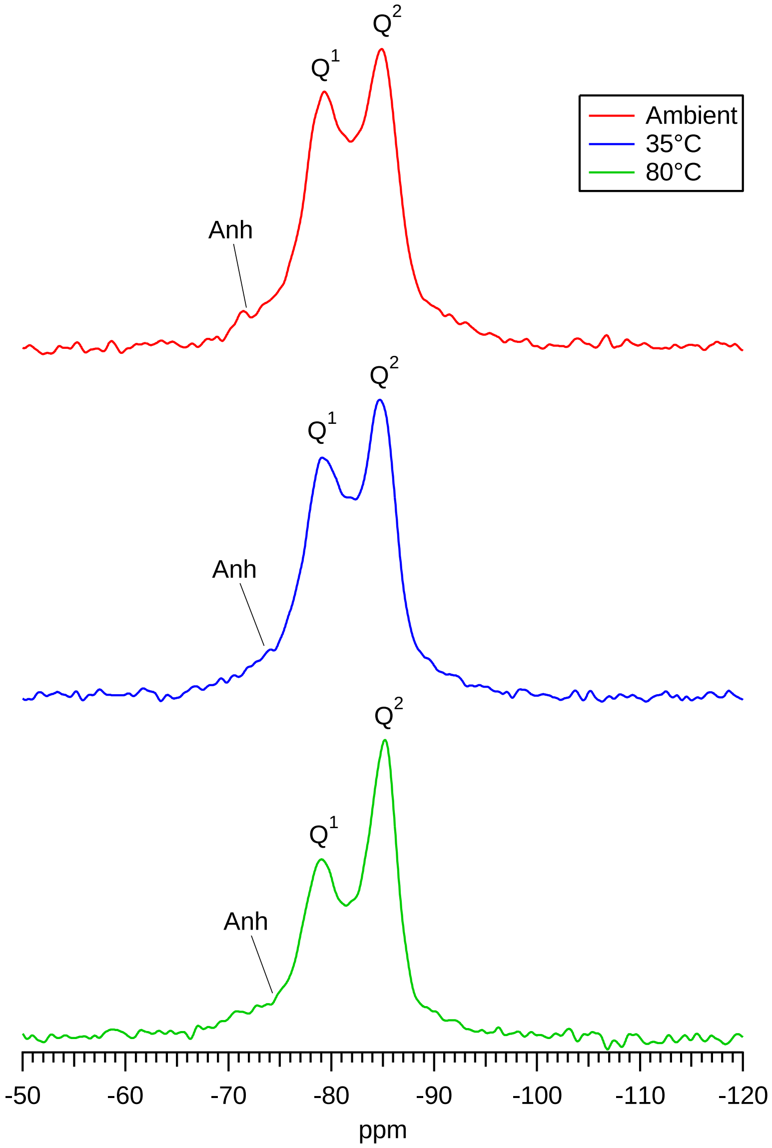

Figure 4-25: ^{29}Si MAS NMR experimental spectrum for NRVB samples

The results for the ^{29}Si NMR for the sample cured at the primary elevated temperature (80˚C) shows a relative increase in the amount of mid chain Q^2 groups when compared to end chain groups Q^1. This agrees with studies carried out on C_3S pastes which found a increased level of polymerisation with time and temperature resulting in increased levels of mid chain units [167, 176, 177]. An additional peak can be attributed to the asymmetric Q^2 peak at ≈-82.5 ppm representing a mid-chain unit with one adjacent tetrahedra occupied by aluminium $Q^2(1Al)$ [181]. This peak has not been fully resolved but it potentially seems larger in the ambient and 35˚C samples due to the observed peak shape. This increase in mid chain units supports the evidence found by TEM-EDX in which the J-type units seemed to increase in chain length with increasing temperature. The incorporation of larger amounts of Q^2 (1Al) for the samples with a lower curing temperature also would seem sensible when a comparison is made with the TEM results and each sample's mean Al/Ca atom ratio.

4.6.1 ^{27}Al MAS NMR

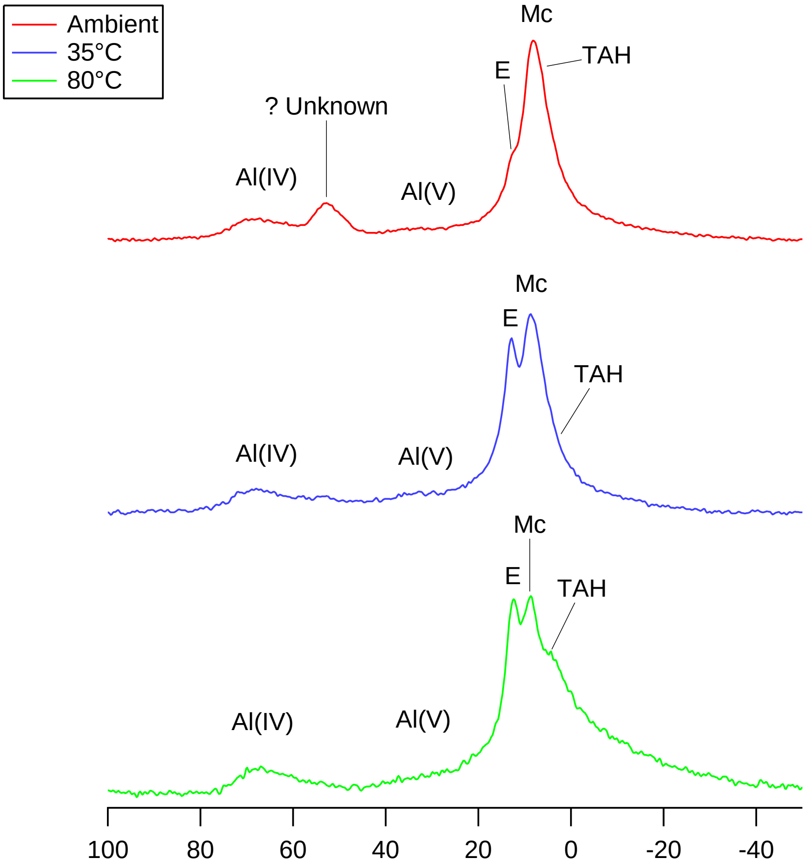

Figure 4-26: ^{27}Al MAS NMR experimental spectrum for NRVB samples; E - AFt, Mc - AFm, TAH - third aluminate hydrate.

The ^{27}Al MAS NMR spectra for the NRVB samples are shown in figure 4-26 and have annotated peaks relating to the centerband resonances from tetrahedrally coordinated Al(IV) (40-90 ppm), five-fold Al(V) (20-40 ppm) and octahedrally coordinated Al (-10-20 ppm)[182, 183, 187, 188].

The octahedrally coordinated responses in the region of (-10ppm - 20ppm) originate from the AFt and AFm calcium aluminate hydrate phases [182, 187] annotated as E (AFt) and Mc (monocarboaluminate) in figure 4-26. Additionally the 'third aluminate hydrate' phase

(TAH) is found at -5 ppm and is attributed to a nano-structural aluminate phase formed at the surface of the C-S-H [188]. ^{27}Al NMR does not allow for individual identification of AFm phases due to different AFm phases having almost identical chemical shifts [157, 187]. Due to the previous XRD results this observed response for AFm at ≈9.8 ppm has been attributed to the formation of monocarboaluminate. The second main octahedral resonance at ≈13 ppm is known to be due to the formation of ettringite [182].

The weak resonance centred at ≈70 ppm is due to the presence of Al^{3+} which has been incorporated within the C-S-H structure. The intensity of this peak is reduced when compared to neat OPC pastes which agrees with studies into limestone - blended cements by NMR [187] and the TEM Al/Ca ratios. The observed resonance for the ambient cured sample between (60-50 ppm) is currently an unknown phase, Le Saout et al [189] observed a similar unknown peak for a Al(IV) in a study on oilwell cements. One line of enquiry is whether this could be related to a ferrite phase similar to the synthetic calcium aluminoferrite samples discussed by Skibsted et al [190], which displayed central transition at 61 ppm.

4.7 Conclusions on the composition of NRVB grouts

The NRVB samples displayed the expected basic phase composition with large quantities of calcium carbonate and calcium hydroxide observed at all temperatures. SEM analysis of the general microstructure showed the presence of fully and partially reacted cement particles and produced C-S-H which was the binder between large amounts of unreacted limestone particles. Analysis by TEM imaging showed the microstructure consisted of a coarse C-S-H binding phase with a high Ca/Si ratio similar to that observed in neat PC and C_3S cements; the C-S-H was interspersed with areas of calcite which acted as nucleation sites. The morphology of the C-S-H phase altered from coarse to a more fine fibrillar nature with a directional aspect as a function of the space constraints locally. The main effect of temperature upon the observed C-S-H was a reported reduction in the mean Al/Ca ratio for the 80˚C sample. This was linked to the reduced diffusion of Al^{3+} into the Op due to densification of the formed Ip under increased temperature curing. The TEM-EDX data was analysed with regards to Richardson and Groves' nanostructural model for C-S-H, this showed the measured atomic ratios for lower temperature samples were partially explained by both the T/CH and T/J models. The higher temperature sample at 80˚C was best explained by the T/J model due primarily to the reduced Al/Ca ratio observed by TEM-EDX. It was proposed the data points could be explained by longer chain length sequences with low levels of Al saturation. This conclusion is supported by the ^{29}Si NMR evidence which showed a large proportion of Q^2 groups when compared to Q^1, this progressively increased with higher curing temperatures indicating the increased chain lengths.

Additional phases formed within the samples included small levels of ettringite and hydrotalcite detected by XRD and the noticeable formation of an AFm phase identified as monocarboaluminate. The primary effect of temperature on these additional hydrated phases was the decomposition of the monocarboaluminate at 80˚C with that sample showing the associated hydrogarnet decomposition product. Few changes were found between the ambient and 35˚C samples in terms of these additional phases with monocarboaluminate still stable up to 35˚C.

In service, the NRVB material's role is to maintain a high near-field pH that minimises the solubility of many radioelements and to additionally provide a high sorption capacity [115, 118]. These combine to retard the migration of radionuclides in the proposed GDF. One major source of interest is the potential for cementitous materials to change over time especially in hydrothermal conditions which maybe present during geological disposal. This study has characterised a 5 year old sample which was hydrothermally cured for one year [119], it has been shown large quantities of C-S-H and calcium hydroxide remain in the system at this age. These phases are of particular interest due to their capacity for chemical sorption and maintenance of pH levels respectively. In service it is likely the NRVB material would undergo increase compositional changes due to dissolution of the calcium hydroxide and C-S-H [191]. Baston et al [115] has shown via accelerated testing the removal of calcium hydroxide after leaching aged NRVB samples. Some evidence of C-S-H alterations due to differing curing regimes has also been observed, however these alterations were reported to have a minimal effect on the sorption capacity of the NRVB material [115, 192].

Chapter 5 : Results and discussion of BFS:OPC + $BaCO_3$ grout

5.1 Introduction

As noted in section 2.4 the primary academic paper which focused on the encapsulation of barium carbonate was carried out by Utton et al [86], it observed the interactions of OPC and blended systems with $BaCO_3$ up to 60˚C. This study concluded there were significant reactions involving the $BaCO_3$ and available soluble sulfate in the mixes. This section looks at the long - term addition of $BaCO_3$ to a blended 9:1 BFS:OPC grout and the resultant interactions and microstructure of the system. The results are referenced to the previous findings of Utton et al and other relevant papers, both with regards to barium inclusion in cements [88, 89, 193] and the addition of $CaCO_3$.

5.2 XRD

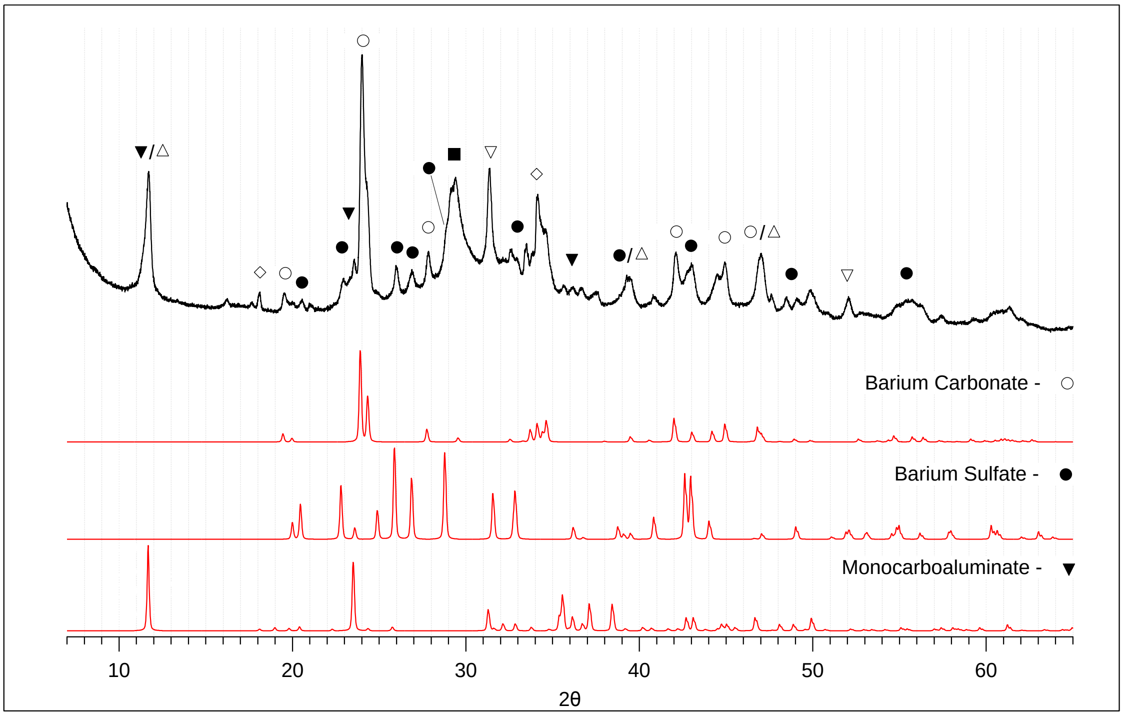

Figure 5-1: XRD trace of BFS:OPC + $BaCO_3$ with simulant waste and primary resultant phases simulated patterns shown, ▼- AFm (Monocarboaluminate), ◇- Portlandite, ○- Barium Carbonate, ●- Barium Sulfate, ■- Calcite, ▽- Gehlenite, △- HT phase.

The hydration products for the 9:1 BFS:OPC + $BaCO_3$ are shown in figure 5-1, and as can be seen a large proportion of the $BaCO_3$ remains unreacted within the grout. The cement hydration products observed by XRD include the AFm phase monocarboaluminate (Mc), calcite, a hydrotalcite-like phase (HT) and a small quantity of portlandite. The primary new phase detected solely associated with the inclusion of the simulant waste was barite ($BaSO_4$).

The formation of $BaSO_4$ occurs due to the reaction between $BaCO_3$ and the available SO_4^{2-} ions from the hydration of OPC in the blended grout. However a large percentage of the $BaCO_3$ remains within the system due to the relatively small amount of OPC added in the composite grout, therefore this greatly reduces the available SO_4^{2-} ions for reaction with the $BaCO_3$. The reason for this uptake in SO_4^{2-} ions relates to the relative solubility of barium sulphate when compared to calcium suphate as discussed in section 2.4. $BaSO_4$ is less soluble than $BaCO_3$ whereas with calcium the opposite solubility is observed with $CaCO_3$ being the least soluble phase. The resultant formation of $BaSO_4$ from soluble sulfate destabilises any ettringite formed during the early - stage hydration of the OPC as the SO_4^{2-} is consumed to form $BaSO_4$ [86, 88]. This results in the aluminate and carbonate ions forming monocarbolauminate (Mc) rather than monosulfate (Ms). As discussed in chapter 4, Mc is formed as the stable phase at ambient temperatures in the presence of additional carbonate ions [46]. In this regard the formation of this carboaluminate phase is similar to that observed in blended OPC- limestone cements [153] due to the addition of $BaCO_3$ and availability of carbonate ions.

The observed Mc phase peak at (11.7˚ 2θ) was slightly asymmetric similarly to that reported by Utton et al [86] at 60˚C where doublet formation allowed easier identification of a hydrotalcite-like (HT) phase. Whilst the detection of HT was difficult in this XRD study its presence is expected in a BFS composite cement [194] and was observed later using TEM EDX. The formation of HT was of interest due to its potential to contain carbonate ions in its structure similarly to its natural mineral analogue [195]. Additionally the presence of calcite in small quantities could be attributed to the liberation of CO_3^{2-} by the $BaCO_3$ forming $CaCO_3$. It cannot however be distinguished whether the $CaCO_3$ came from this reaction or carbonation using XRD. The presence of gehlenite in the XRD results was expected due to the large quantity of unreacted glassy slag remaining due to the high slag replacement levels, this was later confirmed by imaging of the microstructure by SEM.

5.3 Thermal Analysis

The TG/DTA trace from the $BaCO_3$ containing grout is shown in figure 5-2. The trace shows the decomposition at 150˚C which is associated with the AFm - Mc phase [153, 157]. Small mass losses for the portlandite and calcite phases were identified which agree with the results from XRD which identified their presence in small quantities. Additional small mass losses were seen for a hydrotalcite (HT) phase with the DTA showing corresponding weight losses at around 210˚C and 380˚C. This two - stage mass loss pattern for hydrotalcite-like phases has been reported previously in various slag - based cements [38, 196] and for a syntheised HT-LDH phase with a Mg/Al ratio of 2.0 investigated by TGA and HTXRD [197].

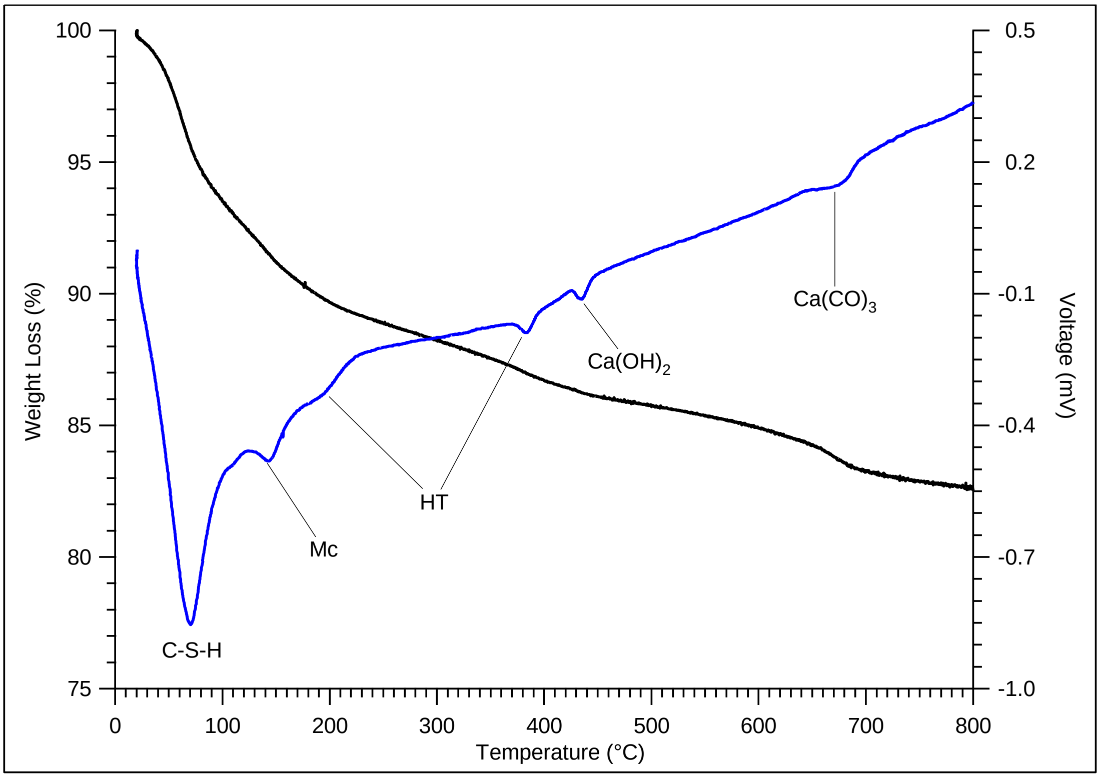

Figure 5-2: STA trace for BFS:OPC + $BaCO_3$; Mc - Monocarboaluminate, HT- Hydrotalcite

5.4 SEM-EDX

Typical BSE images of the 9:1 BFS:OPC + $BaCO_3$ sample can be seen in Figure 5-3; the barium - containing phases identified by XRD ($BaCO_3$, $BaSO_4$) are easily distinguished due to the high atomic number of barium (56) compared to cement hydrate phases resulting in the highly contrasted bright features.

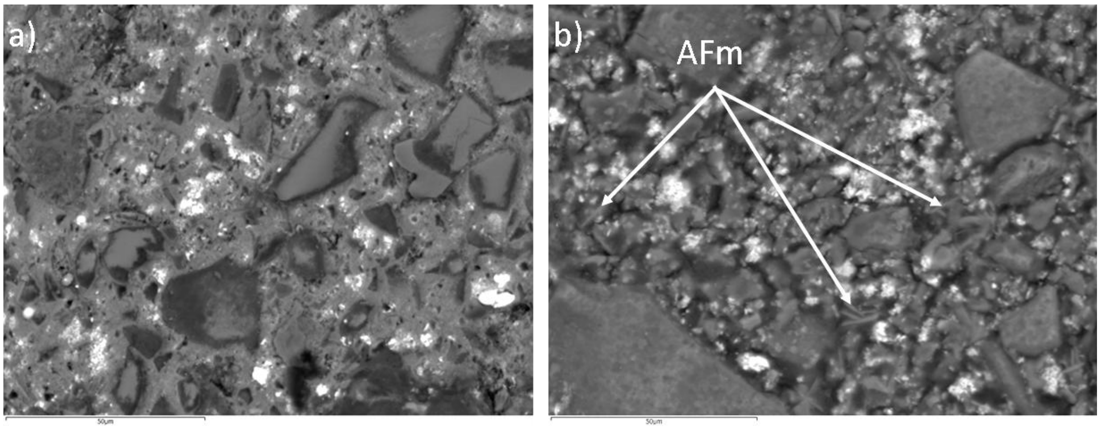

Figure 5-3: BSE image of BFS:OPC + $BaCO_3$ - High contrast areas are linked with barium; a) 500x, b) 1000x

The microstructure contained quantities of partially reacted BFS particles with only minimal hydration rims being observed on the majority of the large slag grains. Very little anhydrous OPC products (C_2S, C_4AF) were seen indicating the near complete hydration of all available OPC. These findings are in agreement with the expected microstructure for high replacement slag cement systems such as 9:1 BFS:OPC [53, 79]. The evidence from BSI suggested a possible interaction with the $BaCO_3$ acting as nucleation sites for hydrate phases in a similar fashion to that described for finer particles of $CaCO_3$ [153, 198].

Barium was distributed throughout the binding matrix and is assumed to be surrounded by predominantly Op C-S-H this is shown by the higher contrast responses in figure 5-3 surrounded by mid grey scale product associated with C-S-H [145]; this was later supported by TEM-EDX. The barium did however tend to agglomerate into more concentrated areas of Ba rich materials as can be seen in the BSE images figures 5-3 and 5-4. The presence of AFm phases can be seen in figure 5-3 b) and indicates that quantities of the monocarboaluminate phase (Mc) identified by XRD are formed throughout the microstructure due to the freed carbonate ions from the formation of $BaSO_4$.

Quantitative elemental mapping by SEM-EDX shows the barium distributed throughout the microstructure with some intense responses showing agglomerations of barium products (Figure 5-4). The quantitative mapping does indicate some association in these intense groupings for barium and sulphate responses linking with the partial reaction of $BaCO_3$ to $BaSO_4$. Additionally figure 5-4 shows the small reaction rims of partially - hydrated slag grains as shown by the magnesium responses indicating the higher Mg content of the Slag Ip product when compared to the Op C-S-H.

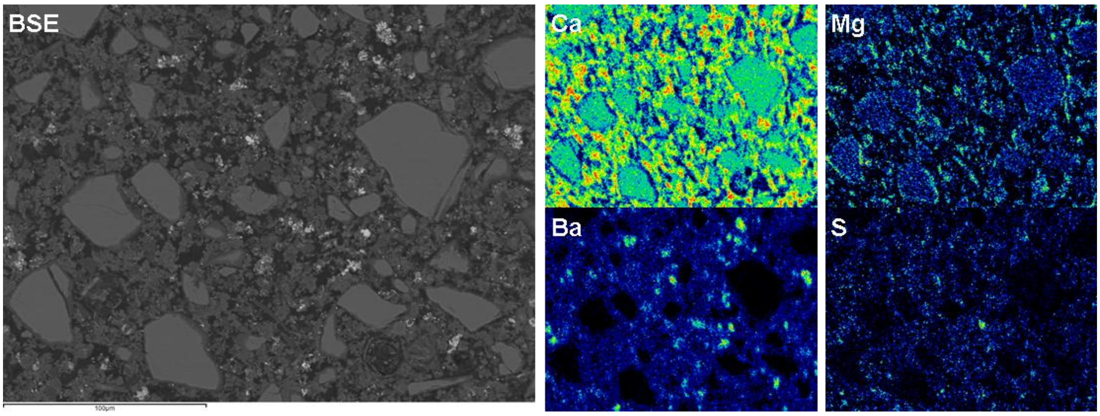

Figure 5-4: Elemental quantitative mapping of BFS:OPC + $BaCO_3$ microstructure (x500)

EDX point analysis and elemental line scanning were carried out in conjunction with the elemental mapping in areas of significant barium response and thus the incorporated simulant waste. The spectra and scans showed a large variation in the association of barium with sulphate in the microstructure agreeing with the XRD results in confirming the presence of large quantities of unreacted $BaCO_3$ alongside relatively low levels of $BaSO_{4,}$; the variation can be seen in figure 5-5.

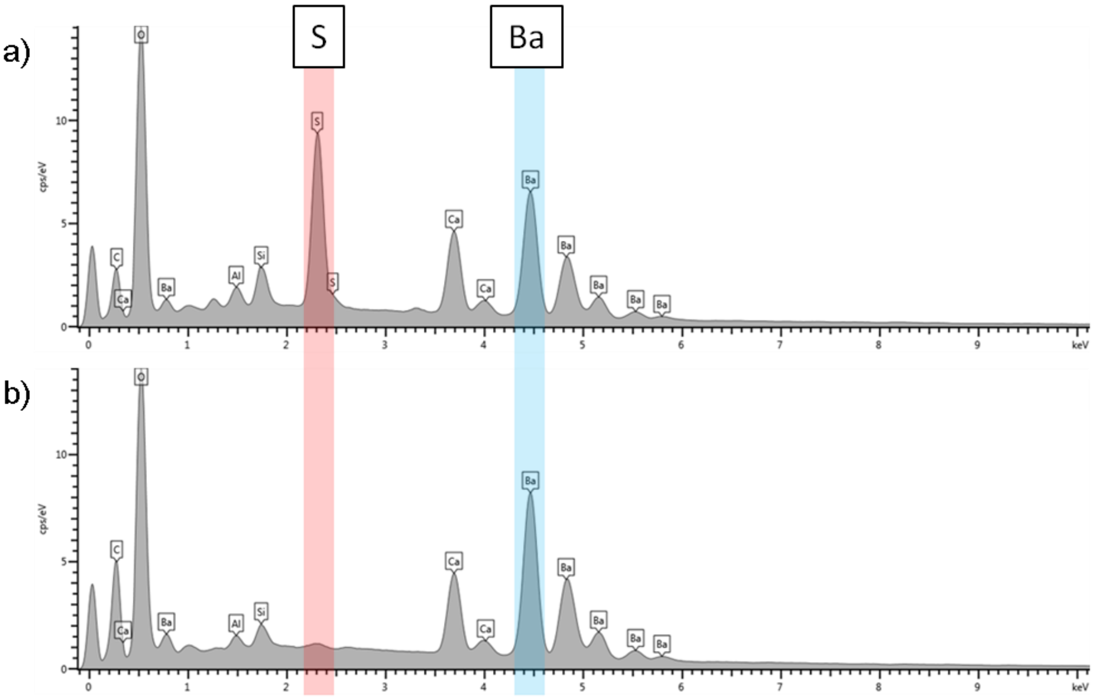

Figure 5-5: Point EDX analyses from a) suspected $BaSO_4$ and b) suspected $BaCO_3$

Figure 5-6 shows the elemental mapping of a barium agglomeration described earlier. Slag particles are identified by the magnesium response map and the location of Ba and C indicates the location of $BaCO_3$ agreeing with the BSE imaging. Utton et al [86, 199] suggested the potential incorporation of Ba^{2+} into the CSH matrix around hydrating OPC particles from EDX analysis. Figure 5-6 however only shows very low levels of barium linked with the binding matrix and the Ba and Ca responses do not seem to be associated in this matrix. The potential effects of $BaCO_3$ addition on the C-S-H phase was investigated in more detail using TEM in section 5.5.

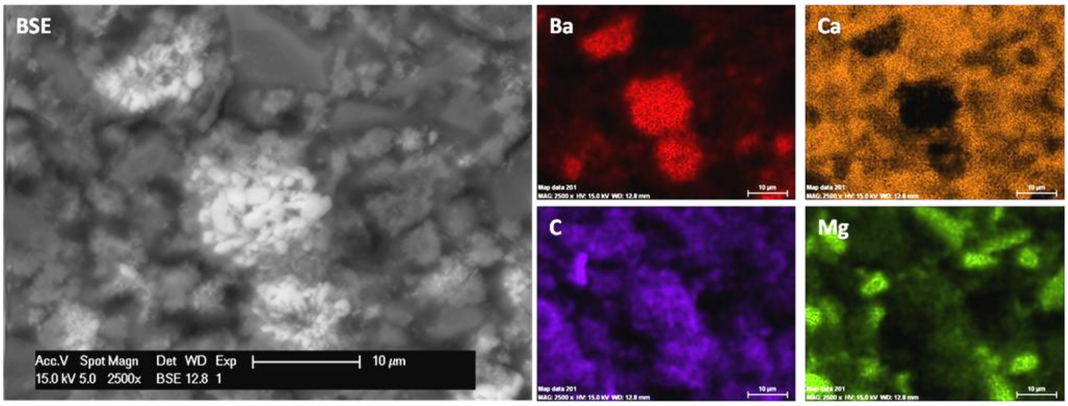

Figure 5-6: BSE image of a Ba rich area (x2500) showing Ba, C associated with $BaCO_3$ and Ca, Mg from hydration products and slag particles.

The presence of $BaSO_4$ was also directly confirmed by the observation of crystalline phases using higher magnification SEM which are shown in figure 5-7. The nature of the $BaSO_4$ seems more obviously crystalline when compared to the nature of the predominantly $BaCO_3$ formation shown in figure 5-6. Figure 5-7 also shows the relatively intimate intermixing of small barium - based crystals within the cement's Op matrix. This could explain the assumption that barium is incorporated into the cements microstructure if SEM-EDX is used for this purpose due to the electron interaction volume.

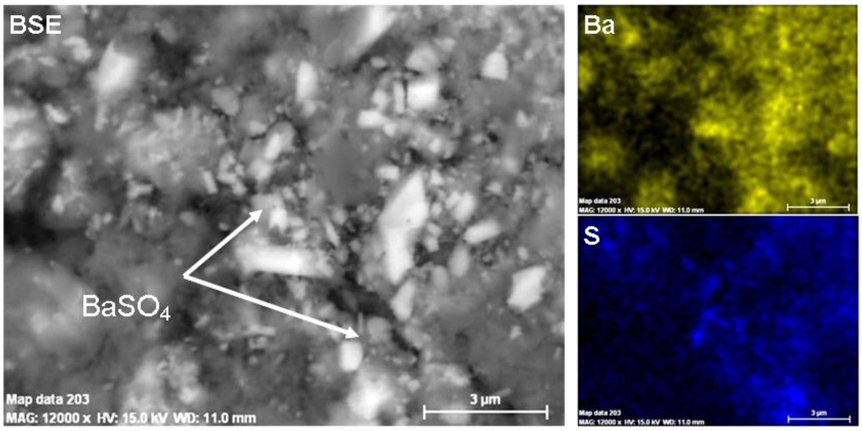

Figure 5-7: BSE image of $BaSO_4$ crystals with the binding matrix (x12000)

Plots of the EDX analyses also show a correlation between barium content and increasing sulphur content indicating $BaSO_4$ formation indicated by a Ba/S ratio of around 1 (see figure 5-8). The dotted circled area in figure 5-8 indicates analyses from the general binding matrix rather than $BaCO_3$ or $BaSO_4$, due to the interaction volume of the SEM a certain level of Ba is measured within this grouping.

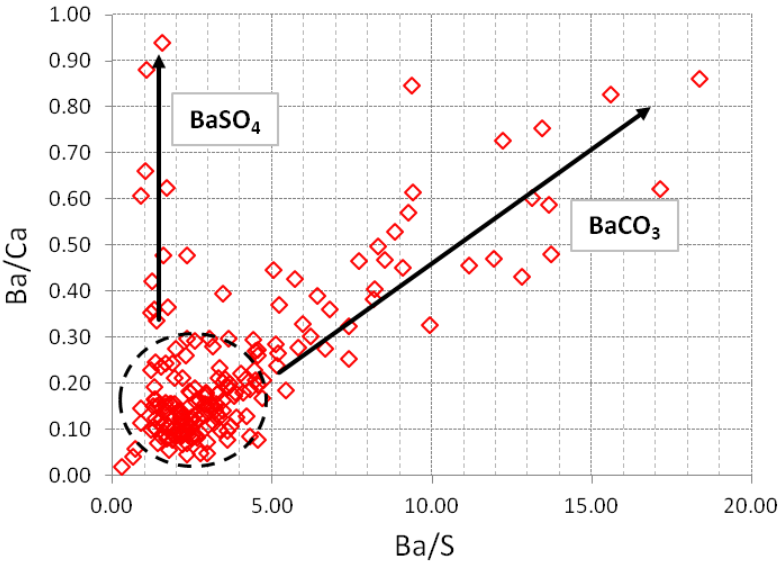

Figure 5-8: SEM EDX analyses showing presence of barium containing phases

5.5 TEM-EDX

The Op C-S-H for the BFS:OPC + $BaCO_3$ paste with 90% slag replacement shows a predominantly foil-like morphology. This has been observed and described in previous studies of high replacement slag cements with foil - like Op becoming more dominant with the increasing slag content [53, 54, 200]. There is however a variation in both the relative 'fineness' of the observed foil-like C-S-H and morphology which can be seen in figures 5-9 through to 5-11 respectively. These changes in fibre length within the same sample potentially relate to local variations in space constraint. Additionally whilst the general microstructure does exhibit as foil - like Op, some areas do show a fine-fibrillar morphology often in the presence of hydrated particles or simulant waste additions (figure 5-11). However the hydration of OPC grains would be expected to exhibit a more fibrillar morphology for the Ip. The nature of the fibrillar product found in this sample was much finer and shorter than that that displayed for a neat OPC paste as described earlier for the NRVB paste. Large quantities of AFm product were identified by XRD analysis of this sample and the presence of AFm was confirmed within the Op by TEM imaging with its chemical composition confirmed by EDX.

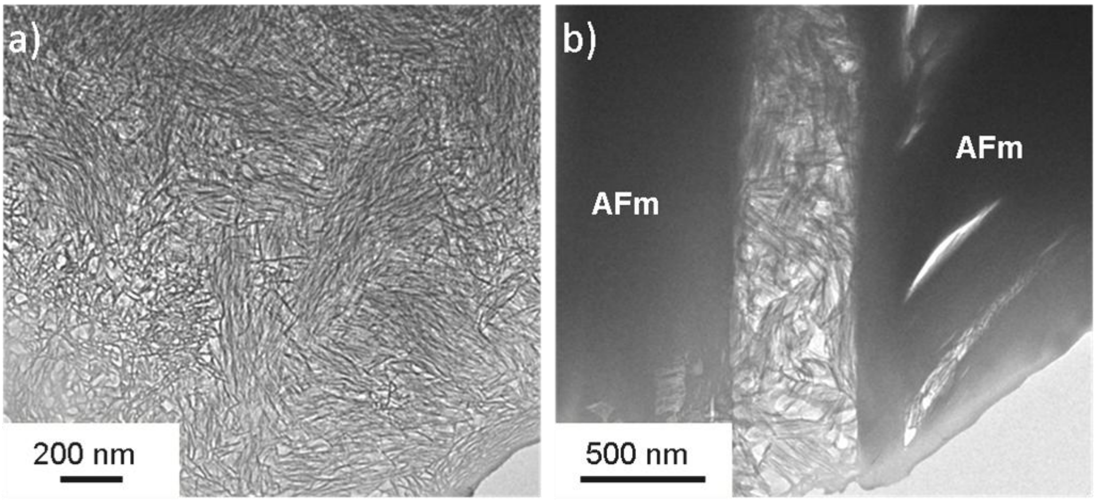

Figure 5-9: TEM Micrographs of a) Fine foil op C-S-H and b) Foil like Op C-S-H surrounded by AFm product

In the hydrated regions of the slag grains the Ip zones displayed a dense and homogeneous morphology of fine C-S-H product intermixed with quantities of a hydrotalcite - type phase (HT); these presented as laths of varying sizes within the Slag Ip (figure 5-10 region B). The identification of HT was useful to confirm the presence of Ip zones within the system, the EDX data for the slag intermixed with the HT phase can be seen in figure 5-14. These data help describe the possible composition of the HT phases and the underlying Al content of the formed slag Ip.

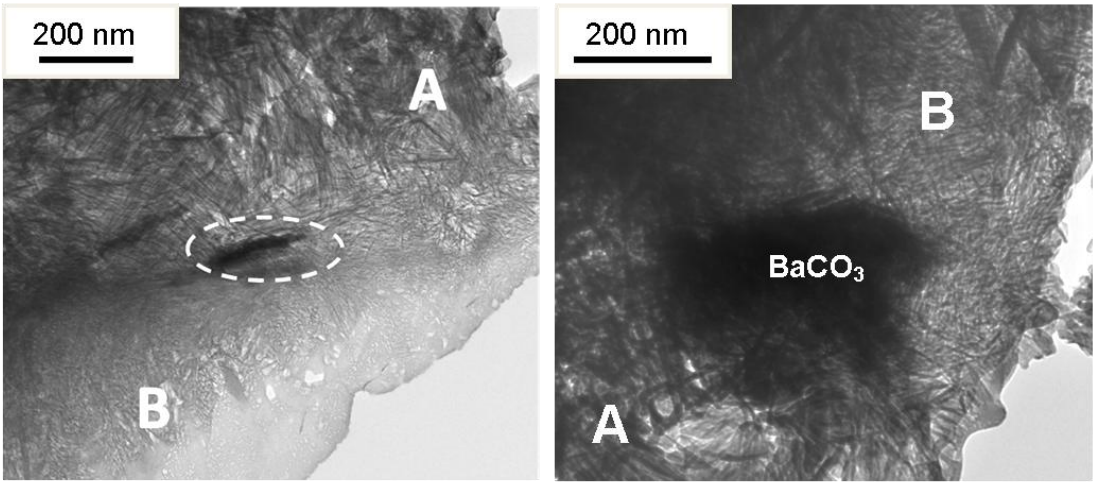

Figure 5-10: TEM micrographs of A) Op C-S-H product B) Fine Slag Ip C-S-H product intermixed with hydrotalcite like LDH phases, $BaSO_4$ crystal circled.

The addition of the simulant waste material $BaCO_3$ was noted in the examination of the sample using TEM as shown in figures 5-10 and 5-11. The agglomerations of $BaCO_3$ observed (figure 5-11 b)) are similar to that described in section 5.4 and observed in figure 5-6. The primary resultant phase ($BaSO_4$) was also observed in the matrix displaying a more crystalline like formation than that of the $BaCO_3$ (figure 5-11 a)), small formations of

$BaSO_4$ were also seen surrounding the large $BaCO_3$ agglomerations which agreed with the SEM imaging. These simulant waste sites seemed well incorporated within the binding matrix and did not show any inclusion issues or apparent increase in porosity compared to normal high slag cements. Evidence of C-S-H hydration products surrounding the waste sites has been observed and the potential for the inclusion of barium into the hydrate phases is discussed using TEM-EDX. However whilst this is interesting it should be noted the primary waste in service would be ^{14}C contained within the $BaCO_3$ rather that the barium itself.

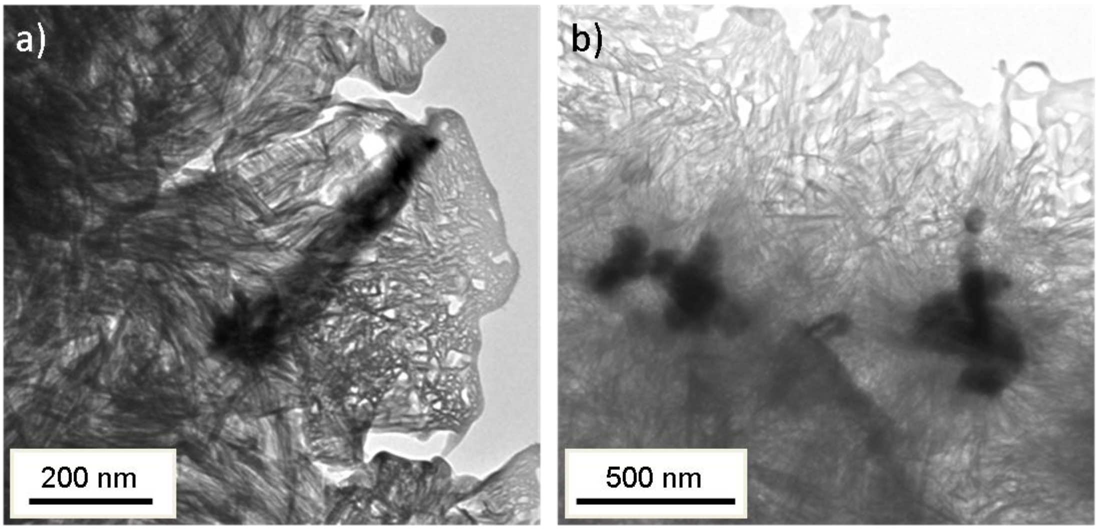

Figure 5-11: TEM micrographs of a) $BaSO_4$ formation and b) $BaCO_3$ agglomerations within the Op C-S-H matrix

TEM-EDX analysis points for the binding matrix are shown in figure 5-12, the analyses include the finer C-S-H shown in figure 5-9 a) and the foil like C-S-H found throughout the rest of the sample. The analysis points from slag Ip and the intermixed HT phase and observed AFm phases have also been included in the scatter plot in figure 5-12. The related atomic ratios for Ca/Si, Ca/(Si+Al) and Al/Si are shown in table 5-1. The mean Ca/Si ratio for the 3 studied C-S-H phases ranged from 1.31 to 1.19 with the lowest Ca/Si ratio present in the Slag Ip. The values for Ca/Si and Al/Si for the Op C-S-H phases fall in between the reported values for a 90% slag cement hydrated for 14 months and 20 years by Richardson and Groves [51] and by Taylor et al [52, 53]; this is acceptable since the slag content and age of this sample sits within the aforementioned studies.

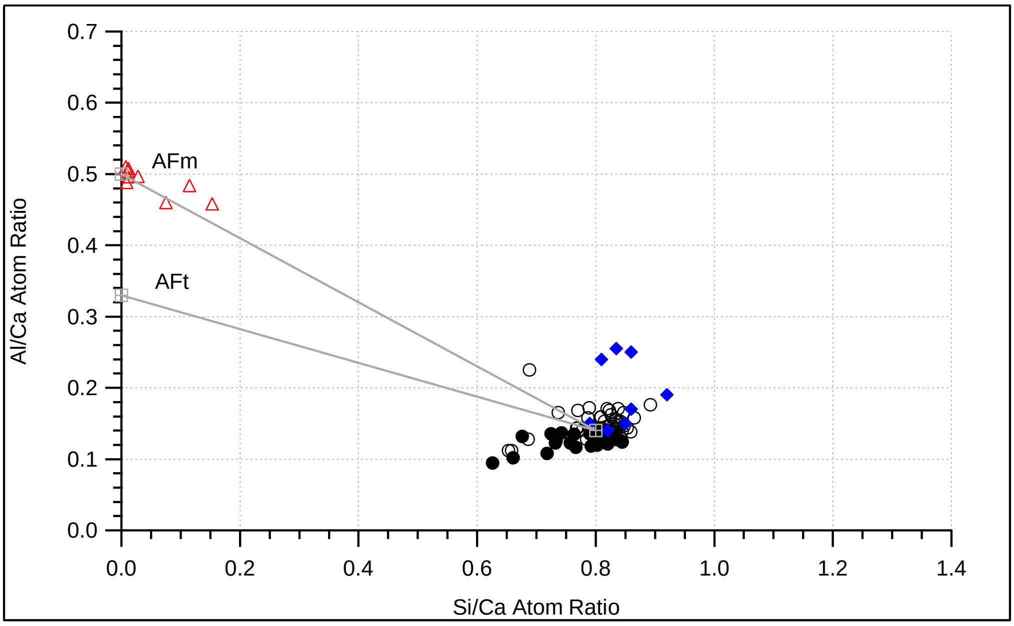

Figure 5-12: BFS:OPC + $BaCO_3$, Si/Ca against Al/Ca atom ratio plot of TEM-EDX analyses of AFm (△), Op (○), Fine Op (●) and slag Ip (◆).

The scatter plot for the barium - related phases is shown in figure 5-13 and presents data similarly to figure 5-8 for the SEM-EDX, again the presence of $BaSO_4$ was confirmed by chemical composition. The most noticeable change between the SEM-EDX data shown in figure 5-8 and the TEM-EDX is the composition of the binding phase labelled as C-S-H in figure 5-13. Due to the smaller interaction volume in the TEM a much tighter composition for the C-S-H is found and the possible substitution of Ba^{2+} into the C-S-H phase can be discussed with more confidence. Any substitution of Ba^{2+} for Ca^{2+} as mentioned by Evans [201] within the cement hydrate phases should be measurable by TEM-EDX as the expected level of Ca will reduce alongside a noticeable increase in Ba. In the observed C-S-H phase the Ba/Ca ratio observed is at or near to 0 suggesting mass barium inclusion is unlikely within the phase.

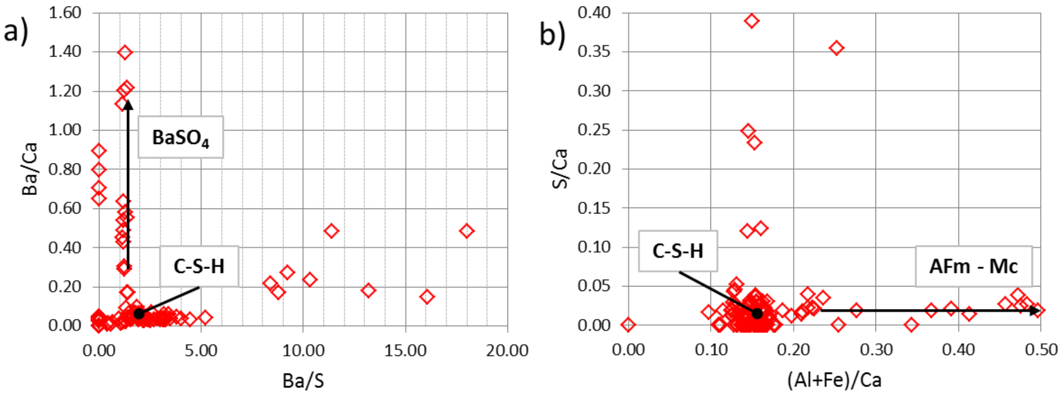

Figure 5-13: Scatter plots of TEM-EDX for Ba/Ca against Ba/S a) and S/Ca against (Al+Fe)/Ca b)

The Mg/Si against Al/Si scatter plot is shown in figure 5-14. The plot indicates that EDX analyses of slag Ip consists of C-S-H intermixed with varying amounts of HT-like Mg-Al LDH phase. The gradient of the linear regression line shown is the Mg/Al ratio of the HT phase (2.45). The Al/Si ratio of the slag Ip is given when Mg/Si=0 (0.15), which is slightly lower than that reported for the Op C-S-H phases of both morphologies discussed in the study and shown in table 5-1. This reported Mg/Al ratio for the intermixed HT phase is within the reported measurements by Richardson and Groves [51] for a slag system at 18 months hydration. Taylor et al [52] reported a lower set of values using the same techniques for the sample after 20 years suggesting a decrease in the Mg/Al ratio of this phase over time. The given value of 2.45 however does seem acceptable when compared to the Mg/Al ratio of the pure mineral analogue of hydrotalcite phases (Mg/Al = 3) and synthesised double - layered hydroxides [197, 202].

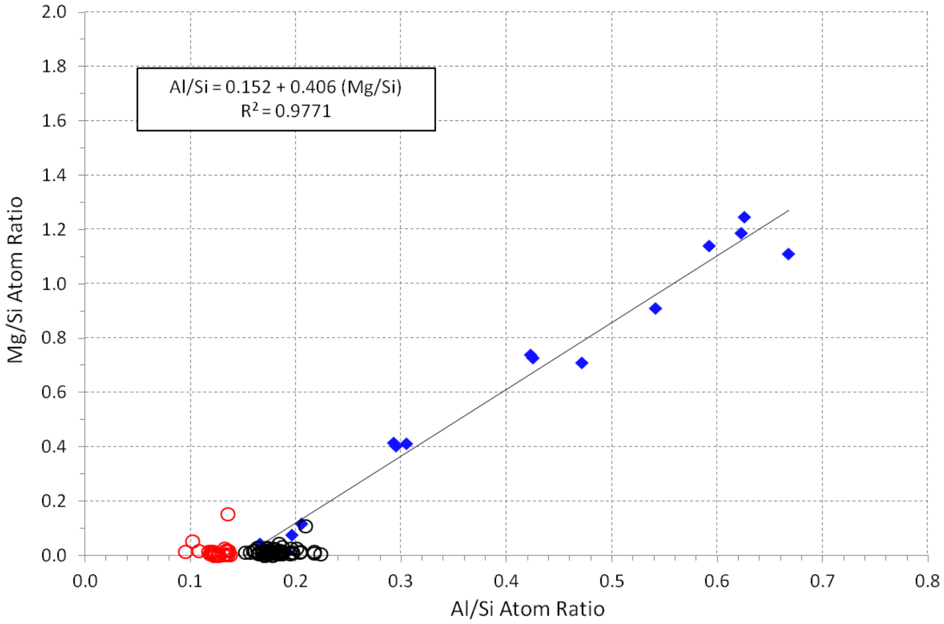

Figure 5-14: Mg/Si against Al/Si atom ratio plots of TEM EDX analyses of fine C-S-H (○), Op C-S-H (○), slag Ip (◆)

		Ca/Si		Ca/(Al+Si)		Al/Si	
	N❖	Mean	SD	Mean	SD	Mean	SD
Fine C-S-H	22	1.31	0.11	1.12	0.09	0.16	0.01
Slag Ip C-S-H	15	1.19	0.12	-		0.15*	
Op C-S-H	55	1.24	0.08	1.05	0.07	0.19	0.03

* Slag Ip Al/Si ratio calculated from regression analysis (Figure 5-14) when Mg/Si = 0

❖N = Number of EDX analysis

Table 5-1: Mean atomic ratios for both Op and slag Ip C-S-H in the 9:1 BFS:OPC + $BaCO_3$ cement paste obtained using TEM-EDX

5.5.1 Nanostructural model for C-S-H

As discussed in chapter 4, the TEM-EDX data can be compared with the tobermorite-jennite (T/J) and tobermorite - 'solid solution' calcium hydroxide (T/CH) models for the nanostructure of C-S-H proposed by Richardson and Groves [24, 26, 175]. The Si/Ca against Al/Ca plots in figures 5-15 to 5-17 show the experimental TEM - EDX and the theoretical structural plots using the approach outlined in the previous chapter.

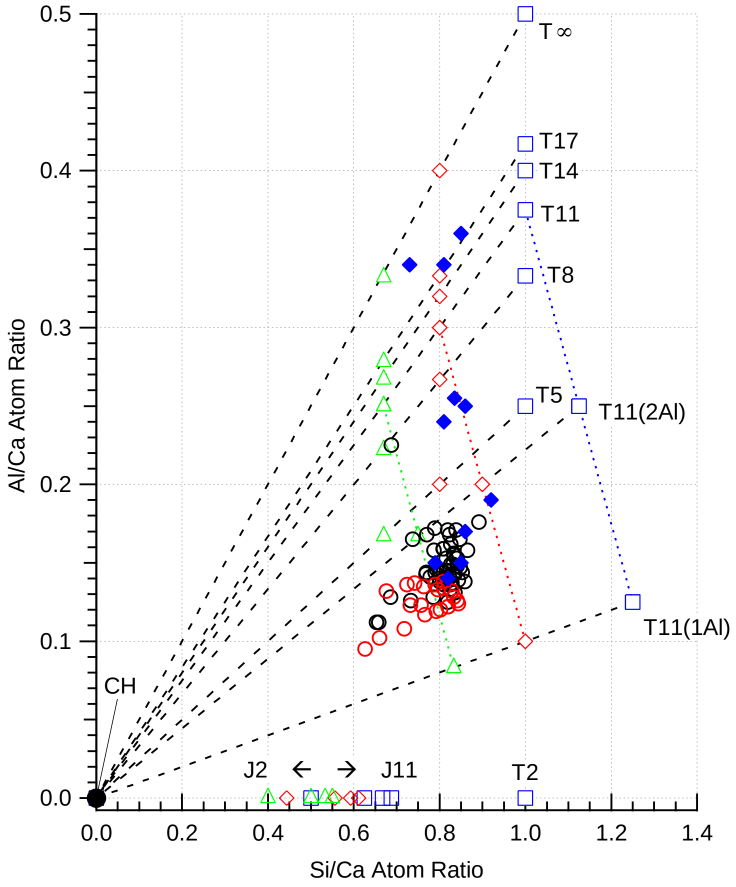

Figure 5-15: Si/Ca against Al/Ca atom ratio plot of TEM-EDX analyses of Fine Op (○), Op (○) and intermixed slag Ip (◆) C-S-H present in 9:1 BFS:OPC + $BaCO_3$ sample. The additional symbols represent the compositions of tobermorite (T) and jennite (J) based structural units with different levels of protonation of the silicate chains: the minimum (△; w/n=0), intermediate (◇; w/n=1) and maximum (□; w/n=2). The additional points included represent tobermorite- based units with chain lengths of 2, 5, 8, 11, 14, 17 and ∞. All units are

assumed to be saturated with Al where possible. (ie all the occupied bridging sites are occupied by Al rather than Si). The only exception is for units with 11 tetrahedral chain length, as additionally to those saturated with Al (T11) those with only one or two of the three possible bridging sites are also shown labelled as (T11(1Al) and (T11(2Al) respectively. The black dashed lines join points for structural units of the same chain length but different degrees of protonation to CH. T11 units with the same protonation but differing Al content are joined by coloured dashed lines.

Examination of the TEM-EDX experimental data in figures 5-15 and 5-17 shows that both the T/CH and T/J structural models can account for the data points for the $BaCO_3$ containing paste. Figure 5-15 shows that while the T/CH model can explain the observed data the displayed trend lines demonstrate that the level of Al incorporation is below that for fully saturated T5 – T8 structures when examining the Op C-S-H. Due to this the theoretical structural units and trend lines were re-plotted (figure 5-16) with regards to more appropriate units. This graph suggests the most appropriate structural units seem to be around T17(3Al), T17(2Al) and T14(2Al) for the Op C-S-H. This indicates the presence of T/CH structural units with a long average MCL which is partially substituted with Al with degrees of protonation between the minimum (w=0) and intermediate (w=1) as is shown in table 5-2. Due to the close approximation to the aforementioned T units only a small amount of CH or J-like structure (figure 5-17) would need to be present within the C-S-H to account for the experimental data. The suggested more appropriate structural units are shown in table 5-2 with their relevant atomic ratios.

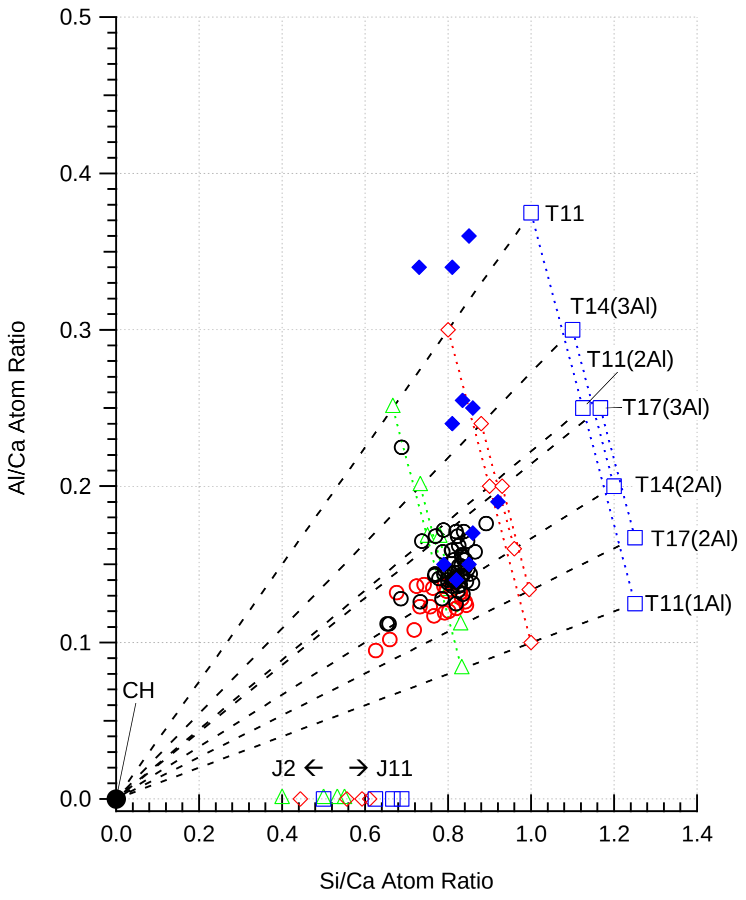

Figure 5-16: As Fig 5-15 except additional points included represent tobermorite- based units with chain lengths of 11, 14, and 17 with varying saturations of Al. Points were chosen to relate to the compositional data for the BFS:OPC + $BaCO_3$ sample. Ip (○), Op (○) and intermixed slag Ip (◆) C-S-H.

The T/J model shown below in figure 5-17 also matches the experimental results with the data sitting around the tie line for T11(2Al) and T17(3Al) again between minimum (w/n=0) and intermediate protonation (w/n=1). The fine Op C-S-H phase with the differing morphology shown in figure 5-9 requires a larger proportion of CH or J-like units to account for its slightly higher Ca values.

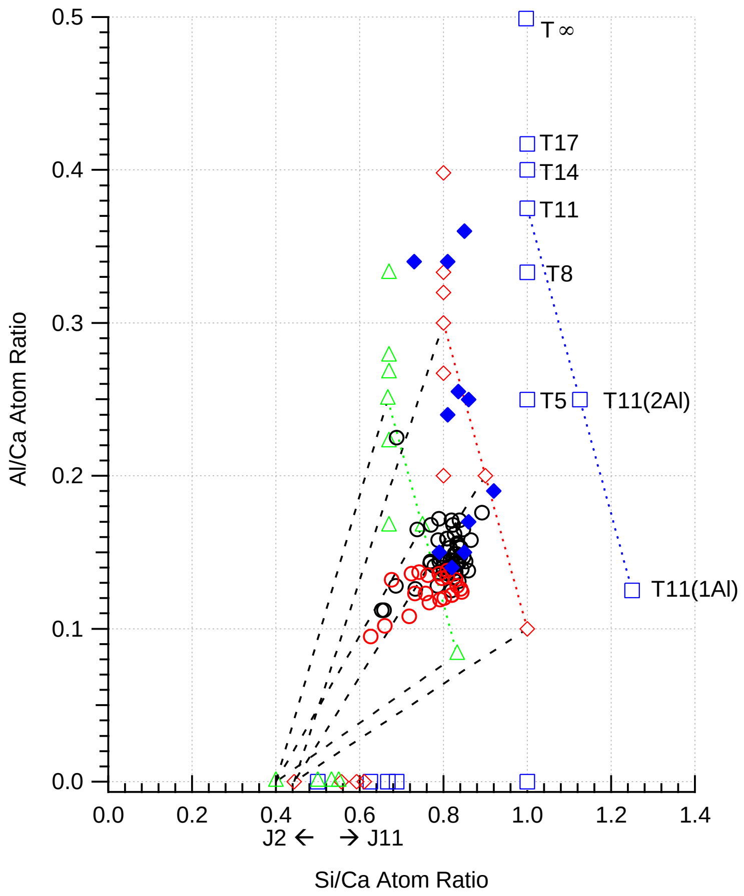

Figure 5-17: As Fig 22 except black dashed lines now join points for T11 structural units with the points representing jennite-based dimer of the same protonation. Fine Op (○), Op (○) and intermixed slag Ip (◆) C-S-H.

Structural Unit	Degree of protonation	Si/Ca	Al/Ca	B (%)*
T11 (2Al)	Minimum w/n=0	0.750	0.167	66
T14 (2Al)	Minimum w/n=0	0.800	0.133	50
T14 (2Al)	Intermediate w/n=1	0.960	0.160	50
T17 (2Al)	Minimum w/n=0	0.830	0.111	40
T17 (3Al)	Minimum w/n=0	0.780	0.167	60
T17 (3Al)	Intermediate w/n=1	0.930	0.200	60

* B(%) Bridging tetrahedra occupied by Al/ bridging tetrahedra occupied by Al and Si

Table 5-2: Selected appropriate T-like structural units for the 9:1 BFS:OPC + $BaCO_3$ sample

5.6 NMR

Solid-state NMR spectra for the $BaCO_3$ containing sample was obtained at the EPSRC UK National Solid-state NMR service at Durham University for comparison with ^{29}Si and ^{27}Al NMR spectra of previously studied GGBS-PC pastes with no additional simulant waste.

5.6.1 ^{29}Si MAS NMR

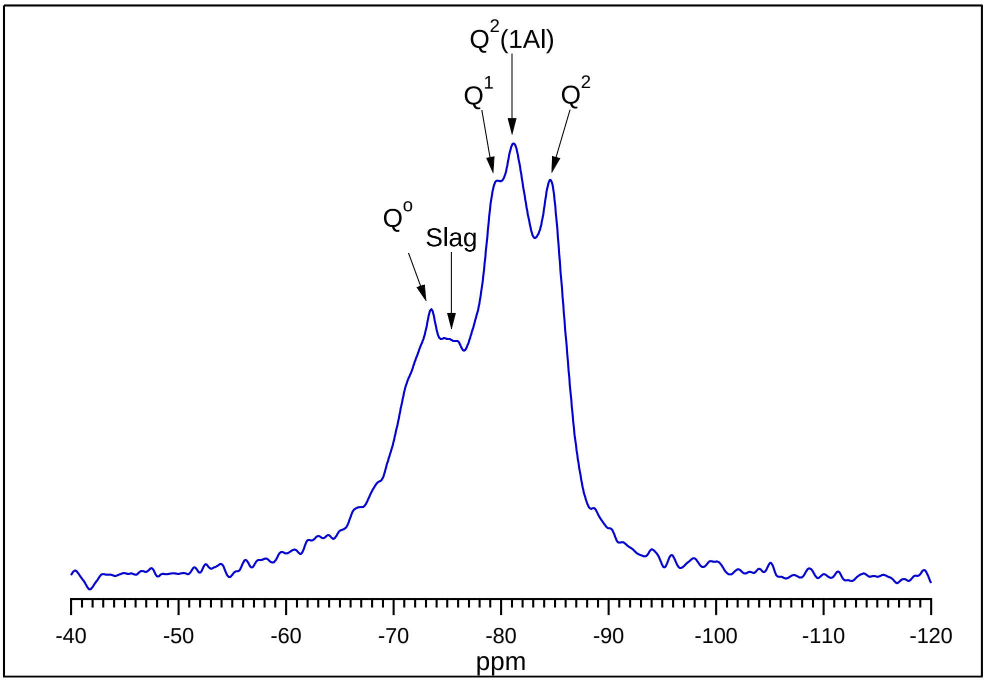

Figure 5-18: ^{29}Si MAS NMR experimental spectrum for BFS:OPC + $BaCO_3$ sample

^{29}Si NMR spectra shows a pair of small peaks at approximately -71.5 ppm and -73 ppm which have been labelled in figure 5-18 as Q^0 and Slag. The sharper peak to the left at -71.5 ppm is attributed to unreacted belite (C_2S) which matches the chemical shift and sharp peak shape observed in references [185, 203]; it is assumed all the alite has reacted at this late stage. The presence of an unreacted belite peak has been noted in previous studies of high replacement slag systems hydrated at 3 weeks with a pair of peaks similar to those observed in figure 5-18 [50, 54]. It is however unusual for significant quantities of unreacted belite to be present in an aged high replacement system as shown by Taylor et al [53]. However a later paper by this research group displaying spectra for various levels of slag replacement for aged pastes indicated the presence of a noticeable Q^0 peak for pastes with 75% - 90% slag [52]. The broad peak which is centred at -73 ppm to the right of Q^0 is known to represent unreacted glassy slag which is expected to be present in high replacement slag cements such as this [50, 53, 54].

The hydrated phases have been annotated using the three peaks for C-S-H discussed previously (Q^1, Q^2(1Al) and Q^2) with chemical shifts at approximately - 79 ppm, -81.5 ppm and -85 ppm respectively. The quantity of Q^2 and Q^2(1Al) peaks observed respectively for mid-chain tetrahedra and a mid-chain unit with one adjacent tetrahedra occupied by Al agrees with the expected spectra for a high slag replacement cement. This result also agrees with the TEM-EDX data when applied to the nano-structural model for C-S-H in the T/CH structural model illustrated in figures 5-15 and 5-16. The T/CH model indicated a larger chain length (MCL) with partial substitution of Al, which is accounted for by the combination of additional Q^2 and Q^2(1Al) sites compared to an ambient cured neat PC paste. It should be noted if Al substitution wasn't present the amount of Q^2 would have to be increased to account for the estimated chain lengths discussed in section 5.5.1. In comparison to other 90% slag replacement systems [51-53] the cement hydration phases detected by ^{29}Si MAS NMR are similar and seem to be unaffected by the inclusion of significant quantities of $BaCO_3$ or the reaction product $BaSO_4$.

5.6.2 ^{27}Al MAS NMR

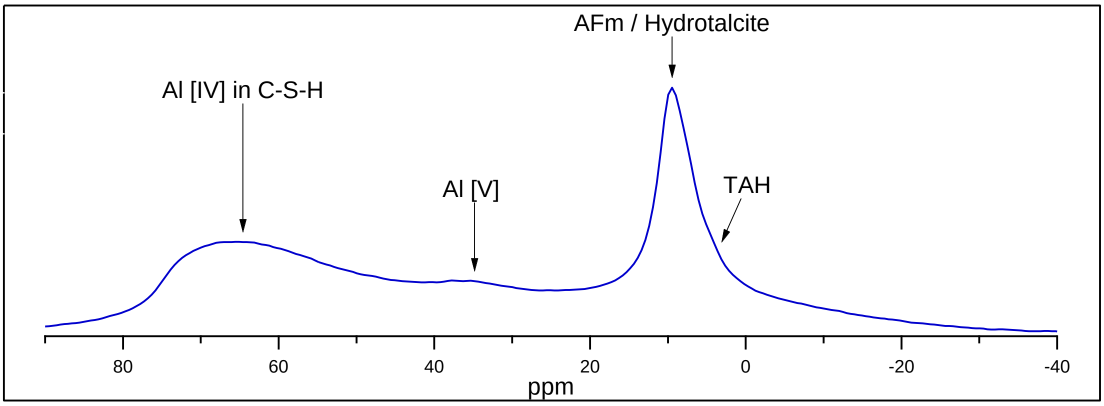

Figure 5-19: ^{27}Al MAS NMR spectra for BFS:OPC + $BaCO_3$ sample

The ^{27}Al MAS NMR results for the $BaCO_3$ containing material are similar to those presented in the previous chapter in section 4.6.2 with resonances for tetrahedrally (Al[IV]) five-fold (Al[V]) and octahedrally co-ordinated Al. The broad peak centred around 65ppm is due to a combination of the unreacted glassy slag [9, 204] which will be present and tetrahedrally co-ordinated aluminium in the C-S-H phase [182]. The presence of a C-A-S-H phase is known from analysis in the TEM and by ^{29}Si NMR. Murgier et al [205] reported the ^{27}Al tetrahedral co-ordinance onto C-S-H at above 70ppm in activated slags, whilst no separate peak is seen here Al-substitution has been shown to be present as mentioned previously.

The octahedral peak centred at 9ppm is due to a combination of resonances attributed to a AFm phase and the hydrotalcite LDH phase [206] which has been observed in the slag Ip product by TEM-EDX. No major resonance was resolved at around 13ppm which is normally linked to the presence of the AFt phase, this supports the proposal that the addition of $BaCO_3$ destabilises the ettringite sulphate phase forming $BaSO_4$. The five-fold Al[V] co-ordinance which is noticed in this sample is attributed to Al^{3+} substituting for Ca^{2+} ions situated in the interlayers of the C-S-H structure [183, 188].

5.7 Conclusions on effects of $Ba(CO)_3$ addition on BFS:OPC paste

$BaCO_3$ seems to have a high level of reactivity in relation to available sulphates supplied from the OPC present in the mix. $BaCO_3$ reacts with the available SO_4^{2-} ions destabilising ettringite and forming $BaSO_4$ the resultant freed carbonate ions CO_3^{2-} then form new phases within the paste. This reaction occurs due to the differences in solubility between $BaCO_3$ and $BaSO_4$ with the carbonate phase being more soluble whilst the opposite is true for $CaCO_3$ and $CaSO_4$. When hydration of OPC occurs in the presence of $BaCO_3$ ($K_{sp} = 2.58x10^{-9}$) the carbonate phase will react with the soluble sulphate available to form the lower soluble species $BaSO_4$ ($K_{sp} = 1.1x10^{-10}$) [5, 207] this was discussed in section 2.4.1. This reaction releases the soluble carbonate anions to form new phases as shown in the equations below described by Utton et al [86].

$$BaCO_3 + CaSO_4 + Ca_3Al_2O_6 + 11H_2O \rightarrow BaSO_4 + Ca_4Al_2(CO_3)(OH)_{12}.5H_2O$$

Equation 5-1: Formation of monocarboaluminate from $BaCO_3$ addition

$$BaCO_3 + CaSO_4 \rightarrow BaSO_4 + CaCO_3$$

Equation 5-2: Formation of calcium carbonate from $BaCO_3$ addition

The formation of substantial quantities of monocarboaluminate has been confirmed by the experimental techniques discussed in section 5.6, this indicates that the primary new phase formed after the addition of $BaCO_3$ is monocarboaluminate. This is of particular interest due to the phases ability to uptake carbonate ions produced in decommissioning process [208] so its stability at higher temperatures must be considered. Although low levels of $CaCO_3$ where identified using XRD and STA, it has not been possible to ascertain whether this $CaCO_3$ was formed due to carbonation or the reaction described in equation 5-2. The study of a similar system by Utton et al [86] did not observe $CaCO_3$ in samples aged for short times as the reaction is limited by the availability of sulphates, consequently it has been assumed the presence of $CaCO_3$ is likely due to carbonation rather than equation 5-2. The levels of $CaCO_3$ and $Ca(OH)_2$ measured are in line with aged high replacement slag systems previously studied by Taylor et al [52, 53], the presence of $Ca(OH)_2$ in small quantities suggests that the presence of $CaCO_3$ in the current work is from conventional carbonation rather than as a result of the $BaCO_3$ addition. The formation of hydrotalcite (HT) in the material is expected due to the high slag content. Electron microscopy analysis suggests the Mg phases are primarily associated only with the slag hydration rather than formed in the Op. This is of interest due to the potential of HT to contain carbonate ions which have been released from the $BaCO_3$, the results however suggest the formation of HT is predominantly located in the slag Ip and is not associated with the reaction of $BaCO_3$. The formation of these phases and others from the carbonation anions is obviously of interest to address the encapsulation of ^{14}C. Since the carbonate ions seem not to remain in the pore solution but within one of the Mc or $CaCO_3$ phases this is a positive as it greatly reduces the possibility of leaching ^{14}C [209].

The chemical immobilisation potential of cements for the absorption of ions into and adsorption onto the C-S-H phase primarily due to its high surface area is well known [210-212]. The potential for this immobilisation will range widely depending upon the species in question. Glasser [210] gives an example of a weak potential for monovalent cations such as Cs but stronger potentials for multivalent cations and very variable potentials for anionic species. There has been a discussion that Ba^{2+} may incorporate into the C-S-H structure substituting for the Ca^{2+} ions in PC grouts [210, 213] in a similar manner to the substitution of Ca^{2+} for waste ions in synthetic C-S-H crystals [214, 215]. However evidence of substitution of Ba^{2+} into the C-S-H structure of non-synthetic blended cement is lacking. If isomorphic substitution of calcium ions for other divalent waste cations such as Ba, Sr and Pb is investigated the basic rules for chemical substitution in solid solution should be considered. Goldschmidt outlined 3 rules for crystal chemistry substitution [216] with the final point a later modification by Ringwood [217]:

- The ions of one element can extensively replace those of another in ionic crystals if their radii differ by less than approximately 15%.
- Ions whose charges differ by one unit substitute readily for one another provided electrical neutrality of the crystal in maintained. If the charges differ by over one substitution is reduced.
- When two differing ions could occupy a particular position, the ion with the higher ionic potential forms a stronger bond with surrounding ions.
- Substitutions may be limited even if points 1 and 2 are satisfied when competing ions have differing electronegativities and form bonds of different ionic character.

When considering Ba^{2+} for Ca^{2+} the ionic radii are 1.38Å and 1.06Å respectively (a radius difference of 30.2%) when in the same seven-fold coordination [218]. This suggests that the substitution of Ba for Ca is unlikely to be extensive by simply considering the first rule outlined above. Reducing the co-ordination number from [VII] to [VI] increases the ionic radii percentage difference to 35% which suggests the potential replacement of Ca^{2+} becomes less likely as the co-ordination number increases.

Experimentally the effect of the barium inclusion upon the nature of the C-S-H phase seems very limited in this sample. Any mass substitution of Ca with Ba would result in a noticeable decrease in the mean Ca/Si ratio when compared to similar samples and should be observed in the local chemical environment around waste sites. As discussed in section 5.5 there is little indication of significant levels of barium being intermixed in analysed Op C-S-H even in the local environment around barium waste sites. Additionally the averaged Ca/Si ratios and scatter plots closely match previous studies on 90% slag pastes with no waste inclusions [52, 53]. Imaging using electron microscopy also shows little effect from the barium inclusion on the C-S-H phase save from providing a potential nucleation site during early stage hydration of the OPC.

It is estimated that a significant quantity of the waste ^{14}C ions will remain within the $BaCO_3$ phase even after prolonged periods of hydration; XRD and direct experimental observation support this conclusion. Since the typical sulfate contents of OPC and BFS are relatively low (<5% weight), it is unlikely the sulfate content of the blends would be sufficient to fully consume the added Ba to form $BaSO_4$ and free the additional ^{14}C. It is proposed the ^{14}C waste will lie predominately within its original $BaCO_3$ waste form, therefore the bulk of the ^{14}C will remain physically encapsulated. The remainder is retained within Mc and potentially formed $CaCO_3$ phases, the stability of which lowers the risk of any ^{14}C release from the waste product.In conclusion the reactivity of the $BaCO_3$ waste addition is dictated by the relative sulphate content in the system, once the available sulphates have been consumed the remaining $BaCO_3$ remains in the system. Due to the high replacement of OPC in the mix design the level of sulphates is much lower than for a neat PC system; this results in a large proportion of the $BaCO_3$ being unreacted especially in the larger agglomerations with the locally available sulphate exhausted. The presented results show that the primary formed carbonate phase Mc and the simulated $BaCO_3$ waste stream are stable over longer time periods of at least a decade with similar phases observed to that of Utton et al [86] after one year of hydration. Due to this stability of phases in the waste form it seems likely that the ^{14}C waste stream inclusion would be effectively encapsulated in high replacement slag cements.

Chapter 6 : Results and discussion of BFS:OPC + Al simulant slurry

6.1 Introduction

A 15-year old BFS: OPC grout was investigated with an Al-based waste-form designed to simulate the worst-case scenario for the encapsulation of an aqueous waste slurry. This waste results from corrosion products which have been generated by irradiated fuels and other components which have resided in the fuel cooling ponds [120]. The composition of this slurry is described in section 3.1 but it is essentially a simplified aluminium floc material containing silicates and small levels of iron. The samples have been compared to previous work on slag-based cements particularly with interest to slag cements with high aluminium contents. The encapsulation potential of the solid phases formed during storage are compared to other academic papers dealing with the treatment of other Al - based industrial wastes [219] and the encapsulation of aluminium as a reactive metal within composite grouts [83, 97].

6.2 XRD

The XRD pattern for the 3:1 BFS:OPC + Al slurry system shows the formation of several cementitous hydrated solid phases such as monosulfoaluminate (Ms) and monocarboaluminate (Mc) alongside C-S-H and a hydrotalcite – like phase (see figure 6-1). XRD reflections were also observed for the formation of strätlingite (hydrated gehlenite), the reflections were relatively broad and weak showing possible poor crystallinity of this phase. The noted reflections agree with the results for synthetic formed strätlingite [154] and for a natural crystal analogue [220]. The presence of unhydrated gehlenite was expected due to the high levels of slag replacement in the mix design and partial reaction of large slag particles.

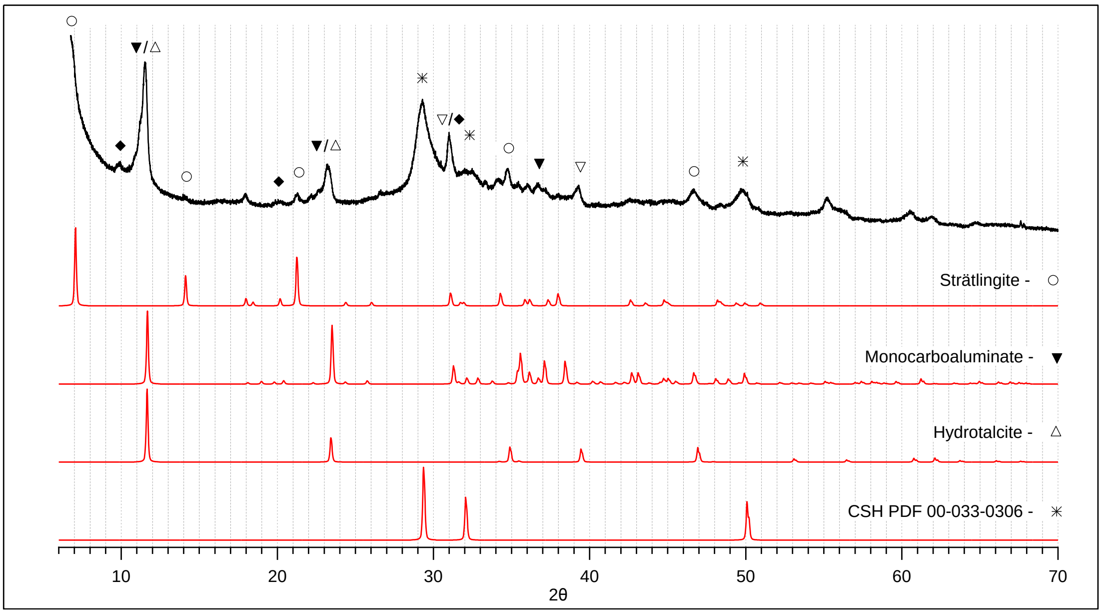

Figure 6-1: XRD trace of BFS:OPC + Al slurry with simulated patterns for resultant phases are shown; ▼ – AFm (Monocarboaluminate), ▽- Gehlenite, △- Hydrotalcite, ✳ - C-S-H, ◆ - AFm (Monosulfoaluminate), ○ - Strätlingite

The results compare well to the XRD analysis for an ambient cured 3.44:1 BFS:OPC which was produced in 2009 (figure 6-2) and studied as part of preliminarily investigations in 2011 [221]. Again the primary hydration products expected for a slag - PC cement were observed with C-S-H formed alongside levels of the hydrotalcite-like phase. However due potentially to the younger age of the sample, quantities of unreacted belite were seen alongside a much greater proportion of portlandite. The main difference between the samples in Figure 6-2 is the noticeable difference in intensity of the labelled hydrotalcite/Mc peaks at around 11° and 23° 2θ, this has been attributed to the mass formation of the AFm Mc phase in the Al simulant paste. The sample with no waste addition also showed no indication of the formation of strätlingite showing that this phase formation is indeed due to the waste interaction with the hydrating system.

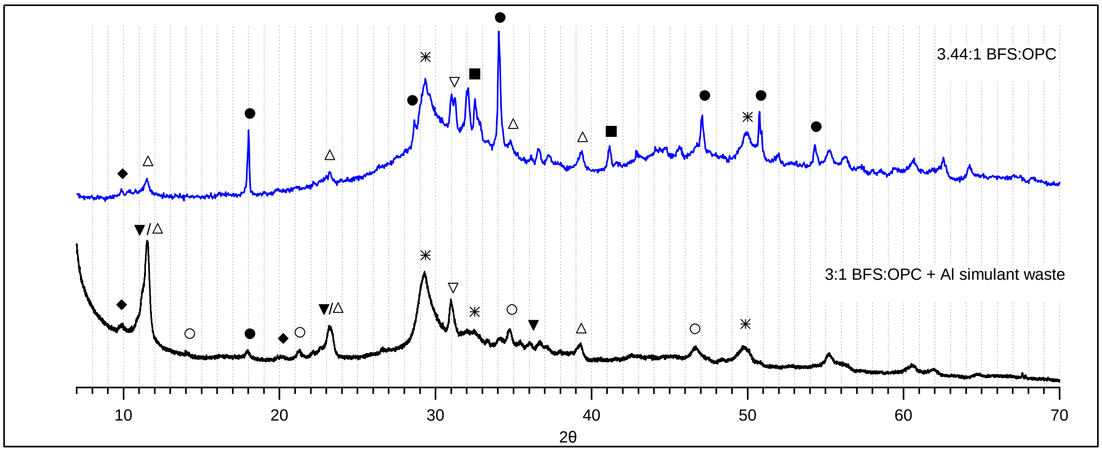

Figure 6-2: Comparison of XRD traces from two studied slag based systems with and without Al simulant waste; ▼ – AFm (Monocarboaluminate), ▽- Gehlenite, △- HT-LDH, ✳ - C-S-H, ◆ - AFm (Monosulfoaluminate), ● - Portlandite (Ca(OH)$_2$), ○ - Strätlingite, ■ - Belite (β-C$_2$S)

6.3 Thermal Analysis

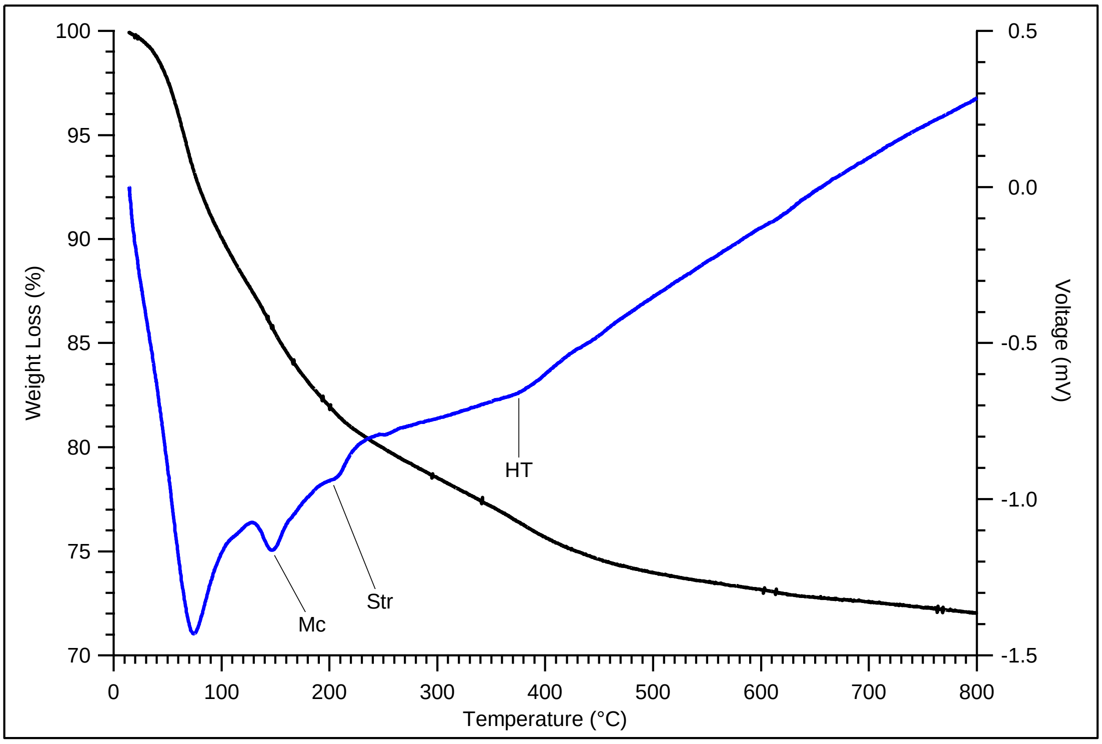

Figure 6-3: STA trace for BFS:OPC + Al slurry; Mc - Monocarboaluminate, Str - Strätlingite, HT- Hydrotalcite-like phase

Thermal analysis using STA helped confirm the findings from XRD that an AFm phase with a mass loss at 150˚C has been formed within the grout; losses at this temperature have been attributed to monocarboaluminate (Mc) in various studies [153, 157] and this would agree with the observed 2θ position by XRD. The formation of strätlingite was supported by STA analysis of the sample with a decomposition at 220˚C which agrees with the experimental data for Al-rich slags reported by Haha et al [39] and the DTG for synthetic strätlingite [39, 154]. The slight decomposition labelled at 390˚C has been attributed to hydrotalcite due to its expected presence and findings from the XRD analysis. Only very small levels of $Ca(OH)_2$ were observed by XRD and the decomposition of that phase usually presents a much sharper profile than that shown in figure 6-3. This temperature matches the reported losses for a hydrotalcite - like phase by Haha et al [39]; Gruskovnjak et al [222] reported a two-stage mass loss at 230˚C and 400˚C however the lower temperature mass loss in this sample is likely to be overlapped by the presence of strätlingite especially since the relative mass loss observed for hydrotalcite phase is minimal.

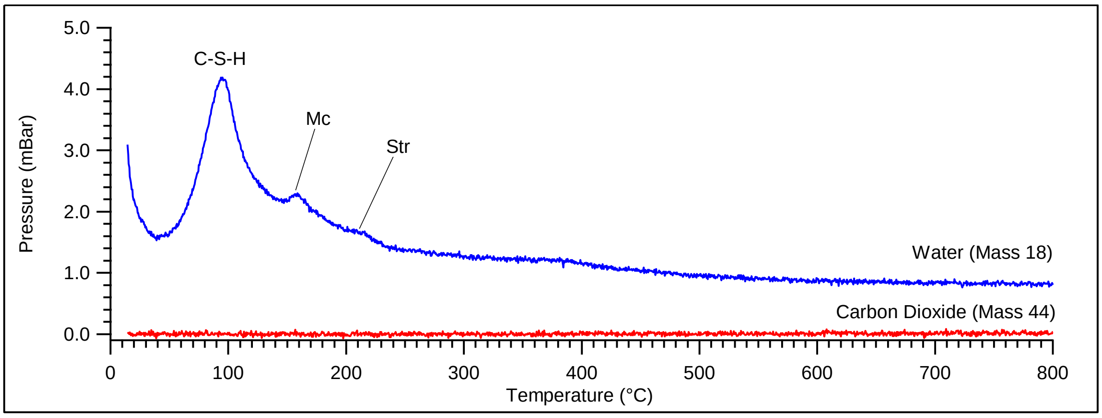

Figure 6-4: Associated mass spectrometer trace for BFS:OPC + Al slurry

The associated mass spectroscopy trace for the Al - simulant sample taken during the STA run is shown in figure 6-4 and shows good consistency with DTA and TG results. The mass spectrometer trace for water is indicated in figure 6-4 and this confirms the loss of water from the C-S-H, AFm and strätlingite constituents on heating at the expected temperatures. In figure 6-4 the flat trace in red indicates no carbon dioxide was detected during the experimental run, this agrees with the XRD and TG evidence that no carbonation of that sample has taken place or calcite formed. The formation of Mc AFm was suggested from the XRD analysis however no CO_2 was noticeably released at 150˚C similarly to the data in chapter 4 for the limestone containing NRVB sample. The lack of a CO_2 detection could be due to the fact CO_2 isn't released in the measured temperature range or that the equipment was not capable of detecting the low quantity of CO_2 released. The sensitivity of the experimental apparatus was investigated using the calculated CO_2 contents of the NRVB sample and pure calcite as controls. It was found that the expected level of CO_2 released in the blended cement from Mc was within the levels of experimental 'noise' due to its relative small quantity. This explained why it proved difficult to detect CO_2 produced from the Mc phase using associated gas analysis during thermal analysis. The lack of any CO_2

detection for the hydrotalcite-like phase is to be expected if no carbonation has occurred. In this case the phase formation can be compared to the HT-like double layered hydroxide Meixnerite ($Mg_6Al_2(OH)_{18}.4(H_2O)$) which contains no CO_2,

6.4 SEM

Typical BSE imaging of the 3:1 BFS:OPC + Al slurry sample can be seen in figures 6-5 and 6-6, with the general microstructure well displayed in figure 6-5 a). The microstructure is dominated by large quantities of slag particles which are observed as both fully and partially reacted particles and marked as A and B respectively in figure 6-5. In this regard the cement matrix is as would be expected for a well reacted slag based cement after extended curing.

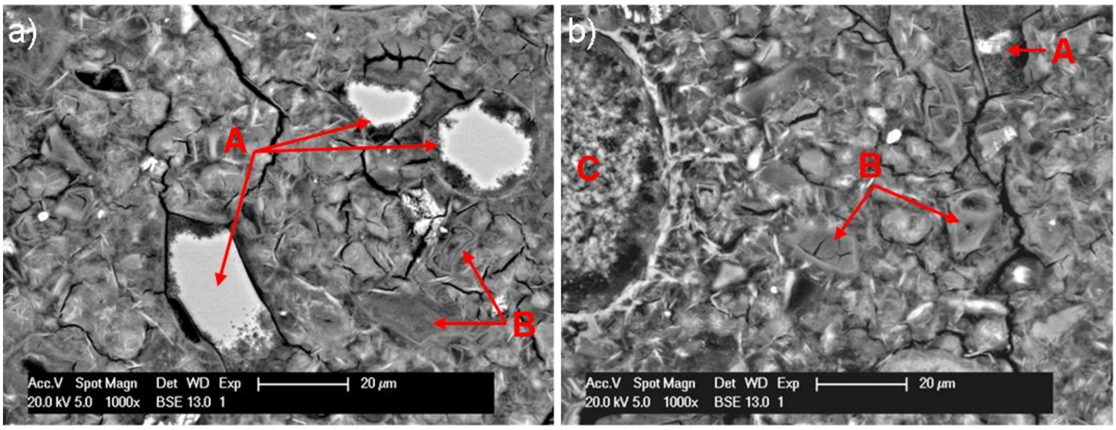

Figure 6-5: BSE image of the microstructure of the BFS:OPC + Al slurry waste (x1000); A - Partially hydrated slag grains, B - Fully hydrated slag grains showing slag Ip, C - Suspected waste agglomeration surrounded by laths

The general matrix of the waste-form was extremely brittle and fragile during preparation with levels of cracking evidenced in the SEM imaging, this was despite identical preparation procedures being followed as for the other samples in this study described in chapter 3. The addition of the simulant aluminium waste has had a dramatic effect upon the microstructure with the obvious formation of large quantities of laths throughout the material. These laths are easily observed within the microstructure by their higher contrast when compared to the grey scale contrast of the C-S-H phase. The second primary affect from the addition of the simulant waste was the presence of large agglomerations of the flocculated waste as indicated by the feature labelled as C in figure 6-5. Figure 6-6 shows another suspected waste site labelled as B which displays similar characteristics to formation C in figure 6-5. In both cases the formation of the laths is concentrated locally to these features suggesting they are linked to the waste addition. The morphology of these laths are similar to that for synthetic strätlingite described by Matschei et al [154], however the relative size and crystallinity of most of the laths indicates they are more likely to be related to the large quantity of AFm found during XRD analysis of the sample. The formation of these laths around waste sites suggests the waste-form is not inert within the matrix and modifies the hydration process of this slag cement.

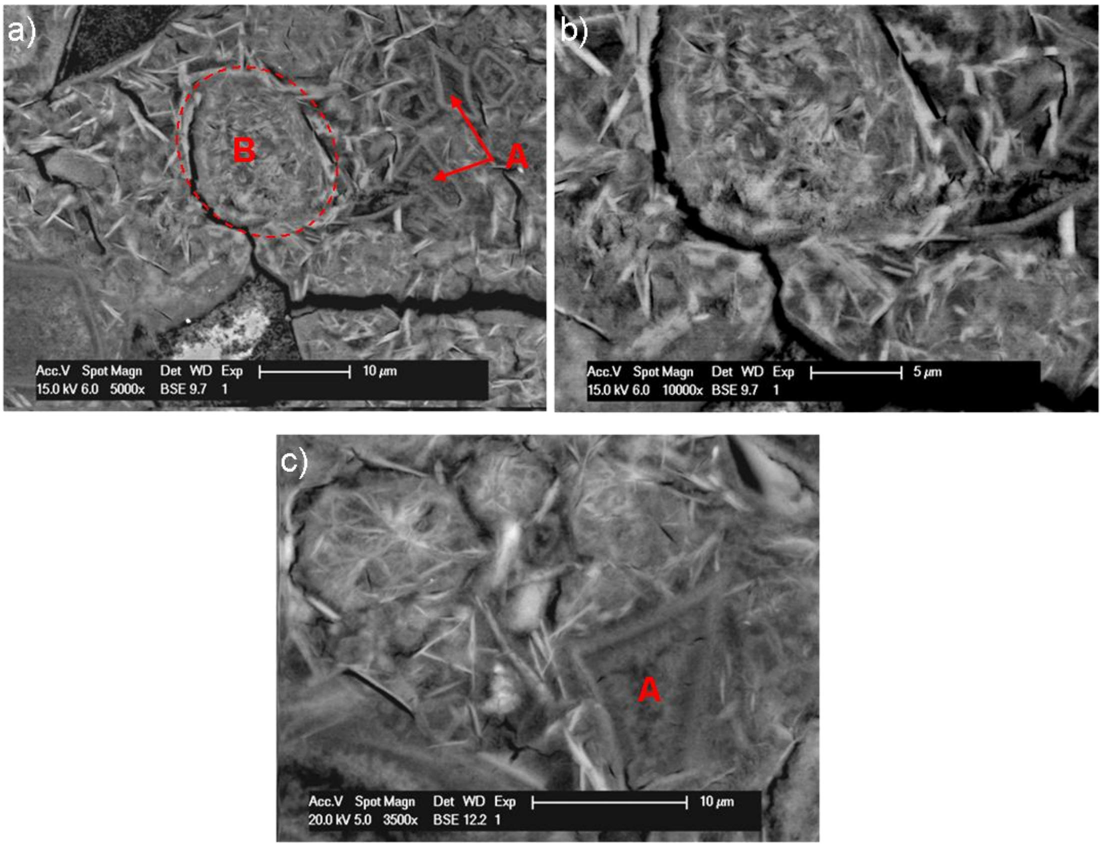

Figure 6-6: BSE images of encapsulated waste areas and formation of products; A - Fully hydrated slag, B - Suspected waste site enlarged in b).

The general microstructure, waste sites and the formation of laths was investigated by elemental mapping as shown in figure 6-7 and in the appendices. The image and mapping in figure 6-7 shows an increase aluminium response which is associated with both the waste agglomeration and surrounding lathe-like products. The calcium map shows the pre-treatment of the Al-based slurry with lime was successful in producing a waste-form which seemed to be well incorporated within the matrix.

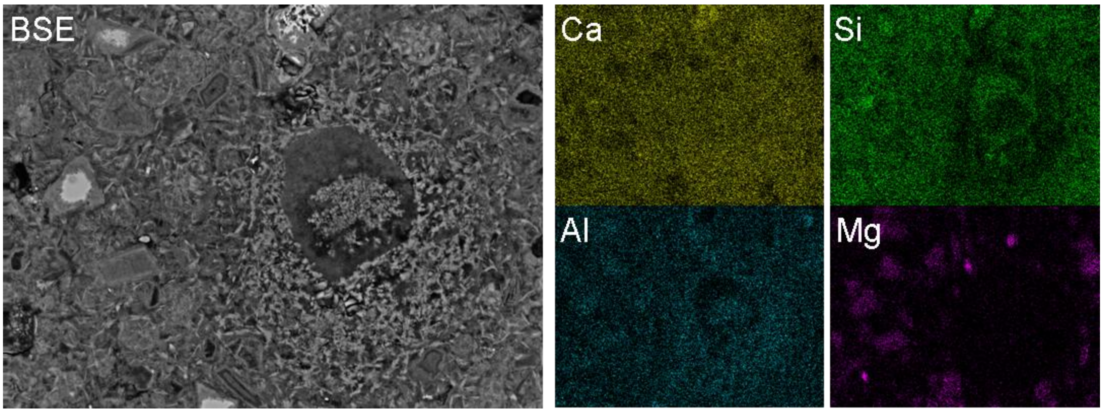

Figure 6-7: BSE image of suspected large waste site and associated elemental mapping

The magnesium and BSE image from figure 6-7 indicates the fully and partially hydrated slag particles within the matrix which are not associated with the primary Al responses. The slag particle reaction rim was imaged by FEGSEM as shown in figure 6-8 which shows two different fully hydrated slag grains in images a) and b).

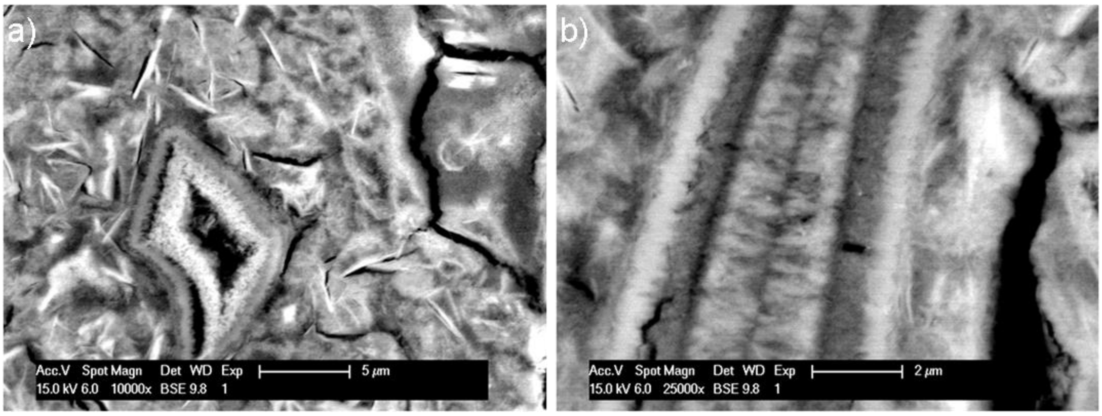

Figure 6-8: BSE imaging of the microstructure and fully hydrated slag grains

The hydration of the slag grains shows the characteristic variation in density as shown by the grey scale contrast from the BSE imaging. As evidenced by images a) and b) in figure 6-8 the hydration of slag particles is not a uniform process producing various layers of hydrated products even after 15 years of hydration. For example, the slag grains in figure 6-8 show a different nature or stage of hydration with a) showing an empty centre and b) a higher density inner product. In each sample however a clear definition was seen between the prior boundary of the slag particles and the outer product C-S-H phase formed around it. Within this boundary a denser product assumed to be related to the hydrotalcite - like phase formation and inside that a lower density formation of what is assumed to be a mixture of slag inner product and the HT-like phase. The hydration of slag particles within this paste was studied using TEM and is discussed in more detail in section 6.5 whilst the estimated chemical composition of the hydrotalcite -like phase using SEM-EDX is discussed below.

Atomic ratio plots for the simulant Al slurry sample have been generated from SEM-EDX analysis with trend lines added for the relevant phases formed within the sample. The analysis points all relate to either hydrated slag particles or the general binding matrix including areas where quantities of the aforementioned laths are present. Figure 6-9 shows the Si/Ca against Al/Ca scatter plot which indicates the presence of the C-S-H phase which is intermixed with an AFm phase and related slag products. The cluster labelled C-S-H indicates a phase with an average Ca/Si ratio lower than that reported for a hydrated Portland cement system [167] with a significant level of aluminium also present for all the analyses. The presence of intermixed AFm phases was expected having observed the level of lathe formation within the binding matrix using SEM BSE imaging which seem to be related to the aluminium waste addition. Due to the amount of hydrated slag particles seen in the matrix a considerable level of hydrated slag products was expected with a hydrotalcite - like phase identified by XRD analysis. This was supported by SEM-EDX and is shown in Figure 6-9 by the 'slag product' formations. The additional aluminium containing analyses seen above the C-S-H cluster in figure 6-9 but not directly related to the formation of AFm or slag products could be due to the intermixing of strätlingite with C-S-H. The relative Al/Ca and Si/Ca ratios for strätlingite would be 1.0 and 0.5 respectively so these analysis are potentially related, a similar analysis of intermixed strätlingite using SEM-EDX was described by Antoni et al [223] in a study of a Portland cement/metakaolin paste.

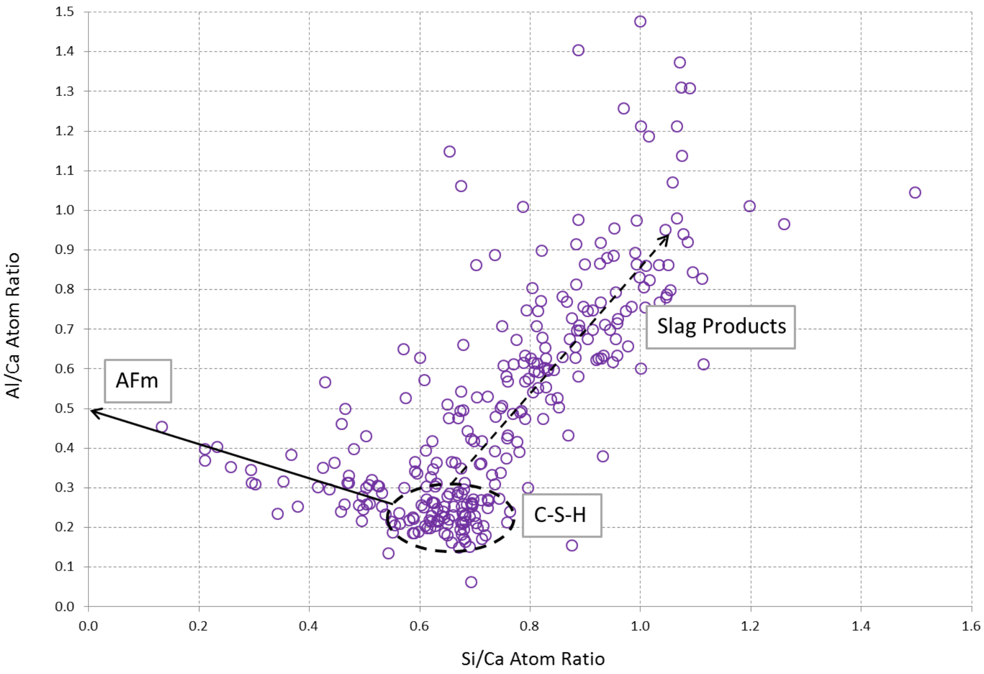

Figure 6-9: Si/Ca against Al/Ca scatter plot for the BFS: OPC + Al slurry sample.

The scatter plot for the Al/Si against Mg/Si atomic ratios is shown in figure 6-10 which displays the C-S-H cluster described in figure 6-9 and the related slag products with a best fit line for these phases added. The estimated level of aluminium incorporation in the C-S-H can be found by observing the average Al/Si value for the CSH cluster when the Mg/Si ratio is 0; in this sample looking at figure 6-10 the average value is over 0.3 for the cluster by SEM-EDX. Since the reported maximum value of Al incorporation of Al in to the C-S-H phase is 0.33 when all the bridging sites in the dreierkette chain structure are occupied this Al/Si value seems unlikely to be accurate. The most likely reason for this high Al/Si ratio is the inclusion of intermixed aluminate hydrate phases particularly strätlingite being intermixed intimately within the C-S-H phase. Due to the interaction volume for SEM-EDX analysis this would increase the general Al/Si value for the C-S-H. This theory suggests the aluminate hydrate phases are associated with C-S-H in a very large proportion of analyses of the binding phase. Therefore the effect of the aluminium waste addition upon the binding matrix is substantial rather than being a purely localised affect. An additional idea for the inclusion of Al incorporation was suggested by Renaudin et al [224] who reported that a level of Al could be inserted into the C-S-H interlayer spacing increasing the potential maximum allowed Al content. An additional way of estimating the Al/Si content of formed C-S-H phases is to find the average Al/Si ratio of the C-S-H formed from slag hydration. Since the formed C-S-H from slag is normally assumed be richer in aluminium than that formed from OPC systems [39, 204] it can be used as a upper boundary for the estimation for the Al/Si content in a system. The EDX analysis points relating the hydrated slag can clearly be seen and show a good linear relationship with the line of best fit having an R^2 value of > 0.95 for the SEM-EDX. Using this fitted line the estimated uptake of Al into the C-S-H phase can be found when the Mg/Si = 0. This estimates that the Al/Si ratio when Mg/Si = 0 is 0.21 which is lower and more sensible when considering the possible Al incorporation within the C-S-H chain structure.

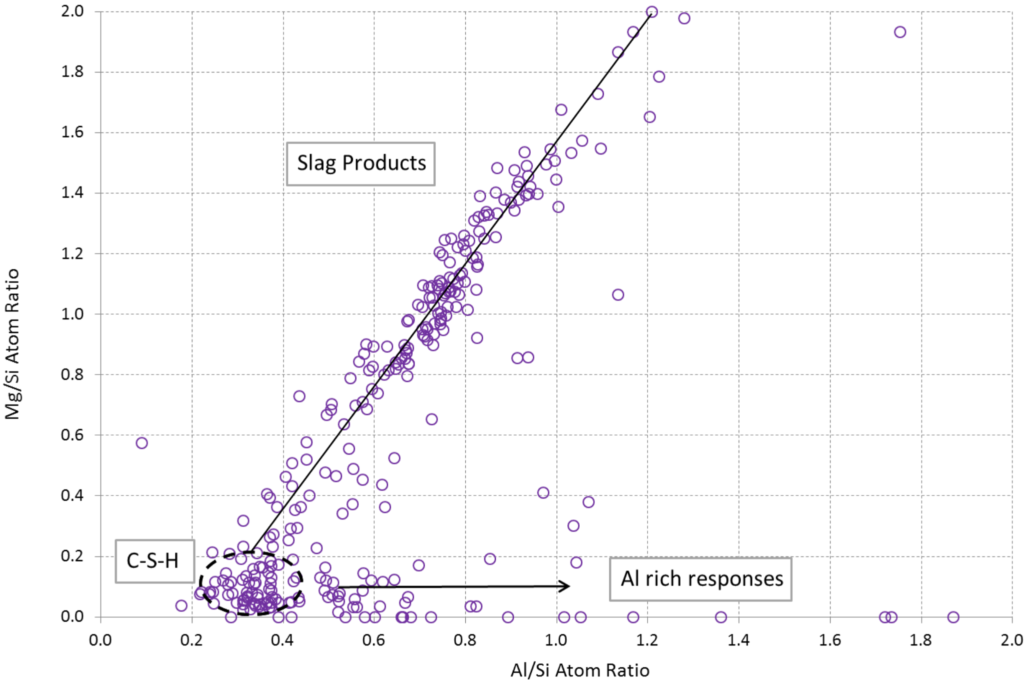

Figure 6-10: Al/Si against Mg/Si scatter plot for the BFS: OPC + Al slurry sample.

The hydrotalcite - like phase composition can also be estimated using the fitted lines gradient. This is of interest due to the fact that the composition of this phase is known to be affected by the Al_2O_3 content of the hydrated slag so possibly could also be affected by the addition of Al to the system. In this sample the estimated Mg/Al ratio for the phase by SEM-EDX was 2.01 which is within the expected limits for this phase reported in literature [38, 39, 52, 225]. It seems therefore that the Mg/Al ratio isn't unexpectedly low thus no major incorporation of Al into the hydrotalcite - like phase seems likely. The majority of Al richer response data points labelled on figure 6-10 were taken from around the larger encapsulated waste sites showing the localised Al phase formation around these phases.

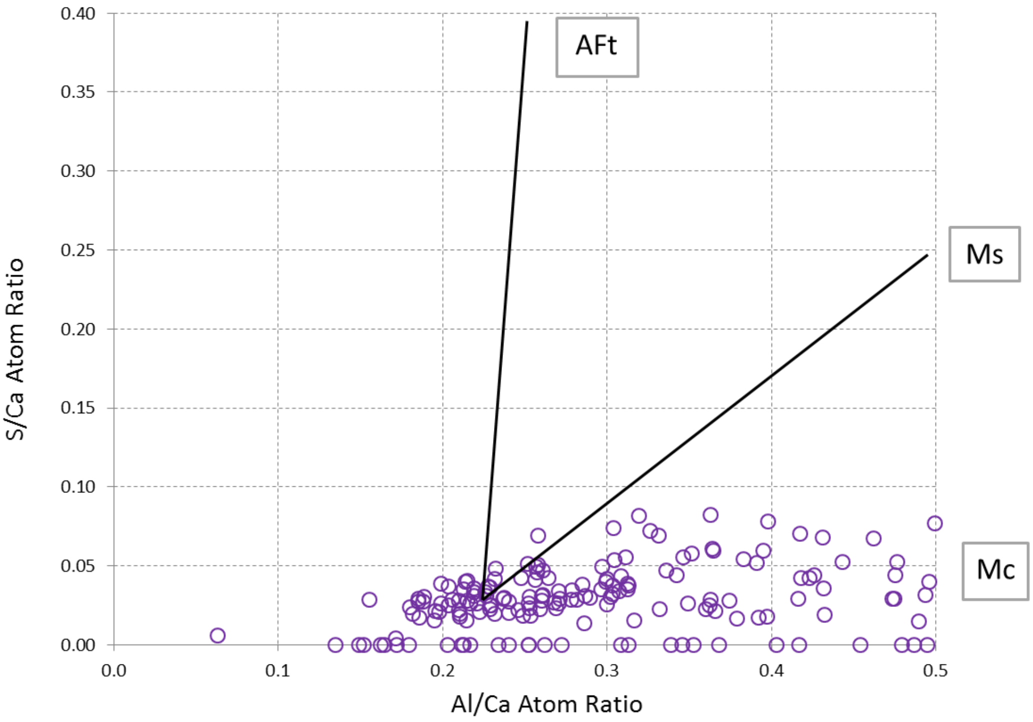

Figure 6-11: Al/Ca against S/Ca scatter plot for the BFS: OPC + Al slurry sample.

The chemical composition of the AFm phase has been investigated by the atomic ratio plot of Al/Ca against S/Ca in figure 6-11, trend lines have been added for the primary aluminate hydrate phases. The data shows a strong correlation to the formation of monocarboaluminate (Mc) as the primary formed AFm phase in the system with low quantities of sulphur generally observed. This is in agreement with the XRD evidence which suggested the mass formation of AFm resulting in the strong 2θ responses at 11.6˚ and 23.2˚.

6.5 TEM

The observed outer product (Op) C-S-H in the 3:1 BFS: OPC + Al slurry sample displayed a predominantly foil-like morphology which has been observed in literature as becoming more dominant with the increasing slag replacement [52-54]. The morphology of the C-S-H is shown in figure 6-12 and this closely resembles the Op reported in the previous chapter. Some areas of the matrix do show a more fine-fibrillar type morphology which is likely to relate to localised hydration of Portland cement grains rather than activated slag particles.

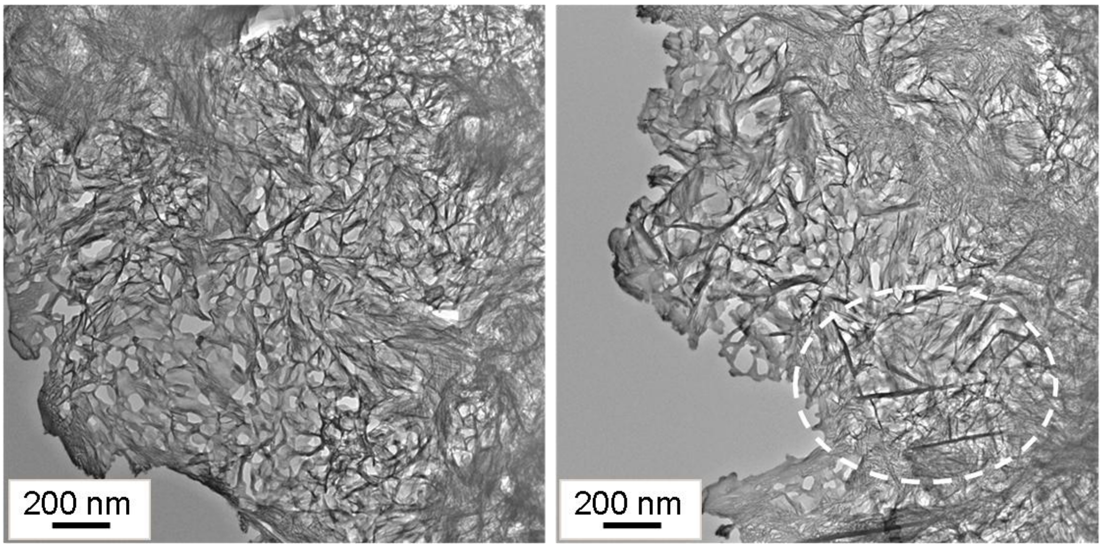

Figure 6-12: TEM micrographs of Op C-S-H areas analysed showing foil morphology, circled area shows suspected strätlingite formation.

The overall nature of the C-S-H exhibited therefore agrees with the expected microstructure with regards to the C-S-H morphologies. Large quantities of foil like C-S-H are present from the activation of slag which reduces the overall porosity of the system, smaller levels of fibrillar C-S-H related to the hydration of Portland cement grains were also observed in smaller quantities. The circled area in figure 6-12 shows suspected strätlingite formation within the C-S-H as exhibited by the slightly larger needle-like formations, however it is also possible these are very fine formations of AFm. Figures 6-13 and 6-14 show the predominately foil like microstructure of C-S-H intermixed with large quantities of AFm and potentially strätlingite with both being aluminate hydrate products they are potentially linked to the added simulant waste.

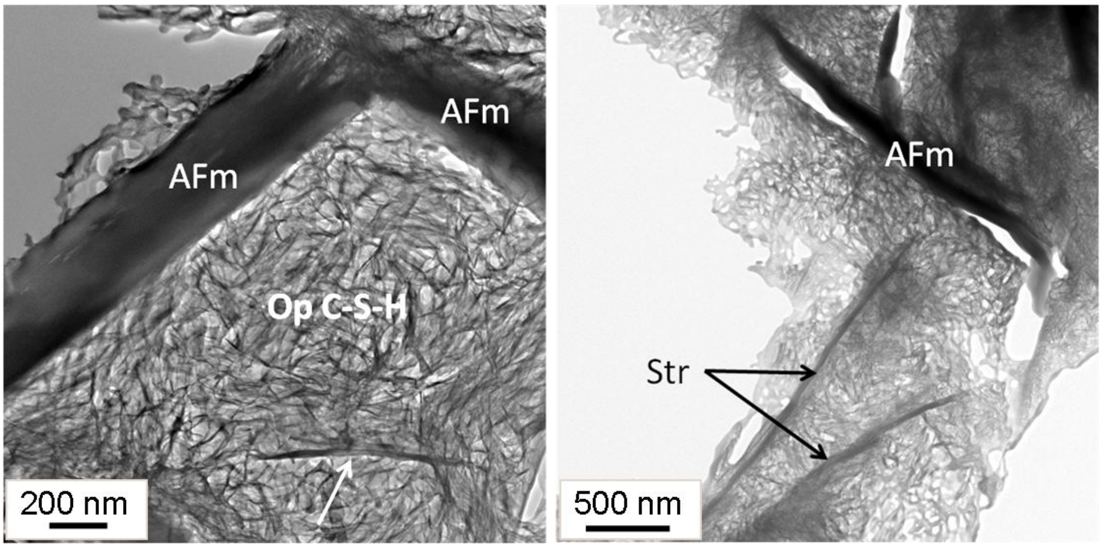

Figure 6-13: TEM micrographs of Op C-S-H with examples of intermixed AFm laths and strätlingite (Str) marked by arrows

The intermixing of these phases at both a fine and larger scale shows the difficulty in achieving 'pure' EDX analyses of the C-S-H without additional aluminium responses. The examination of the material by TEM shows why the SEM-EDX estimation of the aluminium content in the C-S-H was likely to have been overestimated, as the intermixed aluminium containing phases certainty would have been included. The micrographs in figure 6-14 however do compare well with the SEM BSE imaging and show the larger high contrasted laths in figure 6-6 to be formed AFm assumed to be monocarboaluminate. The fineness of the suspected strätlingite labelled in figure 6-13 shows that it would be very difficult to distinguish them in SEM analysis for this sample.

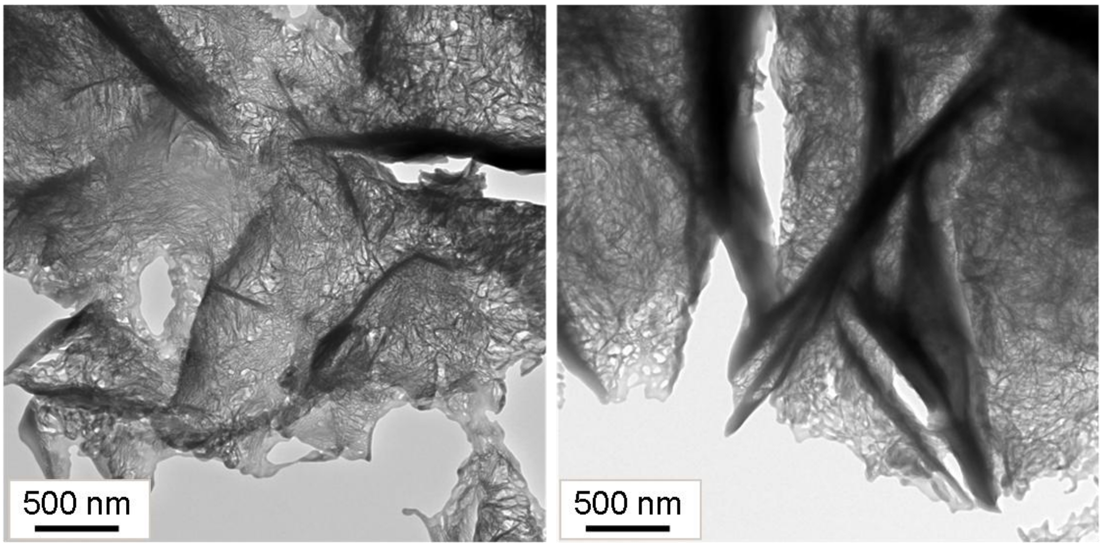

Figure 6-14: TEM micrographs of AFm laths and strätlingite formed throughout the microstructure

The TEM-EDX analysis points from the BFS:OPC + Al Slurry sample are displayed in figure 6-15 which can be compared with the relevant SEM-EDX data shown in figure 6-9. In comparison the TEM-EDX displays an averaged lower Al/Ca ratio of < 0.2 which is in agreement with the allowable Al/Ca ratios for aluminium incorporation into the C-S-H chain structure. As discussed earlier the maximum theoretical value for Al/Ca when all available bridging sites in the drierkette structure are occupied is 0.33, using the TEM-EDX ratios in figure 6-15 it can be seen all the C-S-H analyses are below this value. As shown in figure 6-15 the TEM-EDX data indicates a large amount of both intermixed and relatively pure AFm phases which ties to the micrographs indicated in figure 6-13 and 6-14. Additionally there is a trend for an aluminium containing hydrate phase which is intermixed with the cluster for C-S-H. This has been attributed to the presence of strätlingite as certain data points do fit the relevant trend-line between pure phase strätlingite and the average Si/Ca and Al/Ca C-S-H ratios. These data points generated from the TEM in figure 6-15 compare well to the

SEM-EDX in figure 6-9 with the evidence of intermixed AFm phases and potential Al containing phases also observed.

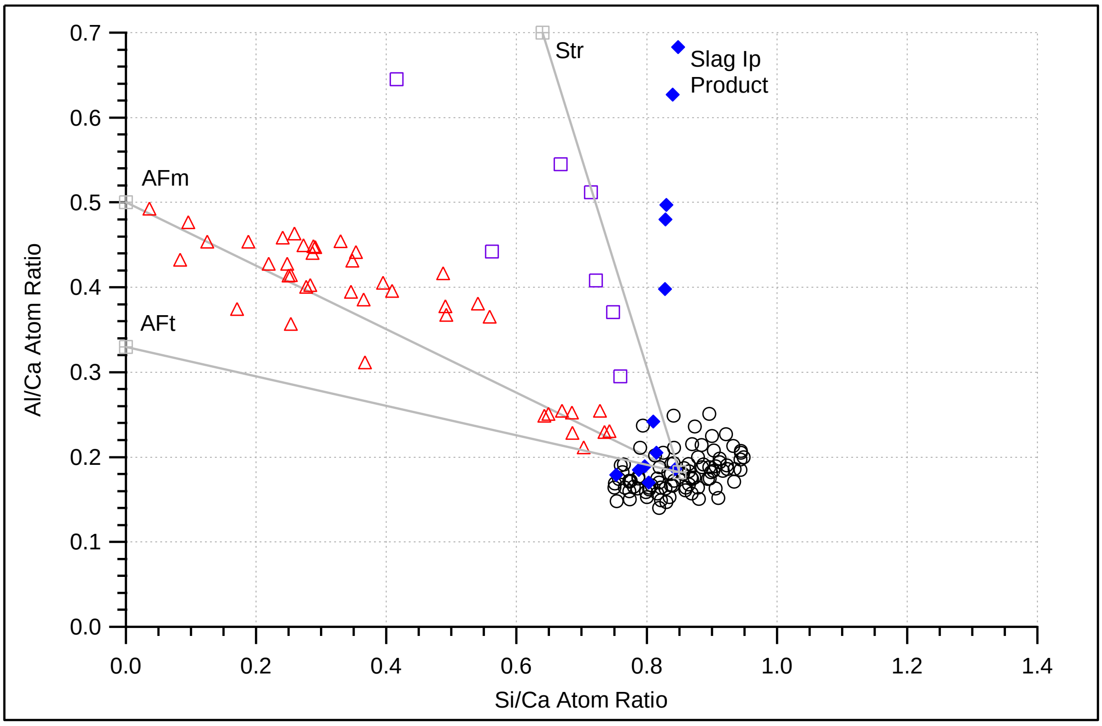

Figure 6-15: TEM-EDX analyses of phases ○- C-S-H, ◆- Slag Ip Product (C-S-H intermixed with Mg-Al LDH), △- Intermixed AFm, □- Suspected intermixed Strätlingite (Str).

The average Al/Ca ratio from the data labelled as C-S-H in figure 6-15 is 0.18 and the Al/Si ratio is 0.16, the average Al/Ca content for the paste is therefore higher than that reported for a similar 75% slag system in literature [52] and in chapter 7. The averaged Si/Ca for the data displayed in figure 6-15 is 0.85 which corresponds to the displayed Ca/Si ratio of 1.18 showing in table 6-1. The average Ca/(Al+Si) ratio is 0.97 which is lower than the comparable aged BFS:OPC pastes in Taylor et al [52, 53] and in the similar paste with added magnesium in chapter 7. This reflects the additional aluminium content seen in the Al/Ca ratio.

		Ca/Si		Ca/(Al+Si)		Al/Si	
	N❖	Mean	SD	Mean	SD	Mean	SD
C-S-H	96	1.18	0.08	0.97	0.06	0.16	0.09
Slag Ip C-S-H	8	1.23	0.04			0.209*	

* Slag Ip Al/Si ratio calculated from regression analysis (Figure 6-19) when Mg/Si = 0

❖N = Number of EDX analysis

Table 6-1: Mean atomic ratios for C-S-H phases in the 3:1 BFS:OPC + Al slurry cement paste obtained using TEM-EDX

The hydration of the slag grains in the paste was studied by TEM imaging in addition to the earlier work using the FEGSEM BSE imaging, a micrograph of a typical small fully reacted slag particle is shown in figure 6-16. As discussed in section 6.4 the hydration of the slag is not a uniform process with layers of hydrated products observed with differing morphologies and densities. The differing chemical composition of these layers of hydration products is well illustrated by figure 6-17 which shows scanning transmission electron microscopy (STEM) EDX mapping of a fully hydrated slag particle. In these images varying layers of a Mg-Al hydrotalcite - like product and C-S-H product can be observed. The hydration of slag is a diffusion controlled process with Ca, Si and Al diffusing out of the slag into the Op C-S-H after activation of the slag particle by increasing alkalinity from the formed $Ca(OH)_2$. The model for the hydration of slag is that as the diffusion process continues the slag grain decreases in size. The resultant space being filled with the hydrotalcite-like phase which is orientated between the later Ip slag product and Op C-S-H. As the slag particle becomes fully reacted from the diffusion reaction the space now created inside the HT phase boundary is then filled with Ip slag C-S-H which is intermixed with finer scale HT Mg-Al product. This model for the slag reaction is well illustrated by figure 6-16, the micrograph shows the formed dense HT Mg-Al product formed around the original edge of the slag particle which has alignment and the latter formed Ip C-S-H product intermixed with HT is observed.

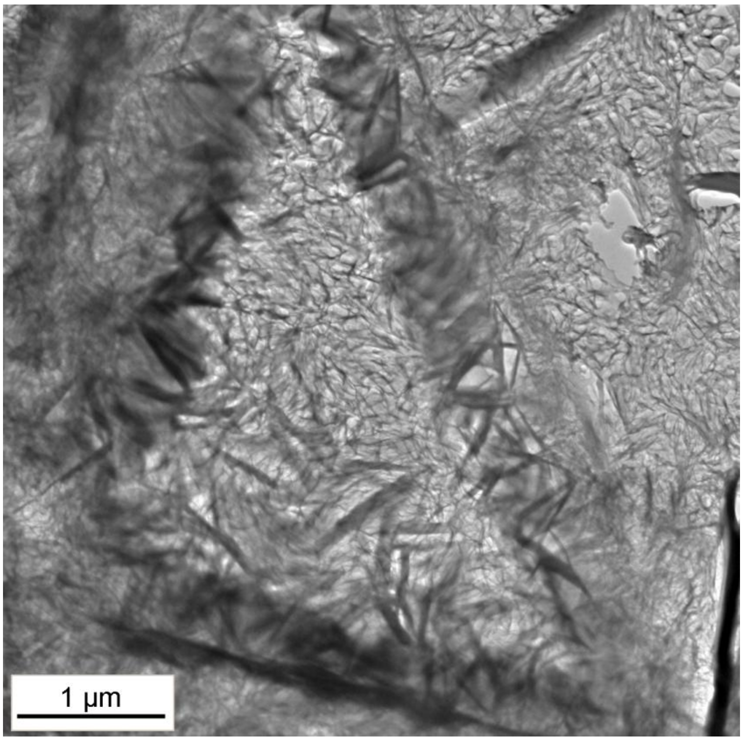

Figure 6-16: TEM micrograph of a fully hydrated slag particle with Mg - Al HT - like phase formed around the boundary and intermixed with the slag Ip product

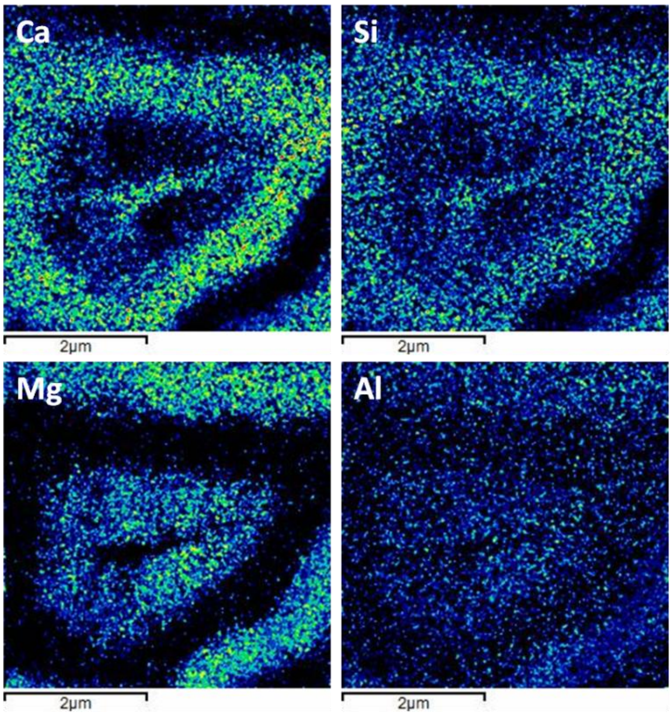

Figure 6-17: STEM quantitative mapping of a reacted slag particle, showing differing chemical compositions of the hydrated products.

The nature of the formed hydrotalcite (HT) - like phase from the slag particles mapped in figure 6-17 is shown in figure 6-18. The presence of the HT - like phase was confirmed by the high magnesium content in conjunction with a lower level of Al, note that Al is also associated in small quantities with the Ca and Si responses related to the slag Ip C-S-H product.

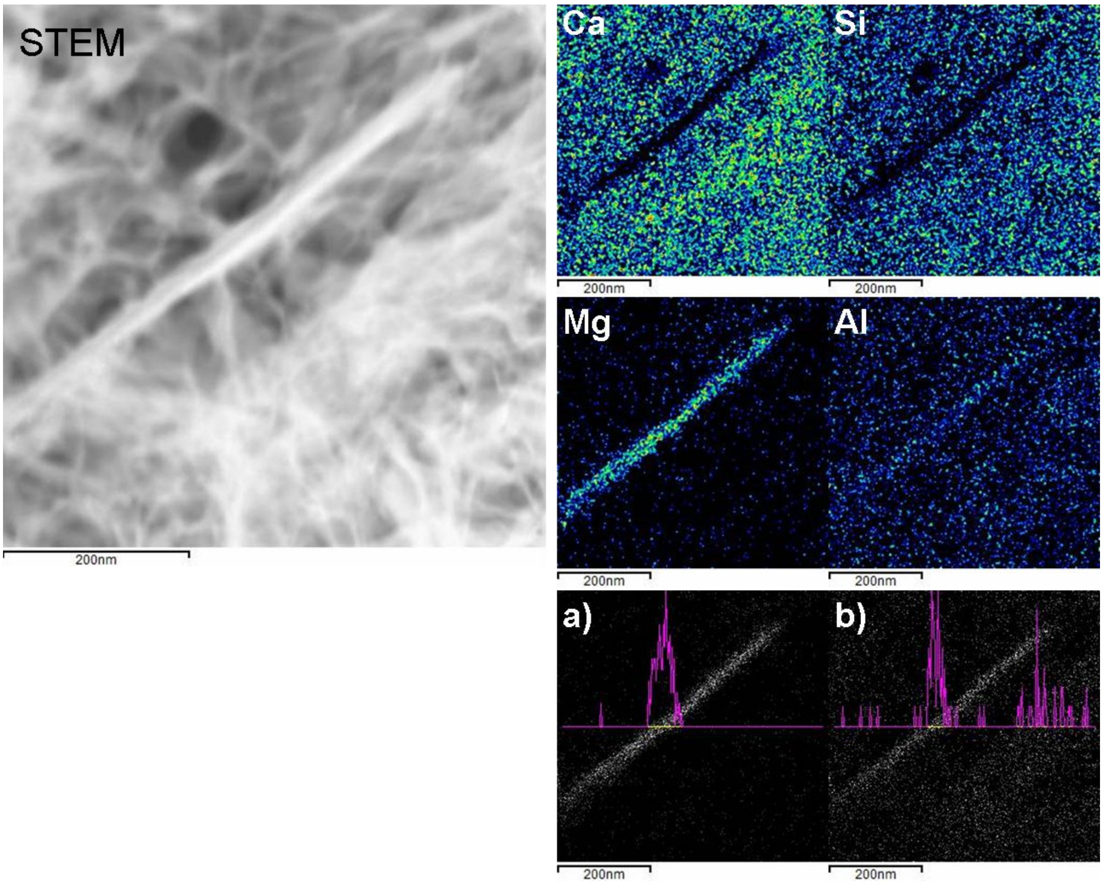

Figure 6-18: STEM mapping of HT-like phase within the Al slurry sample; a) EDX line scan for Mg, b) EDX line scan for Al

The composition of the HT - like phase formed in the slag particle imaged in figure 6-16 has been analysed using the Mg/Si against Al/Si atomic ratio scatter plot in figure 6-19, this plot allows for the estimation of the Al/Si ratio of the C-S-H and the Mg/Al ratio of the HT phase. The gradient of the calculated linear regression line shown in figure 6-19 corresponds to the Mg/Al ratio of that phase (2.27). The Al/Si ratio of the slag Ip is given when Mg/Si=0 (0.209) which is higher than the reported Al/Si for the Op C-S-H phase calculated from TEM-EDX and shown in table 6-1. The reported Mg/Al ratio for the HT -like phase from TEM regression analysis at 2.27 was slightly higher than the calculated Mg/Al ratio using the same technique with SEM-EDX data points (2.01). These Mg/Al ratios can be compared to the reported ratio in the previous chapter (2.45) and literature. Whilst the value measured in this sample by both SEM-EDX and TEM-EDX is lower than that in chapter 5 the level of aluminium incorporation is not dramatically increased. In studies of activated slag pastes with varying slag compositions the reported SEM-EDX Mg/Al ratios for the HT - like phase ranged from 2.1 to 1.24 depending on the Al_2O_3 content of the slag [38, 39]. It should be noted that the SEM-EDX value for this study of 2.01 is nearly identical to the reported Mg/Al ratio by Haha et al [38] for a study of slags with a normal Al_2O_3 content at approximately 11% using the same technique. It was only when the internal Al_2O_3 content of the slag was increased that the resultant Mg/Al ratio lowered. This suggests that the HT phase composition in that system was dependent upon the amount of Al_2O_3 present in the slag. As this study reports a very similar ratio by SEM-EDX and TEM-EDX above 2.0 it suggests the aluminium waste addition does not affect the HT phase composition in a similar manner to the slag's internal Al_2O_3 content.

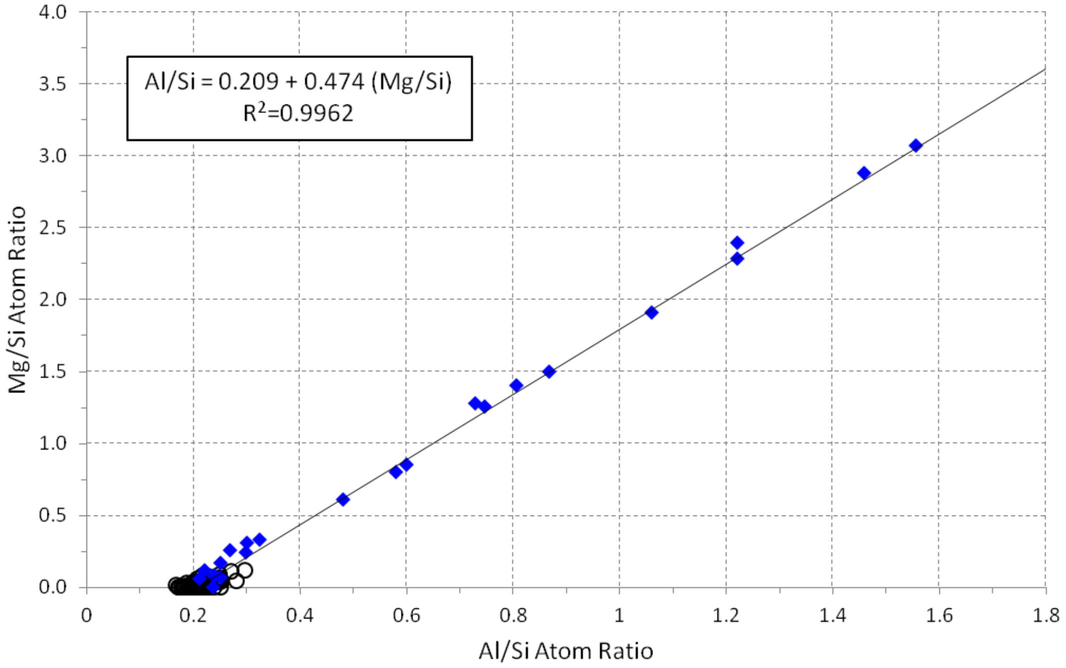

Figure 6-19: Mg/Si against Al/Si atom ratio plots of TEM EDX analyses of fine C-S-H (○), Slag Ip Product (◆) EDX taken from hydrated grain shown in figure 6-16.

6.5.1 Nanostructural model for C-S-H

The applicability of the TEM-EDX data has been discussed in relation to the tobermorite-jennite (T/J) and tobermorite - 'solid solution' calcium hydroxide (T/CH) approaches for the nanostructure of C-S-H reported by Richardson and Groves [24, 26, 175]. The Si/Ca against Al/Ca plots which are displayed in figure 6-20 and 6-21 show the experimental TEM-EDX and the theoretical structural plots similarly to previous chapters.

Examination of the TEM-EDX experimental data shows that both the T/CH and T/J models can be used to account for the observed Si/Ca and Al/Ca ratios. As mentioned in section 6.5 the measured levels of aluminium in the sample's C-S-H structure are slightly higher than those observed for comparable samples in the literature [51-53] and in this study. However this additional Al sits well within the boundaries for aluminium incorporation into the C-S-H phase allowed by the Richardson and Groves' structural model for C-S-H [181]. The T/CH model in figure 6-20 can account for all the observed analysis points for the C-S-H phase. The displayed trend-lines demonstrate that the likely level of Al incorporation is below that for a fully substituted T5 structure at a minimum (w/n=0) to intermediate (w/n=1) level of protonation for the majority of analyses for the Op C-S-H. Therefore similarly to the previous chapter for the 90% slag paste a partially substituted structural unit would be more appropriate than comparison against fully substituted units. To accomplish this the trend lines were again replotted using partially substituted chain units with sensible Al/Ca values in figure 6-21. The T/J viewpoint shown on the right in figure 6-20 can also account for the experimental data with the data suggesting a longer chain unit which is partially substituted (T11(2Al)) again between minimum (w/n=0) and intermediate levels (w/n=1) of protonation. When looking at the observed data both of the discussed models show the data can be accounted for with little or no requirements for CH or J units.

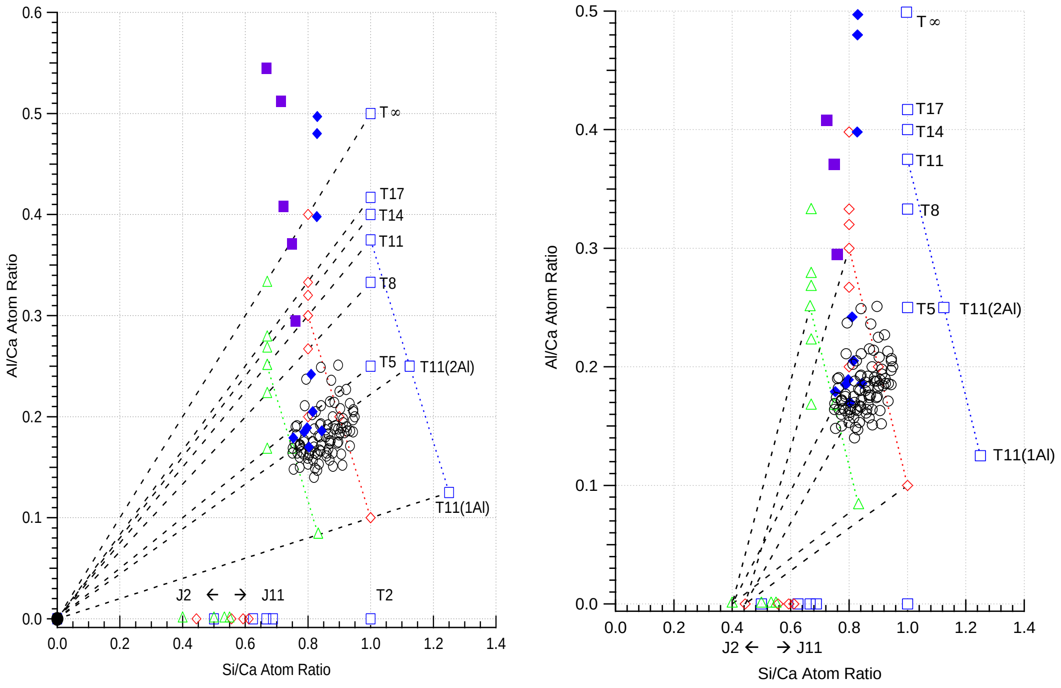

Figure 6-20: Si/Ca against Al/Ca atom ratio plot of TEM-EDX analyses of C-S-H (○), slag Ip (◆) C-S-H and intermixed Strätlingite (■) present in BFS:OPC + Al slurry sample. The additional symbols represent the compositions of tobermorite (T) and jennite (J) based structural units with different levels of protonation of the silicate chains: the minimum (△; w/n=0), intermediate (◇; w/n=1) and maximum (□; w/n=2). The additional points included represent tobermorite- based units with chain lengths of 2, 5, 8, 11, 14, 17 and ∞. All units are assumed to be saturated with Al where possible. (ie all the occupied bridging sites are occupied by Al rather than Si). The only exception is for units with 11 tetrahedral chain length, as additionally to those saturated with Al (T11) those with only one or two of the three possible bridging sites are also shown labelled as (T11(1Al) and (T11(2Al) respectively. The black dashed lines join points for structural units of the same chain length but different degrees of protonation to CH on the left and to Jennite based dimer of the same protonation on the right. T11 units with the same protonation but differing Al content are joined by coloured dashed lines.

The re-plotted T/CH model is shown in figure 6-21, and the most appropriate structural units seem to be from T11(2Al) to T17(3Al) for the Op C-S-H phase. The indication therefore is that the average structural unit has a long average mean chain length (MCL) between 11 and 17, this is partially substituted with Al with degrees of protonation between the minimum and intermediate levels. These limits for the estimated structural units from the TEM-EDX data are similar as those described in chapter 5 and the table of T-like structural units is produced in table 6-2.

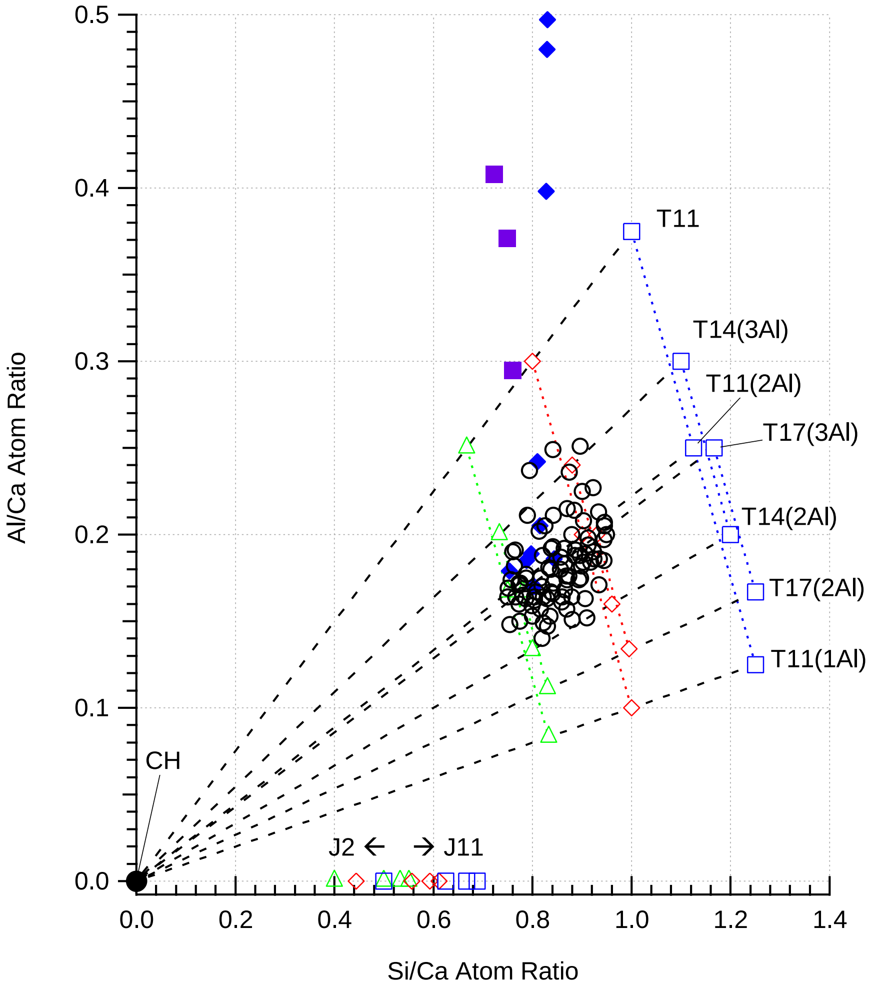

Figure 6-21: As Fig 6-20 except additional points included represent tobermorite- based units with chain lengths of 11, 14, and 17 with varying saturations of Al. Points were chosen to relate to the compositional data for the BFS:OPC + BaCO$_3$ sample. CSH (○), intermixed slag Ip (◆) C-S-H, intermixed Strätlingite (■).

The range of potential structural units identified by TEM-EDX in this sample is wider than that reported in the previous chapter. This is primarily due to the larger range of the observed Al/Ca ratio which requires either an increase in protonation or incorporation of Al into the bridging sites (B%). Comparing table 6-2 with the data presented in chapters 5 and 7, the average level of Al incorporation measured by B% will be higher if the average structural unit is assumed to be a combination of these selected T-like units. This leads to the conclusion that the Al simulant waste has had an effect upon the hydration of the C-S-H phase from the evidence of the TEM-EDX analysis. As previously mentioned a level of strätlingite has been produced which is intermixed with the C-S-H phase, however care was taken to avoid any crystalline phases to achieve 'clean' analysis of the C-S-H. The analysis points of intermixed strätlingite formations with C-S-H have also been plotted in figures 6-20 and 6-21 for comparison. Due to the substantial increase in Al/Ca ratio observed when analysing intermixed phases it has been assumed that the labelled Op C-S-H analyses are representative of the Op C-S-H phase and not intermixed products.

Structural Unit	Degree of protonation	Si/Ca	Al/Ca	B (%)*
T11 (2Al)	Minimum w/n=0	0.750	0.167	66
T11 (2Al)	Intermediate w/n=1	0.900	0.200	66
T14 (2Al)	Minimum w/n=0	0.800	0.133	50
T14 (2Al)	Intermediate w/n=1	0.960	0.160	50
T14 (3Al)	Minimum w/n=0	0.733	0.200	75
T14 (3Al)	Intermediate w/n=1	0.880	0.240	75
T17 (3Al)	Minimum w/n=0	0.780	0.167	60
T17 (3Al)	Intermediate w/n=1	0.930	0.200	60

Table 6-2: Selected appropriate T-like structural units for the 3:1 BFS:OPC + Al Slurry

6.6 NMR

Solid-state NMR spectra for the Al simulant slurry containing sample was obtained at the EPSRC UK National Solid-state NMR service at Durham University for comparison with ^{29}Si and ^{27}Al NMR spectra of previously studied GGBS-PC pastes with no additional simulant waste.

6.6.1 ^{29}Si MAS NMR

^{29}Si NMR spectra shows a low broad peak at approximately -73 ppm which is labelled in figure 6-22 as referring to the unreacted glassy slag remaining within the paste.

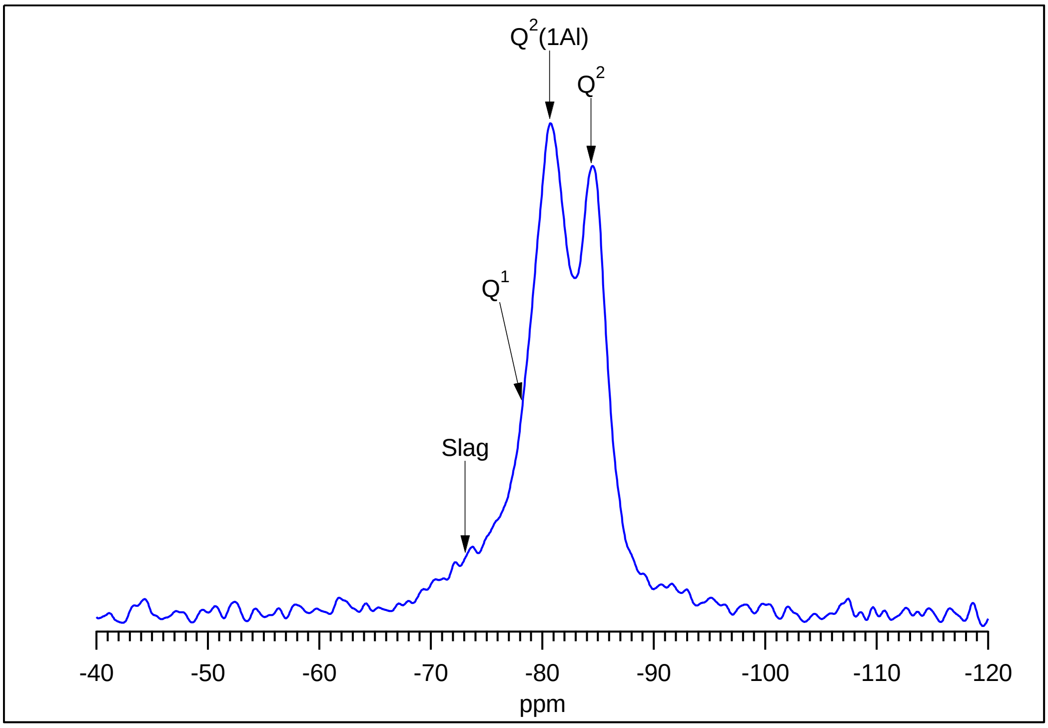

Figure 6-22: ^{29}Si MAS NMR spectra for BFS:OPC + Al Slurry

The hydrated phases in the system have been annotated using the three peaks for C-S-H discussed in the previous chapters (Q^1, Q^2(1Al) and Q^2) with chemical shifts at approximately -79 ppm, -81.5 ppm and -85 ppm respectively. As expected for an aged high replacement slag cement the quantity of mid-chain tetrahedra the Q^2 responses is high when compared to the end-member response of Q^1. Additionally the quantity of Q^2(1Al) representing a mid-chain unit with one adjacent tetrahedra occupied by Al is noticeably higher than for that of Q^2 suggesting a high level of Al substitution into the C-S-H structure. This result agrees with the observed TEM-EDX data when compared to the models displayed in figures 6-20 and 6-21, with the C-S-H phase showing a noticeable increase in the Al/Ca ratio when compared to PC pastes and the sample in chapters 4 and 5. The ^{29}Si NMR result also supports the TEM-EDX selected structural units in table 6-2 which propose a high MCL with levels of partial Al substitution at a higher level than most PC/slag based cements. In comparison to the other 75% slag replacement system in chapter 7 the estimated Al content given by Q^2(1Al) response is higher than reported in that study, additionally the Q^1 proportion seems slightly reduced suggesting the average chain length was longer in this sample.

6.6.2 ^{27}Al MAS NMR

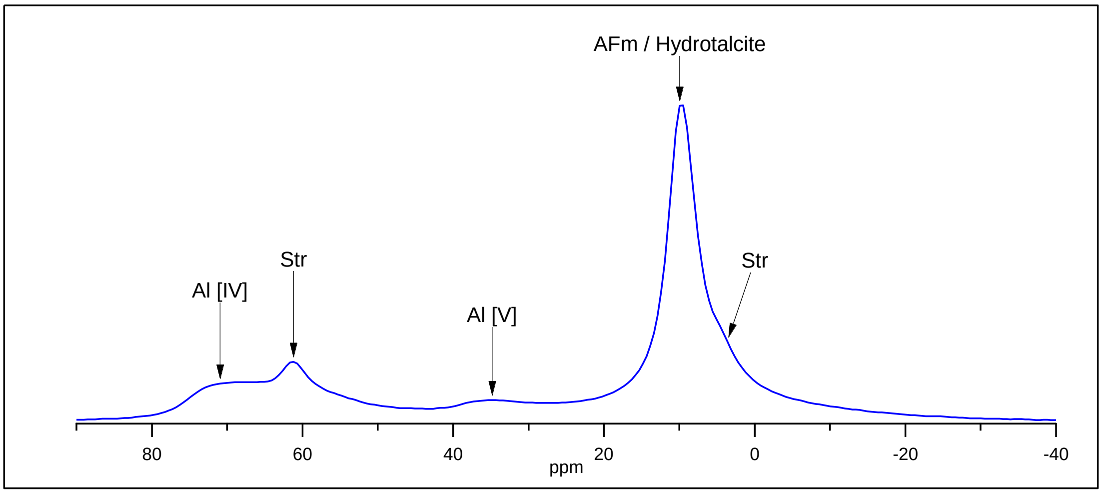

Figure 6-23: ^{27}Al MAS NMR spectra for BFS:OPC + Al Slurry; Str = Strätlingite

The ^{27}Al MAS NMR spectra is shown above, as discussed in previous chapters resonances are observed for tetrahedrally coordinated (Al [IV]) five-fold (Al[V]) and octahedrally coordinated Al. The broad peak centred at 65ppm is associated with levels of unreacted glassy slag and tetrahedrally coordinated aluminium substituted into the C-S-H phase and the presence of an Al substituted C-A-S-H phase has been discussed [9, 182, 204].

The main octahedral peak which is centred at 9ppm has a strong response and is linked to the formation of an AFm and the hydrotalcite-like phase [206]. Due to the relative small mass loss of the hydrotalcite phase by thermogravimetric analysis in section 6.3 it is assumed the majority of this strong resonance is due to the formation of the AFm phase monocarboaluminate. The additional phase found is this sample was a pair of resonances at around 6ppm and 61ppm which closely match the reported chemical shifts for syntheised strätlingite in a study by Kwan et al [226]. This matches the results from other analysis techniques such as XRD and STA which confirms the formation of levels of strätlingite due to the addition of the Al- based simulant wasteform.

6.7 Conclusions

The aged samples of cement paste containing the simulant aluminium slurry on visual inspection showed good physical characteristics with no evidence of extensive porosity or cracking. However sample preparation for the sample was comparatively difficult compared to all other waste-forms studied, with fine micro-structural cracking evidenced by SEM analysis during preparation. While it is uncertain what caused the general instability of the monolith (i.e. was it extensively cracked from phase changes) it can be reported that sample preparation and sectioning of this material required much greater care than similar pastes.

The waste prior to cementation consisted of an alumino-silicate slurry with a dry solids content of approximately 7.5% with traces of iron, unfortunately no additional characterisation of this material was available beyond what is mentioned in chapter 3. The resultant waste-form produced by cementation showed reasonable physical encapsulation of the simulant waste with only large agglomerations of the waste material clearly seen within the pastes matrix. SEM imaging showed that the waste material did have an effect upon the surrounding microstructure with the formation of large quantities of lathe-like products particularly around the waste sites. The composition of these laths showed them to be a calcium aluminate hydrate identified as calcium monocarbolauminate (Mc), additionally the analysis of the sample showed the presence of aluminium-containing strätlingite. The formation of strätlingite and such large quantities of Mc is not commonly reported even for high slag replacement cements so the formation of these phases is of interest especially due to their Al content.

The pre-treatment process with lime was found to be an important part of the encapsulation process, the sample was mixed with hydrated lime at 10 %wt of the dry waste solids and the included slurry water content for 1 hour prior to the addition of the cement (BFS:OPC) binder. It is proposed that this mixing provides a large amount of Ca^{2+} from the dissolution of $Ca(OH)_2$ and a level of CO_3^{2-} ions from the air and mixing procedure. When the subsequent hydration occurs with the addition of the cement powders the waste material is successfully reacted within the cement matrix due to the pre-mixing with reactive $Ca(OH)_2$ and availability of Ca^{2+} ions and silicates contained within the waste. A level of reaction does occur however between the waste and hydrating matrix as a level of aluminates are released or diffused from the waste-form which react locally with the available Ca^{2+} and CO_3^{2-} ions to form calcium monocarboaluminate within the binding matrix [227, 228]. This would explain the formation of large quantities of aluminate phases around the larger waste particles by SEM BSE imaging. Additionally the waste-form does seem to increase the available quantity of aluminate ions within the hydrating matrix which are incorporated as C-A-S-H as indicated by the estimation of structural units by TEM-EDX analysis. The reason for this waste reaction could be due to levels of unconsumed $Ca(OH)_2$ within the mix. While the initial reaction with the slurry allows for its successful incorporation, the levels of hydroxide ions are known to control the extent of aluminium corrosion [97]. Pardal et al [229] studied a synthesied C-A-S-H phase and found that for $Ca(OH)_2$ concentrations higher than 4.5 mmol L^{-1} pure C-A-S-H was not formed with monocarboaluminate and strätlingite also present. This is of interest due to the large quantities of $Ca(OH)_2$ within this mix and the later formation of monocarboaluminate and strätlingite which is discussed below.

The formation of strätlingite has been observed in the activated slag based cements with high Al_2O_3 compositions [39], similarly in this system small quantities of strätlingite were formed. The presence of strätlingite has also been mentioned in studies into the inclusion of aluminium metal [83] and powder [97] in composite grouts as a product from the corrosion process. Strätlingite-type phases have also previously been observed in cements which are aluminium enriched and slag cements [230-233], so its presence is not unexpected. The increase in Al availability for both the formation of strätlingite and C-A-S-H in this system could be due to the reaction of the Al waste slurry in the system or the increased dissolution of the slag particles from the $Ca(OH)_2$ addition. Puertas et al [219] reported strätlingite as a result of industrial wastes containing reactive alumina combining with a $Ca(OH)_2$ saturated solution, and due to the pre-treatment process used in this work is likely to be relevant to this study.

It has not been possible to determine whether the additional Al originates from the waste-stream or increased slag dissolution, as the waste-form contains both the required aluminates and silicates for the formation of both phases. However due to the large quantities of aluminate containing phases in the system (Mc, strätlingite and C-A-S-H) it seems sensible to conclude that a proportion of the available aluminate ions for reaction are supplied from the simulant waste. This proposal is supported by the experimental data, particularly for the increased level of aluminium substituted into the C-S-H phase when compared to a similar system containing pre-treated magnesium; results presented in the following chapter. Additionally the imaging of the microstructure by SEM analysis shows high levels of aluminate phases in the local environment around waste agglomerations, this indicates a link between the waste and formation of Mc and potentially strätlingite alongside a highly substituted C-S-H structure.

The average Al/Si ratio for the C-S-H phases and Mg/Al composition of the HT-like phase was investigated with SEM and TEM EDX analysis. SEM analysis showed very similar results to those for an activated slag systems studied by Haha et al [38, 39]. The Mg/Al ratio was unaffected by the Al waste addition with identical results to the literature data for a slag with average Al_2O_3 contents. The Al/Si ratio for C-S-H was similar to systems of the activated slag's with increased Al_2O_3. A range of Al/Si ratios from TEM-EDX analysis was observed (0.14 to 0.28) which suggested an increased level of aluminium incorporation within the C-S-H phase.

A significant quantity of large agglomerations of pre-formed waste material remains within the cement matrix suggesting the primary form of encapsulation in this system is physical not chemical. However, the study has shown a considerable level of Al-containing phases which are formed during hydration, implying a level of chemical immobilisation is present for an Al^{3+} ion waste. Mass immobilisation of ions via substitution into the C-S-H phase has been discounted in this sample; experimental evidence indicates a level of Al incorporation in line with normal high-slag replacement cements with no waste addition. It is estimated the majority of the simulant waste remains physically encapsulated, with chemical immobilisation linked only to the more minor Mc and strätlingite phases.The waste-form was considered to be 'fresh' and therefore seen as a worst case scenario for encapsulation compared to actual in service waste which will have aged and potentially stabilised over time. Despite this it is likely an in-service industry waste-form would exhibit a much more varied chemical composition and range of ions for encapsulation than the sample examined in this study. As the simulant waste was designed to mirror an aluminium corrosion slurry produced from the storage of metallic Magnox waste the fate of the reacted aluminium ions is of particular interest. The waste therefore seems to be both physical and chemically encapsulated with additional Al ions found in several phases in the system. Due to this it cannot be said that physical encapsulation simply dominates in this sample. The stability of monocarboaluminate has been shown to remain unchanged up to ≤70˚C, beyond this point as discussed in chapter 5 the AFm phase starts to gradually decompose to hydrogarnet and calcite phases [154]. The containment of Al ions in the resulting C_3AH_6 would however be beneficial due to known higher thermal stabilities of hydrogarnets [234]. Similarly the stability of synthesised strätlingite has been observed up to temperature of 85˚C [154]. However the relative calcium and aluminium concentrations are reported to be important due to the mass Al ion availability therefore strätlingite is likely to be stable.

Chapter 7 : Results and discussion of BFS:OPC + $Mg(OH)_2$

7.1 Introduction

A simulated magnesium hydroxide waste sludge produced by industry has been studied to assess the interaction with its selected composite cement encapsulation matrix. The $Mg(OH)_2$ based sludge samples were produced as outlined in section 3.1, encapsulated in a 3:1 BFS:OPC grout and stored for 15 years before their provision for this project. The results for this sample are discussed in relation to previous work by Collier et al [84] into $Mg(OH)_2$ sludges and the encapsulation of Magnox swarfs in cements [82]. Comparisons are made with previous conclusions and the potential long term impact of $Mg(OH)_2$ encapsulation within slag based composite cements.

7.2 XRD

XRD analysis on the BFS:OPC + $Mg(OH)_2$ sample is shown in figure 7-1 the trace shows the hydration products associated with a high replacement slag cement, the primary difference being the presence of large quantities of seemingly unreacted brucite - $Mg(OH_2)$. Figure 7-1 shows the presence of C-S-H, levels of portlandite ($Ca(OH)_2$) and a hydrotalcite- like phase (HT) which would all be expected in a slag cement. The presence of portlandite even at a high replacement level and older age has been observed previously and indicates the sample is unlikely to have carbonated [52, 53]. The observation of the AFm phase has been assigned to monocarboaluminate due to the relevant primary 11.6˚ 2θ response, additionally a small level of monosulphoaluminate (Ms) was also detected by XRD.

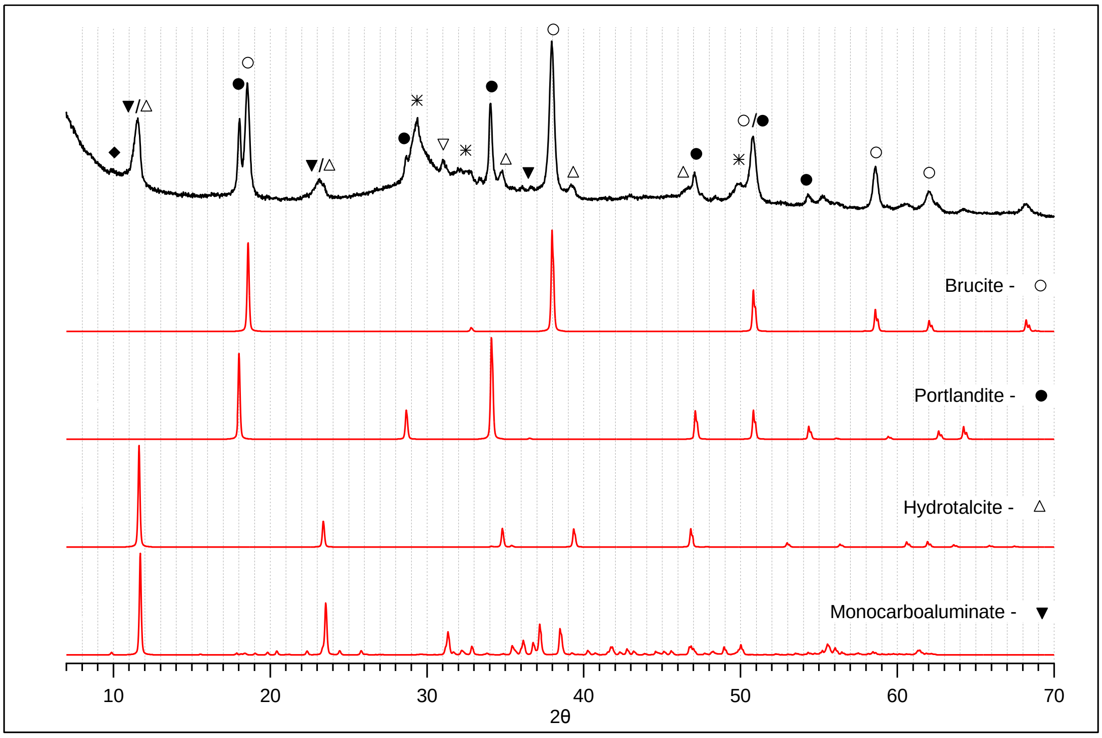

Figure 7-1: XRD trace of BFS:OPC + $Mg(OH)_2$ with simulated patterns for resultant phases shown; ▼ – AFm (Monocarboaluminate), ▽- Gehlenite, △- HT-LDH, ✳ - C-S-H, ◆ - AFm (Monosulfoaluminate), ○ - Brucite $(MgOH_2)$, ● - Portlandite $(Ca(OH)_2)$.

The primary effect of the addition of $Mg(OH)_2$ can easily be distinguished by the large quantities of unreacted brucite indicated in figure 7-1, there was no formation of any additional new magnesium-based phases. The level of detected hydrotalcite (HT) a Mg - Al layered double hydroxide (LDH) phase, was not dissimilar to that found in a similar high replacement slag cement of a younger age studied previously (see figure 7-2) [221]. The primary difference between the hydrated phases was the noticeable increase in the 11.6° 2θ response which has been assigned to both Mc and HT. As this increase only occurs at overlapping 2θ positions where the Mc is present; it is concluded the increase is due to the additional levels of Mc present and not the formation of large quantities of HT due to the Mg addition. The presence of AFm within the system is discussed later using other bulk analysis techniques and electron microscopy. The only other primary phase difference between the samples displayed in figure 7-2, apart from the presence of the discussed unreacted brucite is the inclusion of the unhydrated belite as an anhydrous phase.

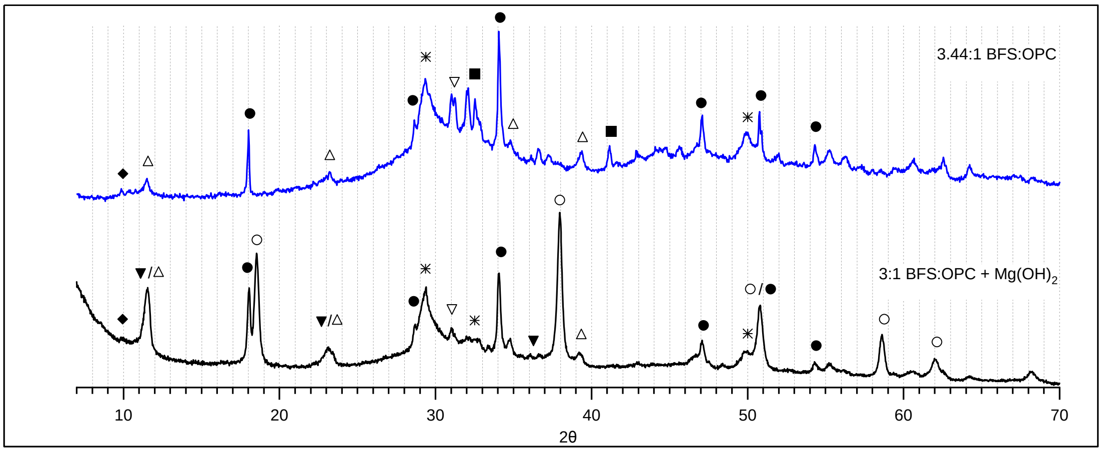

Figure 7-2: Comparison of XRD traces from two studied slag based systems with and without $Mg(OH)_2$ simulant waste; ▼ – AFm (Monocarboaluminate), ▽- Gehlenite, △- Hydrotalcite, ✳ - C-S-H, ◆ - AFm (Monosulfoaluminate), ○ - Brucite ($MgOH_2$), ● - Portlandite ($Ca(OH)_2$), ■ - Belite (β-C_2S)

7.3 Thermal Analysis

STA was carried out to detect crystalline and amorphous phases in the cement grout, Figure 7-3 shows the DTA curve for the grout with the $Mg(OH)_2$ addition. The data shows the primary decomposition peaks found up to 600˚C, this is due to that the only major peak expected above 600˚C would be CO_2 associated with the decomposition of calcium carbonate. Evidence from TGA and XRD however shows negligible amounts of calcite present in these samples when they are not exposed to atmospheric conditions.

As can be seen in Figure 7-3 the two primary peaks were for the dehydration of C-S-H phase (50-300˚C) [235] and the dehydroxylation of Brucite (350-400˚C). The small peak observed at 150˚C was due to an AFm phase assumed to be monocarboaluminate due to the strength of the XRD peaks at 11 and 23˚ 2θ [153, 236]. The peak at 200˚C is linked to the lower temperature stage of the two - stage decomposition of hydrotalcite described by Gruskovnjak et al [222], with the higher temperature mass loss overlapped by the dehydroxylation of the large quantities of brucite or present as a small shoulder at 425˚C. The small peak observed just before 450˚C is linked to the dehydroxylation of $Ca(OH)_2$. This small level of portlandite is consistent with the previous work on high replacement slag systems [48]. It should also be noted this simulant waste was pre-treated with lime (10%wt) to improve the inclusion of simulant waste powders. This inclusion however has had little effect upon the final levels of $Ca(OH)_2$ measured by TGA when compared to systems without this addition.

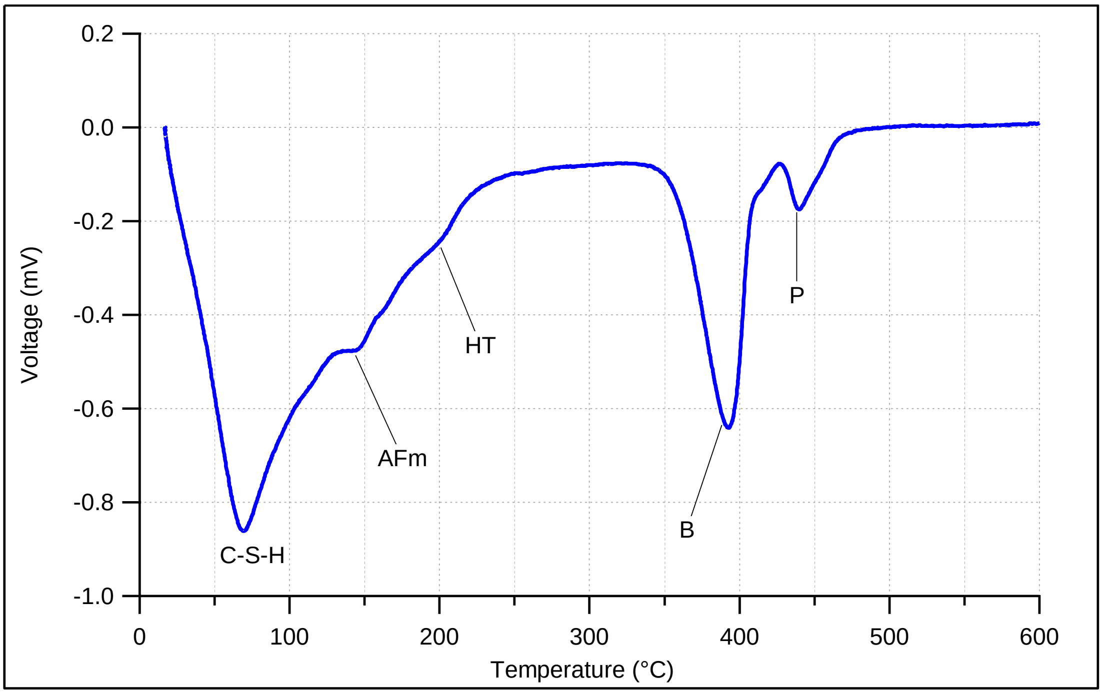

Figure 7-3: DTA trace for BFS/OPC + $Mg(OH)_2$ sample for 0 - 600˚C ; B - Brucite ($Mg(OH)_2$), P - Portlandite ($Ca(OH)_2$), C-S-H - calcium silicate hydrate, AFm - Mc, HT - Hydrotalcite.

The associated mass spectroscopy trace for the evolved gases from the above TG run are shown in figure 7-4, with the EGA for water (mass 18) and carbon dioxide (mass 44) are shown. The results for water show the dehydroxylation of C-S-H and the AFm phase at temperatures up to 175˚C. The later dehydroxylation of the bound water associated with brucite and the formed $Ca(OH)_2$ in the paste are seen as the higher temperatures of 350-400˚C and 400-450˚C respectively, these match well with the reported TG and DTA evidence. Two potential peaks at around 200˚C and 400˚C for water are linked to the mass loss for the hydrotalcite - like phase discussed earlier. As mentioned previously there was no evidence of carbonation in the sample relating to the presence of calcium carbonate by either STA or EGA. The presence of CO_2 from the formation of AFm Mc at 150˚C was not detected however this was also the case in chapter 4 with the limestone containing NRVB sample. It's omission from the EGA trace has been attributed either to the levels of sensitivity in the equipment as discussed in chapter 6 or the failure of the phase to release CO_2 during the dehydroxylation stage. As the presence of monocarboaluminate was confirmed for previous samples containing limestone and barium carbonate but not detected by EGA it is assumed that Mc is still present in this sample despite no CO_2 detection.

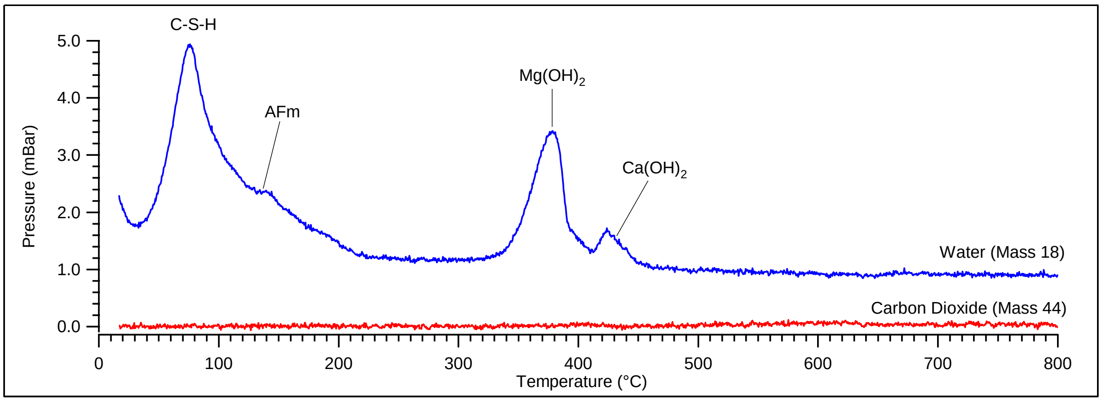

Figure 7-4: Associated mass spectrometer trace for BFS:OPC + $Mg(OH)_2$

7.4 SEM

Figure 7-5 shows a SEM BEI micrograph of the general microstructure of the BFS:OPC matrix with the addition of $Mg(OH)_2$.

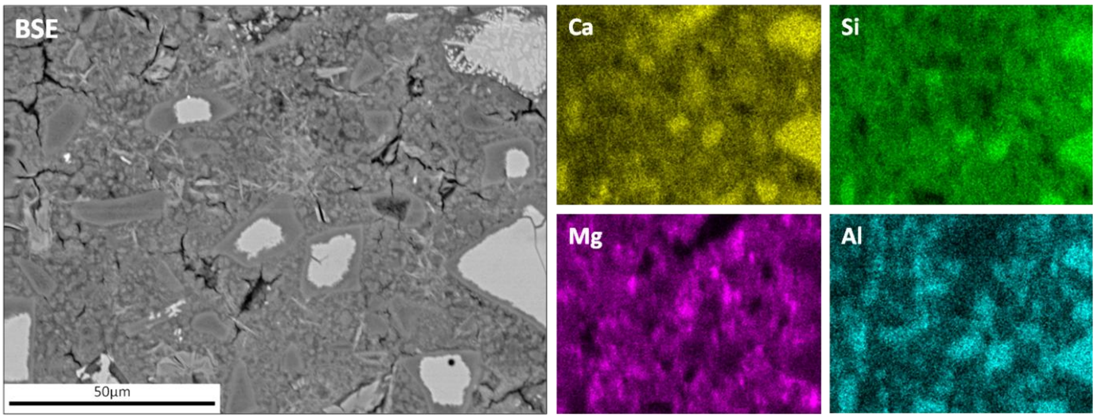

Figure 7-5: BSE image of BFS:OPC + $Mg(OH)_2$ (x1000) with associated elemental mapping

Elemental mapping shows the expected higher aluminium responses associated with both partially and fully hydrated slag particles. The magnesium mapping indicates that the highest levels of magnesium are found particularly intermixed in the general binding matrix although Mg is pervasive in the microstructure. This shows the effect of $Mg(OH)_2$ addition when the mapping is compared to a normal high slag replacement cement matrix where the primary source of magnesium comes from the slag itself [237]. This effect is exemplified by the quantitative elemental mapping shown in figure 7-6, with a strong Mg response which is higher than the relative Ca responses in the paste. This shows that the levels of Mg present within the matrix are far higher than that provided by Mg- based hydration products normally associated with slag cements.

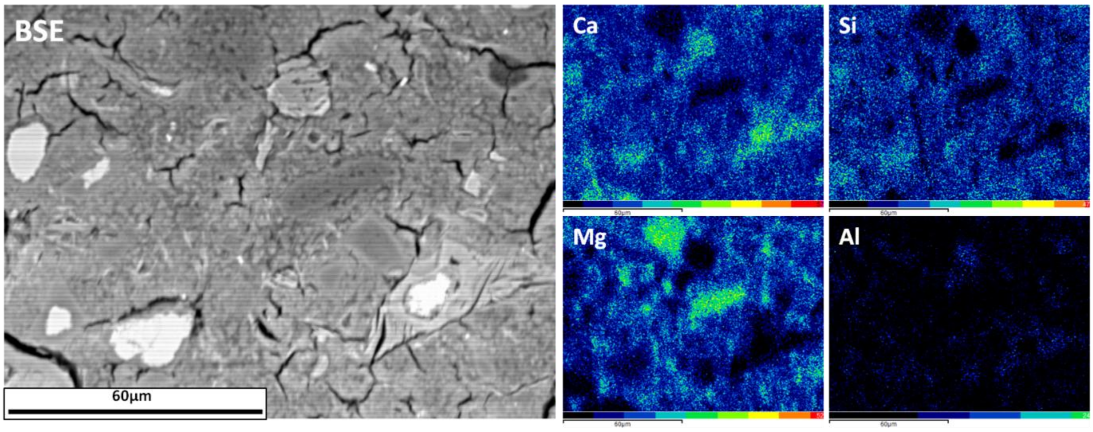

Figure 7-6: Quantified elemental mapping of BFS:OPC + Mg(OH)$_2$ (x1000) showing primary elements

The nature of the binding matrix's microstructure and hydrated phases were examined by FEGSEM in figure 7-7 images a) to d). All of the images showed the presence of AFm calcium aluminate phases, which was confirmed by EDX point analysis and mapping shown in figures 7-8 and 7-9. These AFm phases occasionally were associated with sulphur indicating the presence of Ms alongside the much more dominant Mc AFm phase which is found throughout the system. The AFm phases presented as platelets as seen in figure 7-7 b) and as more crystalline like formations as seen in figure 7-7 c) and d).

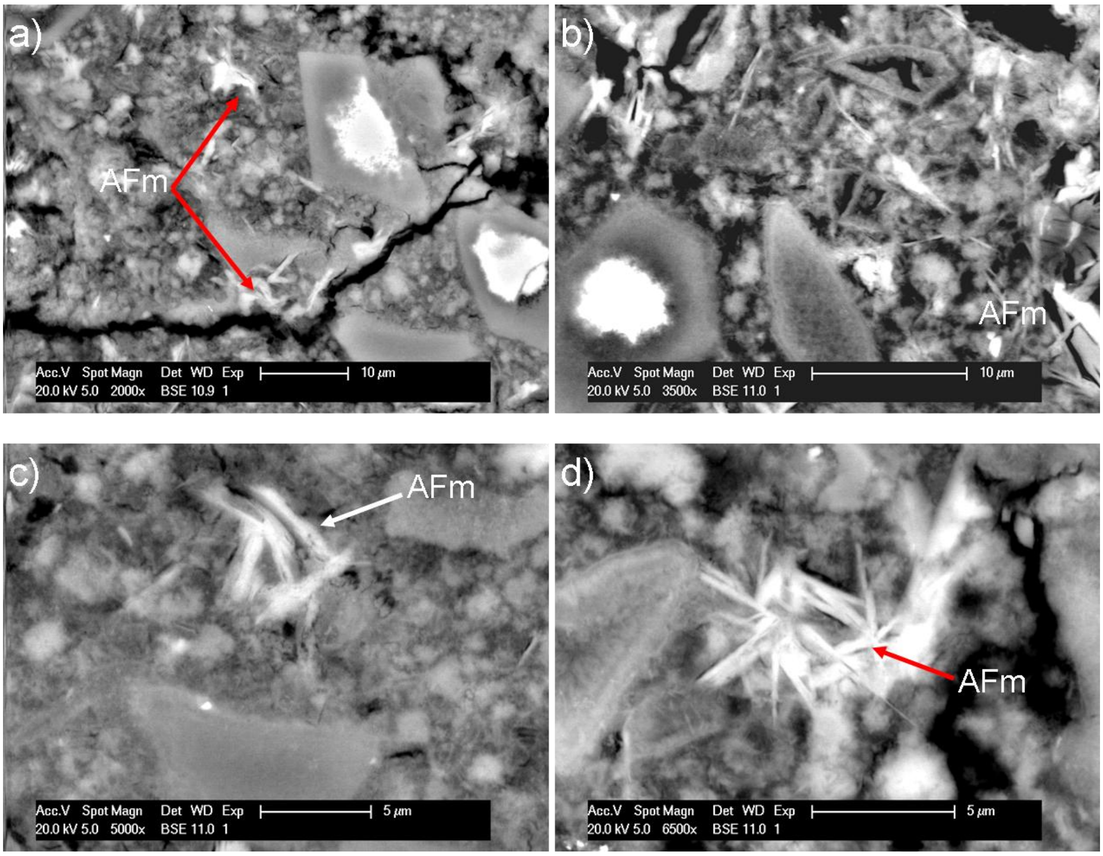

Figure 7-7: FEGSEM imaging of the BFS:OPC + MgOH$_2$ microstructure showing presence of AFm phases, hydrated slag particles and binding matrix.

The microstructure showed a large quantity of partially and fully hydrated slag grains, good examples of which can be seen above in figure 7-7 b) and d). The binding matrix is well observed at higher SEM magnification and shows the hydrated PC particles and C-S-H as the primary binding phase in image c). It is observed in figure 7-7 b) that the produced C-S-H binding phase is well intermixed with additional hydrates with likely crystalline phases found throughout the matrix. This explains the generally wide variation in observed SEM-EDX ratios for the sample, a number of which are displayed in figure 7-9. The simulant waste $Mg(OH)_2$ seems well encapsulated within the matrix without creating additional porosity or other microstructural problems which could lead to an unsound solidified wasteform. The incorporation of the $Mg(OH)_2$ was accomplished by pre-mixing the magnesium hydroxide dry powder with lime before the addition of mix water and the cement powder. Due to this procedure the particles of $Mg(OH)_2$ as seen by the Mg responses in elemental map (figure 7-8) and mid grey scale masses within the binding matrix in figure 7-7 c) seem to be well physically encapsulated by surrounding hydrates, rather than chemically immobilised within a new phase.

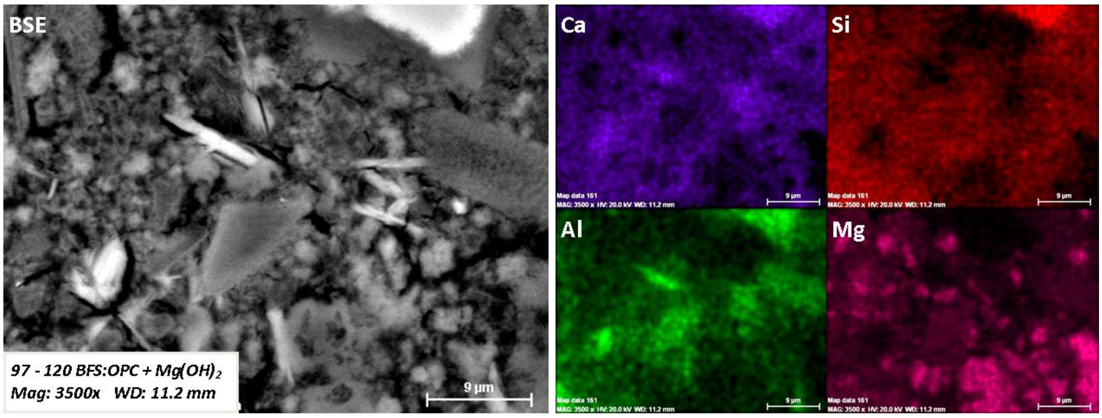

Figure 7-8: Microstructure of BFS:OPC + $MgOH_2$ showing formation of AFm phases and Mg presence

The SEM-EDX results shown in figure 7-9 indicate a trend for the intermixing of the C-S-H phase with both an AFm phase and a high Al content which is associated with the hydration of slag products or anhydrous slag itself. The Al/Si against Mg/Si scatter plot shows the formation of a Mg-Al product indicating hydrotalcite along with the C-S-H phase with a lower associated Mg content. The red plots in figure 7-9 show EDX analysis of areas with higher magnesium response from elemental mapping and therefore are assumed to be primarily linked to the encapsulated $Mg(OH)_2$. These analyses seemed not to be linked to increasing Ca, Si or Al therefore leading to the conclusion that the Mg response was independent of these elements.

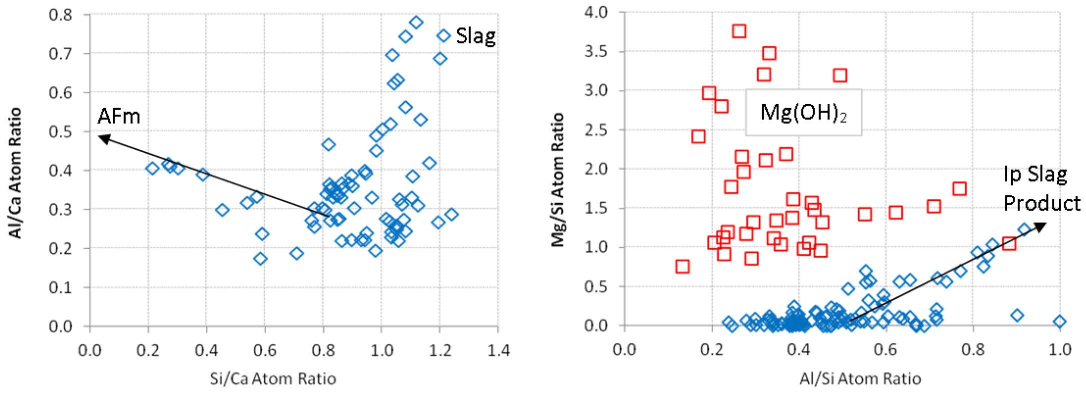

Figure 7-9: SEM-EDX analyses showing presence of $MgOH_2$ within the binding matrix and general atomic ratios for the hydrate phases.

7.5 TEM-EDX

Examination of the $Mg(OH)_2$ containing sample showed a varied microstructure containing large quantities of hydrated C-S-H surrounding magnesium waste sites and laths of AFm product formed throughout. The primary waste product observed by the previous experimental techniques was large quantities of brucite, again under TEM observation brucite was easily found within the binding matrix both as large crystals as shown in figure 7-10 and in smaller groupings shown in 7-11.

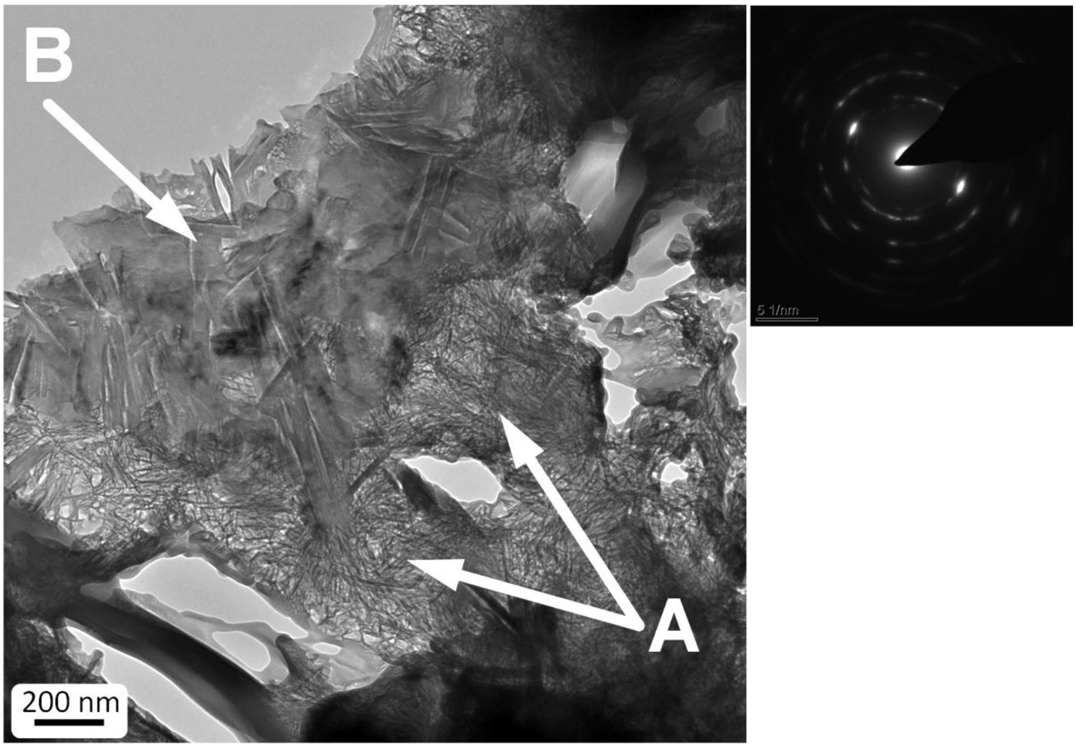

Figure 7-10: TEM micrograph of A) Fibrillar Op C-S-H product surrounding B) Large unreacted brucite crystal within the matrix, Diffraction pattern for area B shown.

As can be seen in figure 7-10 the encapsulation of relatively large crystals of brucite seems successful within the matrix with the simulant waste surrounded by the C-S-H phase and displaying no compatibility issues after a long curing period. Both figures 7-10 and 7-11 show the encapsulation of brucite and the association of $Mg(OH)_2$ with small crystalline formations of $Ca(OH)_2$ labelled B in figure 7-11. This is due to the pre-treatment of the simulant $Mg(OH)_2$ with the addition of hydrated lime, with levels of $Ca(OH)_2$ remaining from this process even after a long period when surrounded by fully formed hydrate phases.

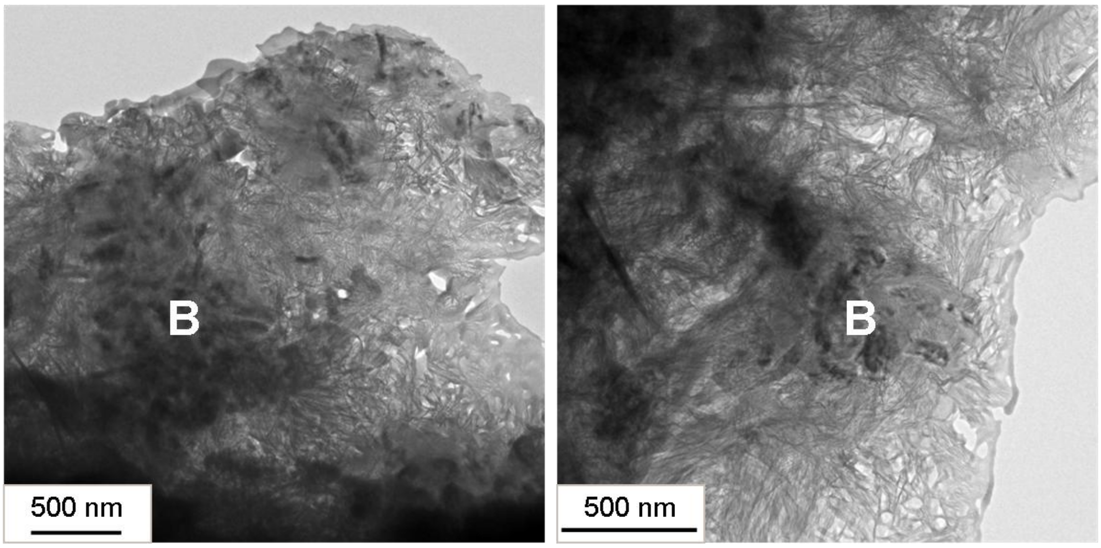

Figure 7-11: TEM micrographs of CSH binding matrix with incorporated brucite and calcium hydroxide simulant wastes labelled B.

As observed in the previous chapters involving BFS - based encapsulation matrices there was evidence of various different C-S-H morphologies on display as shown in figure 7-12. In some regions of the paste the C-S-H exhibited an extremely fine and dense morphology (figure 7-12 a), due to this definition between this phase and OPC inner product often became difficult and it is described as fine dense Op C-S-H is this study. A large proportion of the Op C-S-H consisted of a foil-like morphology as shown in figure 7-12 b) which is consistent with pastes with a high level of slag replacement [51-53, 238]. In areas closer to simulant waste sites and partially hydrated grains the morphology of the C-S-H subtly changed to a more fibrillar and finer nature as shown in figure 7-11. This suggests that there is a nucleation effect created by the presence of the simulant waste. Potentially this is due to the pre-treatment process preferentially producing C-S-H around these waste sites, thus increasing their encapsulation within the binding matrix.

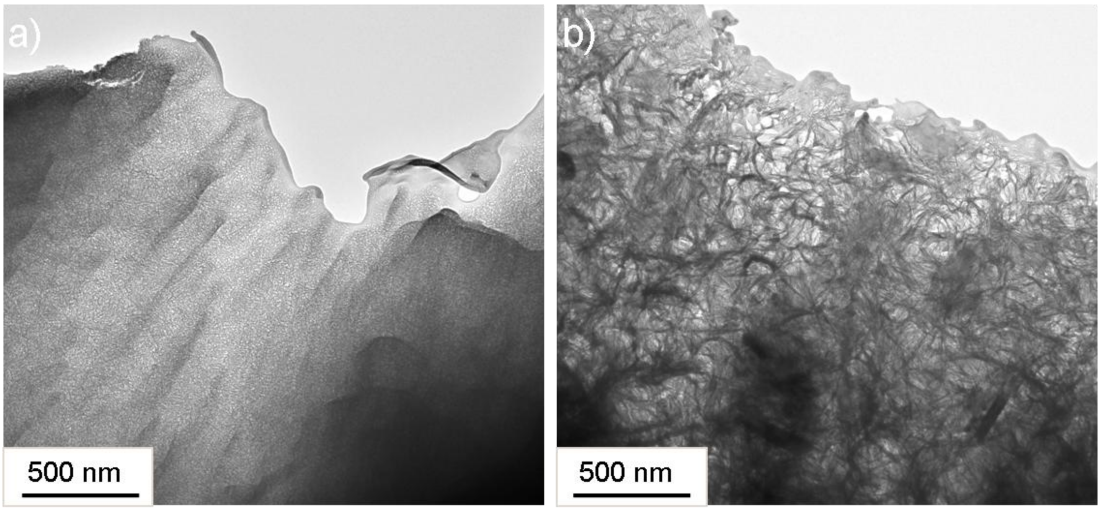

Figure 7-12: TEM micrographs showing a) fine dense C-S-H product and b) foil like C-S-H Op product

Figure 7-13 shows the intermixed hydrotalcite-like LDH phase seen predominantly in the presence of hydrated slag particles, the Ip zones of the hydrated slags are indicated by the white dotted outline in figure 7-13 b). The level of well hydrated and incorporated slag particles agrees with the high resolution SEM imaging shown in section 7.4 and can be compared to figure 7-7. The intermixed LDH hydrotalcite phase was investigated using TEM-EDX to determine its chemical composition by regression analysis (figure 7-16) similarly to the method employed in previous chapters; this is of particular interest due to the Mg content of this phase and the results are discussed later. The presence of fully reacted slag particles is beneficial to the overall strength of the matrix, porosity and therefore the effective encapsulation potential for the binding matrix. As shown from figure 7-13 the activation of the slag particles has not been hindered by the presence of the simulant waste material with good levels of desirable slag hydration observed similarly to that seen by SEM BSI analysis.

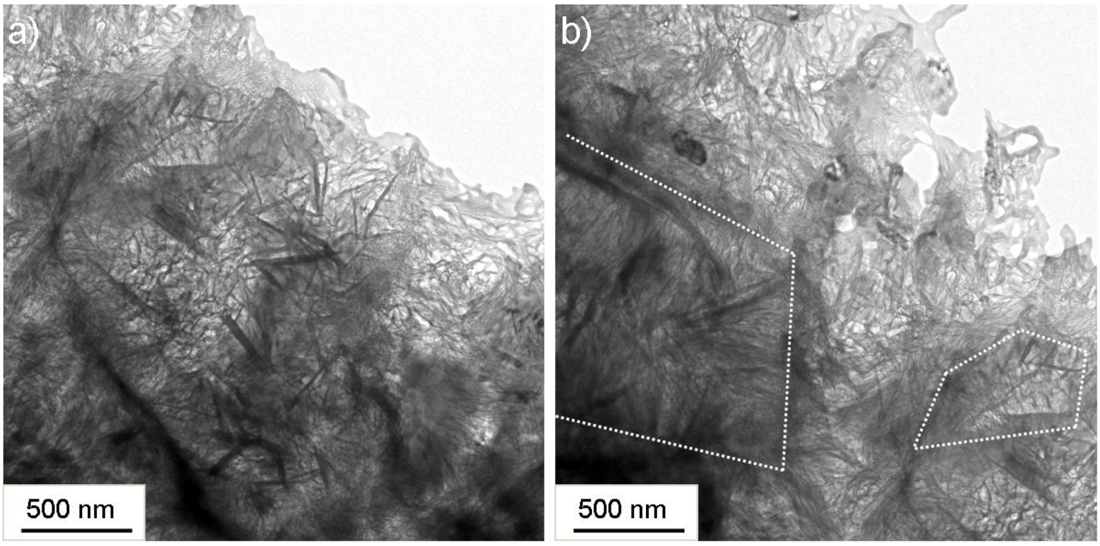

Figure 7-13: TEM micrographs showing C-S-H present with Mg-Al hydrotalcite - like laths associated with hydrated slag particles, boundaries of hydrated slag particles indicated in b) by dotted lines

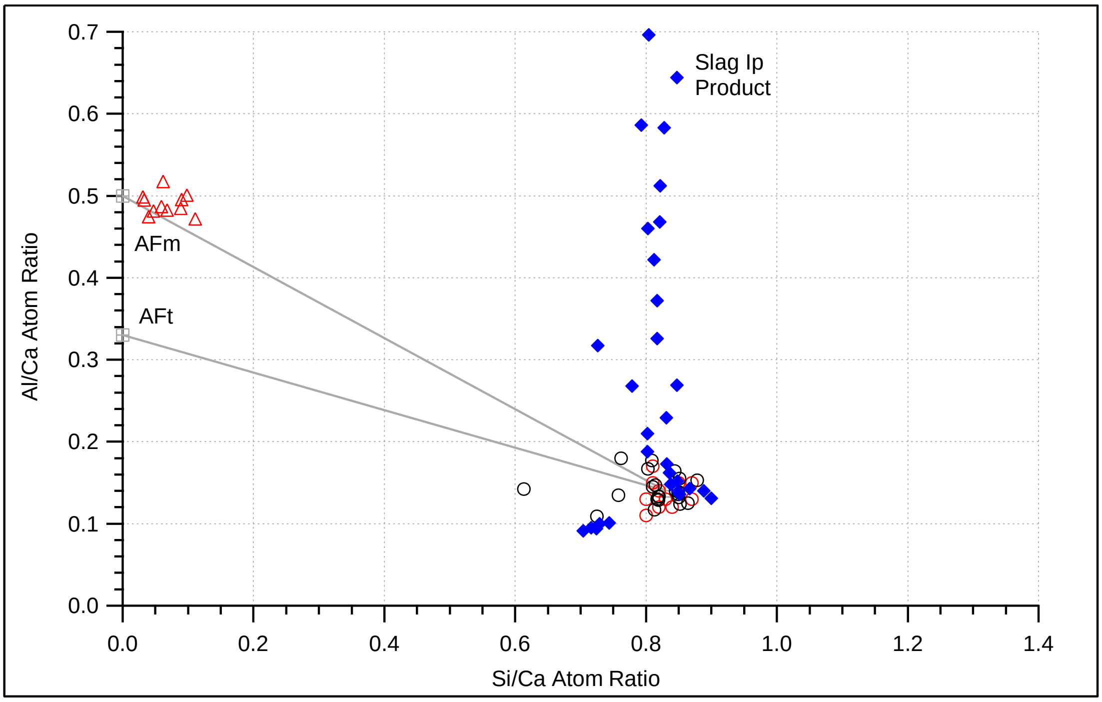

Figure 7-14: TEM-EDX analyses of described phases ○- Op C-S-H, ○- Fine C-S-H, △- AFm and ◆- Slag Ip Product (C-S-H intermixed with Mg-Al LDH).

TEM-EDX analysis points for the binding matrix in the $Mg(OH)_2$ containing paste are shown in figure 7-14. The analysis includes the fine dense C-S-H shown in figure 7-12 a) and the more foil - like C-S-H morphology observed labelled as Op C-S-H. The analysis points from the hydrated slag Ip, intermixed hydrotalcite - like phase and observed calcium aluminate phases such as AFm are also included. The TEM-EDX analysis shows a much tighter grouping than that shown for SEM-EDX analysis of the sample but agrees with the basic findings from the SEM. Both techniques indicate the presence of a lower Ca/Si ratio C-S-H when compared to neat Portland cements and the presence of AFm within the matrix. The related atomic ratios for the Ca/Si, Ca/(Si+Al) and Al/Si are shown in table 7-1; the mean Ca/Si ratio for the 3 studied C-S-H phases ranged from 1.20 to 1.24. These ratios are within the expected range for a high replacement slag cement, with considerable levels of Si and Al contained within the C-S-H phase. When compared to literature of similar systems [51-53] and the work reported in previous chapters of the current study, it can be seen the magnesium addition has no discernible effect upon the C-S-H atomic ratios. Figure 7-15 shows the Al/Ca against S/Ca ratios can allow the identification of calcium aluminate phases such as ettringite, monocarboaluminate and monosulphoaluminate as all have differing S/Ca ratios. The data points show that the AFm phases analysed consist predominately of monocarboaluminates (Mc) due to the low sulphur content which is in agreement with the primary XRD result.

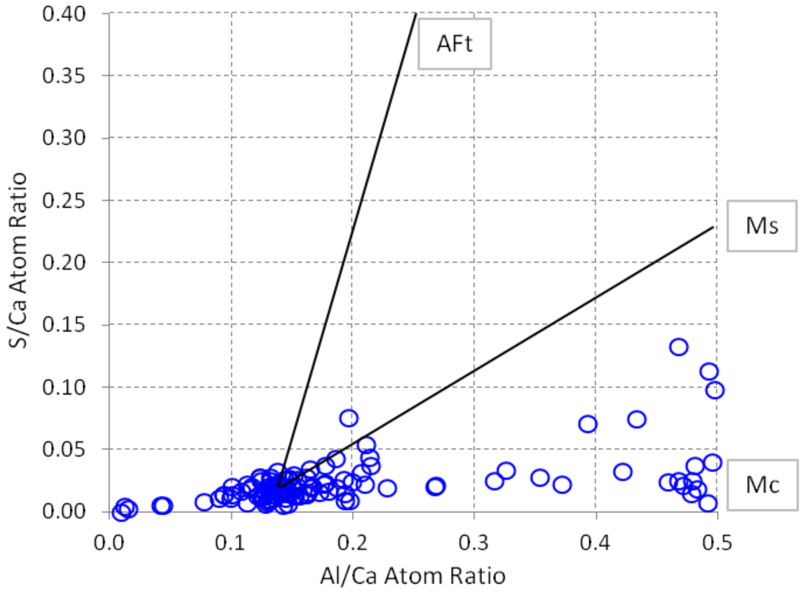

7-15: Al/Ca against S/Ca atom ratio plots of TEM EDX analyses in BFS:OPC + $Mg(OH)_2$ sample

The potential levels of magnesium present in the C-S-H phases can be investigated by examining the scatter plot shown in figure 7-16; the data points for C-S-H phases not associated with the hydration of slag particles are denoted by circles. The data shows a very low level of magnesium linked to most of the Op C-S-H phases analysed, which suggests the mass incorporation of magnesium from the simulant waste into the C-S-H is very unlikely. This view is supported by studies on slag replacements with a high MgO content by Haha et al [38] with no magnesium substitution detected within the C-S-H phase despite increasing

Mg^{2+} availability during the slag activation. This supports the evidence from the electron microscopy imaging which suggested the effective physical encapsulation of the simulant waste as a distinct phase rather than any level of chemical immobilisation within a new phase.

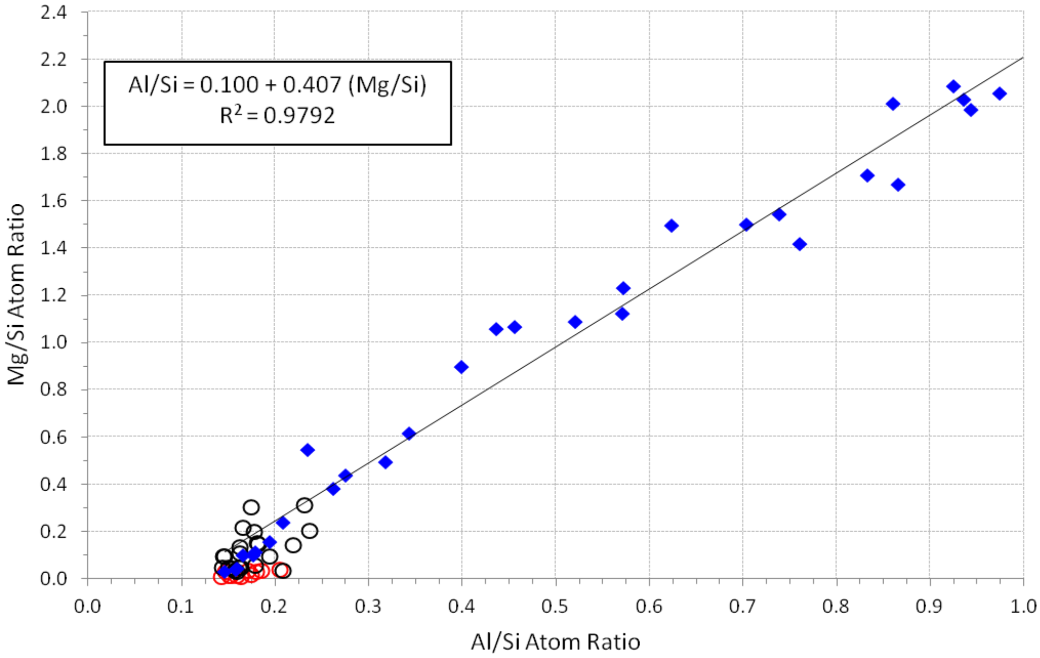

Figure 7-16: Mg/Si against Al/Si atom ratio plots of TEM EDX analyses of fine C-S-H (○), Op C-S-H (○) and Slag Ip Product (◆)

As previously mentioned the hydrotalcite-LDH phase was investigated by TEM-EDX with particular interest to its magnesium content, this was compared to the same phase in similar matrices both in this study and in the published literature. The Mg/Si against Al/Si scatter plot for the sample is shown in figure 7-16; the plot illustrates that the hydrated slag Ip consists of Al substituted C-S-H intermixed with varying amounts of the hydrotalcite LDH phase. The base Al/Si of the slag Ip is given by the best fit line when the Mg/Si = 0 (0.10) and is shown in table 7-1. The value of 0.10 agrees closely with the reported Al/Si content (0.101) for a similar aged paste containing 75% slag by Taylor et al [52] using TEM-EDX regression analysis. The gradient of the calculated linear regression line displayed in figure 7-16 is the relevant Mg/Al ratio for that phase (2.44) calculated from the Mg/Si and Al/Si data points. This value is near identical to the observed Mg/Al ratio of the HT phase in the $BaCO_3$ containing system (2.45) in chapter 5 and similar to the Mg/Al ratio found in chapter 6 (2.28). The reported Mg/Al ratio for the intermixed hydrotalcite phase is also in agreement with the results given by Richardson and Groves for a slag cement [51]. This indicates that the relevant Mg/Al of the hydrotalcite LDH phase found in this system has not had its magnesium content significantly altered when compared to other high - replacement systems. This is at odds with the study by Collier et al [84] who suggest the hydrotalcite phase is likely to be influenced by the quantity of Mg^{2+} and OH^{-} ions present in a similar $Mg(OH)_2$ - containing system.

		Ca/Si		Ca/(Al+Si)		Al/Si	
	N❖	Mean	SD	Mean	SD	Mean	SD
Fine C-S-H	11	1.21	0.04	1.04	0.03	0.17	0.02
Slag Ip C-S-H	33	1.20	0.03			0.10	
Op C-S-H	30	1.24	0.10	1.05	0.08	0.18	0.03

* Slag Ip Al/Si ratio calculated from regression analysis (Figure 7-16) when Mg/Si = 0

❖N = Number of EDX analysis

Table 7-1: Mean atomic ratios for C-S-H phases in the 3:1 BFS:OPC + $MgOH_2$ cement paste obtained using TEM-EDX

7.5.1 Nanostructural model for C-S-H

The applicability of the TEM-EDX data has been discussed in relation to the tobermorite-jennite (T/J) and tobermorite - 'solid solution' calcium hydroxide (T/CH) approaches for the nanostructure of C-S-H reported by Richardson and Groves [26, 175, 239]. The Si/Ca against Al/Ca plots which are displayed in figure 7-17 and 7-18 show the experimental TEM-EDX and the theoretical structural plots as discussed in previous chapters.

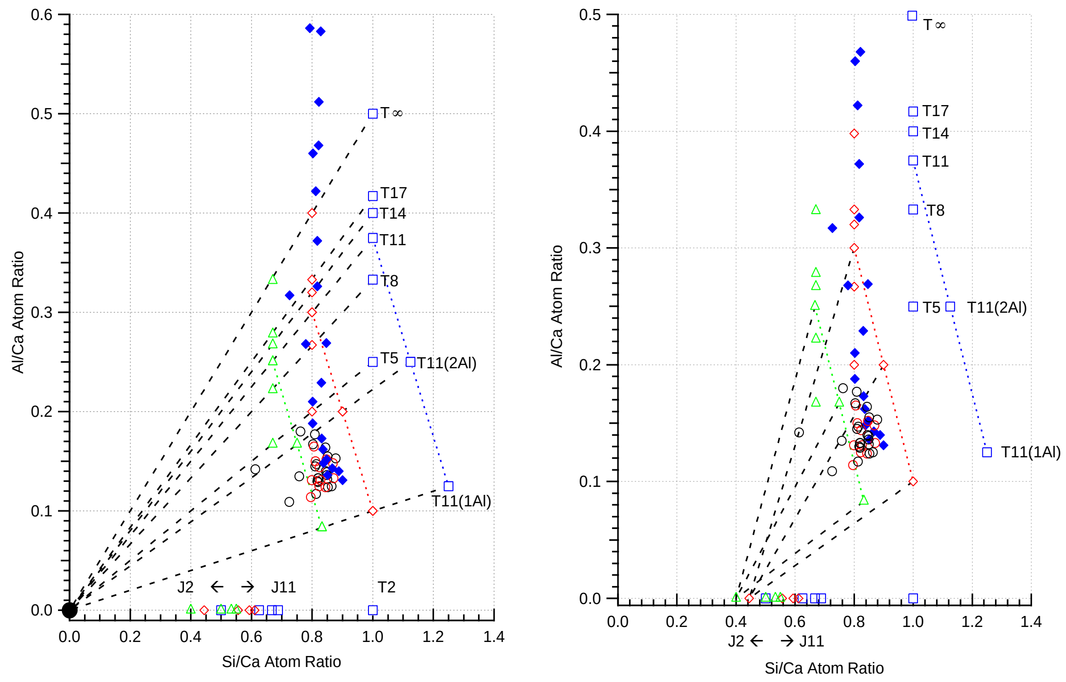

Figure 7-17: Si/Ca against Al/Ca atom ratio plot of TEM-EDX analyses of Fine (○), Op (○) and slag Ip (◆) C-S-H present in BFS:OPC + $MgOH_2$ sample. The additional symbols represent the compositions of tobermorite (T) and jennite (J) based structural units with different levels of protonation of the silicate chains: the minimum (△; w/n=0), intermediate (◇; w/n=1) and maximum (□; w/n=2). The additional points included represent tobermorite- based units with chain lengths of 2, 5, 8, 11, 14, 17 and ∞. All units are assumed to be saturated with Al where possible. (ie all the occupied bridging sites are occupied by Al rather than Si). The only

exception is for units with 11 tetrahedral chain length, as additionally to those saturated with Al (T11) those with only one or two of the three possible bridging sites are also shown labelled as (T11(1Al) and (T11(2Al) respectively. The black dashed lines join points for structural units of the same chain length but different degrees of protonation to CH on the left and to Jennite based dimer of the same protonation on the right. T11 units with the same protonation but differing Al content are joined by coloured dashed lines.

Examination of the TEM-EDX experimental data in figure 7-17 shows that both the T/CH and T/J structural models can account for the majority of data points for the $Mg(OH)_2$ containing paste. The T/CH model trend lines in figure 7-17 indicate that the level of Al incorporation is below that of fully substituted T5 and T8 structures when examining both the fine and Op C-S-H. As the T/CH model with longer chain lengths have been shown in previous chapters to be the most suitable for aged slag - based cements the T/CH model was replotted (figure 7-18) for more appropriate units. The trend lines in figure 7-18 indicate that in agreement with previous chapters, the most appropriate structural units lie around T11 to T17 at minimum to intermediate degrees of protonation with varying levels of partial Al substitution to account for the observed Al/Ca ratios. The more appropriate units are plotted in table 7-2 and lie between the similar trend lines as for the high - slag replacement cements previously discussed in chapters 5 and 6.

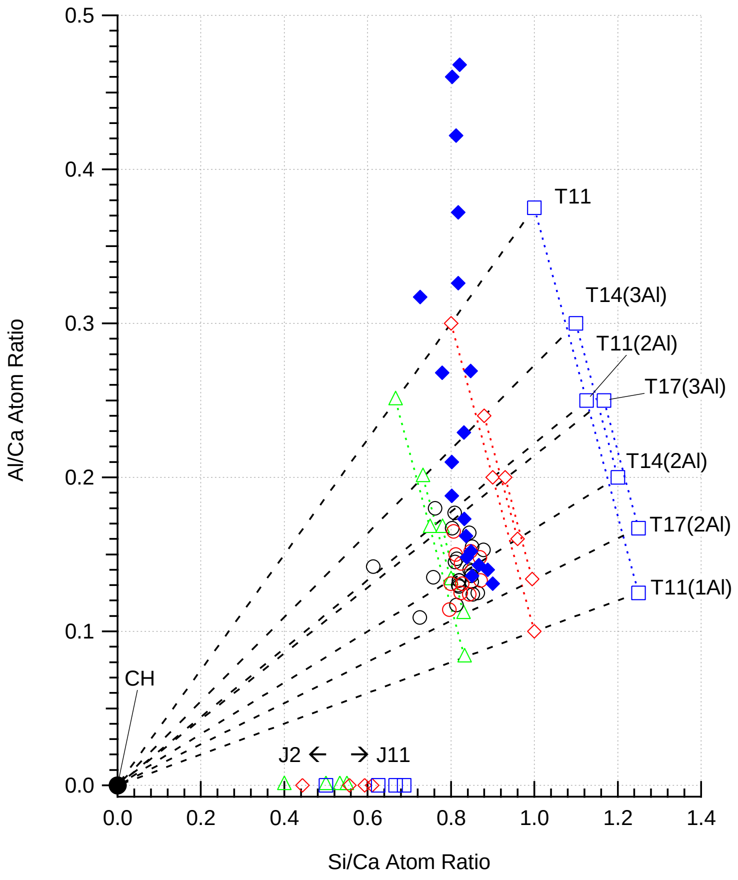

Figure 7-18: As Fig 7- except additional points included represent tobermorite- based units with chain lengths of 11, 14, and 17 with varying saturations of Al. Points were chosen to relate to the compositional data for the BFS:OPC + $BaCO_3$ sample. Fine (○), Op (○) and intermixed slag Ip (◆) C-S-H.

Structural Unit	Degree of protonation	Si/Ca	Al/Ca	B (%)*
T14 (2Al)	Minimum w/n=0	0.800	0.133	50
T14 (2Al)	Intermediate w/n=1	0.960	0.160	50
T17 (2Al)	Minimum w/n=0	0.830	0.111	40
T17 (3Al)	Minimum w/n=0	0.780	0.167	60
T17 (3Al)	Intermediate w/n=1	0.930	0.200	60

* B(%) Bridging tetrahedra occupied by Al/ bridging tetrahedra occupied by Al and Si

Table 7-2: Selected appropriate T-like structural units for the 3:1 BFS:OPC + $Mg(OH)_2$

Based on previous work within the group, quantitative NMR data is available for this sample as discussed in the following section 7.6 making it possible to analyse the chemical formulae for the C-S-H gel using both the TEM-EDX and NMR data. The modified Richardson and Groves model allowing for the incorporation of substituent's into the C-S-H such as Al^{3+} is shown in equation 7-1.

$$[Ca_{2n}H_w(Si_{1-a}R_a^{[4]})_{(3n-1)}O_{(9n-2)}]I^{c+}_{\frac{a}{c}(3n-1)}\cdot(OH)_{w+n(y-2)}\cdot Ca_{\frac{n.y}{2}}.mH_2O$$

Equation 7-1: Formulation for the nanostructure of C-S-H in the T/J structural model [26]

$R^{[4]}$ is the trivalent cation commonly Al^{3+} in tetrahedral coordination within the C-S-H and I^{c+} is an interlayer ion, either a monovalent cation or Ca^{2+} which charge balances the R^{3+} substitution for Si^{4+}. As discussed in section 4.5.1 the Al only substitutes for Si in the bridging sites leading to the (3n-1) chain length sequence, so if full substitution is assumed then the Ca/Si and aluminosilicate structure are determined by equation 4-2 in chapter 4. Additionally if the charge compensation of the Al^{3+} substitution for Si^{4+} is by the Ca^{2+} ions then equation 4-2 is modified to equation 7-2.

$$Ca/Si = \frac{n(4+y') + a(3n-1)}{2(1-a)(3n-1)}$$

Equation 7-2: Calculation for Ca/Si of a chain length *n* with smaller y due to charge balancing [26]

A full discussion explaining the formation of the model can be found in Richardson [26] which also explains the benefits of the model being measurable by experimental data generated from TEM and NMR data. Richardson and Groves also presented an alternative formulation for the nanostructure of C-S-H in the aforementioned T/CH model rather than the T/J, this is shown in equation 7-3. In the T/CH model *X* is the number of Ca^{2+} ions required for charge balancing and *z* is the number of $Ca(OH)_2$ units which will be in solid-solution.

$$Ca_X H_{(6n-2X)} (Si_{1-a} R_a^{[4]})_{(3n-1)} O_{(9n-2)} I^{c+}_{\frac{a}{c}(3n-1)} . zCa(OH)_2 . mH_2O$$

Equation 7-3: Formulation for the nanostructure of C-S-H in the T/CH viewpoint [26]

The estimated average C-S-H chemical composition according to the T/J structural model (equation 7-1) for the BFS:OPC + $Mg(OH)_2$ is shown below in equation 7-4. The chemical composition inside the square brackets represents the tobermorite-like structure of the C-S-H. As no hydroxyl group is present outside the square bracket in equation 7-4 this indicates that there is a highly reduced or no jennite units present.

$$[Ca_{10.87} H_{2.65} (Si_{0.85} Al_{0.15})_{15.31} O_{46.92}] Ca_{4.11} . mH_2O$$

Equation 7-4: Average structural unit for T/J model for BFS: OPC + $Mg(OH)_2$

Equation 7-5 shows the estimated average structural unit in terms of the T/CH model as described by equation 7-3, in this model no $Ca(OH)_2$ units have to been incorporated to account for the experimental data.

$$[Ca_{14.98} H_{2.65} (Si_{0.85} Al_{0.15})_{15.31} O_{46.92} Ca_{1.11} . mH_2O]$$

Equation 7-5: Average structural unit for T/CH model for BFS: OPC + $Mg(OH)_2$

These average structural units displayed in equations 7-4 and 7-5 are in good agreement with the observed experimental data from the NMR and TEM studies. Figures 7-17 to 7-18 show no indication for the presence of either quantities of jennite or CH within the relevant T/J or T/CH models as seen by the added trend lines.

7.6 NMR

^{29}Si MAS NMR was collected for the sample at Leeds University using the experimental conditions described in chapter 3. The NMR experimental data was then fitted using IGOR pro which was then used in conjunction with the TEM-EDX data as discussed in the previous section to allow approximation of the average structural units present for the C-S-H phase.

Additional solid-state spectra for the BFS:OPC + $Mg(OH)_2$ sample were obtained at the EPSRC UK National Solid-state NMR service at Durham University. This was compared to ^{29}Si MAS NMR collected at Leeds University during this study and previous investigations into BFS:OPC - based pastes.

7.6.1 ^{29}Si MAS NMR

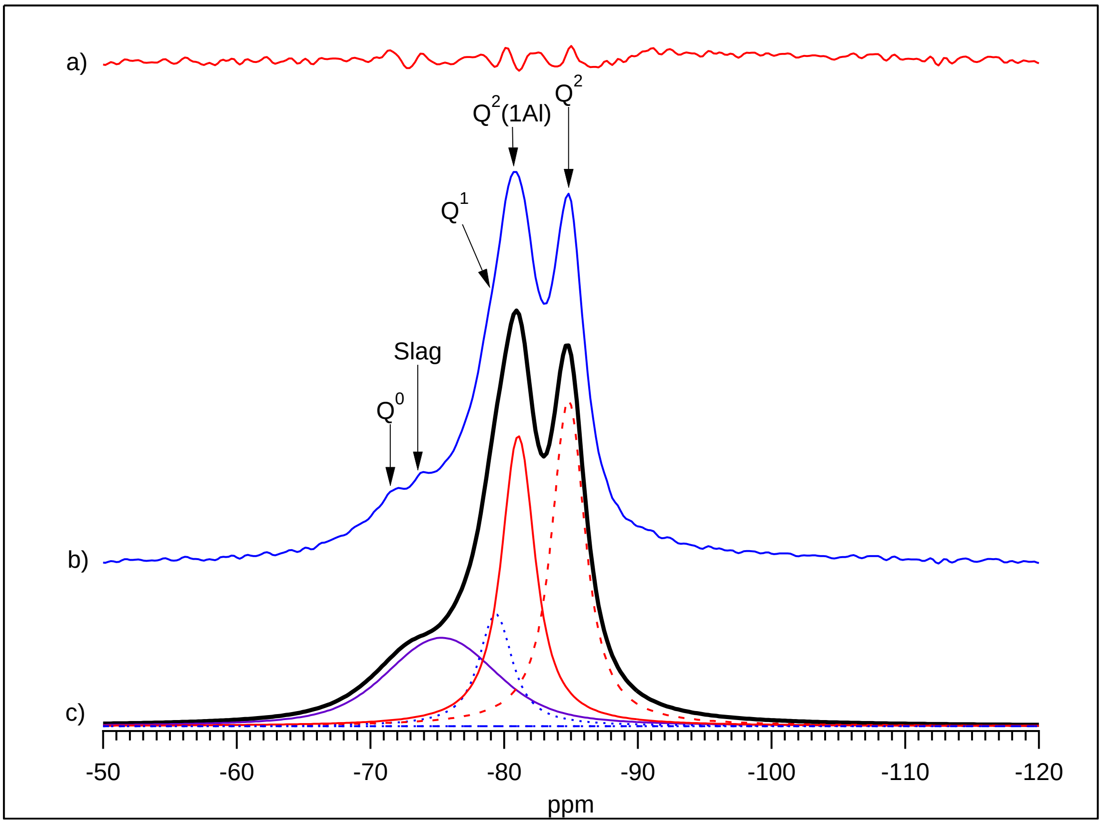

Figure 7-19: ^{29}Si MAS NMR collected at Leeds University showing a) residual trace, b) experimental spectrum, c) fitted spectrum with Q^0 excluded.

The ^{29}Si MAS NMR traces for the BFS:OPC + $Mg(OH)_2$ sample are shown in figures 7-19 and 7-20 for the experimental data collected at Leeds and Durham respectively. Figure 7-19 shows the experimental data spectrum b) and the fitted peaks and resultant spectrum c) as outlined in section 3.4.1. The peaks were fitted for C-S-H using the same peaks discussed in the previous chapters with Q^1, Q^2 and Q^2(1Al) fitted along with anhydrous phases for unreacted belite and slag. The integrated areas of the fitted peaks have then been used to calculate the mean chain length (MCL), Al/Si ratio and estimated percentage of phases within the sample. These were then used to calculate the average structural units in section 7.5.2, the results from this fitting are shown in table 7-3.

MCL	Al/Si	Anh %[#]	Slag Reaction %	B (%)*
15.3	0.17	7.3	58	51

* B(%) Bridging tetrahedra occupied by Al/ bridging tetrahedra occupied by Al and Si

[#] Anh (%) Anhydrous material from cement assumed to be unreacted belite marked Q^0 in figure 7-19

Table 7-3: Results from deconvolution of ^{29}Si NMR spectra for the 3:1 BFS:OPC + $Mg(OH)_2$ sample

This analysis of the NMR spectra indicates the presence of structural units which contain a large quantity of the Q^2 and Q^2(1Al) mid - chain groups which results in a longer mean chain length (MCL) of 15.3. This is observed in the experimental spectrum b) and fitted curves c) with a much larger proportion of these mid-chain groups detected when compared to the end chain groups (Q^1). The percentage of slag reaction was calculated from the level of unhydrated material present minus the known sharp peak for belite. This results is an estimation of around 58% of the slag having reacted, this is in agreement with the published data for an aged high slag replacement cement cured and stored in ambient conditions [52]. The derived MCL and B (%) can be compared to the selected appropriate T-like structural units in table 7-2; the NMR data supports the credence of these units with comparative chain lengths and bridging site occupation.

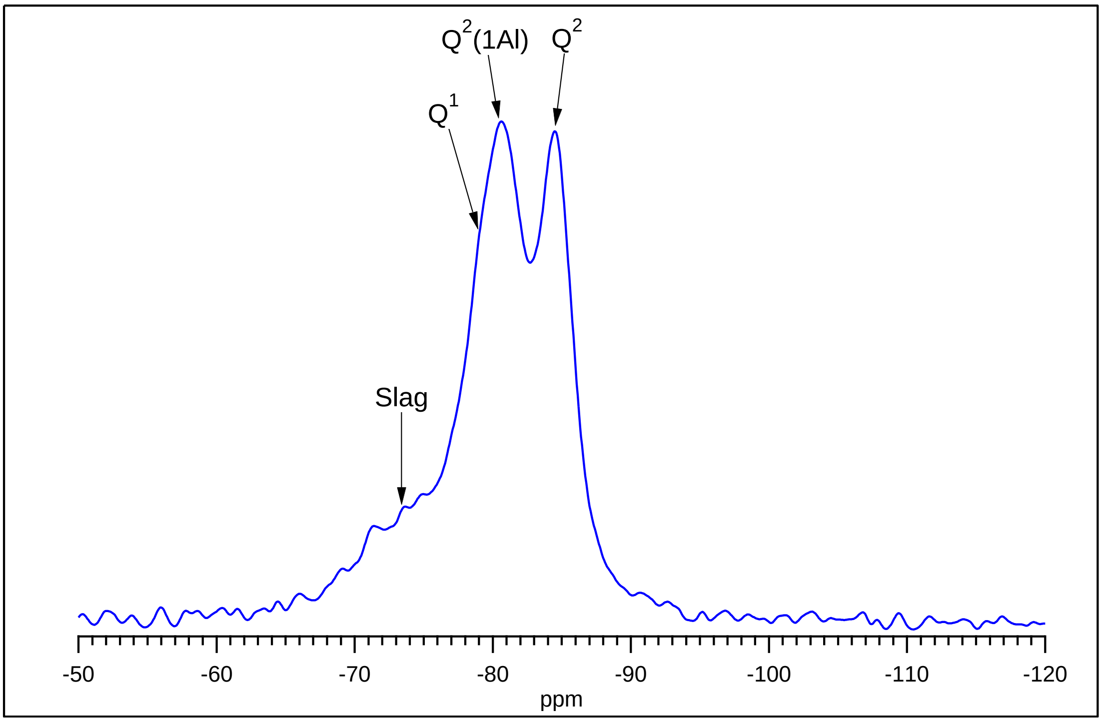

Figure 7-20: ^{29}Si MAS NMR collected at Durham University with peaks labelled

The ^{29}Si NMR spectra collected from Durham has been included for comparison, the experimental data is similar to that collected at Leeds with significant levels of mid-groups (Q^2 and Q^2(1Al)) in comparison to end - members (Q^1). Figure 7-20 also shows a similar presence for large quantities of unreacted slag as indicated in figure 7-19 which agrees with the estimated reported level of unreacted slag. Overall the spectra showed high level of similarity and both support the conclusions from the TEM-EDX experimental data and the nanostructural model for C-S-H.

7.6.2 ^{27}Al MAS NMR

The ^{27}Al MAS NMR spectra for the BFS:OPC + $Mg(OH)_2$ sample is shown in figure 7-21 and has annotated peaks relating to the centerband resonances from tetrahedrally coordinated Al(IV) (40-90 ppm), five-fold Al(V) (20-40 ppm) and resonances in the range for octahedrally coordinated Al (-10-20 ppm) [182, 183, 188].

The broad peak from 65-70 ppm is due to the combination of Al^{3+} which has been incorporated within the C-S-H structure and the unreacted glassy slag [9, 204]. The presence of C-A-S-H via the incorporation of tetrahedrally coordinated Al^{3+} within the bridging sites has been shown from analysis of the TEM-EDX and ^{29}Si MAS NMR. No separate peak for the presence of Al^{3+} within the C-S-H was resolved however due to the large quantities of unreacted slag present in the system and given the broad peak shape this produces this was not an unexpected result. The five-fold Al(V) co-ordinance which is seen in figure 7-21 is attributed to Al^{3+} substituting for Ca^{2+} ions situated in the interlayers of the C-S-H structure [183, 188].

The octahedrally coordinated responses in the region of -10 ppm to 20 ppm originate from the presence of AFt and AFm calcium aluminate hydrate phases [187, 188]. Additionally the response for hydrotalcite LDH phase overlaps the resonance for AFm at 9 ppm [52, 206] so this octahedral peak has been labelled as a combination of the two phases. Figure 7-21 shows the presence of a significant quantity of AFm/hydrotalcite type phase which agrees with the data from both the bulk analysis techniques and electron microscopy imaging and EDX. As discussed previously ^{27}Al NMR does not allow for individual identification of AFm phases due to different AFm's having almost identical chemical shifts [157, 187]. A noticeable resonance was resolved at around 13 ppm which is associated with the presence of the AFt phase. Whilst significant quantities of AFt were not identified in the XRD trace for this sample isn't unusual due to the varying difficulties in characterising this phase, the existence of AFt in small quantities as indicated by ^{27}Al NMR would not be unexpected. The third resonance labelled in this region was for the 'third aluminate hydrate' phase (TAH) at 5 ppm which was been attributed to a nano-structural aluminate phase formed at the surface of the C-S-H [188].

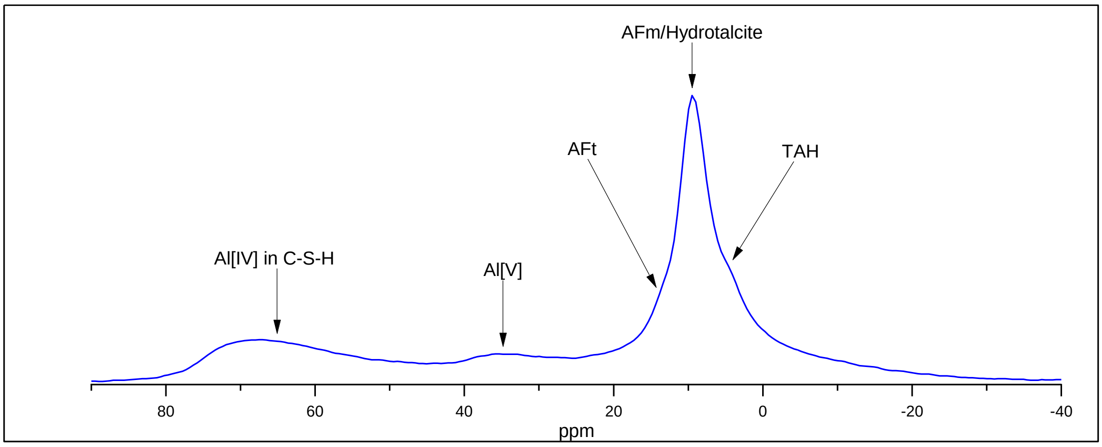

Figure 7-21: ^{27}Al MAS NMR spectra for BFS:OPC + $Mg(OH)_2$ sample, TAH- third aluminate hydrate

7.7 Conclusions

The hardened cement paste with the additional $Mg(OH)_2$ simulant waste showed good physical properties with a proportion of well - reacted slag particles intermixed with formed AFm phases and unreacted brucite. Despite the addition of large quantities of simulant waste material overall porosity and long - term physical durability of the waste-form was good. Potentially this was due to the pre-treatment of the $Mg(OH)_2$ with lime during the mixing process. The effective physical encapsulation of $Mg(OH)_2$ within the binding matrix was confirmed using electron microscopy, particularly in the TEM imaging which showed brucite crystals surrounded by C-S-H.

There was no noticed substitution or incorporation of magnesium into the C-S-H phase after long - term storage. The waste-stream was successfully encapsulated by the hydrating cement material rather than being chemically immobilised within newly forming phases. Whilst a magnesium silicate hydrate which is related to a M-S-H mineral phase has been reported to be possible and coexist alongside the C-S-H phase [240] there was no indication in this work for its formation due to the added magnesium content. The conclusion that the $Mg(OH)_2$ waste-stream had little effect upon the cement grout in the long-term is supported by the TEM-EDX and ^{29}Si MAS NMR evidence. The data indicates a hydrated slag cement with the expected structure of developed chain lengths and levels of Al substitution. This data can be compared to the studies into long - term hydration of slag cements by Taylor et al [52, 53] which exhibit similar results to those presented in this study. Additionally the levels of slag hydration are also very similar in this study to the aforementioned papers suggesting that the long - term hydration of the material is unchanged despite the simulant waste addition.

The formation of a hydrotalcite-like phase (HT) has been confirmed by XRD, TG and EDX analysis of the sample, this phase having previously been suggested as being potentially affected by the inclusion of $Mg(OH)_2$ [84]. TEM analysis has shown quantities of HT in the microstructure of the sample linked to the hydration of slag particles, the analysis did not associate HT formation with the presence of $Mg(OH)_2$ waste sites. Additionally TEM-EDX analysis has shown that the chemical composition of the HT - like phase is unchanged from those reported in the literature [52, 197, 202] and in previous chapters. This has led to the conclusion that the HT phase formed in the samples analysed in these studies is unaffected by the addition of $Mg(OH)_2$. The formation of AFm phases within the cement paste has also been confirmed; the small level of monosulfate (Ms) is consistent with the normal hydration of Portland cements and so is linked to the hydration of OPC not the addition of simulant wastes. The observation of quantities of the monocarbonate AFm phase (Mc) has also been confirmed. The presence of a carbonate ion containing AFm phase within a high replacement slag cement has been reported in literature [52] but in smaller quantities than observed in the BTS:OPC + $Mg(OH)_2$ analysed in this study. The reason for this considerable increase in the AFm Mc phase is unlikely to be directly linked to the addition of $Mg(OH)_2$, as this compound has been shown to be chemically inert within the system and does not contain any constituents for additional Mc formation. As with the previous chapter the pre-treatment process with lime could account for this increase in the AFm phase [227, 228]. The procedure involved mixing with hydrated lime at 10 % wt of the dry waste solids and water for 1 hour prior to the addition of the cement (BFS:OPC) binder. As in the last chapter, it is proposed that this mixing provides a large amount of Ca^{2+} from the dissolution of $Ca(OH)_2$ and a level of CO_3^{2-} ions from the air and the mixing procedure. When the subsequent hydration occurs with the addition of the cement powders the $Mg(OH)_2$ is successfully reacted within the cement matrix due to the pre-mixing with reactive $Ca(OH)_2$; however the $Mg(OH)_2$ does not react to form a new phase due to its relative solubility compared to calcium. The available carbonate ions then react with the aluminates in the hydrating system provided by the dissolution of slag which is encouraged by the additional $Ca(OH)_2$ added during pre-treatment subsequently forming calcium monocarboaluminate.

The fact that no $CaCO_3$ has been detected from STA analysis shows that the majority of monocarboaluminate formation is unlikely to come from mass carbonation of pre-existing phases in the cement. Therefore it has been concluded monocarboaluminate formation occurs during the earlier stages of hydration alongside the dissolution of the slag particles rather than longer term carbonation.

The long-term stability of the wasteform in the presence of normal concrete degradation mechanisms can be discussed. Long - term carbonation of the sample will result in the formation of $CaCO_3$ from consumption of the available $Ca(OH)_2$ or decalcification of the C-S-H [168, 241] rather than the development of $MgCO_3$. This absence of $MgCO_3$ is explained by the solubility of the hydroxide phase for magnesium which is the less soluble than when in its carbonate form as discussed in section 2.4. The potential M-S-H phase formation has also been linked to magnesium sulphate attack on portland cement pastes [242, 243]. This sulphate reaction is not favoured within this system however, again due to the relative solubility's of magnesium and calcium with AFt and $CaSO_4$ which are the more favoured reaction products rather than $MgSO_4$ or M-S-H. Since the stability of the $Mg(OH)_2$ is high, which is the primary potential corrosion product from the treatment of Magnox metal wastes [83, 244]; the major long-term worry is around managing the corrosion reaction. This can be accomplished by control of the physical and chemical composition of the mixing powders and the free water content [82]. The experimental evidence indicates the added

$Mg(OH)_2$ simulant remains physically encapsulated within the cement matrix and does not react to form new phases. Furthermore, due to the relative solubilities of Mg^{2+}, Ca^{2+} and relevant anions such as CO_3^{2-} and SO_4^{2-} it is very unlikely typical cement degradation mechanisms would affect the waste form. Therefore the $Mg(OH)_2$ waste form has a very low risk profile, with the physically encapsulated $Mg(OH)_2$ expected to be stable over extended storage periods.

In conclusion, the successful physical encapsulation of a simulated $Mg(OH)_2$ based waste-stream has been studied after extended hydration. The pre-treatment process has allowed for the incorporation of the $Mg(OH)_2$ in the matrix but potentially has increased the production of quantities of monocarboaluminate (Mc) within the hydrating cement. The long-term stability of Mc however is favourable when compared to other aluminate hydrates and its formation is not directly linked to the magnesium waste. No additional magnesium-based phases were observed in this study with the expected magnesium containing phase hydrotalcite purely associated with the reacted BFS particles rather than the waste-stream. As this study looked at a system involving chemically pure $Mg(OH)_2$ it should be noted in service a waste-stream would likely contain many other additional ions especially after prolonged storage. As discussed in section 2.4.3 studies on magnesium samples from the fuel pond storage facilities have identified a Mg-hydrocarbonate phase linked to artinite alongside brucite and hydrotalcite [80, 81]. Any additional ions may have a much greater potential to substitute into cement phases than the described simulant waste in this chapter.

Chapter 8 : Results and discussion of PFA:OPC + Encapsulation Flocs

8.1 Introduction

Three metal hydroxide flocs used for the treatment of liquids generated during nuclear fuel reprocessing have been studied and the results presented in this chapter. Two of the waste streams are iron-based flocs labelled as Fe floc A (IDM 93-12) and Fe floc B (IDM 91-13), the third floc is an alumino-ferric system labelled as Al floc (IDM 93-001). These flocs are typically encapsulated in a PFA:OPC matrix and all have undergone a level of pre-treatment with $Ca(OH)_2$ as outlined in chapter 3. Considerable work has been completed by both industry and academia on the disposal, pre-treatment and subsequent encapsulation of waste flocs [77, 91, 93, 122] which this study builds on. Additional characterisation of the formed cement phases is required however to fully understand the location of the Fe and Al wastes in service. Suggestions of sorption and substitution of iron onto the C-S-H have been reported and current assumptions are that flocs are primarily physically encapsulated in the cement matrices rather than chemically immobilised [77, 122, 245]. The following chapter will investigate the formed cement phases and attempt to further current knowledge into the potential levels of immobilisation and long-term stability offered by these systems.

8.2 XRD

The major detected crystalline phase for all of the encapsulated floc samples was the presence of large quantities of a hydrogarnet phase which can be of a variable composition. Initial XRD analysis matched the observed hydrogarnet in the iron-based flocs (Sample ID's 92-13 and 91-13) to a heavily Fe-substituted siliceous katoite of the general chemical composition $C_3(A,F)SH_4$ from the ICDD database (Ref code 00-032-0147) which was proposed by Collier et al [91]. That study reported an iron-substituted silicated katoite as the main crystalline phase in work on laboratory prepared pre-treated floc samples in OPC:PFA matrices. The presence of large quantities of hydrogarnet is unusual in ambient cured traditional cement systems with hydrogarnet forming normally only as a minor phase [235]. The presence of a hydrogarnet was also observed in the Al-floc sample with the closest match being an Al-based siliceous katoite of the general chemical composition C_3ASH_4. However it seems the formation of hydrogarnets is greatly encouraged by several factors including the increased availability of iron as described by Collier et al [91, 93], the increased aluminium in CAC cements [246] and elevated temperature curing [172, 189, 247, 248]. This wide range of potential compositions for the hydrogarnet phase with varying possible levels of Fe and Si incorporation is discussed in more detail in section 8.2.1. The main crystalline phases not related to the formation of hydrogarnet were quartz (SiO_2) and mullite ($Al_6Si_2O_{13}$) present from the mass addition of PFA and levels of calcite. Additional cement hydrate phases observed included the AFm phase monocarboaluminate, weak responses for AFt and for the Al-floc sample small levels of strätlingite. The formation of strätlingite potentially indicates the chemical effect of the Al-floc addition as the Fe-floc samples did not display any evidence of this phase. No evidence was found for the continued presence of CH after this long storage period suggesting the full consumption of the available CH via a pozzolanic reaction [70, 249]. The only additional peak was a weak reflection for the presence of hematite at seemingly very small levels which can be attributed to PFA.

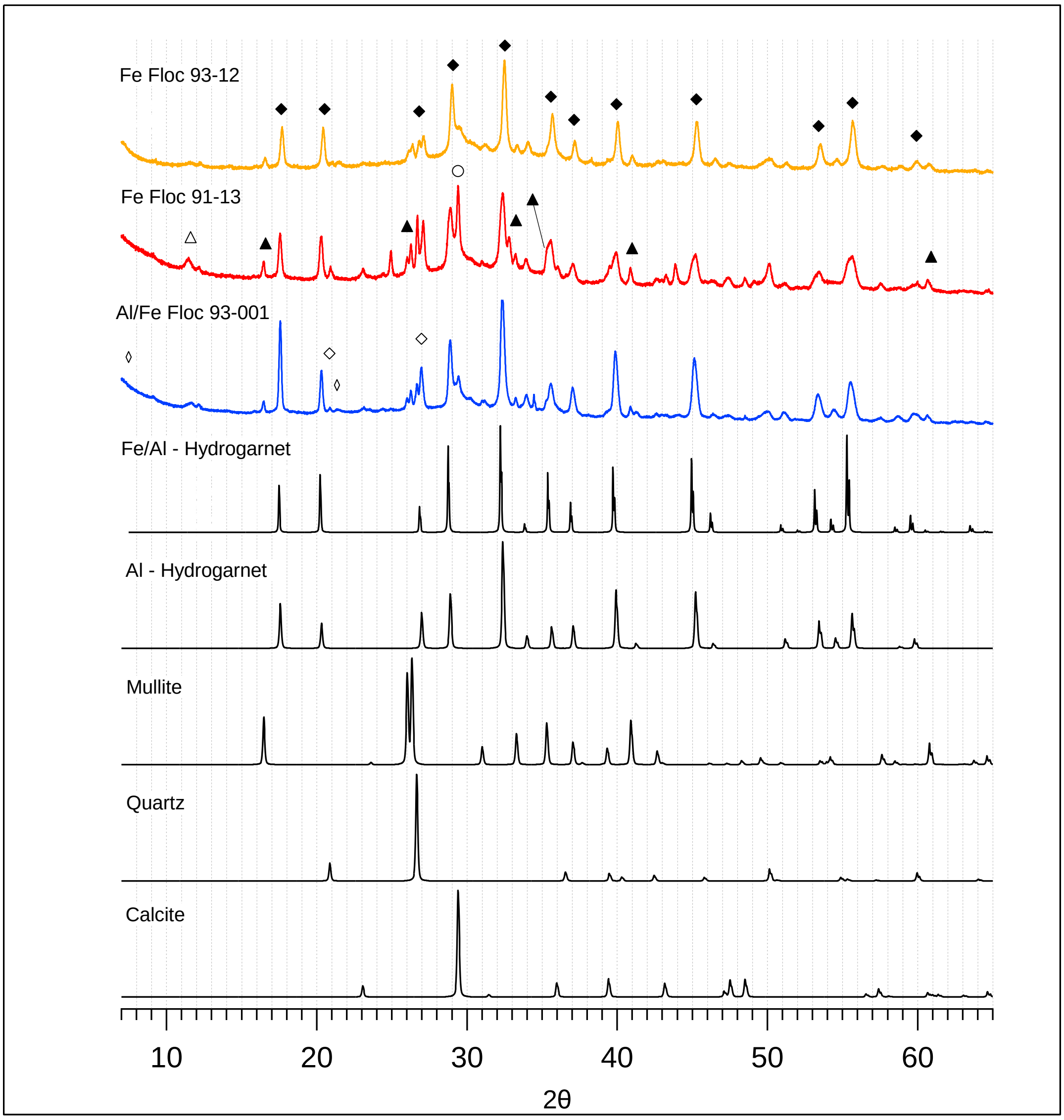

Figure 8-1: XRD plots for the 3 floc samples with simulated patterns for relevant phases; ◆ - Hydrogarnet, ▲-Mullite, △- AFm, ◇- Quartz, ○- Calcite, ◊- Strätlingite

8.2.1 Introduction to Hydrogarnet Analysis

Due to the prevalence of a formed hydrogarnet phase in the experimental XRD (figure 8-1) and in literature, additional analysis of this data was undertaken. This was seen as important due to the correlated formation of the hydrogarnet with the encapsulated waste floc and its potential to include Fe and Al ions within its structure.

The analysis first calculated the unit cell parameter (a) of the observed hydrogarnet phases to ascertain its classification within the nomenclature of hydrogarnet minerals. This was compared with previous reported literature into cement formed hydrogarnets and used to substantiate its probable silicon and Al/Fe content. Additional analysis was also completed on line broadening associated with the hydrogarnet peaks in an attempt to establish the estimated particle size of the crystalline phase. This was expanded into discussions on additional factors such as lattice strain which could affect the XRD results.

8.2.2 Estimation of Hydrogarnet Composition

Hydrogarnet (HG) phases are known to crystallise in various cubic forms, of which at normal temperatures icositetetrahedra are seen as the most usual with the space group Ia3d [235]. Garnet cubic minerals consist of an octahedral and tetrahedral 3D framework joined to each other by common oxygen atom corners, SiO_4 occupy the tetrahedral sites whilst octahedral sites are normally occupied by a trivalent cation such as Al^{3+} or Fe^{3+} [250] As discussed by Dilnesa et al [159] the reported general formula for the formation of an aluminium/iron siliceous hydrogarnet was $(Ca_3(Al_xFe_{1-x})_2(SiO_4)_y(OH)_{4(3-y)}$. The mechanism of incorporation of $(OH)^-$ groups via the substitution of SiO_4 tetrahedra with (OH) in the garnet group has been well recognised and reported in the literature by several authors investigating differing possible compositions [251-256].

The nomenclature of the minerals that make up the hydrogarnet group as recommended by Passaglia and Rinaldi [257] is shown in figure 8-2. As can be seen, members of the garnet group with a substitution of the SiO_4 tetrahedra by $(OH)^-$ groups less than 50% and with x within the range of $0 < x < 1.5$ for the structural formula $C_3AS_{(3-x)}H_{2x}$ are classed as Hibschite [250]. Members with a substitution greater than 50% will be classified as Katoite with x in the range $1.5 < x < 3.0$, within this nomenclature the substitution of Al by Fe can take place which again affects the classification of the garnet as shown in figure 8-2.

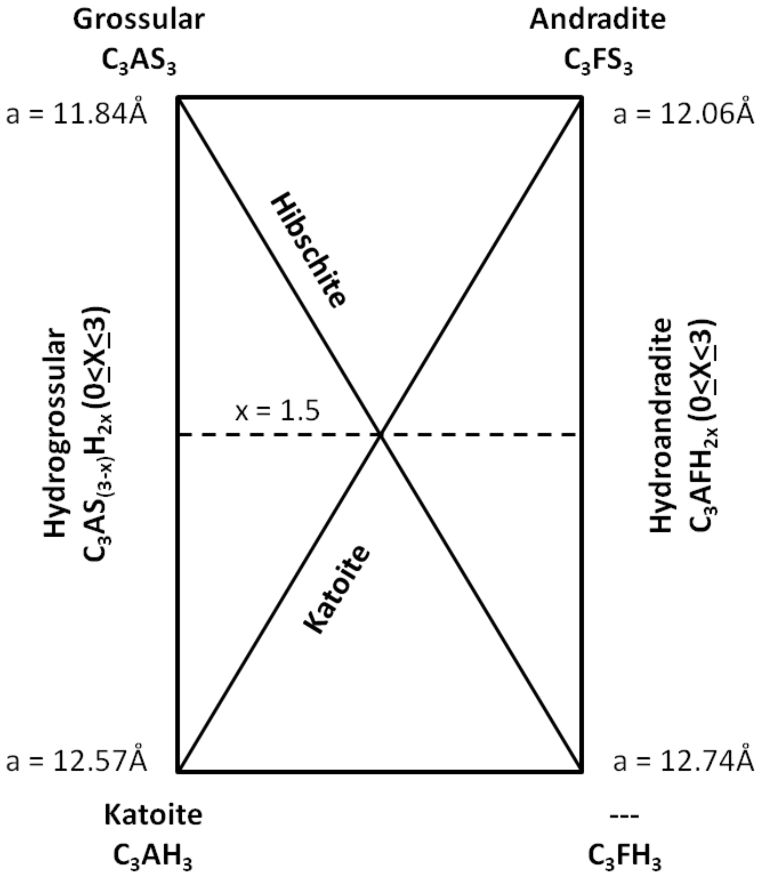

Figure 8-2: Nomenclature of minerals of the hydrogarnet group recommended by Passaglia and Rinaldi [257] reproduced from Pertlik [250] with cement chemistry notation added.

In figure 8-3 the unit cells for hydrogarnets from the crystal databases (ICSD and ICDD) were classified into two distinct groups for those with and without substituted Fe in the Al octahedral sites. The two groups therefore form a grossular - hydrogrossular - katoite link and a andradite - hydroandradite - C_3FH_6 link which are shown with best fit lines in figure 8-3 assuming a linear relationship, the equations and R^2 values for these lines were as follows:

$$a = 12.561 - 0.236(3 - x) \qquad R^2 = 0.9917$$

Equation 8-1: Equation for the $C_3AS_{(3-x)}H_{2x}$ Fe free hydrogarnets plotted in figure 8-3

$$a = 12.719 - 0.227(3 - x) \qquad R^2 = 0.9848$$

Equation 8-2: Equation for the $C_3FS_{(3-x)}H_{2x}$ Fe containing hydrogarnets plotted in figure 8-3

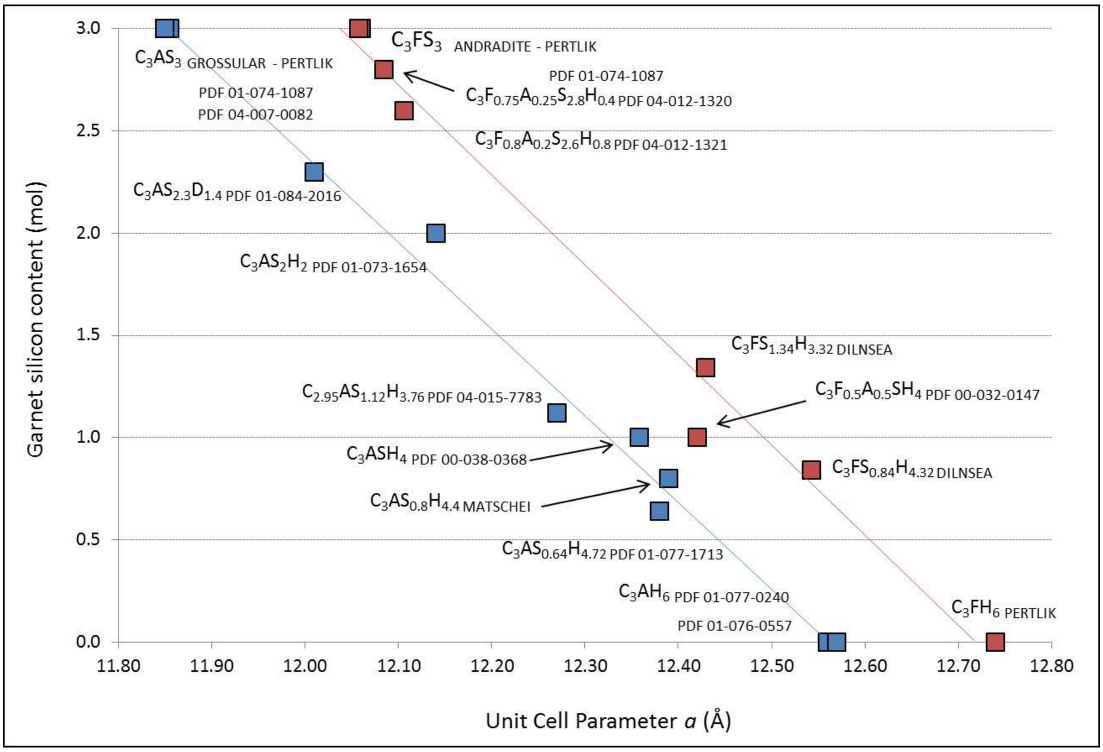

Figure 8-3: Silicon content against reported unit cell parameter for hydrogarnets, data points with associated PDF numbers are Powder Diffraction Files obtained from the ICSD or ICDD databases. Hydrogarnets with only Al contained are in blue, Fe substituted hydrogarnets are shown in red.

The structures used to produce figure 8-3 and referenced later in this section are shown in table 8-1, and these are classified into the categories described in figure 8-2 by Pertlik [250] for the minerals of the hydrogarnet group and their basic compositions are also shown.

Phase	Composition	PDF Number	Reference
Grossular	C_3AS_3	04-007-0082	Sawada et al [258]
		01-074-1087	Prandal et al [259]
		01-084-1349	Lager et al [260]
Hydrogrossular	$C_3AS_{2.6}D_{1.4}$	01-084-2016	Lager et al [261]
	$C_3AS_2H_2$	01-073-1654	Pabst et al [262]
	$C_{2.95}AS_{1.12}H_{3.76}$	04-015-7789	Ferro et al [263]
	$C_3AS_{1.0}H_4$	00-038-0368	Passaglia et al [257]
	$C_3AS_{0.8}H_{4.4}$		Matschei et al [154]
	$C_3AS_{0.64}H_{4.72}$	01-077-1713	Sacerdoti et al [254]
Katoite	C_3AH_6	01-077-0240	Flint et al [264]
		01-076-0557	Cohen-Addad et al [251]
Andradite	C_3FS_3	01-075-8633	Quartieri et al [265]
			Pertlik [250]
Hydroandradite	$C_3F_{0.75}A_{0.25}S_{2.8}H_{0.4}$	04-012-1320	Lager et al [261]
	$C_3F_{0.80}A_{0.20}S_{2.6}H_{0.6}$	04-012-1321	Lager et al [261]
	$C_3FS_{1.34}H_{3.32}$		Dilnesa et al [159]
	$C_3FS_{0.84}H_{4.32}$		Dilnesa et al [159]
	$C_3F_{0.5}A_{0.5}SH_4$	00-032-0147	Taylor [266]
	C_3FH_6		Pertilik [250]

Table 8-1: Structures used for the estimation of unit cell parameters for hydrogarnets

Using comparison with the experimental hydrogarnet data and published possible quadratic forms of Miller indices for a cubic crystal structure the measured hydrogarnet peaks for the samples were labelled with their relevant *hkl* values. The unit cell parameter *a* can then be calculated for the hydrogarnet phase in each sample using Braggs Law and the *hkl* values and their relevant 2θ positions. For a cubic crystal the unit cell (*a)* is related to the spacing d of any particular set of planes by the following expression [129, 267].

$$a = d\sqrt{n}$$

Equation 8-3

where n is given as:

$$n = h^2 + k^2 + l^2$$

Equation 8-4

Using the above, estimated unit cell parameters for the hydrogarnet phase in the floc samples was calculated and the results summarised in table 8-2.

Sample	*hkl*	2θ	*n*	*d*	*a* (nm)
Fe Floc A *93-12*	211	17.67	6	5.0193	1.2295
	420	32.52	20	2.7533	1.2313
	521	40.05	30	2.2513	1.2331
	642	**55.67**	**56**	**1.6510**	**1.2335**
Fe Floc B *91-13*	211	17.56	6	5.0505	1.2371
	420	32.38	20	2.7649	1.2365
	521	39.92	30	2.2583	1.2369
	642	**55.63**	**56**	**1.6521**	**1.2363**
Al Floc *93-001*	211	17.58	6	5.0477	1.2364
	420	32.34	20	2.7682	1.2380
	521	39.88	30	2.2611	1.2385
	642	**55.53**	**56**	**1.6557**	**1.2390**

Table 8-2: Summary of values and calculated unit cell parameters

The selected λ value was for CuKα mean (1.541838 units) as examination of the XRD traces at higher angles showed that the two CuKα_{1-2} peaks were unresolved. Precision in the values of *d* and therefore *a* will depend upon the precision of sin θ, the value of sin θ will contain a fractional error which is known to increase at lower angles. The fractional error contained in *a* increases as the value of θ approaches zero, the contained error therefore will reduce as θ approaches 90˚ or as 2θ approaches 180˚. The key to true precise measurements therefore lies in the use of back reflected beams having 2θ values as near to 180˚ as possible [267]. As can be seen in table 8-2 the estimated values for *a* range depending upon the 2θ position, for example for Fe floc A the value changes from 12.295 at a low angle to 12.335 at the highest clearly observed angle which reflects the varying precision of measurements. Table 8-2 shows the observed unit cell parameter *a* varies less as the incidence angle 2θ increases, due to this the higher values of θ were utilised to reduce the level of fractional error contained within the estimation.

The estimated particle or crystalline size for the observed HG responses in the XRD data can be found by using the following Scherrer equation:

$$\beta_c = \frac{0.9\ \lambda}{D\ cos\theta}$$

Equation 8-5: Calculation for line broadening in XRD

Where β_c = FWHM (full width at half maximum) of the broadened diffraction line expressed in radians, 0.9 is the shape factor and D is the estimated particle size of the crystalline phase [267]. The method for finding β_c is shown in figure 8-4 and the results of the calculation using a CuKα mean value of λ=1.5418 for the (611) and (642) indices are expressed in table 8-3.

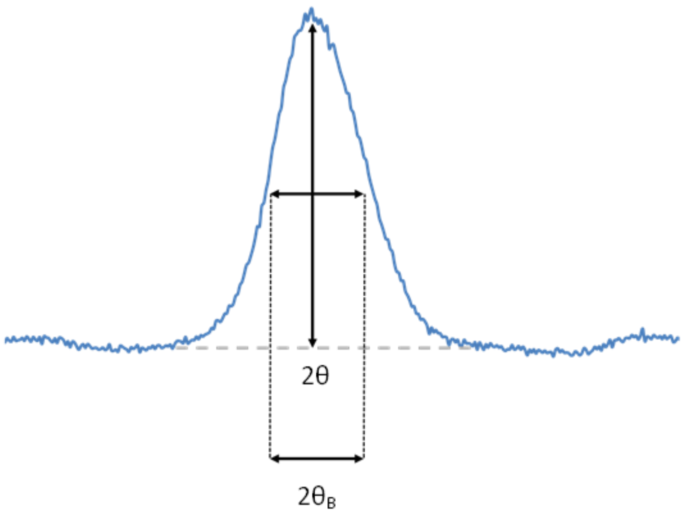

Figure 8-4: Estimation of $2θ_B$ at FWHM for line broadening calculation

Sample	*hkl*	$2θ_B$	Radians	Cos $θ_B$	$D=\frac{0.9\,λ}{\beta_c \cos θ}$ (nm)
Fe Floc A	611	0.345	0.00602	0.9228	25.0
93-12	642	0.404	0.00705	0.8842	22.3
Fe Floc B	611	0.494	0.00862	0.9233	17.4
91-13	642	0.750	0.01309	0.8850	12.0
Al Floc	611	0.402	0.00702	0.9234	21.4
93-001	642	0.519	0.00906	0.8847	17.3

Table 8-3: Estimations of particle size from XRD peak line broadening

The estimated particle sizes found using the line broadening technique are relatively smaller than those reported by Kyritsis et al [268] for synthetically-formed hydrogarnets (with an approximate size of 500nm). Estimation of the crystal particle sizes from observation in the TEM, discussed in detail later in section 8.5 showed a potential size in the order of 100-500nm in this study; both of these therefore suggest a potential underestimation in crystal sizes by the line broadening technique. The limitations of crystal size estimations by direct observation in the TEM should be recognised; firstly the guarantee that single crystal formations were being observed cannot be made. Due to difficulties in analysing suitable stable examples of the HG phase no SAED patterns were obtained for direct comparison to the XRD data. Additionally the small sample size in this study should be considered, for a degree of confidence a greatly increased number of direct observations would need to be made for an accurate consideration of crystal size. Cullity and Stock [267] explained that the difficulties in measuring crystal sizes by line broadening increased with the relative size of the measured crystals, especially when in the range over 500Å (50nm), however the use of equation 8-5 for powder samples should be applicable. Additionally it is well known that the Scherrer's equation provides only the lower boundary to the crystallite size [269, 270]. Due to this the crystallite size value calculated from Scherrer's equation is compared to values obtained from a Williamson-Hall method (W-H) below.

It is recognised that the estimations of crystal size for the hydrogarnets from XRD peak broadening was completed using the α_{mean} values for Cu radiation, as the peaks for α_1 and $\alpha_2$were unresolved. Whilst this approach was estimated to have little to no effect upon the peak positions it could potentially overestimate the peak broadening, leading to incorrect conclusions from the FWHM measurements for crystal size. To ascertain the possible effect of this FWHM estimations were also completed using peak shape assignment estimations in X'Pert Highscore and manual graphical fitting as demonstrated in appendix A. These basic fitting procedures allowed for the particle size estimation from what was fitted as only the α_1 peak; the results for the [611] and [642] peaks indicated a slightly increased crystal size, however the evidence for a level of broadening beyond that from crystal size and instrumental effect remained. Due to this an estimation of potential peak broadening due to microstrain was completed using the original data used in table 8-3; the following section is intended to provide an indication of possible strain broadening effects rather than provide a definite empirical value for strain.

In XRD analysis the line broadening present in the spectrum due to both the crystallite size and additionally the lattice strain can be calculated, the broadening due to crystallite size (β_c) by the Scherrer's equation has been discussed and presents a minimum possible value. It's underestimation of the crystallite size compared to TEM evidence suggests broadening due to lattice strain (β_e) should be considered as represented below:

$$\beta_e = 4e\ tan\theta$$

The Williamson-Hall method [271] of estimating strain-induced line broadening doesn't follow a 1/cosθ dependency as in the Scherrer equation but varies with tanθ, this allows for a separation of reflection broadening when both microstructural causes (crystallite size and microstrain) occur together [272]. The total broadening is therefore a sum of these two contributions in addition to the possible instrumental broadening (β_0), the total broadening (β_t) can be described by:

$$\beta_t = \left(\frac{K\lambda}{D\ cos\theta}\right) + (4e\ tan\theta) + \beta_0$$

Rearranging the above equation with respect to *K* gives:

$$\frac{\beta\ cos\theta}{\lambda} = \frac{1}{D} + \frac{4e\ sin\theta}{\lambda}$$

Where λ is the wavelength of CuKα radiation used, θ is the Bragg angle and e is the strain measured, from the above equation a plot of $(\beta\ cos\theta/\lambda)$ against $(2\ sin\theta/\lambda)$ can be plotted as line of best fit for the measured Bragg angles where the slope = $2e$ and the intercept = $1/D$. In the W-H plot therefore the estimated crystallite size is given by the intercept of the linear fitted line and the strain present in the material by the gradient [269]. If the data from the W-H plot representing different orders of the same reflection is horizontal then there is either no measurable strain or the crystallite size broadening is overwhelmingly larger than the strain-induced broadening [273]. The resultant calculations for the hydrogarnet samples are shown below in figure 8-5 with the underlying data points included in appendix A, the plots clearly show that all the hydrogarnet samples have strong indications for the presence of significant microstrain broadening. The estimated crystallite sizes from the W-H method are also greatly increased from that of the Scherrer equation with a maximum size for the hydrogarnet calculated at 420nm. The strain calculations from the gradients in figure 8-5 showed a range of measured strain of 0.23 to 0.53% within the hydrogarnet phase.

As mentioned previously the calculations used data from the α_{mean} rather than a preferable monochromatic α_1 source; due to this the estimation of strain shown in figure 8-5 could be overestimated as the FWHM value has been increased. To estimate this possible effect manual fitting of the [642] and [611] was completed, additionally the technique was completed for non-HG peak (mullite) which presented more resolved α_1 and α_2 peaks. The results for the α_1 estimated peaks indicated that a level of potential strain remained for the HG phase, supporting the hypothesis that microstrain is involved in the peak broadening displayed by the HG phase in the floc samples. The analysis of potential strain in the mullite data resulted in a W-H plot with no noticeable gradient presented; this shows the strain had no broadening effects on this phase which accounted for its reduced broadening. This 'control' study supports the theory that the hydrogarnet phase contains peak broadening effects beyond that provided by instrumental, procedural or crystal size sources. The potential sources of microstrain in the hydrogarnets to account for the additional observed peak broadening can be theorised. Firstly the large scale substitution of elements into the lattice structure may cause additional levels of strain; additionally small local changes in chemistry could also result in increased lattice strain. An added theory could be made for crystal imperfections being common within the formed hydrogarnet which will could create further potential for strain in this phase.

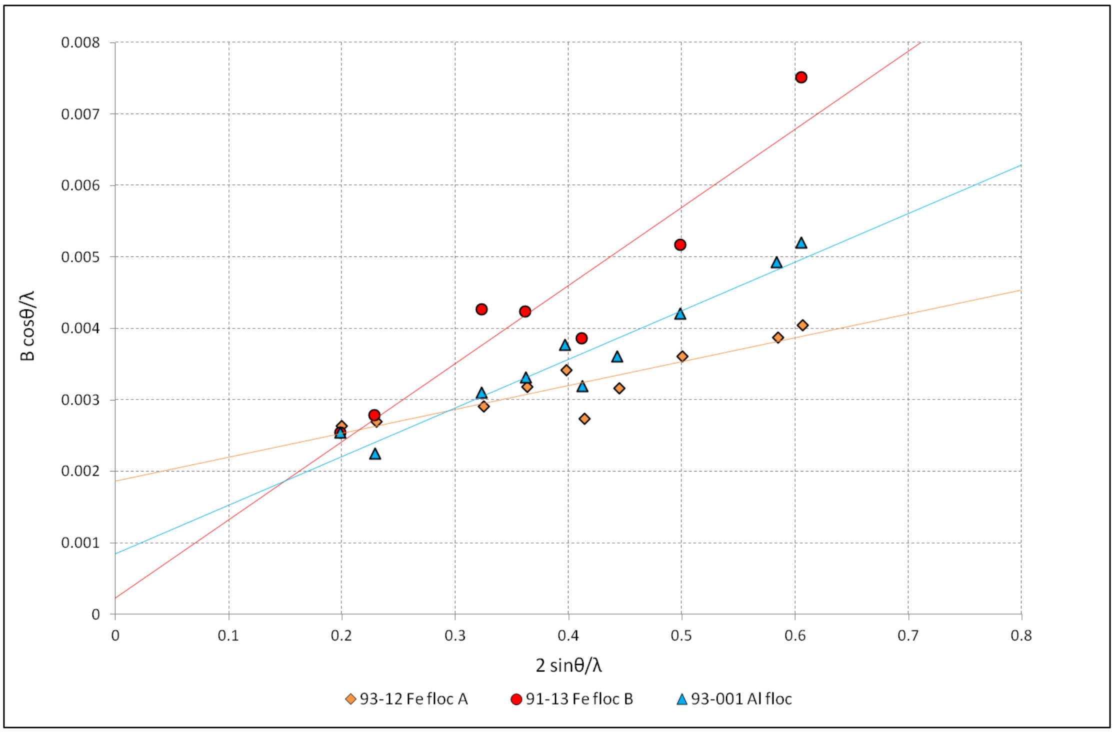

Figure 8-5: Williamson-Hall plot for the 3 floc samples indicating potential microstrain

The presence of a miscibility gap has been reported by several authors investigating the thermodynamic stability and composition of hydrogarnets [159, 268, 274, 275]. When there is complete solid solubility at higher temperatures which breaks into two stable solutions at lower temperature this situation is called a miscibility gap. A necessary condition for the formation of a miscibility gap in the solid state is that both components should crystallize in the same lattice form. With increasing temperature then the proportion of the two phases decreases until the single solid solution is more stable. The work of Dilnesa et al [159, 276, 277] suggests that this temperature must be greater than 110˚C although some slightly lower temperatures have been reported by previous authors, the miscibility gap described is displayed graphically in figure 8-6.

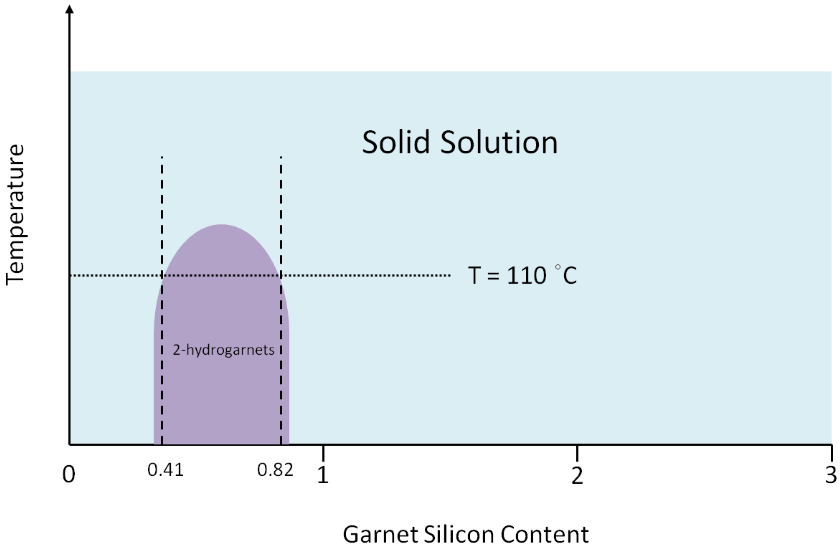

Figure 8-6: Diagram representing the miscibility gap present for hydrogarnets discussed by Dilnesa et al [159, 277]

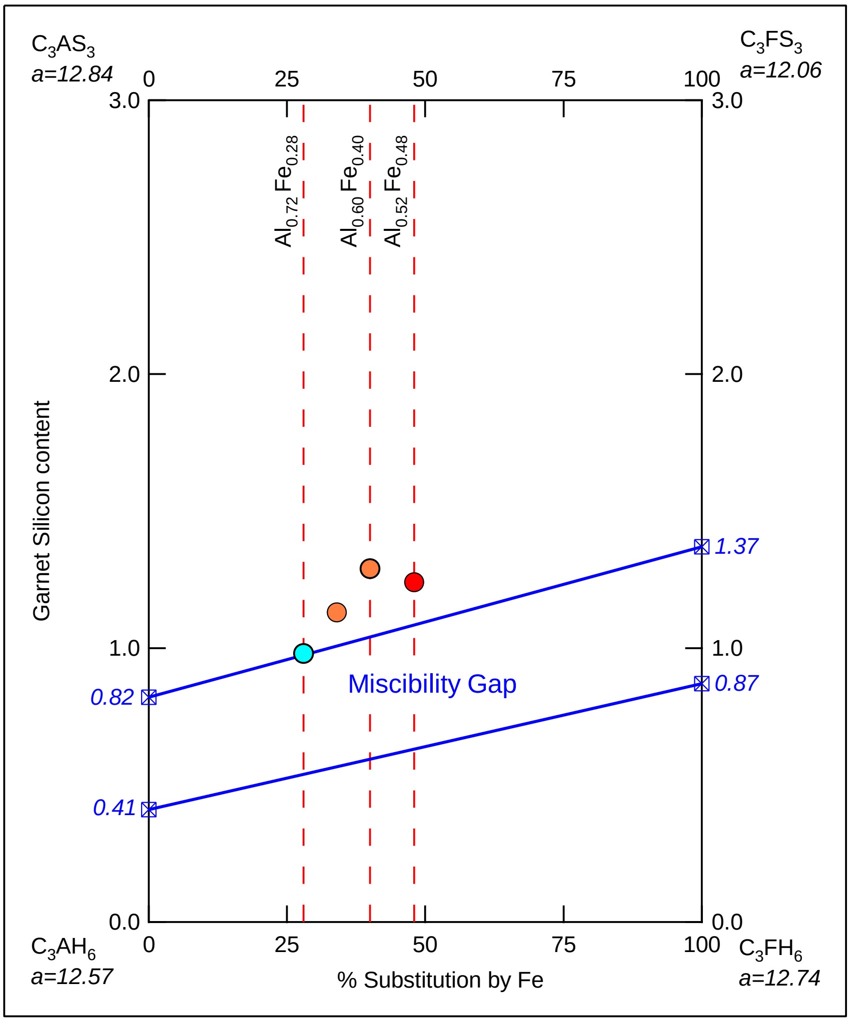

Figure 8-7: Estimated hydrogarnet compositions showing calculated miscibility gap present in the garnet group, ● - Al floc HG (93 001), ● - Fe floc A HG (93-12), ● - Fe floc B HG (91-13). Fe/Al data comes from TEM-EDX analysis.

The estimated composition of the hydrogarnet phases can be determined using the calculated unit cell parameters when the dilation due to Fe^{3+} substituting for Al^{3+} is known along with the relative percentage of substitution in each sample. The samples can then be compared to the calculated miscibility gap which has been reported in investigations into the C_3AS_3 - C_3AH_6 and C_3FS_3 - C_3FH_6 solid solutions of synthesized hydrogarnets by Dilnesa et al [159, 277]. The dilation effect due to iron and the garnet silicon content calculations for the miscibility gap can be found in appendix A and are plotted onto figure 8-7. The estimated Fe/Al compositions for the three flocs are shown by the dashed tie lines in figure 8-7 and have been found from TEM-EDX analysis of the samples which is discussed in more detail in section 8.5; the resultant hydrogarnet compositions estimated from XRD analysis and plotted on Figure 8-7 are given below:

$$Fe\,floc\,A\;(93/12){:}\;C_3A_{0.60}F_{0.40}S_{1.29}H_{3.42}\;\;a = 1.2335\;nm\;(est\;i)$$

$$Fe\,floc\,A\;(93/12){:}\;C_3A_{0.66}F_{0.34}S_{1.13}H_{3.74}\;\;a = 1.2335\;nm\;(est\;ii)$$

$$Fe\,floc\,B\;(91/13){:}\;C_3A_{0.52}F_{0.48}S_{1.24}H_{3.52}\;\;a = 1.2363\;nm$$

$$Al\,floc\;(93/001):\;C_3A_{0.72}F_{0.28}S_{0.98}H_{4.04}\;\;a = 1.2390\;nm$$

Equation 8-6: Estimated hydrogarnet estimations from XRD and TEM-EDX analysis

The Fe floc A sample has two estimated compositions due to two distinct groupings of data points where identified in the TEM-EDX analysis, later in this study the estimated Si content from the XRD and TEM studies will be compared. As can be seen in figure 8-7 the compositions do fit in with the estimated parameters for a heavily-silicated hydrogarnet moving towards the pure katoite-type phase, all of the compositions fall outside the predicted miscibility gap which agrees with the observed XRD patterns for the phases. The compositions have also been plotted onto figure 8-8 for comparison with previously reported structures in the hydrogarnet group, examination of this figure shows the estimated phases are in close agreement with the findings from other studies. These parameter estimations are later compared to the results from Taylor's empirical formula for hydrogarnets in section 8.5.1.

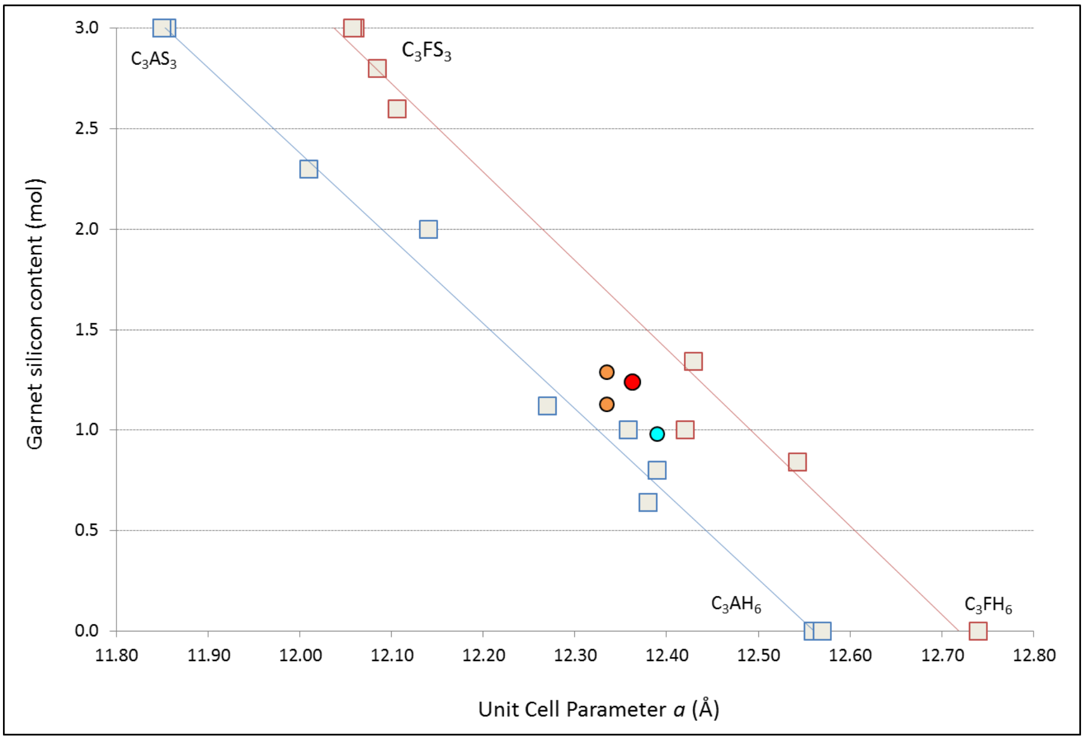

Figure 8-8: Estimated hydrogarnet compositions given in figure 8-7, ● - Al floc HG (93 001), ● - Fe floc A HG (93-12), ● - Fe floc B HG (91-13), plotted in Å for comparison to figure 8-3.

8.3 Thermal Analysis

Thermal analysis showed weak decomposition responses for a hydrogarnet phase and these are labelled for the floc samples in figure 8.9. The decomposition temperatures shown in figure 8-9 to figure 8-10 correspond to the temperature reported for synthetically-produced katoite hydrogarnets [159, 234]. Passaglia and Rinaldi [278] discussed TG curves for various hydrogarnets with C_3AH_6 showing a major loss at 250-310˚C; interesting the authors described katoite specimens as having greatly reduced losses which is similar to the katoite specimens examined in this study and in other literature [159]. The Al-floc sample showed a shift change at 380˚C in the major decomposition step associated for the suspected HG phase; this agrees with the XRD data that a different hydrogarnet composition is being formed in this sample. The increased mass loss observed in figure 8-11 for the Al-based floc suggests a possible greater OH^- presence in this sample for the hydrogarnet phase; this would link to a lower level of Si substitution into the hydrogarnet structure in the Al-floc sample.

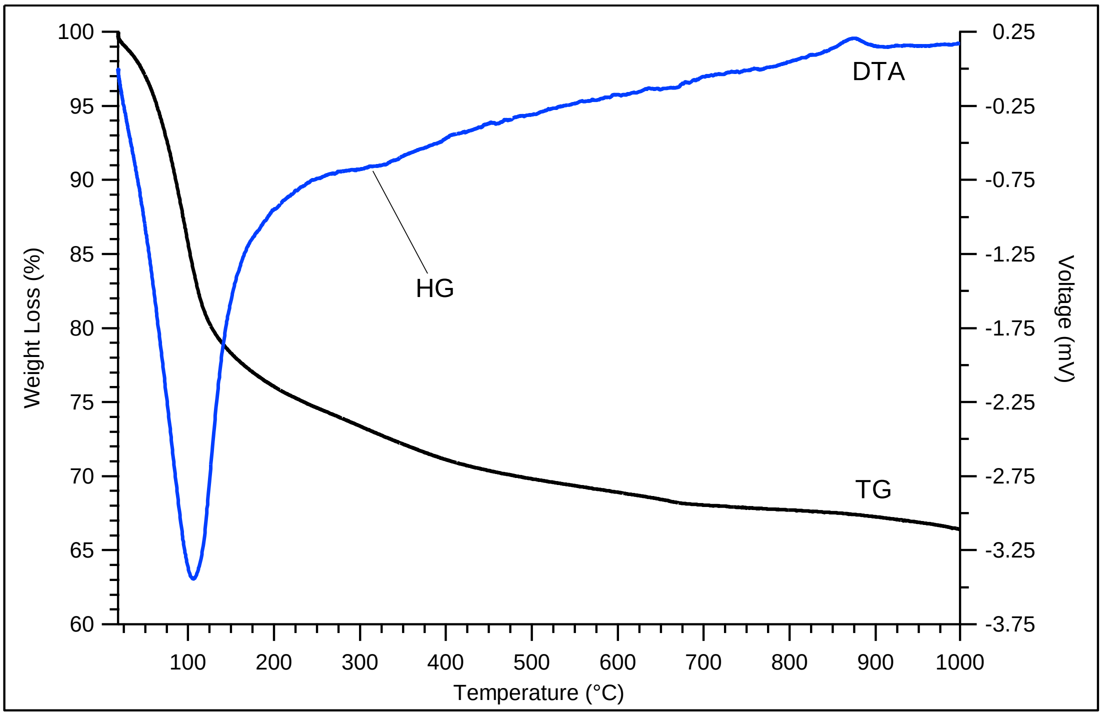

Figure 8-9: STA trace for Fe floc A sample (IDM 93-12); HG- Hydrogarnet

The primary decomposition stage in all floc samples centred at 100˚C is attributed to the weight loss from the C-S-H phase [235]. The DTA in this study did not detect the two-stage low temperature loss peaks at approximately 80˚C and 130˚C observed by Collier et al [91] by DTG analysis, attributed to an amorphous hydrated calcium ferrite and iron-substituted C-S-H. The observed peaks at temperatures over 800˚C are associated with the presence of unreacted PFA particles with transitions of the glassy phases at higher temperatures.

No noticeable peaks were observed for either of the principle cement phases calcium hydroxide (CH) or calcite in the Fe-floc samples, only a minor level of calcite was identified in the Al-floc with again no CH observed. This negligible level of CH and calcite agrees with the DTG work of Collier et al [93] for cemented Fe-flocs and the reported XRD analysis in the previous section. This reduced level of CH content is expected from high replacement PFA blended cements especially after longer hydration ages, lower CH contents are observed due to higher levels of consumption via the pozzolanic reaction [68, 279].

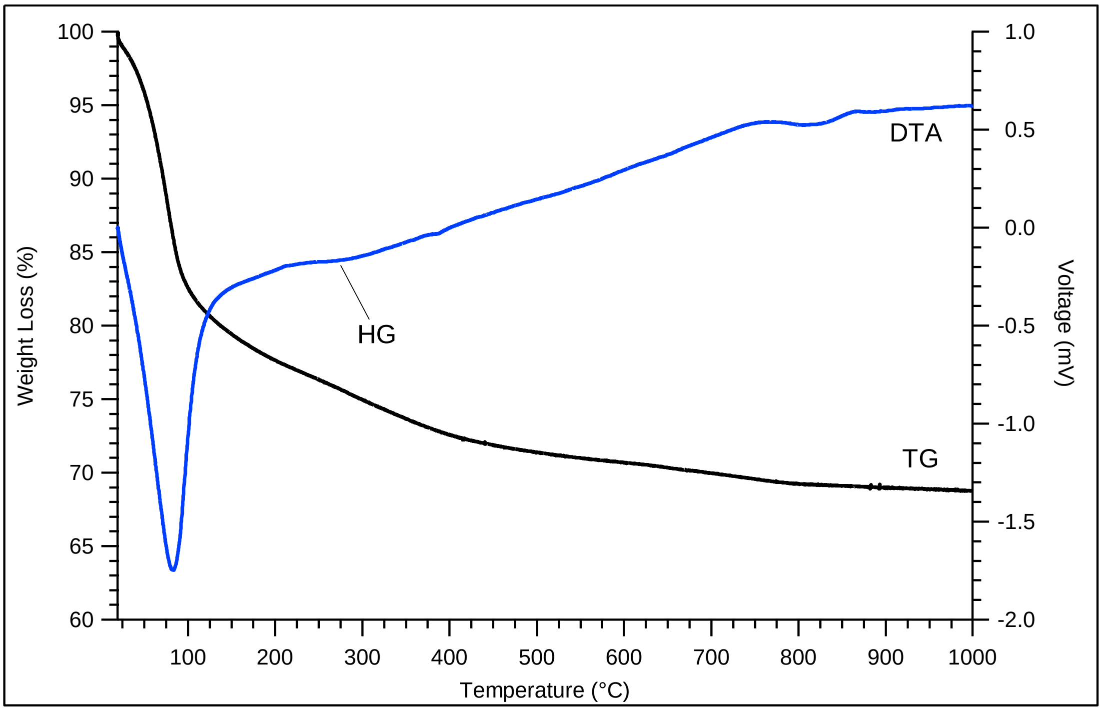

Figure 8-10: STA trace for Fe floc B sample (IDM 91-13); HG- Hydrogarnet

The Al-based floc showed a different TG/DTA trace when compared to the Fe-based flocs shown in figures 8-9 and 8-10; a small decomposition peak was observed at approximately 200˚C which has been attributed to strätlingite (C_2ASH_8). The formation of strätlingite is not unusual in the hydration of PFA:OPC blended cement and is especially favoured in PFA's with higher aluminium contents [280]; in this waste system however the additional aluminium could be provided by the waste material in addition to the internal Al content of the PFA. Due to this, the formation of strätlingite alongside the C-S-H phase is of interest and potential Al^{3+} containing phases should be considered regarding their long-term stability.

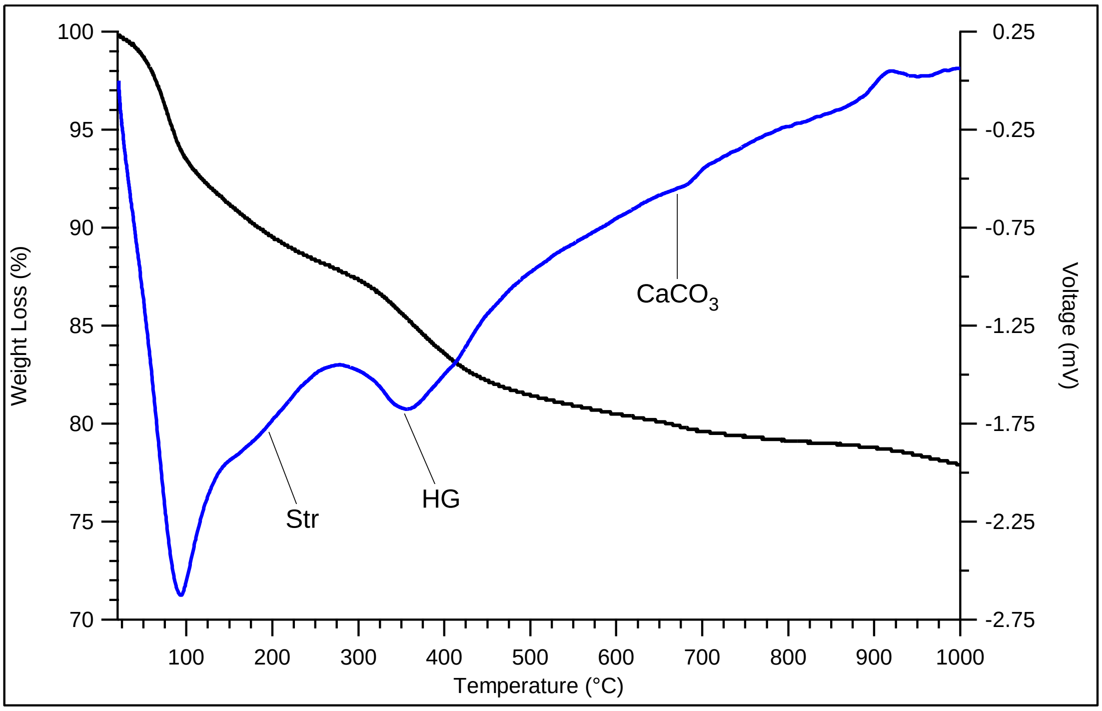

Figure 8-11: STA trace for Ae floc sample (IDM 93-001); HG- Hydrogarnet, Str - Strätlingite

The characteristic weight loss associated with the bound water content of the C-S-H phase was relatively unaffected when compared to PFA:OPC cements with no waste addition. Despite the high waste to cement powders addition (9:8) the relative levels of mass loss for the primary decomposition peak is comparable with approximately 23% loss by weight found for the Fe-floc samples up to 200˚C.

8.4 SEM

The microstructure of the PFA:OPC + waste floc samples were investigated using SEM backscattered electron imaging with X-ray analysis and secondary electron imaging of fracture surfaces. The microstructure of a typical encapsulated floc sample is shown in figure 8-12 which indicates large quantities of partially reacted or unreacted fly ash particles. Fine C-S-H binding matrix was observed which has been produced from the reaction of cement particles and subsequent pozzolanic reaction [235]. Denser areas of the C-S-H matrix are observed closer to fully reacted smaller fly ash particles indicated by the asterisk's in figure 8-12; larger particles of over 5µm seemed to remain at least partially unreacted as shown in figures 8-12 and 8-13. The level of unreacted fly ash particles accounts for the quantities of mullite and quartz identified in the samples by XRD analysis.

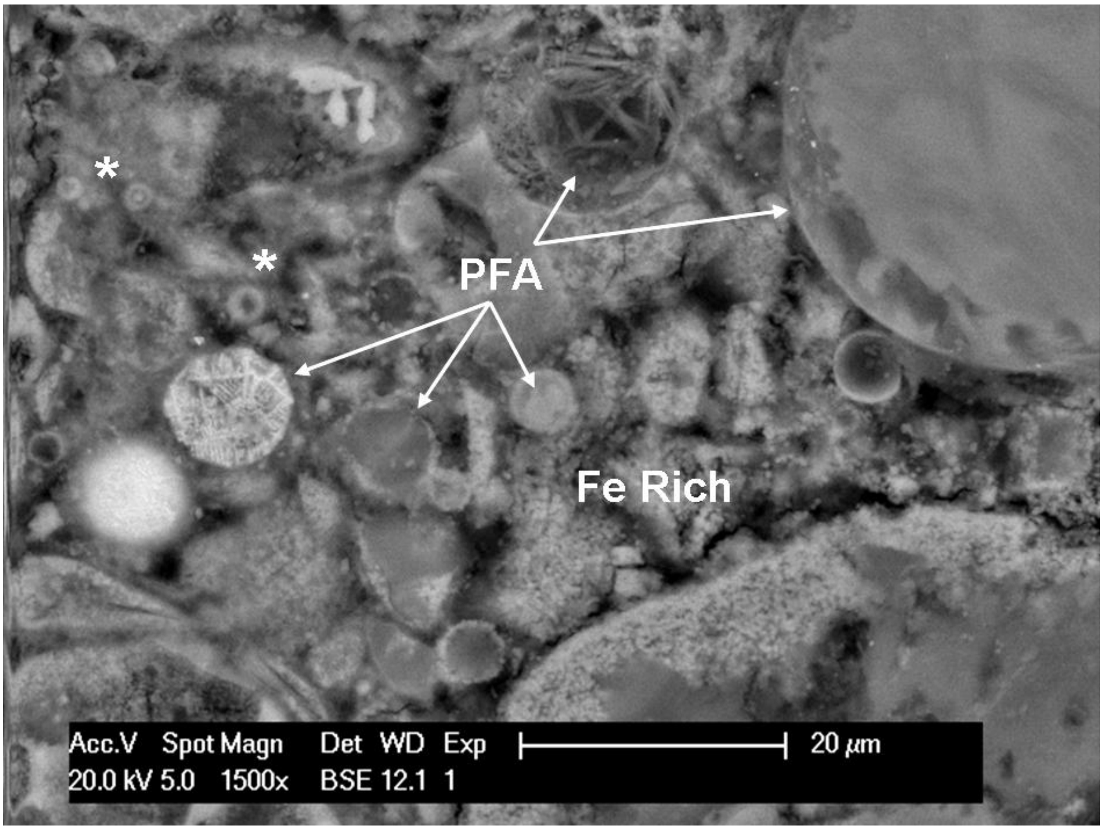

Figure 8-12: SEM BSE of the microstructure for the Fe floc A (93-12) indicating large proportion of small fully (★) and partially reacted fly ash particles, Fe rich agglomerations

Figures 8-12 and 8-13 both show the general microstructure at various magnifications of the Fe-floc A sample (IDM 93-12). The sample presents a consistent level of porosity which is higher than that expected for PFA:OPC cements of a lower replacement level with no waste addition [68, 70]. Collier [122] suggested an approximate value of 50% porosity by volume for a similar younger Fe-floc sample; SEM BSI investigation in this study agreed with this value as a maximum for areas in-between reacted cement grains well illustrated in figure 8-13 images c) and d). This agreement was based upon a small selection of grey scale analyses of the sample where the porosity was estimated; it should be noted porosity could possibly be overestimated due to remaining resin in the sample. The long-term storage of this sample suggests that the porosity doesn't change significantly over time with no additional cracking or changes detected due to phase changes or expansion. Additionally figure 8-13 images a) and b) show the presence of unreacted anhydrous cement likely to be a combination of C_2S and C_4AF.

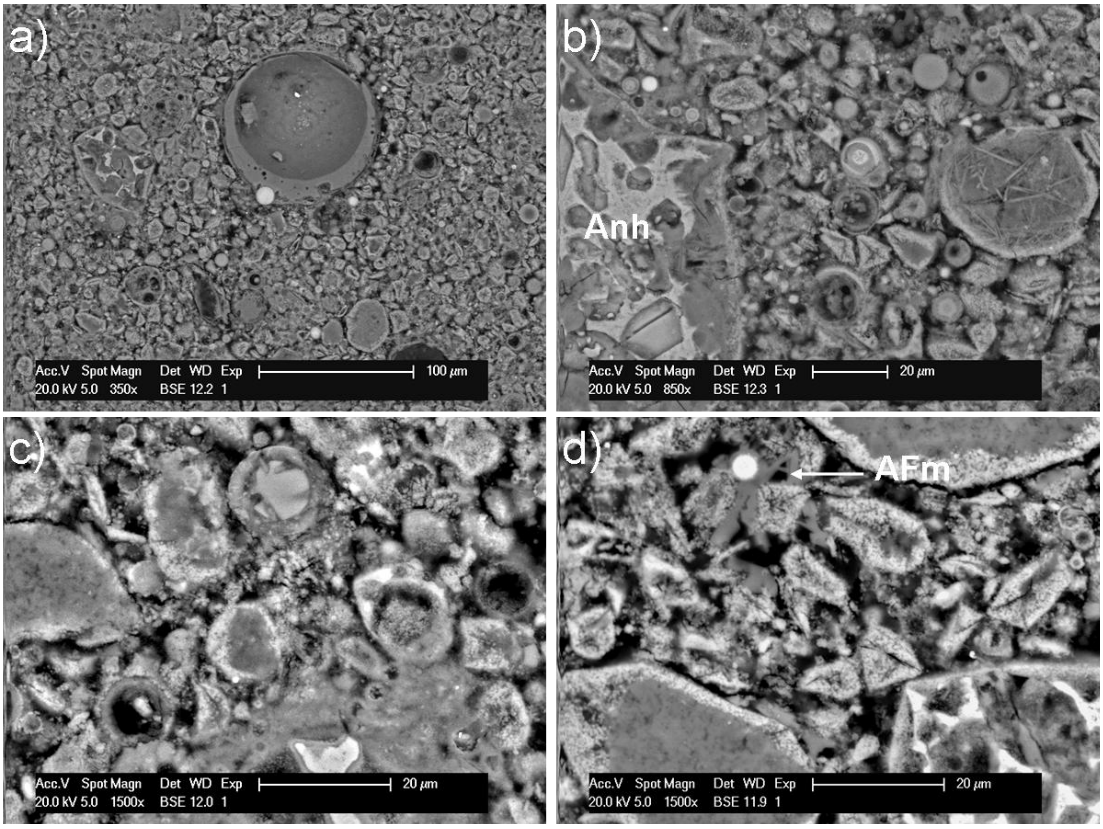

Figure 8-13: SEM BSE images of the Fe floc A (93-12) microstructure, Anh = Anhydrous cement

The treated flocs formed into agglomerations of particles often chaotic in nature, the average longest dimension of these agglomerations was 11µm however the sizes were extremely variable when measured in SEM imaging. The chaotic and generally amorphous nature displayed by the flocs in agglomerations agrees with the SEM SE imaging collected by Collier et al (2006) for pre-treated bulk flocs treated with $Ca(OH)_2$. Good examples of the agglomerations encapsulated in the cement matrix are shown in figure 8-12 labelled as Fe-rich and in figure 8-13 images b) - d). The flocs do seem to be physically encapsulated successfully within the cement matrix with no noticeable cracking or localised issues seen in the general microstructure at lower magnifications (figure 8-6 a)). The pre-treatment with $Ca(OH)_2$ is reported to increase the amount of C-S-H formation in the sample increasing the compressive strength and stability of the waste-form [77, 92, 93]. However even with pre-treatment the level of binding C-S-H seen in areas with large quantities of floc is quite low (figure 8-13 d). Due to the level of waste addition and the associated water content of the floc slurry the matrix continues to produce a highly porous microstructure. This indicates the definite need for pre-treatment as its very unlikely a untreated waste-form would be successfully incorporated into the matrix without the reported additional C-S-H production.

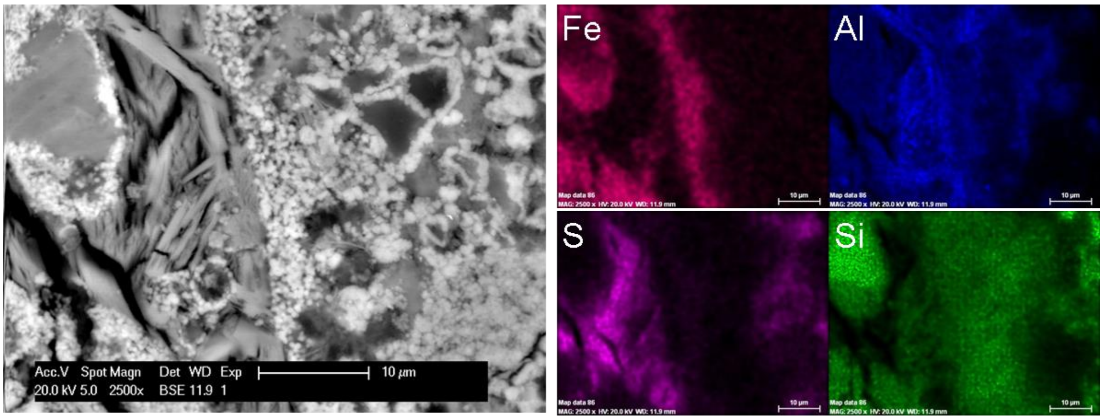

Figure 8-14: SEM BSE image and mapping of AFm plates (Ms) and floc concentration in Fe floc Sample A (93-12)

Figure 8-14 shows an image from the Fe floc sample A and indicates the additional products formed with the cement matrix for the floc systems, elemental mapping was used to help identify both the hydrated aluminate phases and iron content associated with the waste floc. The mapping shows the presence of an aluminate hydrate phase with strong responses for sulphate which is assumed to be either the AFm phase monosulfate or ettringite. Again the Fe-flocs were identifiable by the spherical appearance of the massed particles in agglomerations and by the high contrast caused by the higher atomic mass associated with iron compared to most other present elements such as aluminium , silicon and calcium. Interestingly the treated waste floc indicated by the Fe responses in figure 8-14 is not solely associated with the calcium response expected from the pre-treatment with $Ca(OH)_2$. Iron responses were observed on the surface of silicon rich areas as shown in figure 8-14 suggesting the precipitation of flocs onto other cement products in the matrix. Additionally Si and Al in smaller levels have been associated with very strong Iron responses which could indicate the substituted $C_3(A,F)SH$ hydrogarnet forming in close proximity to the waste flocs.

The nature and location of floc waste was investigated further using FEGSEM imaging of the microstructure with particular interest in the high contrast areas signifying iron-containing phases. Figure 8-15 shows the imaging of two areas of the Fe-floc A sample which contained significant areas of encapsulated treated flocculants. In figure 8-15 images a) and c) the flocs are labelled as A with partially reacted fly ash particles as FA, plates of AFm product as seen formed in the cements microstructure indicating the presence of hydrated aluminate phases are perhaps underestimated by the XRD analysis. As shown previously in figure 8-12 and in figure 8-13 the flocs are still formed in agglomerations which have been labelled. Higher magnification imaging of these flocs is shown in figure 8-15 image b) and shows the general spherical nature of the flocs which have potentially been reacted or surrounded by hydrate products. Flocs were also shown to have an affinity with the outside edges of fly ash particles as shown by the spherical high contrast features labelled as B in figure 8-15 images a) and c). This was also found during SE SEM imaging which was carried out on this sample, the results of which are included in appendix B of this study.

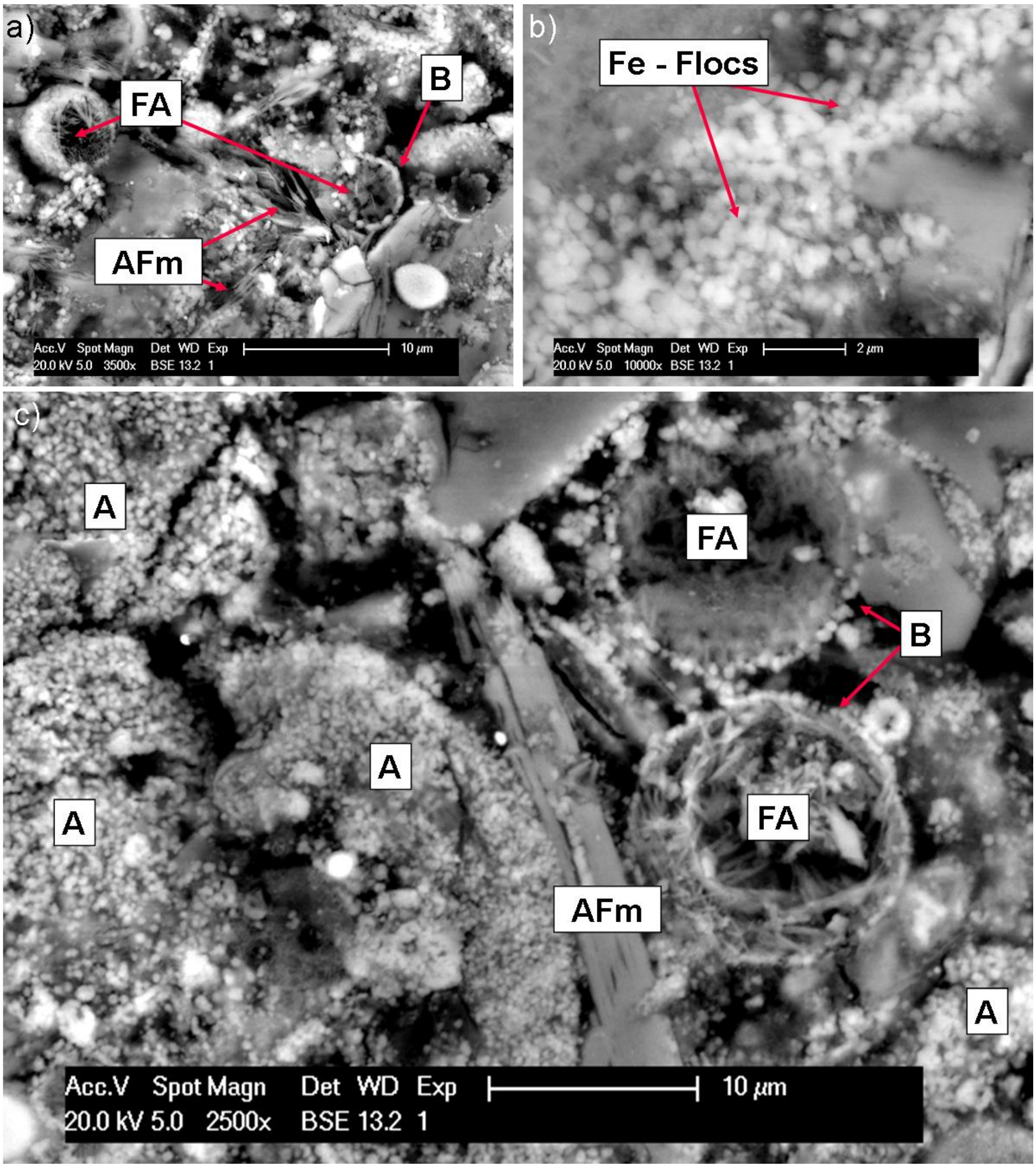

Figure 8-15: BSE FEGSEM imaging of Fe floc A (93-12) microstructure showing A - Fe floc rich areas , B - Fe flocs surrounding reacted fly ash particles, FA - reacted fly ash.

Similarly to the previous figure the formation of floc agglomerations was examined in additional areas; figure 8-16 shows imaging of a floc-rich area which is surrounded by a level of hydrated binding phase as indicated by the mid-grey scale contrast. The nest of unreacted mullite shown in figure 8-16 b) is assumed to be from a partially unreacted fly ash particle with the formation of C-S-H and encapsulated flocs in close proximity. As can be seen the floc areas indicated by the slightly higher contrast seem to contain more crystalline cubic formations labelled in image b). These formations also show a higher contrast ratio suggesting an iron content is still present; this means the formation maybe linked to the substituted hydrogarnet phase intermixed with the encapsulated waste flocs after hydration.

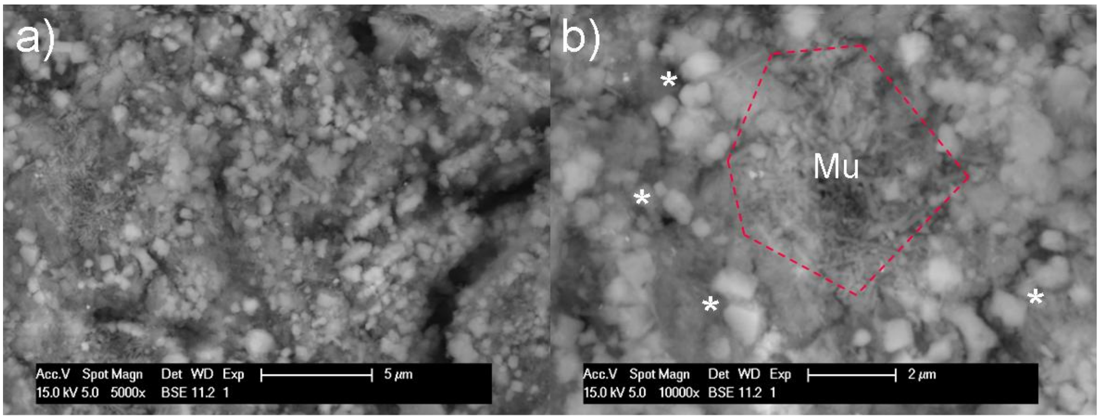

Figure 8-16: SEM BSE images of a) Fe flocs in embedded in matrix b) enlargement of first image, nest of mullite crystals outlined. Cubic crystalline phases formed at marked by *

The microstructure of Fe floc B (IDM 91-13) is shown in figure 8-17 images a) - d) with the general microstructure displayed in image a). The image shows a similar microstructure to that displayed for floc A with a potentially less porous matrix observed. Large quantities of fly ash particles can be seen, again large fly ash particles showed only partial reaction with small hydration rims observed for most indicating a basic level of activation during hydration. Image b) shows in more detail a typical microstructure with larger partially reacted fly ash particles present with hydration rims; a denser C-S-H binding phase associated with small (< 1µm) fully reacted fly ash particles and large quantities of floc waste sites usually associated with high porosity areas. The physical encapsulation of the treated flocs is observed with agglomerations of the waste material seen throughout the microstructure. A good example of the incorporation of a floc agglomeration can be seen in figure 8-17 image c) which shows the waste site surrounded by a dense hydrated structure of C-S-H. Small levels of localised cracking were observed in this sample as shown by the images in figure 8-17 however this was not extensive and did not suggest failure of the waste-form due to expansion from phase changes. Once again the mass of treated flocs was examined using FEGSEM imaging as depicted in figure 8-17 image d); the small spherical nature of the flocs was well represented with some areas seemingly connected by a hydrated phase shown by the underlying lower grey scale.

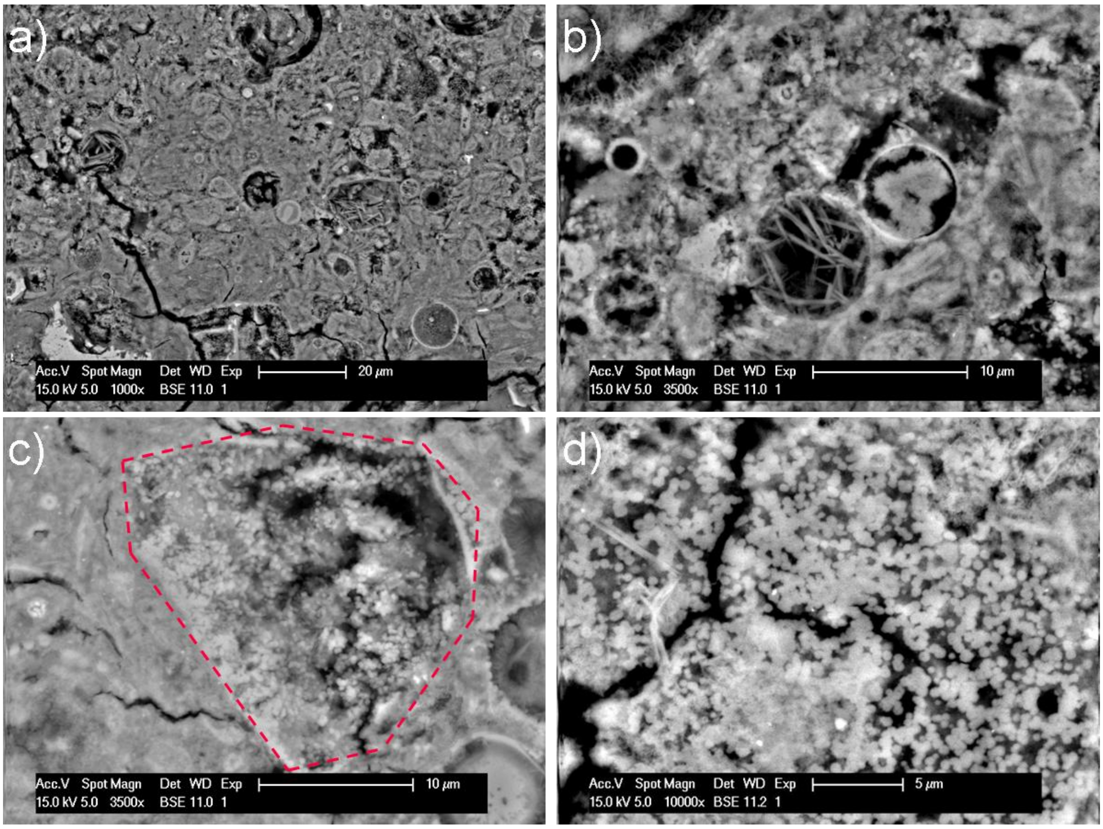

Figure 8-17: SEM BSE images of the Fe floc B (91-13) microstructure; c) outlines a encapsulated agglomeration of waste flocs, d) FEGSEM image of floc's

Elemental mapping of the second Fe floc sample was conducted and is displayed in figure 8-18; as expected the calcium and iron responses was pervasive throughout the matrix with exception to the Al or Si-based fly ash particles. The calcium response was due to both the formed C-S-H binding matrix and the pre-treated waste-form, whilst the expected the iron response was present from the flocs. Suggestions have been made for the presence of a C-S-H which has levels of incorporated iron from the waste forming a C-F-S-H phase in similar samples [77, 92, 93]. However the close interaction suggested by the SEM analysis in this section between the flocculent particles and the binding phase means this would be difficult to quantify using SEM EDX analysis. The potential composition of the C-S-H phase is discussed in more detail later in this section and in the discussion of TEM analysis.

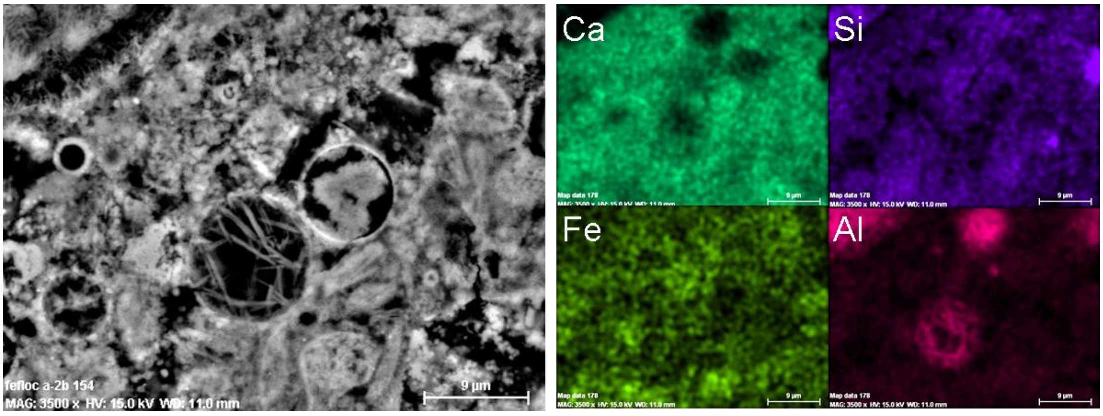

Figure 8-18: SEM Mapping of Fe floc B (91-13) matrix showing Fe presence throughout

The microstructure of the Al floc sample (93-001) is shown in figure 8-19 and displays some differing characteristics to that discussed for the ferric-floc systems. The primary difference displayed by this sample was the apparent denser microstructure as evidenced by figure 8-19 image a), in this image more numerous areas of monotone grey areas are displayed corresponding to dense C-S-H potentially due to additional hydration of the PFA or cement grains. Image b) shows an area of this dense C-S-H product which in this case is assumed to be from the hydration of cement; A denotes the original cement particle and anhydrous material surrounded by the dense hydrated phase this again shows that even at extended curing periods some anhydrous material can remain. The areas marked B in image c) denote the smaller dense hydrated zones, higher magnification imaging of these areas showed many contained crystalline structures corresponding to mullite and quartz due to their relative chemical response and physical appearance. It is assumed therefore these zones are predominantly Ip C-S-H from the full reaction of fly ash particles. So whilst there seems to be increased levels of hydration creating additional C-S-H zones the general porosity of the microstructure is not greatly affected; image c) shows that areas away from these dense zones display quite high levels of porosity from the grey scale imaging.

Identifying agglomerations of waste floc particles was more difficult in this sample than for the ferric-based systems potentially due to improved physical encapsulation of the waste-form. This could make agglomerations less 'distinct' from the surrounding phases, an example of this can be seen by examining figure 8-19 image d) and comparing it to an earlier image for a ferric floc (figure 8-13). However once imaged and identified the Al-floc samples displayed similar characteristics to the ferric samples discussed earlier; all flocs showed a tendency to agglomerate and a reasonable level of physical encapsulation often surrounded by hydrated phases such as C-S-H.

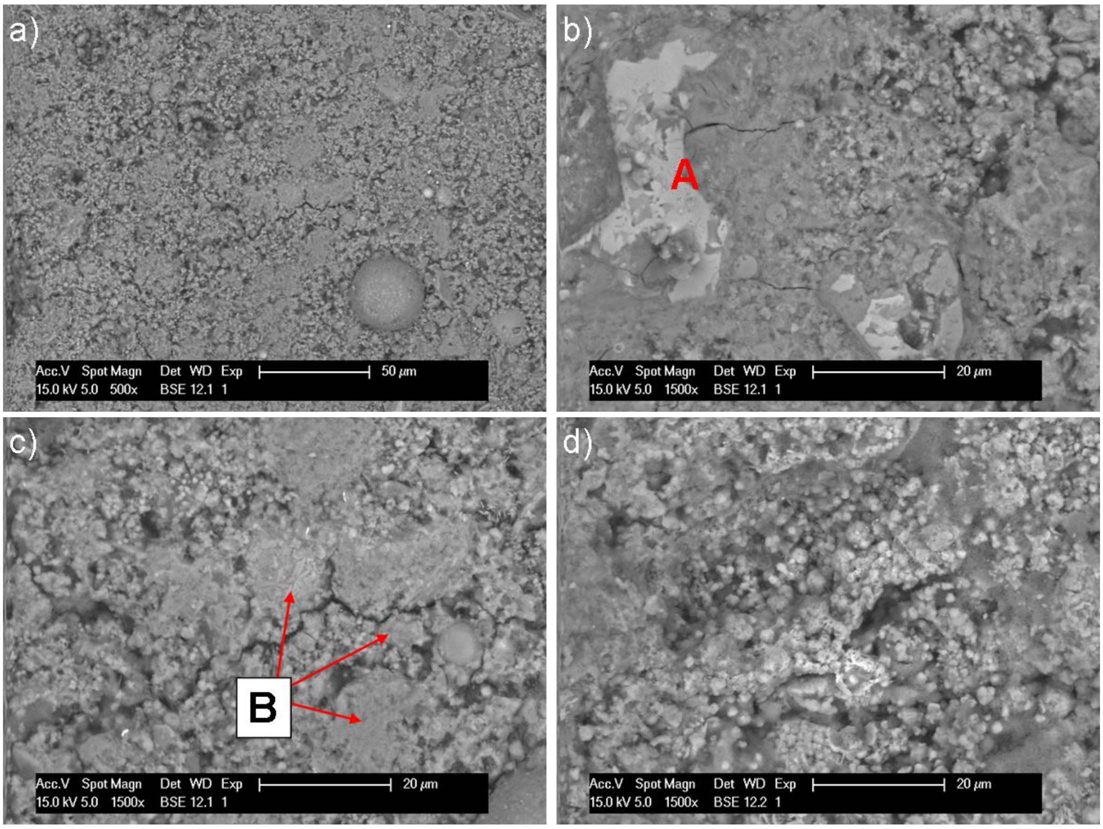

Figure 8-19: SEM BSE images of the Al floc B (93-001) microstructure; A = anhydrous cement and surrounding dense hydrate product B= fully reacted fly ash particles

A more detailed study of the waste encapsulation within the Al-floc sample by SEM imaging is displayed in figure 8-20; in this figure potential waste areas are imaged along with formations of crystalline phases which have been previously discussed in this section and displayed in figure 8-16. The images in figure 8-20 indicate floc agglomerations labelled as A in images a) and c), both of these images show the flocs are well encapsulated or indeed surrounded by an amorphous phase assumed to be C-S-H. This suggests the pre-treatment process for these alumino-ferric flocs was successful in creating a waste-form which is able to be incorporated within blended PFA:OPC cement matrices. Again additional crystalline phases where identified during imaging by SEM; B indicates potential cubic-like crystalline phases which were described previously and maybe linked to the mass formation of the hydrogarnet phase. As observed earlier this phase was only identified by higher magnification imagining due to their relevant size and intermixed nature, its dimensions also restricted the ability to accurately characterise them chemically by SEM-EDX. Image c) also displays crystalline needle-like phases within the cement matrix denoted by the C label in the image. It is unclear at this point whether these needles are related to hydrotalcite which has been shown to be present and associated with waste flocs by TEM imaging (section 8.5) or another phase. It is predicted they also could be related to unreacted crystalline phases found from the PFA (mullite, hematite etc) and small needles like this have been imaged in high replacement PFA:OPC systems [66, 281]. Within the matrix levels of fly ash reaction are also observed; FA indicates a fly ash particle which is essentially unreacted but surrounded by a reaction rim of C-S-H. As discussed previously however many fly ash particles do seem to be fully reacted within this sample.

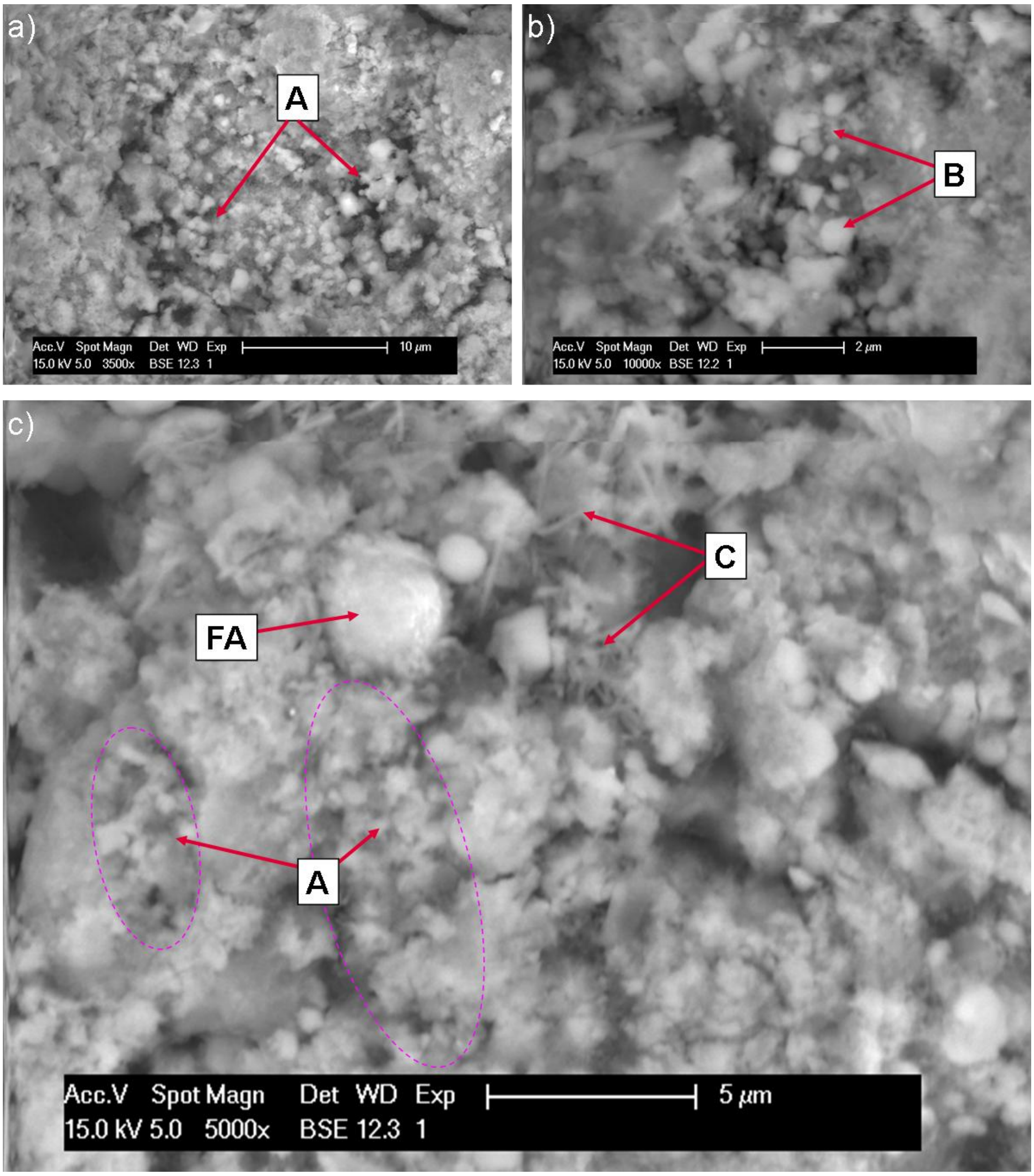

Figure 8-20: BSE FEGSEM imaging of Al floc (93-001) microstructure showing A - Al floc rich areas , B - crystalline phase, FA - fly ash C - needle formations.

Elemental mapping for the Al-floc sample is shown in figure 8-21 with mapping conducted on the region displayed in figure 8-20 image a). As expected there are a number of strong Al responses linked to potential agglomerations of Al flocs or fly ash; additionally a noticeable background level of Al is measured throughout the sample by EDX in potential waste phases, hydrated material and fly ash. Linked to this a measured level of Fe has been recorded across the sample. Due to the fine nature of Fe shown in figure 8-21 it is assumed this response is linked to the Al-floc waste which is known to contain levels of iron, hematite from the fly ash would be expected to produce a stronger more localised response. In addition the expected responses for calcium and silicon where measured which are linked to the hydrate phases, it should be noted however calcium is also linked to the waste phase due to the pre-treatment process and silicon is also associated with fly ash.

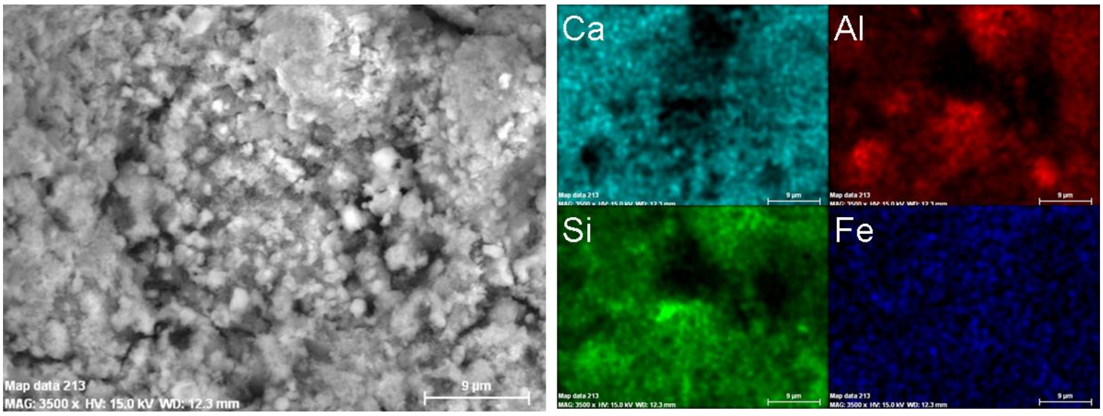

Figure 8-21: Elemental mapping of Al floc sample showing 8-20 image a)

8.4.1 SEM EDX

Due to the compact nature of the waste flocs and their small physical size it was not possible to use the SEM-EDX for general analysis of their composition in the paste or the chemical analysis of any individual phase. To demonstrate this a histogram of the Ca/Si ratios of the SEM-EDX analyses for the Fe-floc A sample is shown in figure 8-22; this indicates a trend towards a high Ca/Si ratio for the binding phase and around waste sites with a mean of 1.9. This goes against the general viewpoint that blended PFA cements at higher replacements exhibit a lower Ca/Si ratio than for pure OPC blends reported by several studies [70, 282]. The reason for this high Ca/Si ratio by SEM-EDX is thought to be due to the relative interaction volume even at lower operating voltages and the pre-treatment with $Ca(OH)_2$ of the waste form. It is unexpected that the actual Ca/Si ratio of the C-S-H phase would be near an average of 1.9, so the mass addition of a calcium-ferrite phase produced by pre-treatment would explain the displayed increased levels of measured calcium.

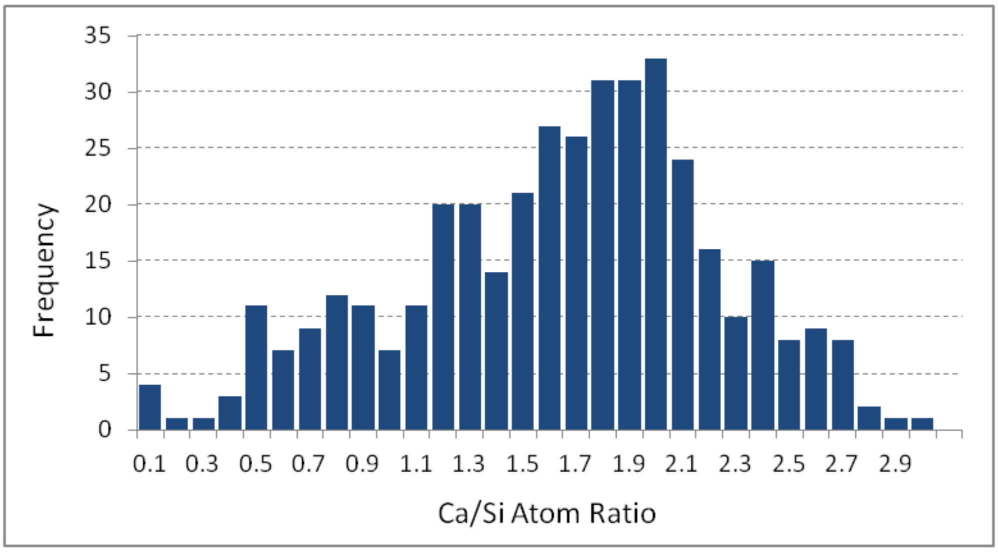

Figure 8-22: Histogram of the measured Ca/Si ratio for SEM-EDX analyses of Fe floc A (93-12)

The SEM-EDX data points for the samples are shown in figure 8-23 displaying the Si/Ca against Al/Ca and Al+Fe/Ca ratios, as expected the data showed a wide variation in the reported Si/Ca ratio. As mentioned previously there is a trend in the data indicating an additional level of Ca within the binding matrix and floc agglomerations; this is assumed to be from the amorphous calcium ferrite phase the flocs form after pre-treatment with $Ca(OH)_2$. Due to this the actual cluster of analyses for C-S-H cannot be accurately predicted due to the additional calcium response. The prediction, however, is any C-S-H ratio would be much lower than that found from SEM-EDX displayed in figure 8-23, assuming that the PFA has reacted significantly. In figure 8-23 plot b) the Al+Fe/Ca data points are examined as can be seen nearly all data points have a level of contained Fe signal. Analysis was primarily taken on the binding phase and waste sites. This has resulted in a trend of analyses pointing towards the potential composition of the hydrogarnet phase as discussed in XRD analysis. To determine the approximate composition of this phase a tie line for the HG end members has been annotated onto figure 8-23 b), this gave an estimation of $C_3A_{0.58}A_{0.48}S_{1.92}H_{1.83}$ for the HG phase in the Fe floc A sample. This estimation compares reasonably well to estimation (i) for this sample in XRD analysis (equation 8-6), with an approximately similar Fe addition with a small overestimation of Si content. Due to the large interaction volume and intermixing with phases containing Ca, Si, Al and Fe being probable in all analyses this composition will be used only as a guide to the possible accuracy of the XRD analysis, however the SEM-EDX data seems to support its conclusions.

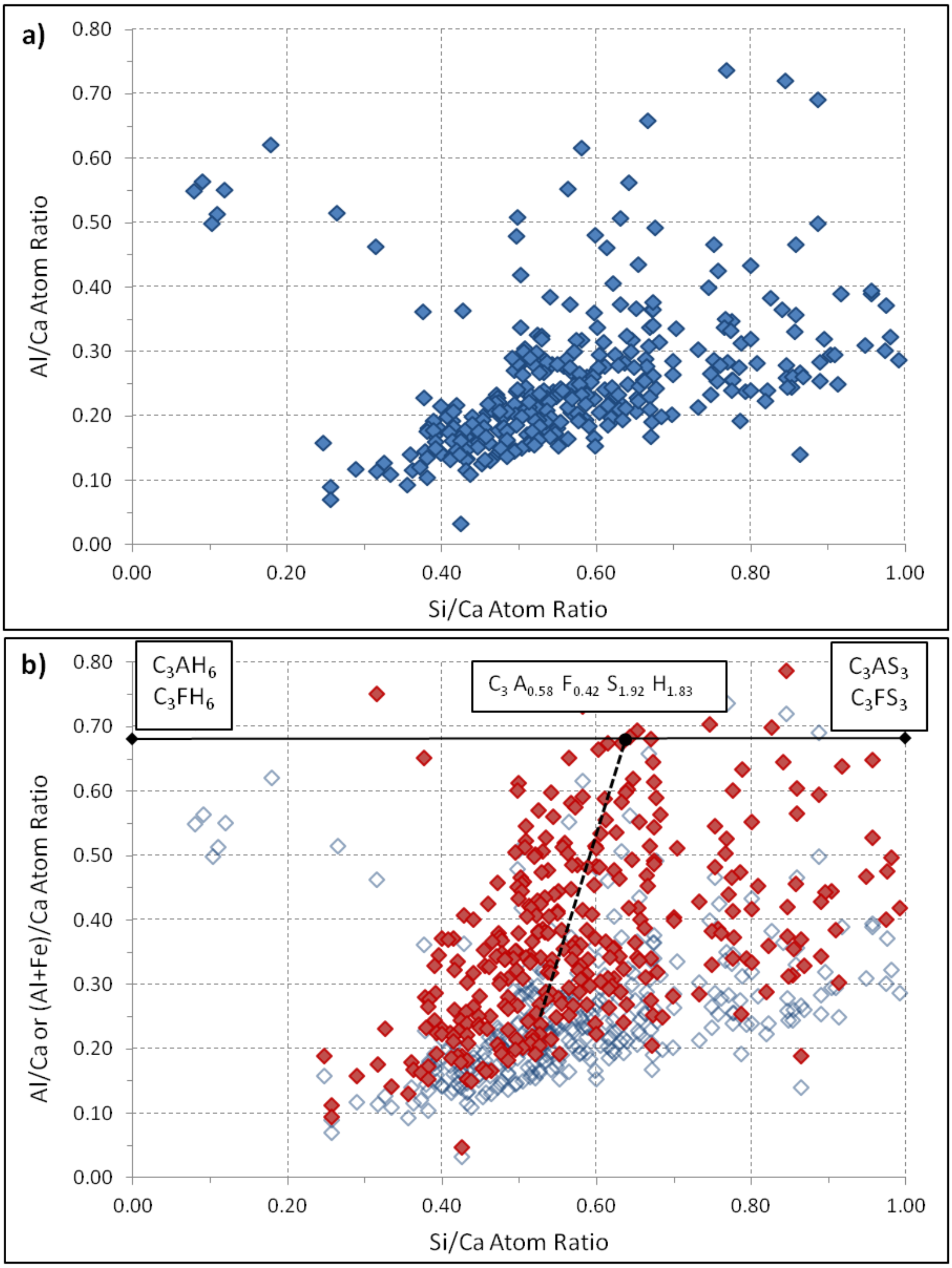

Figure 8-23: SEM EDX analyses for Fe floc A (93-12) showing a) Si/Ca v Al/Ca ratios and b) Si/Ca v (Al+Fe)/Ca ratios with indication of estimated Fe-Si substituted hydrogarnet composition

Additional SEM-EDX analyses were taken from the Fe-floc B and Al-floc samples in the same manner as shown in figure 8-23, the results from these samples were similar with no definite clear clusters for C-S-H or other phases identified by SEM-EDX. This again shows the relative difficulties in using this technique for quantitative analysis of the floc containing samples, due to this TEM-EDX analysis of the floc samples was greatly preferred and is discussed in the following section.

8.5 TEM

In this section the TEM analysis of the 3 floc systems is discussed in relation to both the imaging and EDX data. All 3 samples showed similar microstructures under TEM investigation related to the high replacement levels of OPC with PFA in the grouts.

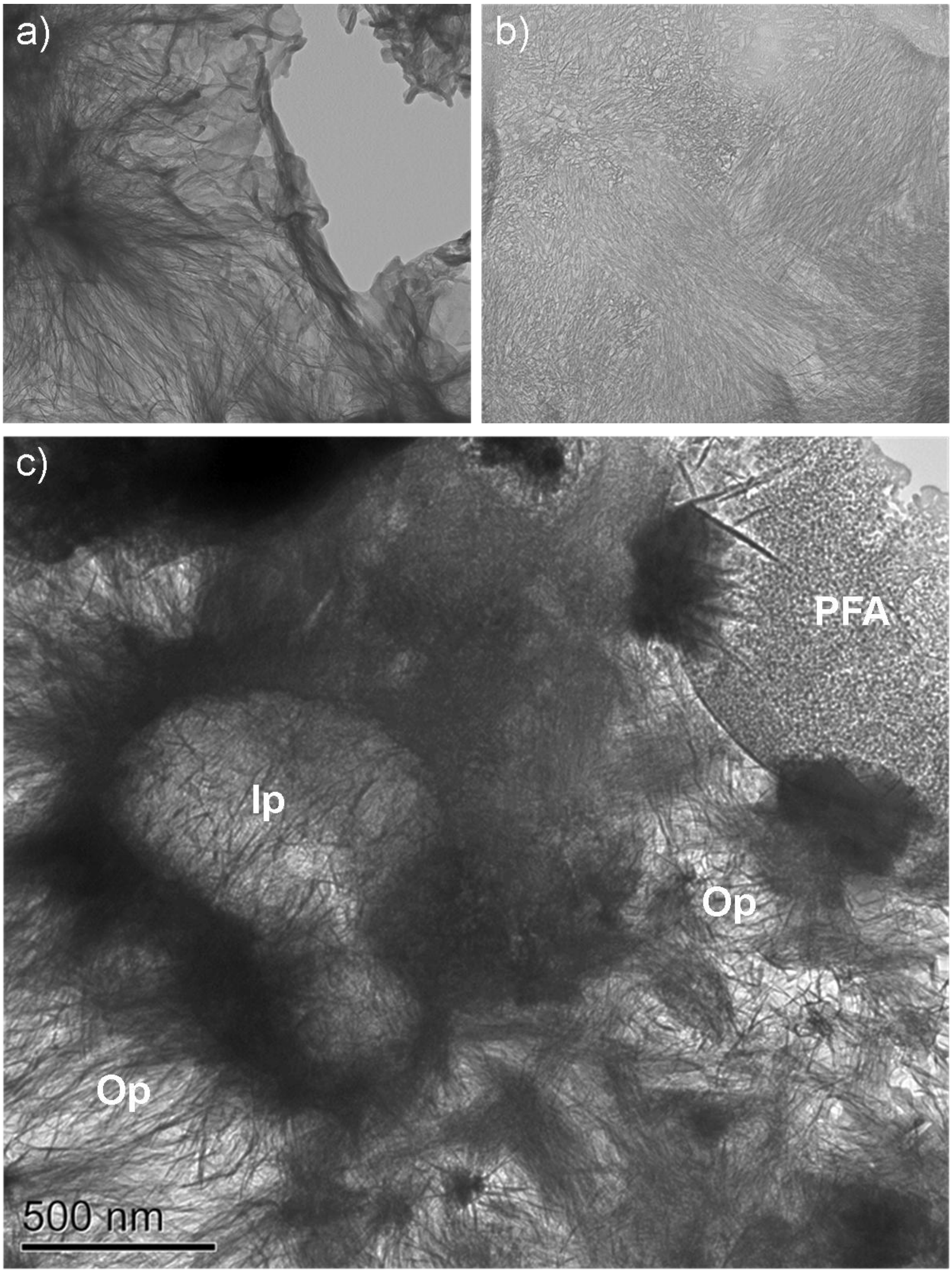

Figure 8-24: TEM micrographs of Fe floc Sample A (93-12) showing a) Fibrillar and b) Fine-fibrillar C-S-H, c) shows the microstructure of area without waste flocs showing PC Ip C-S-H, Op and PFA particle.

The TEM micrographs in figure 8-24 show the nature of the C-S-H morphologies commonly displayed in the Fe-floc A (IDM 93-12) sample, a wider field of view of the general microstructure is shown in image c). Figure 8-24 images a) and b) show the fibrillar and designated fine-fibrillar C-S-H observed in this sample; the fibrillar C-S-H was consistent with the Op C-S-H observed in the general microstructure displayed in image c) and is in agreement with the C-S-H morphology expected for a water-activated PFA:OPC cement blend. Image c) shows various hydrated phases within the system; including the fibrillar Op product and the lower density Ip C-S-H product due to hydration of a Portland cement (PC) grain. The presence of fully-reacted PC particles is also shown in figure 8-25 b) which displays the same nature of C-S-H as seen previously. Figure 8-25 image a) shows a fully hydrated fly ash particle with produced fine-scale C-S-H, the particle is surrounded by seemingly partially reacted floc particles which have been reacted with $Ca(OH)_2$ during pre-treatment. The presence of floc particles in relation to the fly ash was also observed in the SEM BSE and SE imaging and is interesting as the flocs do seem to precipitate onto the surfaces of present phases in the mix.

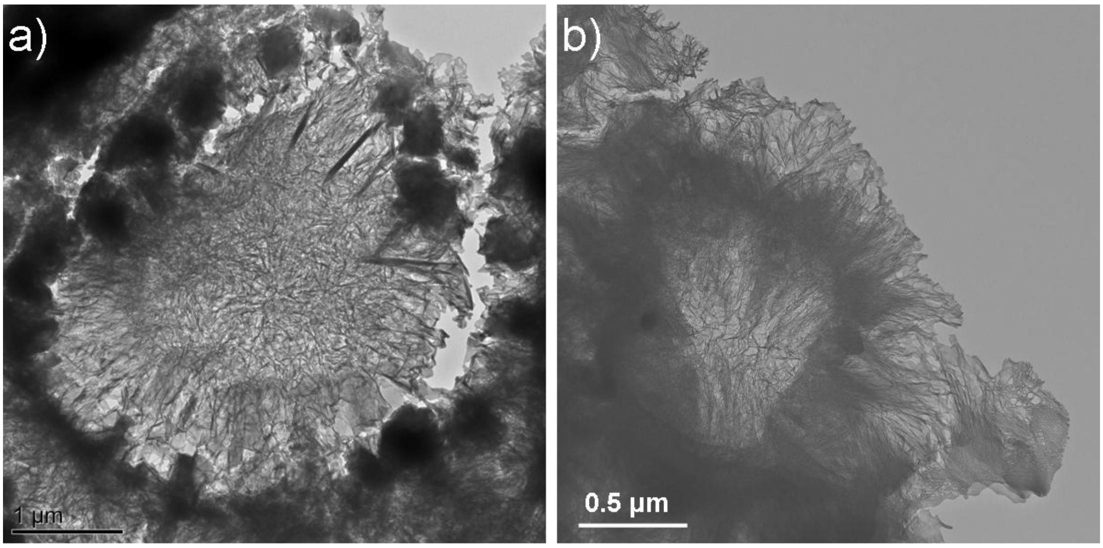

Figure 8-25: TEM micrographs of Fe floc Sample A (93-12) showing a) Well reacted fly ash particle and associated hydration products, b) Fully reacted PC particle showing Ip and Op C-S-H

The images a) to d) in figure 8-26 are all related to the incorporation of the Fe-floc waste-form within the PFA:OPC cement matrix, the presence of flocs is easily distinguished by the dark opaque forms in the images. As discussed in the SEM section the flocs display a normally spherical nature which can become less uniform due to a reaction with $Ca(OH)_2$ or the sample preparation procedure during ion milling. The flocs were identified from other hydrate phases by their chemical composition and amorphous nature under investigation by SAED. Images a) and b) in figure 8-26 show the TEM images of a dense grouping of flocs within the sample, as shown in b) even in very dense groups an amount of binding hydrated material exists between the floc particles which is assumed to be C-S-H in small quantities. Image a) shows a larger field of view for a similar region to that discussed for image b) here again the floc is intermixed or on top of hydrate phases, assumed, by their nature to be C-S-H. Intermixed with the flocs and C-S-H in a) are noticeable needle-like laths of material morphologically separate from the C-S-H phase. EDX identified substantial responses for magnesium in the presence of these phases. Due to the magnesium and underlying aluminium detected by EDX, the needle-like phases are suspected to be a Mg-Al hydrotalcite phase, which seems to be formed locally to the floc. The presence of hydrotalcite has been reported in OPC:PFA blends in literature [237] with the liberation of Mg^{2+} ions into the aqueous phase during activation of the cement and fly ash particles.

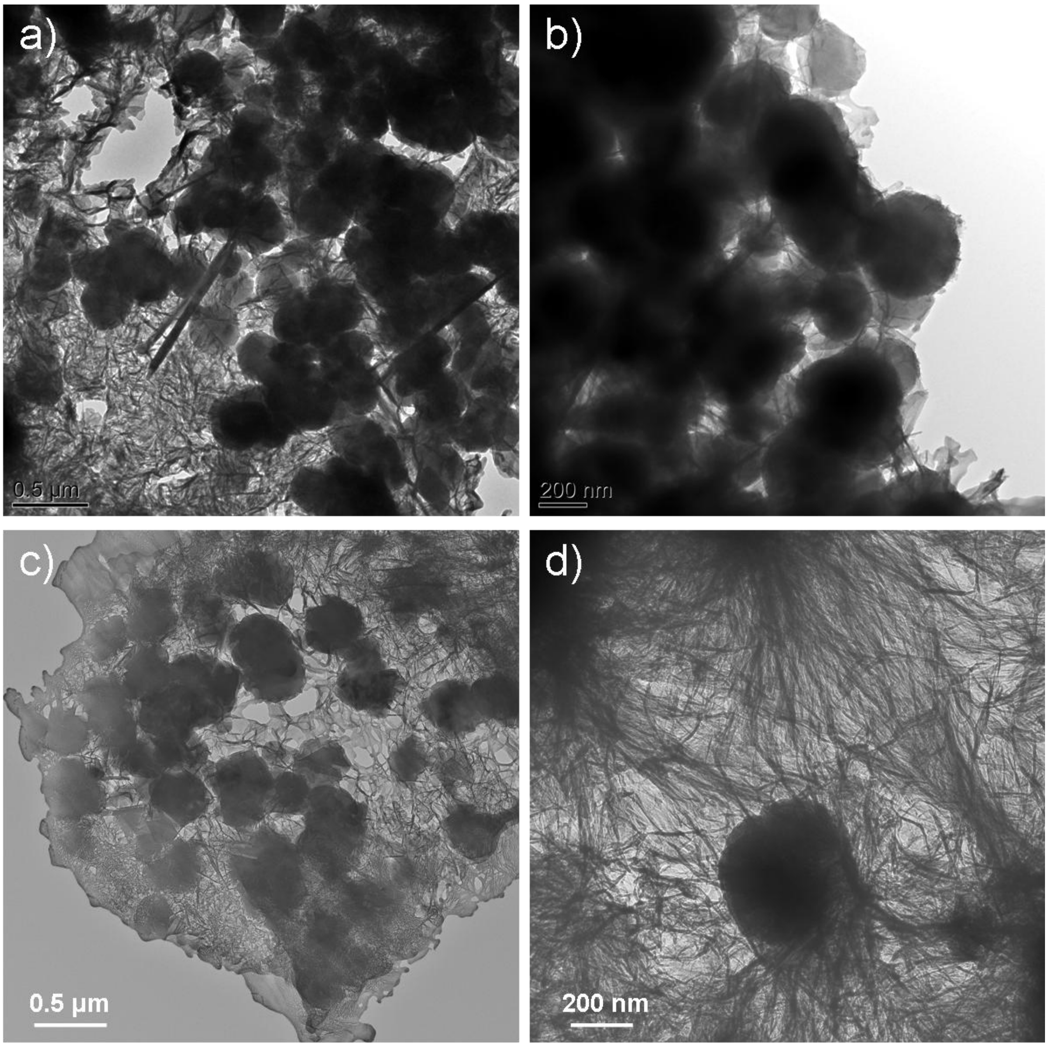

Figure 8-26: TEM micrographs of Fe floc Sample A (93-12) showing floc incorporation within the cement matrix.

Images c) and d) in figure 8-26 show a more open microstructure containing less dense agglomerations of flocs; in the less compact areas shown in image c) the C-S-H has shown a more foil -like morphology perhaps related to the reduced space constraints and relatively porous microstructure created by the floc inclusion. Again in image c) there is a presence of small laths or needles intermixed within the waste products which resulted in magnesium responses from EDX analysis; additionally the presence of crystalline phases less spherical in nature can be seen. It is proposed these formations are linked to the formation of the hydrogarnet crystalline phase clearly observed by XRD analysis and the EDX analysis of these sites is discussed later. The relative thickness of these phases could inhibit accurate compositional determination of this phase, additionally identification of these phases against flocs was at times morphologically difficult to differentiate. It is interesting that the magnesium-rich needles are associated with this phase and the waste floc; Rodgers and Groves [66] discussed observing poorly crystalline iron-containing material which was interspersed with magnesium needles in their studies on OPC-PFA blends. The authors concluded in that study the iron phase as $C_3A_{0.3}F_{0.3}SH_x$, a magnesium hydrotalcite derivative of $Mg(OH)_2$ with small levels of aluminium and calcium. Image d) shows the effective physical encapsulation of an individual waste floc which has been well incorporated into the cement matrix surrounded by the fibrillar C-S-H phase. These images illustrate the positive effect of pre-treatment on the waste flocs and how they are predominantly physically included within the matrix by small amounts of C-S-H product. Due to this the basic physical encapsulation of the waste flocs can be confirmed by TEM analysis with the flocs intimately associated with cement hydration products.

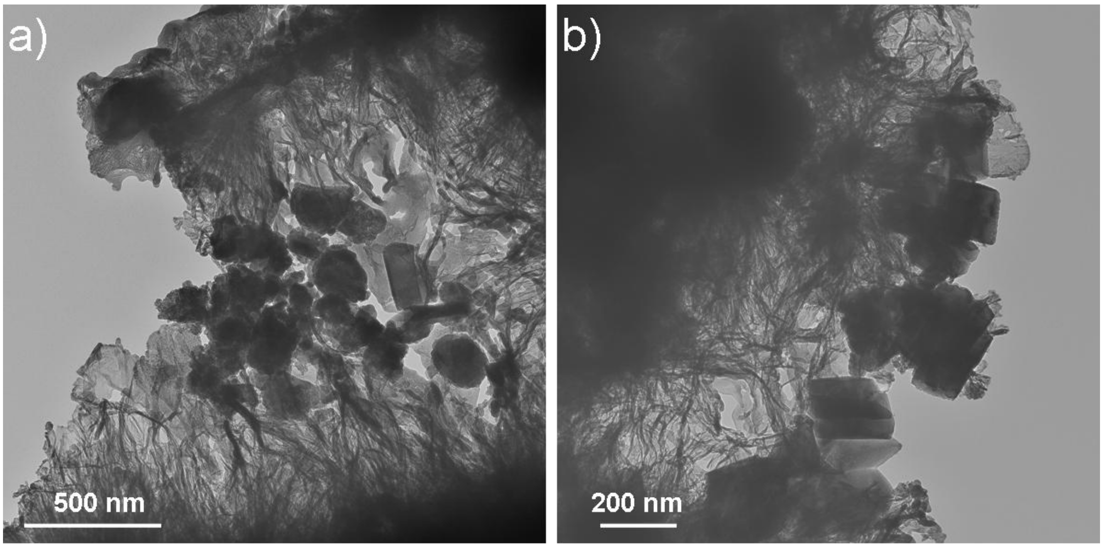

Figure 8-27: TEM micrographs of Fe floc Sample A (93-12) showing crystalline formations within the matrix suspected as cubic Fe containing hydrogarnets

Additional crystalline formations for the Fe-floc sample are shown in figure 8-27, as mentioned previously these formations are often produced in close proximity to the waste floc material. Examination of the crystals suggests a range of dimension between 100 - 250 nm; however the structures shown in figure 8-26 image c) are larger with a diameter of around 200-500nm. These proposed sizes are reasonable when compared to those estimated by XRD peak broadening calculations when potential micro-straining was accounted for using the W-H method; additionally the results agree with reported dimensions for hydrothermally-formed hydrogarnets [268, 283], however those samples were produced at elevated temperatures (>200˚C). Only limited EDX analysis has been carried out on these features due to the instability of the sample, caused by the relative lack of binding material surrounding these formations. This can be observed in the micrographs in figure 8-27, the crystal phase did however seem to be stable under the electron beam of the TEM.

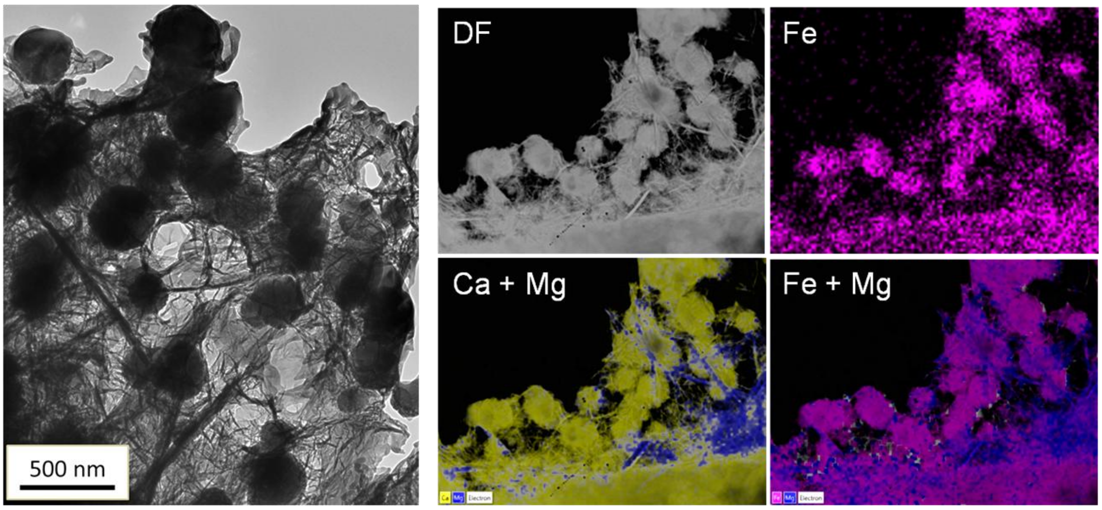

Figure 8-28: TEM micrograph of Fe flocs with associated laths within the C-S-H matrix, STEM mapping for a similar area shown on the left; DF= Dark field image, Ca - Yellow, Fe - Pink, Mg - Blue.

Figure 8-28 shows elemental mapping using scanning transmission microscopy (STEM) on an area similar to that shown on the left; it confirms the formation of Fe flocs which are interspersed with magnesium-based needles and the C-S-H binding matrix encapsulating the waste formations. The mapping confirms that the needles contained magnesium with reduced levels of aluminium, the iron response indicated the location of waste material and the smaller background response shows the potential incorporation of Fe within other phases in the system. In addition to the calcium response in the mapping a strong level of silicon was also detected, this indicated the presence of the C-S-H binding phase and potentially additional Si-substituted hydrates such as katoite.

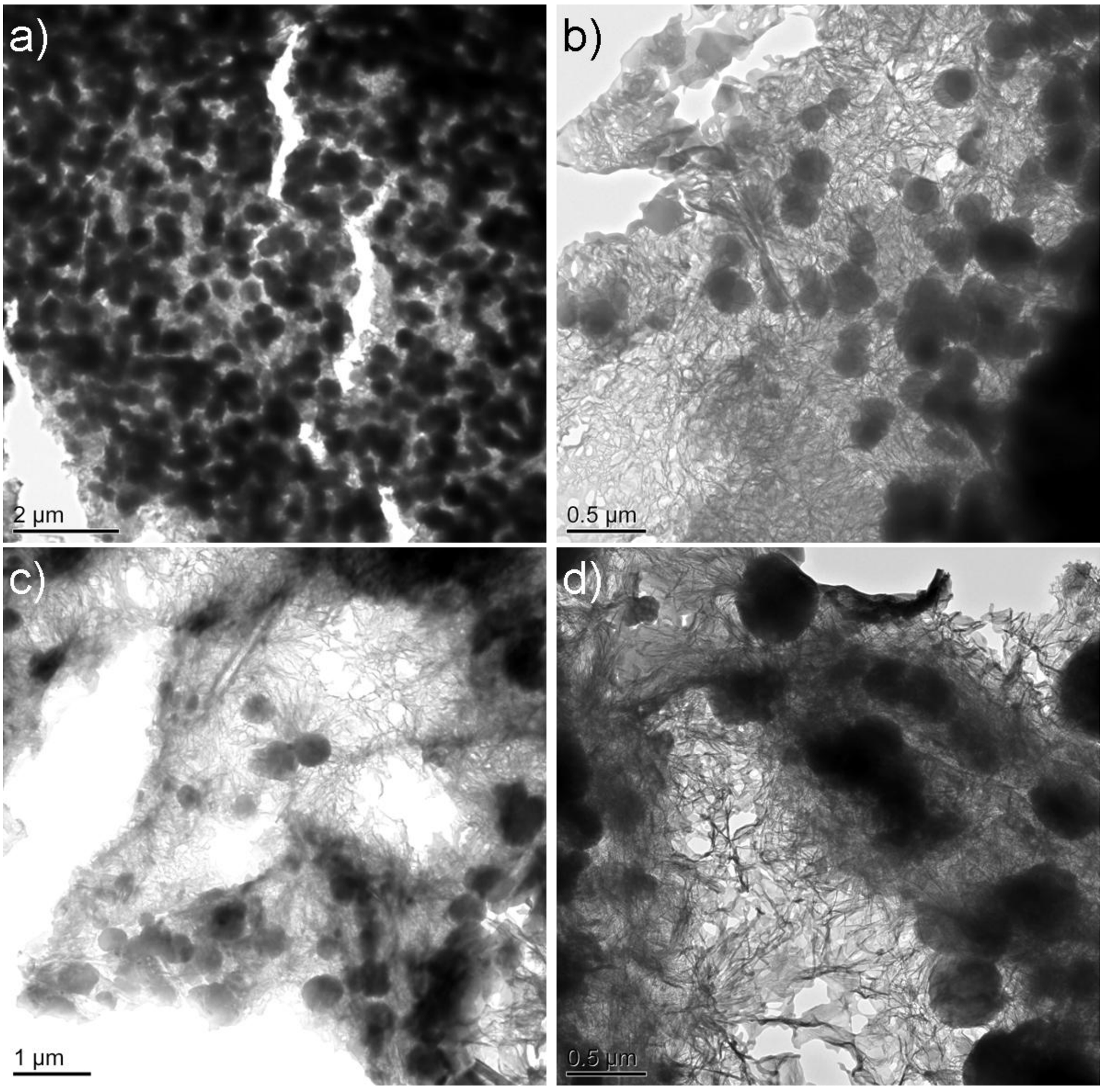

Figure 8-29: TEM micrographs of Fe floc Sample B (91-13) showing Fe-flocs incorporated within the cement matrix in varying densities with cement hydrate products

Figure 8-29 shows images from the Fe-floc B sample (91-13); image a) contains a mass agglomeration of waste floc particulates which have been bound together during the pre-treatment process with CH and incorporated within the cement matrix, this image can be compared to the SEM analysis of the same sample in figure 8-29 images c) and d). Image b) in figure 8-29 displays an area of varied C-S-H morphology with both the fibrillar and foil-like forms surrounding the edge of a floc waste region, again there is an indication of needle- like products in the vicinity of the waste material. Images c) and d) show the continued presence of waste flocs within the general microstructure of the paste, both images show more opaque dense areas and more open regions with noticeably less waste material. In image c) the morphology of the waste in the bottom left area suggests the formation of crystalline products which have formed the basis of EDX analysis indicating the presence of HG formation in this sample. Image d) shows the differing nature of the binding

C-S-H present in the darker waste encapsulated areas and much more open foil-like nature displayed in the less space constricted regions of the sample.

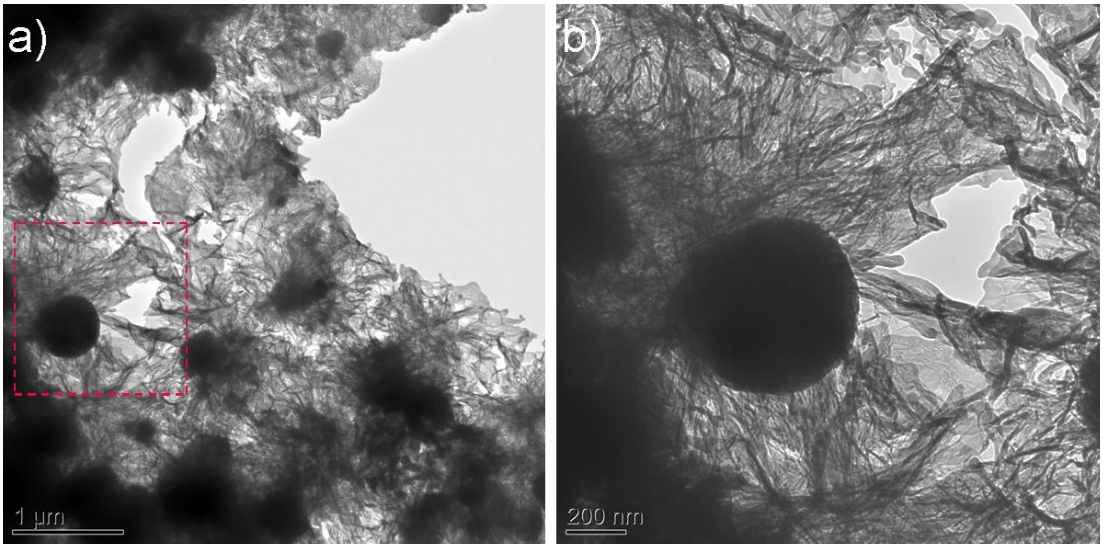

Figure 8-30: TEM micrographs of Fe floc Sample B (91-13) C-S-H surrouding Fe-flocs and enlargement of floc particulate shown in b).

Figure 8-30 displays a region which can be compared to the other Fe-floc sample (93-12) imaged in figure 8-26 images c) and d). Both samples have shown a level of incorporated flocs which have been well physically bound within the matrix as depicted in image b). Image a) shows formations in the centre which suggest the formation of differing Fe-containing phases as the morphology changes away from the uniform spherical nature of the flocs to one which is less uniform and electron opaque.

Imaging for the microstructure of the Al-floc sample (93-001) is shown in figure 8-31 images a) to d); this figure shows the hydration of PC cement particles within the matrix and the differing C-S-H morphologies formed in the respective Op and Ip regions. In the figure fully reacted cement particles are typically surrounded by higher density rims. The images show the Ip C-S-H is more foil-like and surrounded by fibrillar dense Op C-S-H presenting with an orientation away from the hydration Ip region. The Op present in this sample shows a mixed morphology, areas closer to the hydrated cement particles display a more dense fibrillar nature which is well illustrated in images c) and d). Regions further away from hydrated particles display a less dense more open morphology which becomes increasingly foil-like; this mirrors the structure for the Fe-floc sample shown in figure 8-29 image d). Thin laths of hydrated phases have been observed in the Al-floc sample shown in figure 8-31 image d), these phases have been linked to the possible formation of aluminate hydrates such as AFm and strätlingite due to their increased Al response by EDX. Small levels of AFm were detected by XRD analysis with a 2θ position consistent with monocarboaluminate, small reflections were also observed for strätlingite in the Al-floc sample which could be linked to the waste floc addition. The mixture of both fibrillar and foil-like Op morphologies for the C-S-H in the regions not in close proximity to hydrate cement particles is very similar to the TEM imaging results reported by Girão et al [68] for a PC:PFA blend at 28 days.

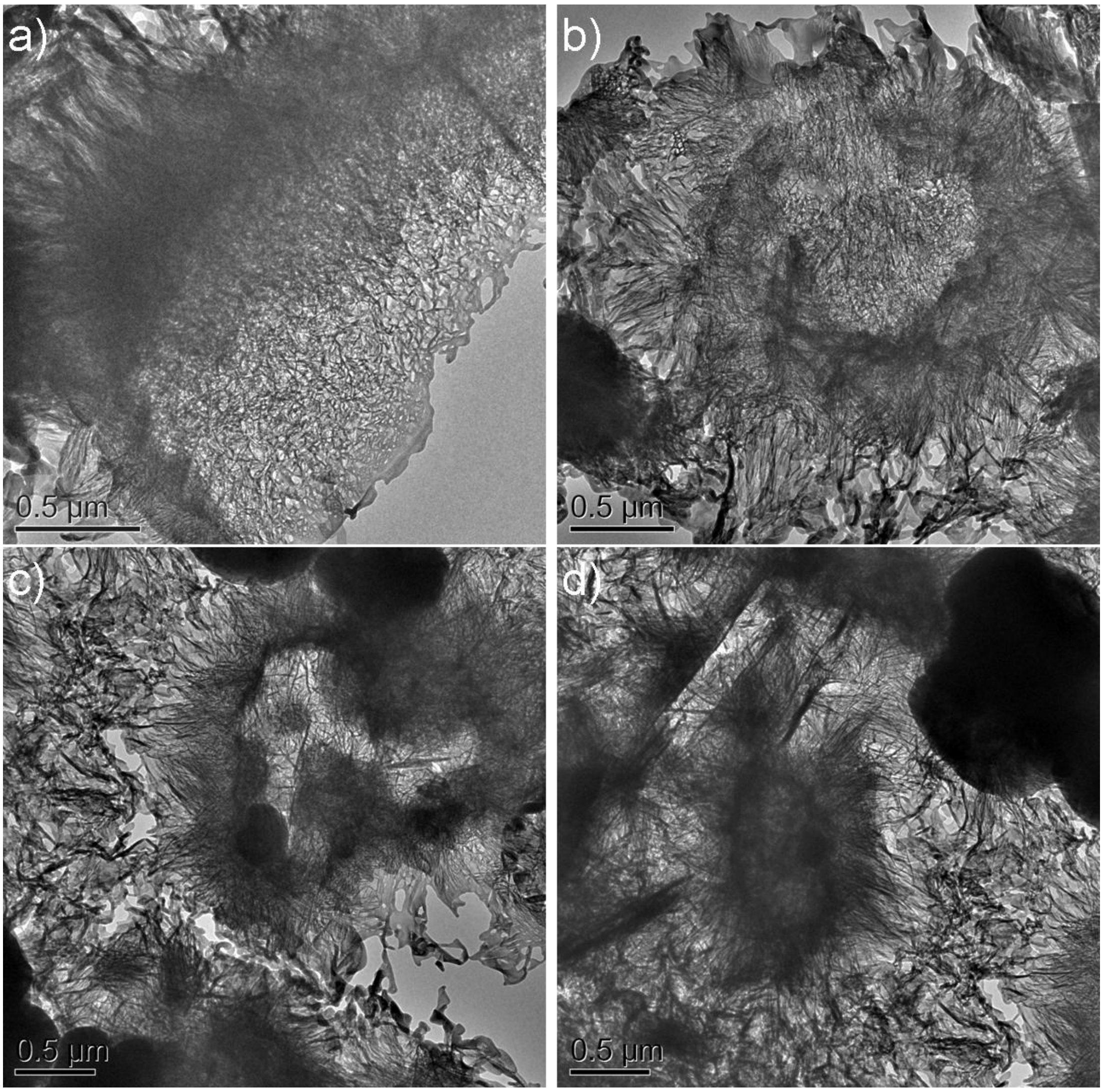

Figure 8-31: TEM micrographs of Al floc Sample B (93-001)

Figure 8-32 displays the partially and fully-reacted fly ash particles within the microstructure of the blended paste; image a) clearly displays a thin reaction rim with directionally aligned fine Ip hydrate forming inside the fly ash particle. This partially reacted sphere is surrounded by outer product C-S-H and crystalline formations which represent as darker regions around 200-500 nm in size, these have a chemical composition indicating a hydrogarnet phase. Image b) shows a fully-reacted fly ash particle containing Ip product with a noticeably different morphology to that typically exhibited in the local Op structure.

This is assumed to be due to both the differing chemical composition containing additional Al and Si and the reduced space constraints from filling the space previously occupied by the fly ash particle. This area is clearly marked by a noticeable dark, dense hydration rim formed at the original boundary for the fly ash particle; again the reaction rim shows hydrogarnet formation which was typical for the examined samples.

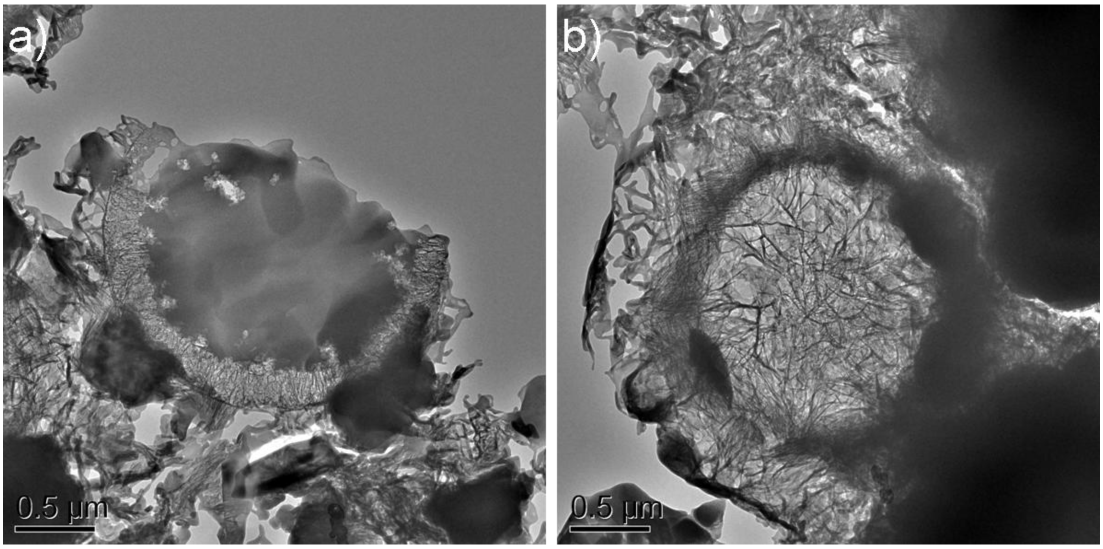

Figure 8-32: TEM micrographs of Al floc Sample B (93-001) of a) partially reacted fly ash particle with HG formations, b) fully reacted fly ash particle with formed C-S-H

The fibrillar nature of the Op products is again shown below in figure 8-33 which is typical for this sample, the microstructure in the locality to the encapsulated waste-stream is shown in image b). As can be seen in this image the morphology of the C-S-H is variable with more dense filbrillar C-S-H observed around hydrated particles, additionally formations of products rich in Al were found intermixed in the microstructure.

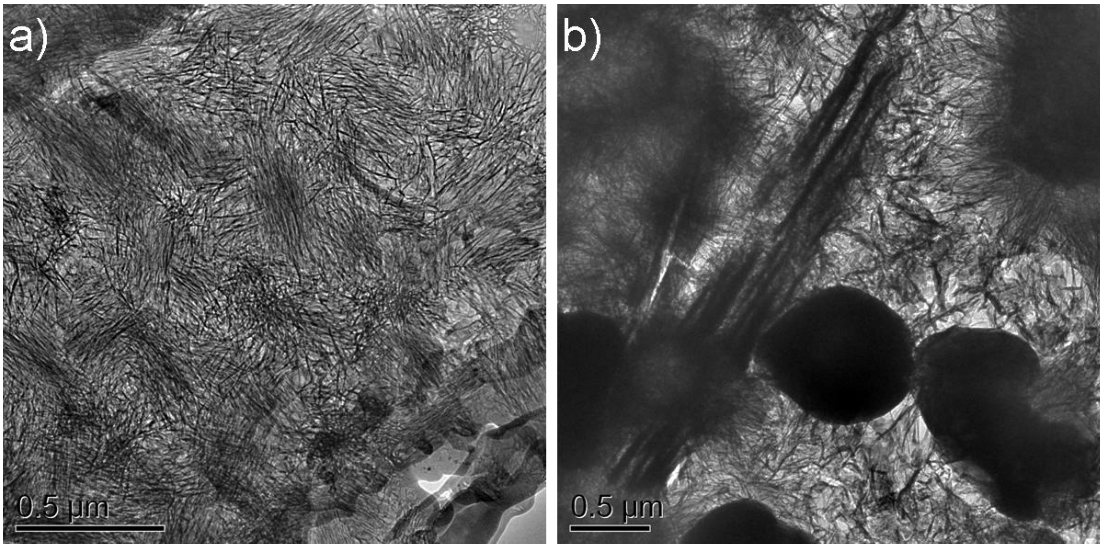

Figure 8-33: TEM micrographs of Al floc Sample B (93-001) of a) formed Op C-S-H and b) Incorporated flocs and AFm laths

8.5.1 TEM-EDX

The TEM-EDX analyses for the 3 floc samples are displayed through figure 8-34 to 8-39, all samples showed a relatively similar distribution for the C-S-H composition. Due to the potential for Fe incorporation from the floc waste addition, these figures report both the Si/Ca against Al/Ca and Al+Fe/Ca atomic ratios. All samples showed a varying response from the inclusion of flocs with potential formation of a hydrogarnet phase associated with the waste addition and PFA.

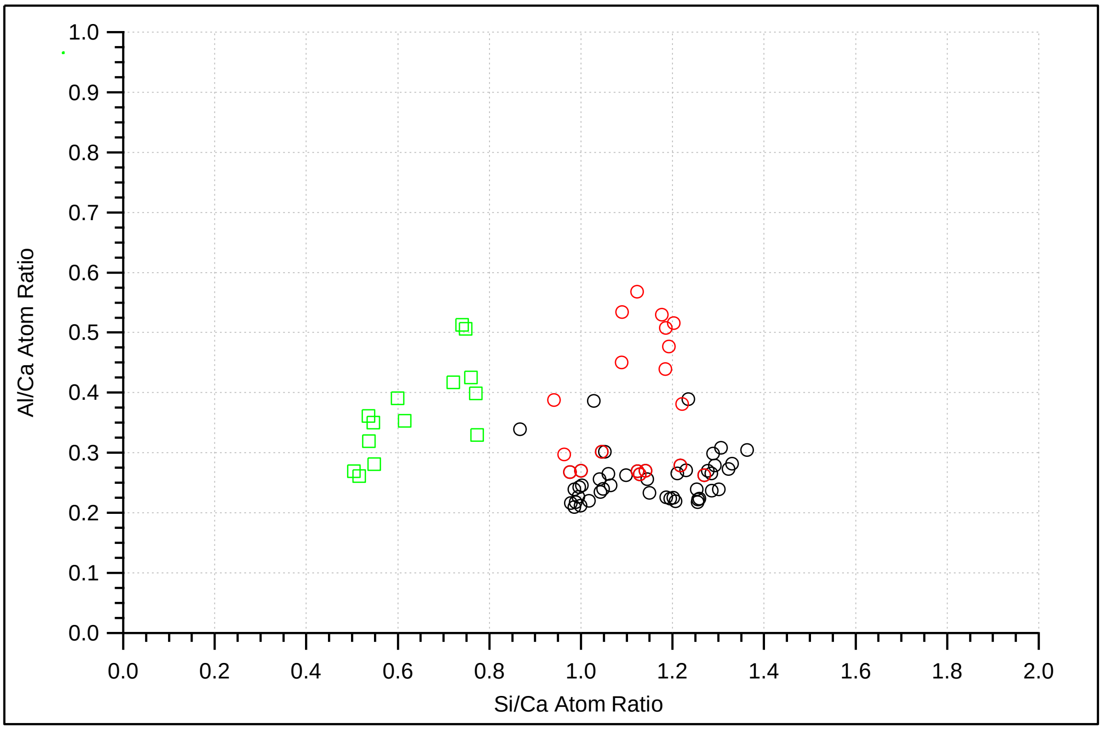

Figure 8-34: TEM-EDX showing Si/Ca v Al/Ca atomic ratios of Fe Floc A 93-12; C-S-H - ○, C-S-H + Mg phase -○, Waste associated phase - ☐

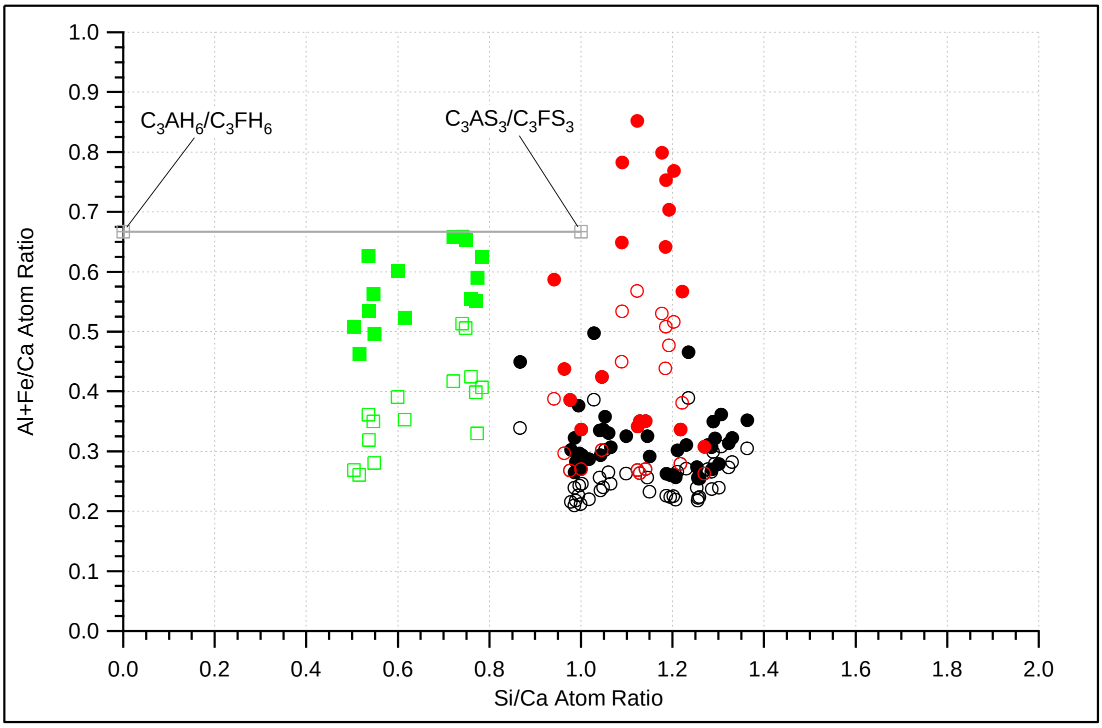

Figure 8-35: TEM-EDX showing Si/Ca v Al+Fe/Ca atomic ratios of Fe Floc A 93-12 plotted over the EDX points shown in figure 8-34; C-S-H - ●, C-S-H + Mg phase - ●, Waste associated phase - 🟩

Figures 8-34 and 8-35 show the Fe-floc A sample data points which displayed a wide ranging Si/Ca distribution of 1.0 - 1.35 with a mean value of 1.14. The averaged Al/Ca ratio of the C-S-H cluster in figure 8-34 was 0.26 which is within the estimated boundaries of a highly substituted Al-binding phase. When the Al+Fe/Ca atomic ratio for the C-S-H cluster is compared to the Al/Ca ratios an average increase of 0.061 is observed; a summary of the atomic ratios is listed in table 8-4. Additionally an Mg containing phase is shown which is assumed to be a hydrotalcite phase similar to that described in slag cement pastes due to the added aluminium content; the composition of this phase is discussed later in figure 8-40. The tie-line indicating the possible HG compositions relating to the Si/Ca and Al+Fe/Ca ratios is included in figure 8-35; the waste associated phase denoted in figure 8-35 was found in proximity to the flocs and was imaged in figures 8-26 and 8-27 for this sample. This phase presented two distinct groupings for the Si/Ca content so were analysed separately for this sample, the cluster on the left (a) and right (b) of figure 8-35 gave the following values if the averaged Si/Ca ratios where used to estimate their composition.

$$a)\ C_3A_{0.60}F_{0.40}S_{1.62}H_{2.76}$$

$$b)\ C_3A_{0.66}F_{0.34}S_{2.23}H_{1.54}$$

Equation 8-7: Estimation of hydrogarnet composition in Fe floc A sample by TEM-EDX

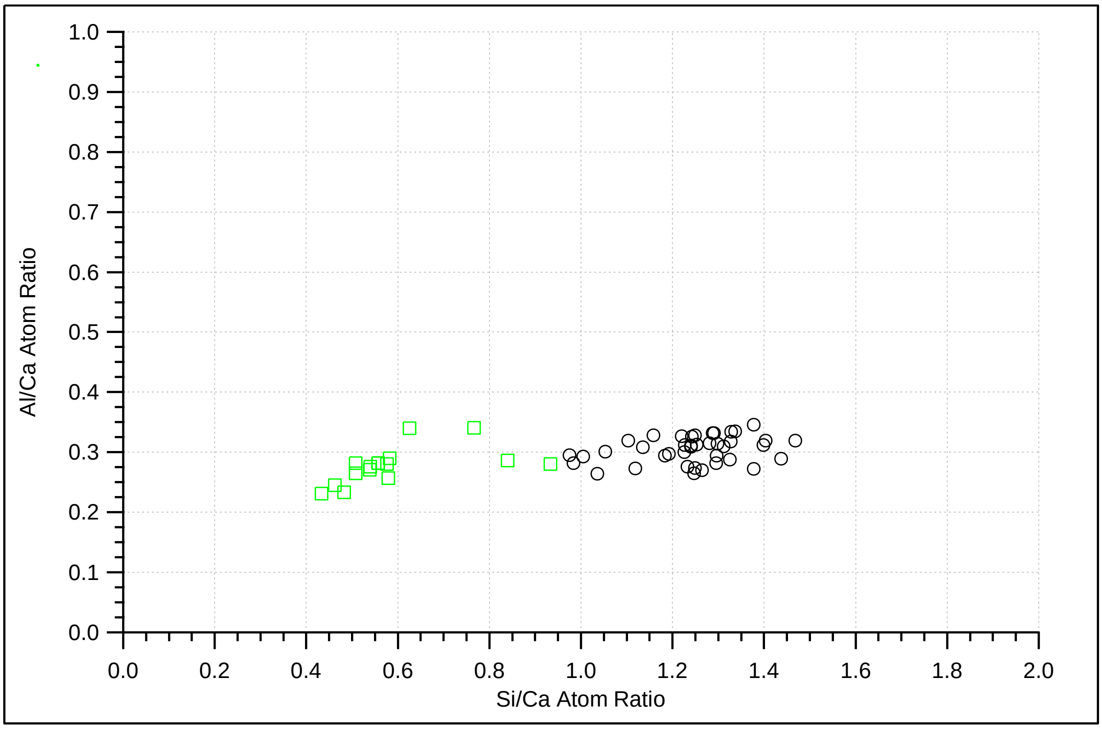

Figure 8-36: TEM-EDX showing Si/Ca v Al/Ca atomic ratios of Fe Floc B 91-13; C-S-H - ○, Waste associated phase - □

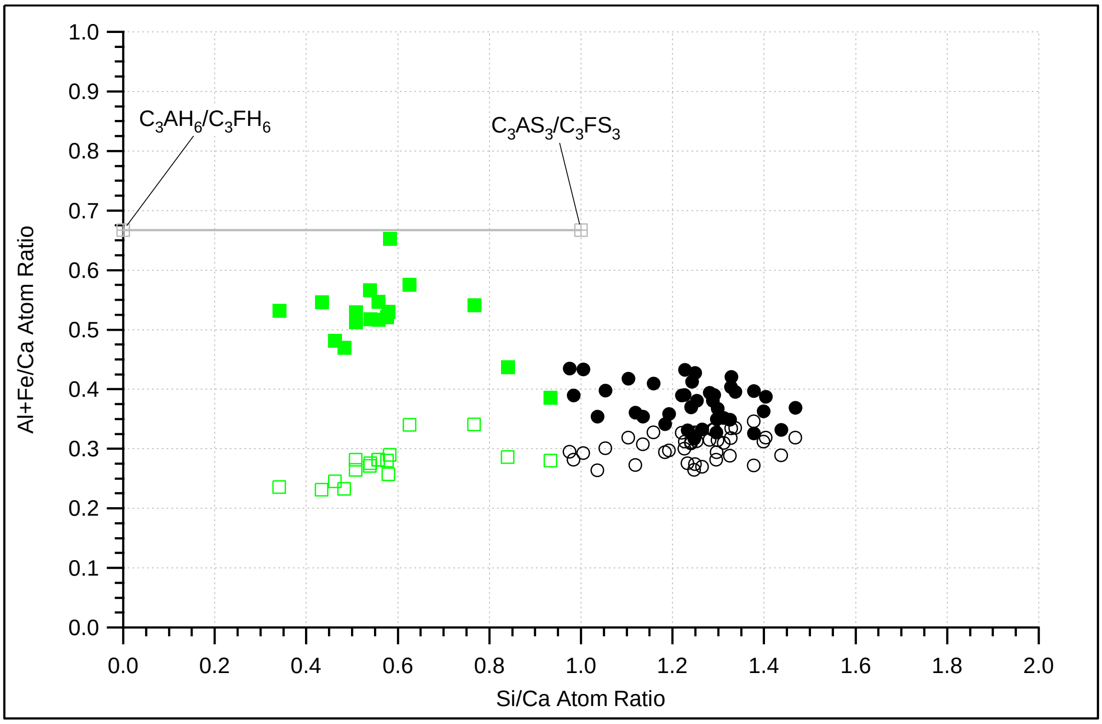

Figure 8-37: TEM-EDX showing Si/Ca v Al+Fe/Ca atomic ratios of Fe Floc B 91-13 plotted over the EDX points shown in figure 8-36; Op C-S-H - ●, Waste associated phase - 🟩

The Fe-floc B sample shows a similar response for the C-S-H cluster with a Si/Ca ratio mean of 1.24 and a Al/Ca mean of 0.30 as shown in figure 8-36, no magnesium - aluminium product was analysed for this sample. Figure 8-37 shows the Al+Fe/Ca ratios overlaid over the previous data points this again shows a level of Fe addition with the mean Al+Fe/Ca ratio for the C-S-H cluster showing an average increase of 0.072. The phase associated with the waste flocs was again analysed and the composition sat within the limits for a HG phase displayed in figure 8-8. Using the averaged Si/Ca, Al/Ca and Al+Fe/Ca ratios from TEM-EDX the estimated composition of this phase in the Fe-floc B sample was:

$$C_3A_{0.52}F_{0.48}S_{1.63}H_{2.74}$$

Equation 8-8: Estimation of hydrogarnet composition in Fe floc B sample by TEM-EDX

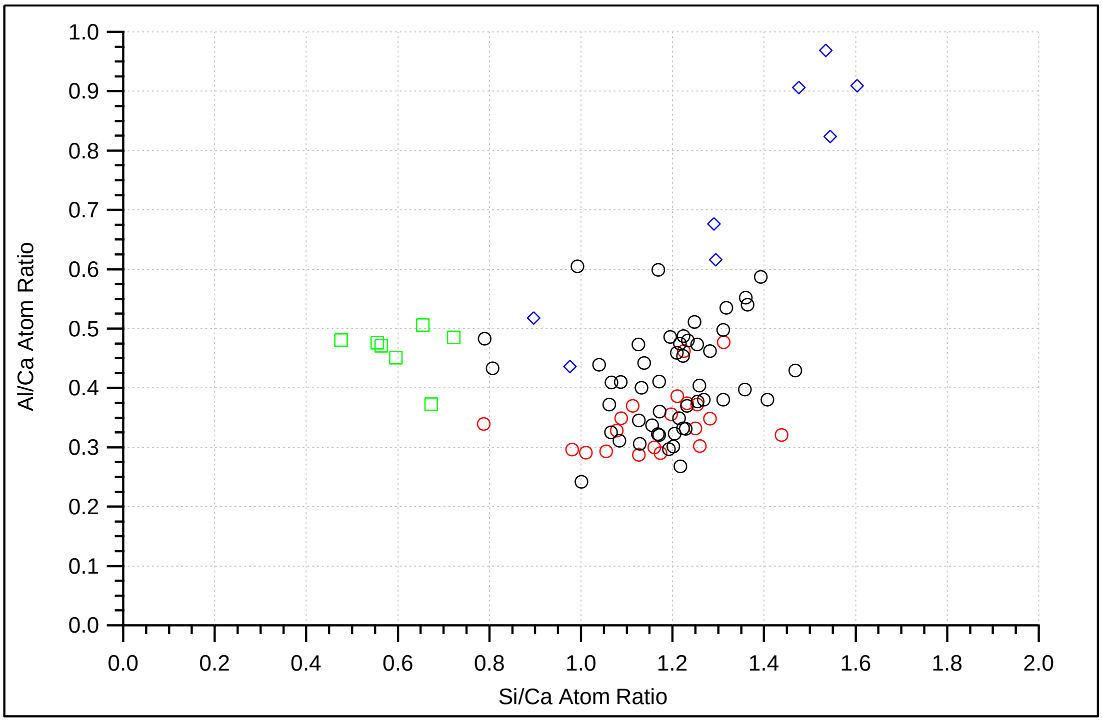

Figure 8-38: TEM-EDX showing Si/Ca v Al/Ca atomic ratios of Al Floc 93-001; PC Ip C-S-H -○, Op C-S-H - ○, Ip PFA formations -◇,Hydrogarnet associated with PFA - ☐

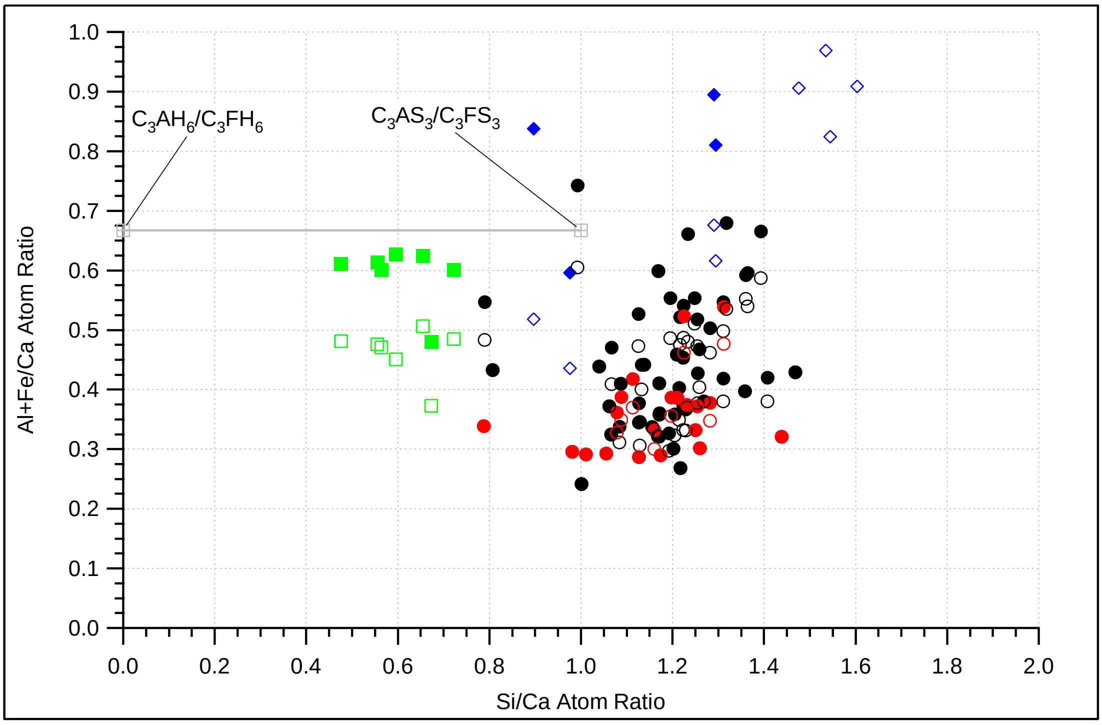

Figure 8-39: TEM-EDX showing Si/Ca v Al+Fe/Ca atomic ratios of Al Floc 93-001 plotted over the EDX points shown in figure 8-38; PC Ip C-S-H - ●, Op C-S-H - ●, Ip PFA formations - ◆, Hydrogarnet associated with PFA - ■

Figures 8-38 and 8-39 show the Al-based floc sample data points, these again show a range of Si/Ca ratios from 1.05-1.25; in this sample a number of Ip regions were analysed as imaged earlier in figures 8-31 and 8-33. The mean Si/Ca atomic ratio for the Op and Ip phases analysed was 1.19 and 1.16 respectively. The phases both showed a range of Al/Ca contents from 0.3-0.4 with a mean of 0.41 for the Op and a lower value of 0.34 for the Ip phase. Figure 8-39 shows the Al+Fe/Ca ratio overlaid on the previous data points due to the suspected Fe content which is still present in the encapsulated waste material; the data shows a potential small increase in the value when compared to the Al/Ca ratios for some data points. The mean values for the data reflect that the Op seems to be more affected than the Ip phase by the inclusion of Fe with an increase to 0.45 for the Op Al+Fe/Ca ratio whilst the Ip showed a smaller increase to 0.36. The suspected HG crystal phase was again analysed for this sample and an example can be seen in figure 8-30; due to the proximity of these crystals to the PFA in the image they are described as being associated with the PFA and not the waste phase. Using the averaged Si/Ca, Al/Ca and Al+Fe/Ca ratios from TEM-EDX the estimated composition of this phase for the Al floc sample was:

$$C_3A_{0.72}F_{0.28}S_{1.79}H_{2.42}$$

Equation 8-9: Estimation of hydrogarnet composition in Al floc sample by TEM-EDX

Sample		Ca/Si	Si/Ca	Al/Ca	Al+Fe/Ca
Fe floc A 93-12		0.88	1.14	0.26	0.32
Fe floc B 91-13		0.81	1.24	0.30	0.37
Al floc 93-001	**Ip C-S-H**	0.86	1.16	0.34	0.36
	Op C-S-H	0.84	1.19	0.41	0.45

Table 8-4: Mean atomic ratios for CSH phases in the floc samples examined by TEM-EDX

All of the samples indicated a hydrogarnet phase from TEM-EDX analysis showing a level of partial substitution of SiO_4 by OH groups to form a katoite-like phase; additionally the Al^{3+} in all the hydrogarnets measured has been substituted with a pronounced level of Fe^{3+} measured by EDX . The presence of Si and marginally substituted hydrogarnets has been reported previously for PC:PFA blends [68, 69, 279]. However the level of Fe substitution and relevant intensity of the XRD peaks for this phase suggests the waste incorporation has had a major effect upon the formation of the hydrogarnet. Both of the Fe-floc samples showed the highest levels of Fe^{3+} incorporation according to the TEM-EDX at between 35-50%, as would be expected the Al-based floc sample has a lower level of Fe incorporation at approximately 28%.

Taylor [235] gave the following empirical equation for deriving the unit cell parameter of the hydrogarnet from the chemical composition:

$$a = 1.171 + 0.016Fe_2O_3 + 0.0144H_2O$$

Equation 8-10: Cell parameter estimation for hydrogarnet by Taylor [235]

Where a is the unit cell parameter expressed in nm, use of the above equation gives the following values for the unit cell parameter for the floc samples:

$$Fe\ floc\ A\ (93/12)\ a = 1.171 + 0.016(0.40) + 0.0144(3.42) = \ 1.2266\ nm\ (est\ i)$$

$$Fe\ floc\ A\ (93/12)\ a = 1.171 + 0.016(0.34) + 0.0144(3.74) = \ 1.2303\ nm\ (est\ ii)$$

$$Fe\ floc\ B\ (91/13)\ a = 1.171 + 0.016(0.48) + 0.0144(3.52) = \ 1.2294\ nm$$

$$Al\ floc\ A\ (93/001)\ a = 1.171 + 0.016(0.28) + 0.0144(4.04) = \ 1.2337\ nm$$

Equation 8-11: Cell parameter estimations using Eq 8-10; values obtained from estimations provided in Eq 8-6

These values can be compared to the equations 8-1 (*a=12.561-0.236(3-x)*) for a Al-hydrogarnet and 8-2 (*a=12.719-0.227(3-x)*) for a Fe-hydrogarnet by using the Si (*3-x*) found by TEM-EDX to calculate the possible range of unit cell for a given level of Si substitution. Both of the estimations for the TEM-EDX data can then also be compared to the unit cell parameter calculation determined from XRD measurements outlined earlier in section 8.2, these values are all plotted in table 8-5 which includes the two estimations generated by sample 93-12 from TEM.

Sample	Eq 8-10 (Taylors)	Eq 8-1 ($Al_{1.00}$)	Eq 8-2 ($Fe_{1.00}$)	XRD
Fe floc A *93-12 (Est i)*	1.2266	1.2179	1.2351	1.2335
Fe floc A *93-12 (Est ii)*	1.2303	1.2035	1.2213	1.2335
Fe floc B *91-13*	1.2294	1.2176	1.2349	1.2363
Al floc *93-001*	1.2337	1.2138	1.2313	1.2390

Table 8-5: Comparisons of Hydrogarnet unit cell parameter estimation by differing techniques (values given in nm)

The values for $Al_{1.00}$ and $Fe_{1.00}$ indicate the possible minimum and maximum values for the unit cell parameter given the measured Si content from the TEM analysis, as the relationship between Si content and unit cell size has been expressed by these show the potential cell size change due to Fe substitution. As can be seen in table 8-5 the values calculated by Taylor's equation 8-10 are the lowest and are similar to the predictions for a Al-hydrogarnet given by equation 8-9. As the unit cell size increases with the substitution of Fe into the crystal structure the relative silicon content for Taylors value to be correct would have to be quite large (1.7-2.3), increasing with additional Fe content whilst this is possible it does not agree with the measured levels of Si from TEM analysis or the reported unit cell size by XRD. Comparison of the estimated cell parameter by use of the TEM-EDX Si content and figure 8-3 gave a good comparison for the Fe-floc A (Eq 8-7) to the XRD with the value (1.2335) lying in-between the values agreeing with a Fe-substituted hydrogarnet. However the other results generally placed the calculated XRD value beyond the $Fe_{1.00}$ maximum for that given Si content, this suggests the Si content is potentially overestimated by TEM analysis as even slight reductions in the Si value would place the results in line with the XRD unit cell values. By comparison the compositions determined by XRD with input from the TEM-EDX data discussed in section 8.2 predicted a reduced Si content which was discussed in section 8.2.1.

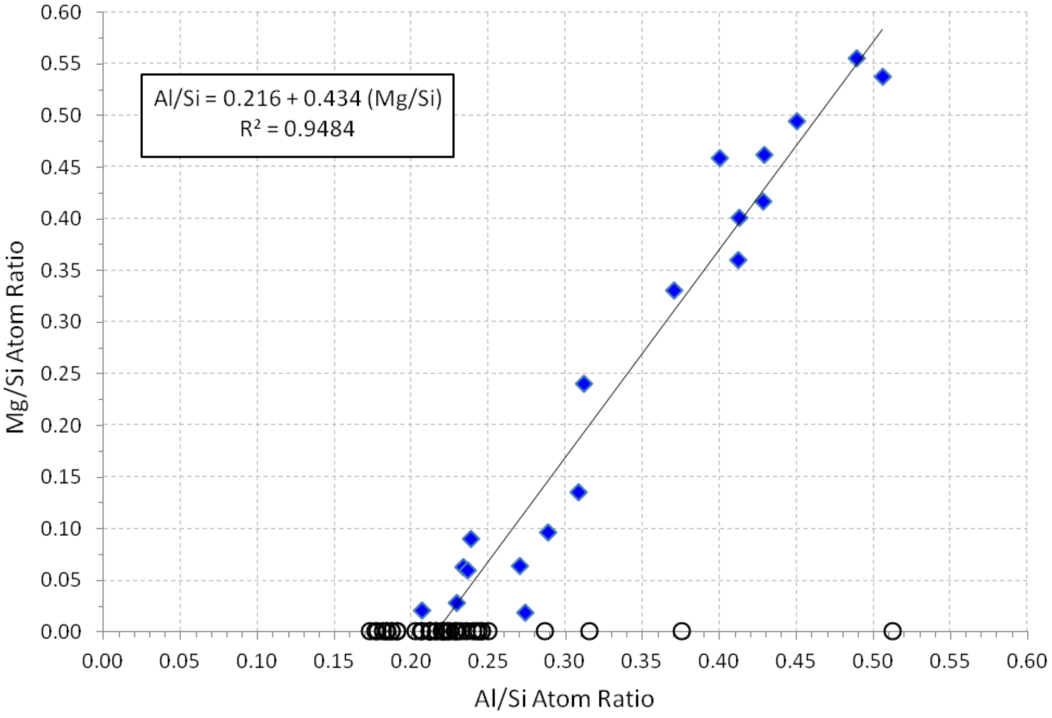

Figure 8-40: Mg/Si against Al/Si atom ratio plots of TEM EDX analyses of Op C-S-H (○) and intermixed hydrotalcite product (◆) observed in Fe floc A sample (93-12)

The hydrotalcite-like magnesium bearing phase discussed earlier and shown in figures 8-26 and 8-28 was analysed using TEM-EDX to determine its atomic ratio, the EDX analyses of the magnesium-bearing laths intermixed with C-S-H did indicate a trend line which suggested the presence of a hydrotalcite-LDH like phase. The analysed phase is shown in figure 8-40 with the linear regression line indicating a Mg/Al ratio of 2.03 which is in the expected range for a hydrotalcite-like phase in hydrated cement pastes [38, 39, 43]. The estimated Al/Si ratio when Mg/Si=0 is 0.216 which is comparable to the average Al/Si atomic ratio measured for the C-S-H phase in this sample.

8.5.2 Nanostructural model for C-S-H

As discussed in previous chapters the TEM-EDX data can be compared with the tobermorite-jennite (T/J) and tobermorite - 'solid solution' calcium hydroxide (T/CH) models for the nanostructure of C-S-H proposed by Richardson and Groves [24, 26, 239]. The Si/Ca against Al/Ca plots in figures 8-41 to 8-43 show the experimental TEM-EDX and the theoretical structural plots using the approach outlined in previous chapters. The addition of Al+Fe/Ca ratio plots was deemed necessary in this chapter due to the potential for Fe^{3+} inclusion into the bridging sites in a similar fashion to the Al^{3+}.

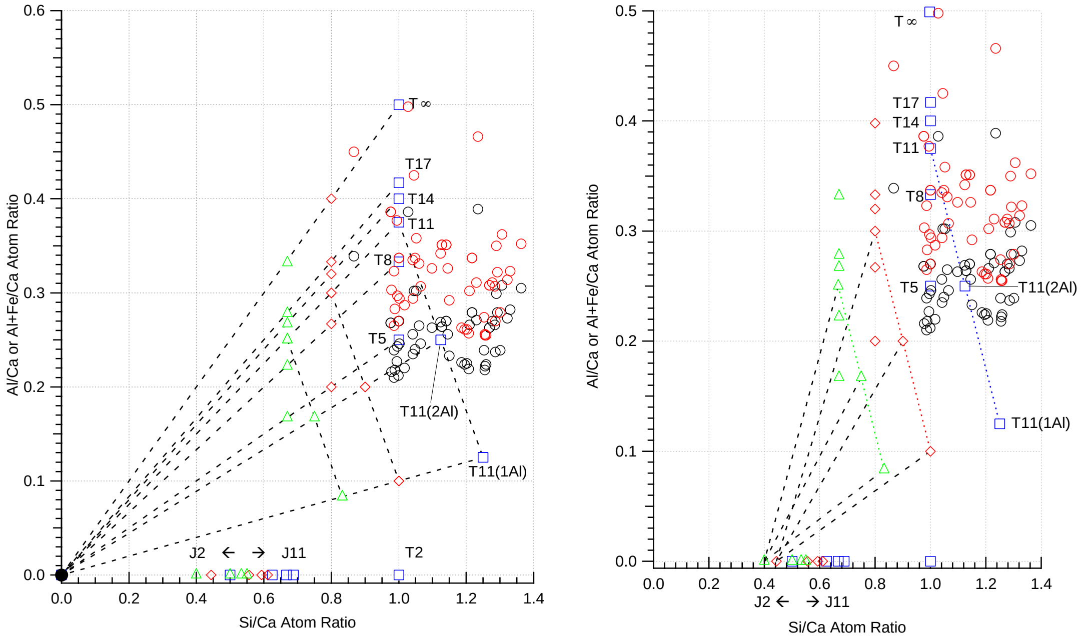

Figure 8-41: Si/Ca against Al/Ca (○) or Al+Fe/Ca (○) atom ratio plot of TEM-EDX analyses of C-S-H present in PFA:OPC Fe floc A sample (93-12). The additional symbols represent the compositions of tobermorite (T) and jennite (J) based structural units with different levels of protonation of the silicate chains: the minimum (△; w/n=0), intermediate (◇; w/n=1) and maximum (□; w/n=2). The additional points included represent tobermorite- based units with chain lengths of 2, 5, 8, 11, 14, 17 and ∞. All units are assumed to be saturated with Al where possible. (ie all the occupied bridging sites are occupied by Al rather than Si). The only exception is for units with 11 tetrahedral chain length, as additionally to those saturated with Al (T11) those with only one or two of the three possible bridging sites are also shown labelled as (T11(1Al) and (T11(2Al)

respectively. The black dashed lines join points for structural units of the same chain length but different degrees of protonation to CH on the left and to Jennite based dimer of the same protonation on the right. T11 units with the same protonation but differing Al content are joined by coloured dashed lines.

The atomic ratio plots for the Fe-floc A sample (93-12) are presented in figure 8-41, as expected from the mean atomic ratios in table 8-4 the measured Si/Ca ratio is very high with portion of analyses beyond that expected in normal conditions. The Al/Ca and Al+Fe/Ca atomic ratios fall generally within the confines expected for a highly substituted tobermorite (T/CH) model. When the Al/Ca is only considered the data suggests that a partially substituted T11(2Al) chain would be the most suitable structural unit. However when the Fe content is also considered a general upward shift in the Al+Fe/Ca ratio is observed on average by 0.061. This indicates a higher level of bridging site occupation with the tie-lines in figure 8-41 suggesting partially and fully substituted chain lengths in a range of T5 to T11.

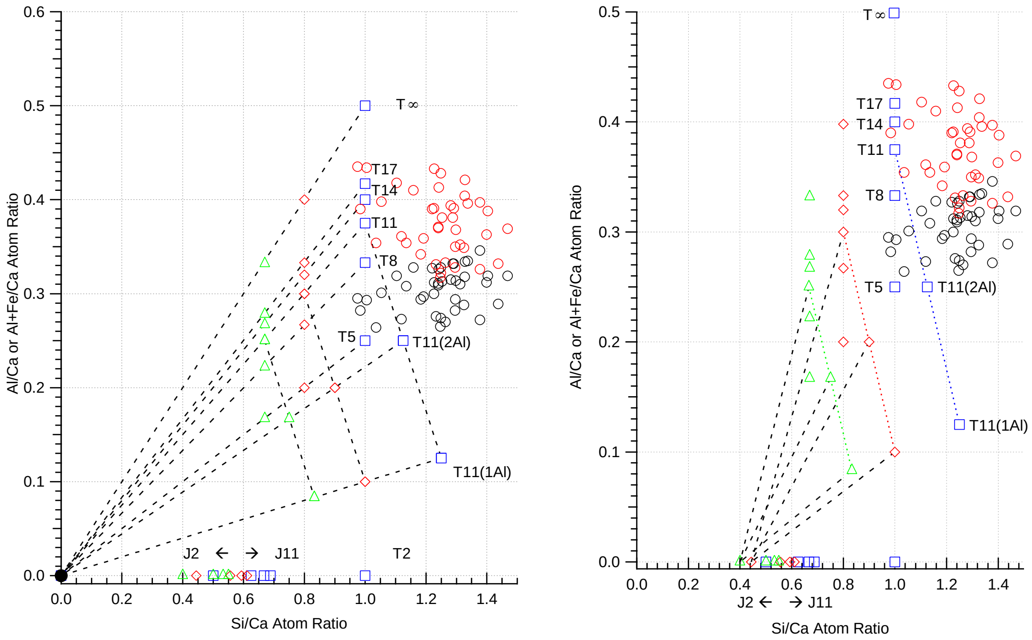

Figure 8-42: As figure 8-31 but TEM-EDX analyses of C-S-H relate to the PFA:OPC Fe floc B sample (91-13)

The results for the Fe-floc B sample (91-13) show a similar trend to that reported for the Fe-floc A, again the Si/Ca is high and beyond that reported for fly ash/PC grouts [68, 279]. The measured Al+Fe/Ca ratios are within the potential boundaries for the structural models with a noticeable shift on average of 0.072 when the detection of iron is considered. This leads to a similar conclusion to the previous Fe-floc sample with a fully substituted chain length being the most appropriate in the order of T5 to T17.

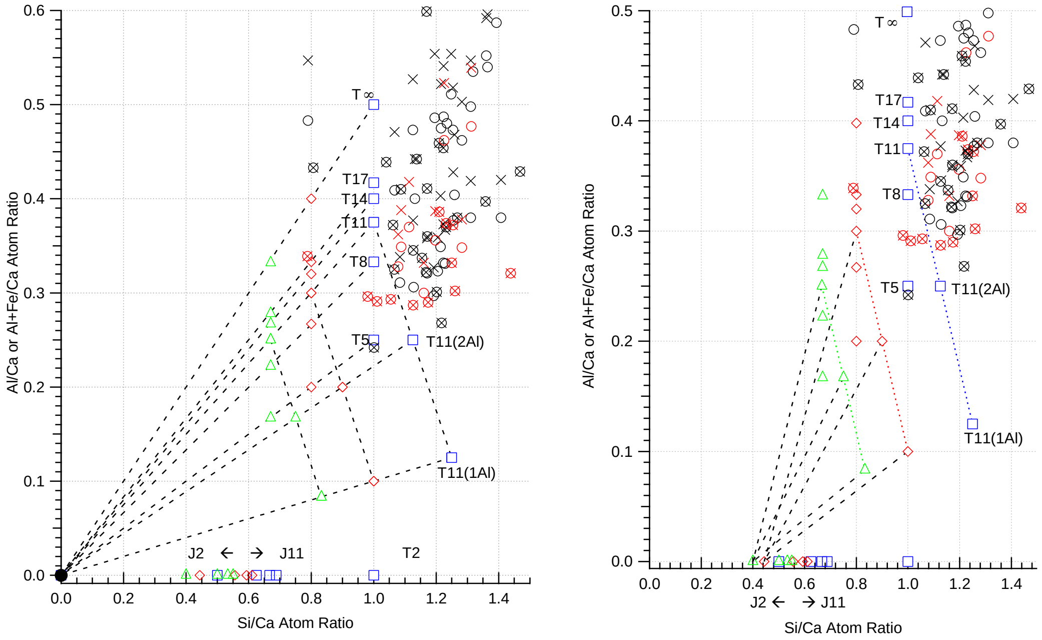

Figure 8-43: As figure 8-31 but TEM-EDX analyses of C-S-H relate to the PFA:OPC Al floc sample (93-001); Ip C-S-H Al/Ca - (○) Al+Fe/Ca -(×), Op C-S-H Al/Ca - (○) Al+Fe/Ca -(×)

The Al-floc results are presented in figure 8-43 and show a similarly high Si/Ca atomic ratio which is slightly reduced in comparison to the Fe-flocs, in this sample substantial Ip and Op C-S-H analyses were completed so they can be compared. The Al/Ca and Al+Fe/Ca atomic ratios for the Ip product show very similar results with only insubstantial level of iron detected in the phase. The overall ratios for the Ip suggest a high level of primarily Al incorporation with fully substituted chain lengths being the most appropriate. When considering the Op product a higher more varied iron content is presented with an average increase of 0.041 detected, this is however noticeably lower on average than that observed in the Fe-floc samples. Again for the Op product a fully substituted chain is the most appropriate proposed structural unit at potentially longer chain lengths. Generally across the 3 floc samples there was a noticeably lower Al/Ca ratio in the iron based flocs compared to the Al-floc agreeing with the starting waste compositions. This shows the measurable effect the waste-stream is having upon the hydrated phases. As the Al content decreased in the Fe-flocs the measured atomic percentages for iron increased; this results in all the flocs showing evidence for highly or fully substituted silicate chain lengths in their respective nanostructures.

The TEM-EDX data for the floc sample displayed a high Si/Ca atom ratio consistently across the three samples, these fell beyond the boundaries for a single-chain tobermorite model. To explain this the average C-S-H unit could be described as a mixture of single, double or cross-linked C-A-S-H phases. This would explain the observed experimental data and allows for the samples to be discussed within the Richardson and Groves' nanostructural model. The structural-chemical formulae for double-chain and cross-linked C-A-S-H phases has been recently discussed by Richardson [284], further discussion into double-chain tobermorite is included in section 8.6.1.

8.6 NMR

The solid-state 27Al NMR spectrum for the Al-floc sample was measured at the EPSRC UK National Solid-state NMR service at Durham University due to the potential Al interactions in this sample. The application of MAS NMR on the PFA based samples particularly for these ferric systems was limited due to the extremely high levels of paramagnetic material. Some work on ^{29}Si NMR was completed at the University of Leeds this was normally accomplished after the removal of the magnetic material prior to analysis.

8.6.1 ^{29}Si MAS NMR

NMR studies were completed on the Fe-floc A sample (93-12) as discussed, initial results however were limited due to the nature of the samples. Figure 8-44 displays a NMR spectrum for the sample after the removal of magnetic material which on average accounted for 70% wt of the sample. Q^0 indicates the presence of significant quantities of unreacted anhydrous material such as C_2S which has a chemical shift at -71ppm, the presence of un-hydrated material was found during examination of the microstructure using SEM and was confirmed as being present by NMR. For the hydrated material the smallest noticeable peak was at -79ppm assigned to the resonance for the Q^1 end-chain group, the large peak assigned to the Q^2 resonance (-85ppm) represented mid-chain units in this sample. Between the two aforementioned peaks a definite step can be identified at around -82ppm attributed to the presence of Q^2(1Al) groups within the silicate anion structure. These results suggest that at these extended curing periods and fly ash replacement levels substantial polymerisation of the C-S-H phase occurs; which results in the relative lower intensity of the Q^1 group and higher relative intensity of the Q^2 groups. The spectra also indicates the large-scale substitution of Al^{3+} ions into the bridging sites within the C-S-H drierkette chain lengths, these results in part agree with and explain the observed TEM-EDX results.

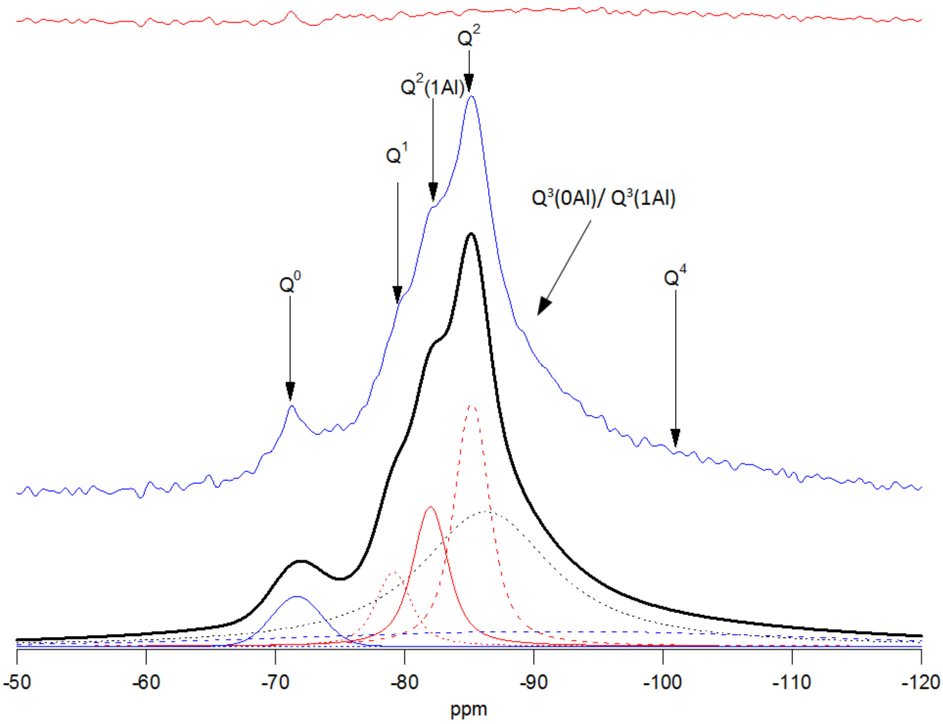

Figure 8-44: ^{29}Si MAS NMR spectra for PFA:OPC + Fe floc (93-12) magnetic particles removed

The effect of the removal of paramagnetic materials can be observed by the extremely small response of the Q^4 peak which is attributed to the presence of unreacted anhydrous PFA particles; prior to the removal this Q^4 was dominant in the spectrum. Due to the extremely large proportion of the sample removed due to their magnetic properties the NMR results for the sample should be used as only an indication of the possible silicate anion structure of the material.

As discussed in section 8.5.2 an explanation for the observed experimental EDX data was the inclusion of double or cross-linked C-A-S-H chain lengths. In addition to the Q tetrahedra present in single-chain C-A-S-H phases, double-chain tobermorites also have Q^3(0Al) and Q^3(1Al) sites [284]. As annotated in Figure 8-44 there is a noticeable response potentially for a Q^3 phase for the Fe floc 93-12 sample, this would support the proposal that double/cross-linked chain lengths are present in the C-A(F)-S-H phase.

8.6.2 ^{27}Al MAS NMR

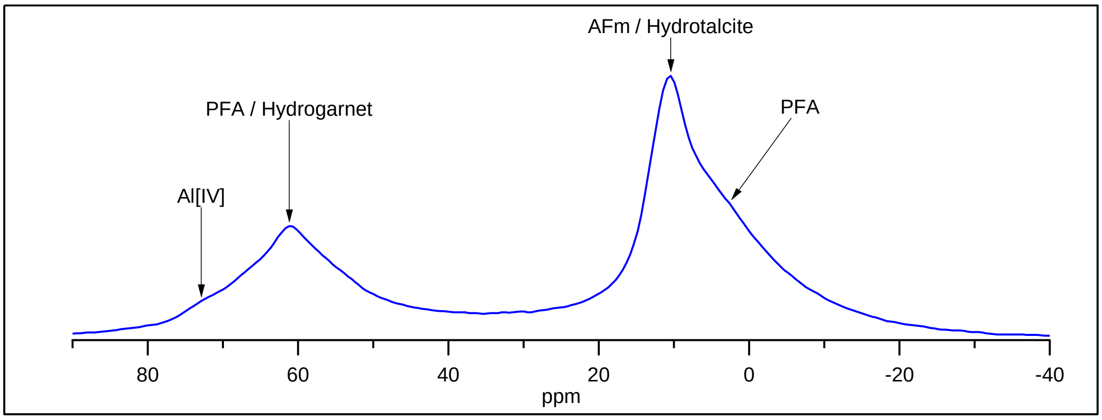

Figure 8-45: ^{27}Al MAS NMR spectra for PFA:OPC + Al floc (93-001)

The ^{27}Al MAS NMR spectra for the Al-based floc sample is shown above in figure 8-45 as discussed in previous chapters, phases for tetrahedrally (Al [IV]) coordinated and octahedrally coordinated Al are labelled which correspond to hydrated calcium aluminate phases [285]. A broad peak labelled (Al [IV]) is associated with levels of tetrahedrally coordinated aluminium substituted into the C-S-H phase as discussed in earlier chapters.

The strong resonances at approximately 62 ppm and 8 ppm have been linked to the Al (IV) and Al (VI) responses for Al-containing unreacted PFA particles in literature on hydrated PFA containing cements [286]. As the replacement levels of PFA in this system are high and the presence of unreacted PFA particles containing Al have been confirmed by SEM analysis (figure 8-12) this response is not unexpected. However there are additional phases which could be attributed to the Al responses measured in figure 8-45, strätlingite has been mentioned as hydration product in this sample and is known to produce chemical shifts at around 6ppm and 60ppm [226]. Additionally the composition of the hydrogarnet phase found from XRD analysis is of interest, as the hydrogarnet is known to contain a level of aluminium which resides within a tetrahedral coordination within the crystal structure.

The main octahedral peak in this sample is centred at approximately 10ppm which can be linked to the formation of AFm phases and the magnesium-aluminium hydrate hydrotalcite. The presence of small quantities of AFm phases within the floc samples have been confirmed by XRD analysis and electron microscopy imaging of the microstructure, unfortunately as previously discussed the composition of the AFm phase cannot be determined by ^{27}Al NMR analysis alone due to near identical chemical shifts [136]. The formation of hydrotalcite is possible due to its presence in proximity to flocs as found during TEM imaging of the samples.

8.7 Conclusions

The aged simulant floc PFA:OPC systems all produced a well solidified waste-form which seemed largely defect free. The microstructure displayed a relatively porous matrix containing large agglomerations of waste particles which showed good levels of physical encapsulation. Significant quantities of C-S-H were identified within the microstructure both from the hydration of OPC and substantial levels of fly ash activation. No evidence of CH was identified in these aged systems suggesting the CH produced during hydration of the PC particles has been fully consumed by the resultant pozzolanic reaction. The additional CH added during pre-treatment was considered to have primarily reacted with the flocs prior to encapsulation, no significant evidence for its effects were found aside from the successful encapsulation of the simulant waste. TEM-EDX analysis of the binding phase showed it to have a very low Ca/Si ratio which is partially expected due to the large quantity of fly ash which has shown a high level of activation, the measured atomic ratios however where lower than previously reported for OPC:PFA pastes in other studies [70, 287-289]. The ratios seen here are potentially more similar to purely CH- activated fly ash systems than an OPC grout, however EDX analysis of the Al floc sample did include analyses of C-S-H in proximity to PC particles which still present similarly low calcium results. The potential effects from the simulant waste addition are discussed later in this section with particular regard to the incorporation of additional ions.

The presence of a crystalline katoite-like hydrogarnet phase was identified in all the samples with a varying composition. In the Fe floc samples the phase was similar to the C(A,F)SH reported by Collier et al [93, 245]; the Al floc sample hydrogarnet showed differing XRD intensities more similar to un-substituted CASH katoite [257]. Investigations by SEM and TEM in this study suggest the prevalence of the hydrogarnet is higher than that proposed by previous studies in these aged samples. Since this phase is heavily associated and intermixed with the simulant waste material, identification and imaging of this phase can be difficult without higher magnification microscopy. The composition of the hydrogarnet is variable and linked to the floc addition as displayed by XRD evidence and TEM EDX estimations of composition; as expected the Fe-floc samples produced higher levels of Fe^{3+} substitution while all the hydrogarnets were shown to be highly siliceous.

The potential fate of iron associated with the flocs has been discussed, the fact that iron is detected during TEM-EDX analysis of the C-S-H phase and in the significant hydrogarnet phase discussed in sections 8.2 and 8.5 strongly suggests the chemical incorporation of Fe into hydrated cement phases. This will be in addition to the noticed physical encapsulation from SEM and TEM imaging studies.

The incorporation and stabilization of metal ions within cement phases has been investigated and studied by many authors for a variety of applications including radioactive waste encapsulation [290-295]. It has been suggested that there appear to be three basic types of binding mechanisms for metal ions [292, 294-296]:

i. Precipitation into the alkaline cement matrix as an oxide, mixed oxide or other solid phase.
ii. Sorbed or precipitated onto surfaces of cement minerals
iii. Incorporated into hydrated cement phases

Glasser (1994) mentioned that the solubility of discrete metal solid phases is a limiting factor in regards to the second and third mechanisms. Studies have suggested the incorporation and/or binding of metal ions as mentioned in mechanism (iii) into the C-S-H silicate chains [297-299]. However Jantzen et al [296] discussed that opinion is divided as to whether the primary binding site is at the bridging position or at the end of the silicate chains.

When the incorporation of Fe into silicate chains is considered a couple of studies should be mentioned, Pannaparayil et al [300] investigated the isomorphous substitution of Fe^{3+} for Si^{4+} in the structure of tobermorite. In that study Fe^{3+} substituted 11Å tobermorite was synthesised, Mössbauer spectroscopy was used to identify tetrahedrally co-ordinated Fe^{3+} which was attributed to the successful substitution of Fe^{3+} for Si^{4+} in the tobermorite structure. Richardson and Groves [24] presented an extended model for C-S-H which incorporated additional elements present in hardened OPC and blended cement pastes. The model outlines at low Ca/Si ratios, R^{3+} (typically Al^{3+} or Fe^{3+}) substitutes for Si in tetrahedral sites and is structurally limited by the available bridging sites for occupation. The alkali cations can be accommodated in the authors general model by interlayer ions or additional interlayers of Ca^{2+} which charge balance the substitution of R^{3+} for Si^{4+}. When this is considered for the observed data it can be proposed that a significant proportion of the measured Fe content from TEM-EDX analysis of the C-S-H is incorporated within the tetrahedral bridging sites of the silicate chains. However as mentioned in [24] the level of R^{3+} substitution is limited by the available bridging sites within the silicate chains that can be occupied; the data outlined in Figure 8-41 to 8-43 in section 8.5.1 shows an increased level of Al+Fe/Ca which is beyond the expected maximum for a pure C-S-H phase which is fully substituted by Al^{3+} and Fe^{3+}. Interestingly the data for potential substitution for purely Al^{3+} (Al/Ca) is generally within the accepted maximum of 0.33 and its only when Fe^{3+} is additionally included that the majority of analyses go beyond the accepted maximum, due to this the additional mechanisms mentioned previously should also be considered.

Examples of additional mechanisms other than silicate substitution can be found in literature; Atkins et al [301] and Chen et al [302] have noted that various elements are liable to substitute for Ca in cement phases (Sr, Ni, Co), with sorption and formation of hydroxides also observed as a significant form of immobilisation for other elements. Faucon et al [303, 304] investigated the possible substitution of calcium in C-S-H for Fe during the physiochemical degradation of cement pastes from the leaching process, and additional observations can be found in several review articles. It is also known that sorption onto the C-S-H seems to be higher at lower Ca/Si ratios [100, 292] a situation which is present within these samples. With a more highly negative surface charge represented in an alumino-silicate rich system when compared to a calcium-rich OPC based C-S-H, this may lead to a greater adsorption potential for cations.

When reviewing the data with regards to the three possible binding mechanisms there doesn't seem to be any formation of new mixed oxides or solid phases which are unfamiliar to cement science. The only major additional phase found during examination of the samples was the hydrogarnet phase which has been discussed with regards to the possible compositions. This leads to the conclusion that the floc will primarily remain within its pre-treated form rather than forming new additional precipitates. The third possible mechanism describing the incorporation of ions into hydrated cement phases has been discussed relating to the substitution into the silicate chains. The evidence indicates the likely formation of a highly substituted C-S-H phase with Al^{3+} and Fe^{3+} into the silicate chains, additionally the incorporation of Fe^{3+} into the siliceous hydrogarnet was confirmed. Due to the high levels of Al^{3+} and Fe^{3+} found during EDX analysis an added process should be considered in addition to silicate chain substitution. It is proposed the additional levels and therefore the observed Ca/Al+Fe atomic ratios could be explained by the second mechanism, with ions either being sorbed or precipitated onto the surface of the C-S-H. The potential for the replacement of Ca ions in the C-S-H with other ions such as Fe^{3+} in a manner similar to degraded or synthesised samples has not been discounted as potentially explaining the low Ca/Si ratios; however identification of these mechanisms is difficult using the current range of techniques in this investigation.

Three competing immobilisation/encapsulation mechanisms have been described for these floc containing systems; physical encapsulation of the pre-treated flocs, immobilisation or sorption within a C-A(F)-S-H phases and the immobilisation within the hydrogarnet phase. It is considered the majority of the Fe and Al ions will remain within the pre-treated floc waste form, as minimal chemical reaction between the cement matrix and the floc material was observed. The physical encapsulation of the floc and cement was considered as the primary form of waste management, with the flocs seen to be well incorporated into the C-S-H matrix. The formation of new chemical phases such as the iron-substituted hydrogarnet has indicated a level of potential chemical immobilisation associated with the flocs; immobilisation in this phase would be seen as acceptable due to its relative stability. The hydrogarnet phase however is only observed as a minor phase so it is anticipated only a minority of the waste ions could be immobilised via this phase. The potential for chemical immobilisation is greater in the C-S-H phase, analysis of which has indicated possible substitution into cross-linked chain lengths of a C-A(F)-S-H phase. Due to the relative large quantity of C-S-H compared to any other competing immobilisation mechanisms it is proposed the majority would be associated with C-S-H. This would be achieved via the mechanisms discussed in the previous paragraph regarding substitution and potential sorption. However, as discussed earlier, due to the extremely high proportion of waste loading in these systems (1:1) it is highly likely the primary encapsulation system is physical. In summary the 3 pre-treated floc systems all were successfully incorporated within their PFA:OPC encapsulant grouts, all resultant microstructures are relatively porous in nature but displayed an acceptable level of physical encapsulation by the C-S-H phase. Analysis of the samples showed a predominant crystalline phase identified as a katoite-like hydrogarnet with a variable composition depending upon the encapsulated waste material. The estimated compositions of the hydrogarnet showed the chemical immobilisation of Fe^{3+} and potentially Al^{3+} within the phase. Additional evidence for the potential chemical immobilisation of Fe^{3+} and Al^{3+} ions within the C-S-H phase was discussed particularly with regards to occupation sites within the silicate chain lengths. Potential sorption onto the C-S-H and other hydration products should also be considered as a strong possibility. In service Uranium, Plutonium and other active species will be adsorbed onto the iron hydroxide particles during the formation of the flocculants; this is likely to affect the chemical immobilisation potential of the flocs due to possible changes in ionic charges present, sorption and ionic substitution. Investigation of these possibilities is outside the brief of this simulant study and no experimental work has been completed on studies of radionuclides, however the consideration of the possible effects seems sensible.

Chapter 9 Conclusions and future work

9.1 General conclusions

As discussed by Milestone [5], it can be often difficult to distinguish between immobilisation and encapsulation of wastes in cement grouts. This distinction is further reduced when considering the flocculants and inorganic process slurries studied as part of this project. It was concluded that in many cases these waste streams did indicate levels of chemical immobilisation, often in addition to significant physical encapsulation which usually acted as the primary treatment process.

This dual route to stabilisation for the studied simulant wastes was particularly the case for the barium carbonate and aluminium slurries and the Fe/Al flocs. The $Mg(OH)_2$ waste sample did not show any indications for chemical immobilisation with no additional phase formations or noticeable effects upon the primary hydrated phases such as the C-S-H. This lack of interaction was due to the relative insolubility of the waste $Mg(OH)_2$ compared to Ca^{2+} and the relevant anions, therefore it was unlikely any typical cement reaction mechanisms involving the waste would occur. As a result, the pre-treated $Mg(OH)_2$ was physically encapsulated effectively and presented excellent stability.

The barium carbonate slurry simulated by the inclusion of $BaCO_3$ into the cement grout displayed significant levels of reactivity. $BaCO_3$ readily reacts with available sulphate during hydration forming stable $BaSO_4$; additionally this formation destabilises the ettringite phase and released waste carbonate ions form into monocarboaluminate. It was concluded that the addition and later formation of the barium phases had little effect upon the formation and composition of the C-S-H phase. This theory is supported by comparison with previous studies into high replacement BFS:OPC grouts. Large quantities of unreacted $BaCO_3$ remained in the microstructure due to the reduced levels of sulphate in blended cements; in this case the barium was well encapsulated in the binding matrix.

The results indicated that any ^{14}C waste would predominately remain within its treated $BaCO_3$ wasteform, therefore the bulk of ^{14}C will be physically encapsulated in the cement matrix. The remaining ^{14}C which would be freed during the formation of $BaSO_4$ is retained within Mc and $CaCO_3$ phases, the relative stability of which lowers the risk of any potential ^{14}C release. Consequently the study has supported the previous research into the suitability of using blended cement systems for the encapsulation of ^{14}C pre-treated with $Ba(NO_3)_2$. This work has characterised in enhanced detail the formation of the phases produced and the stability of those phases after prolonged hydration. The blended cement sample containing the simulant aluminium slurry also showed varying levels of both physical and chemical immobilisation. Large areas and quantities of the simulant waste product were identified by microscopy and were shown to be largely well integrated into the cement matrix after pre-treatment with $Ca(OH)_2$. However, the sample also displayed distinct morphological changes throughout the cement binding matrix, with the formation of Al-rich hydrated laths. The formation of these laths, identified as AFm was significantly more pronounced in the immediate locale of the encapsulated Al waste form although levels were found throughout the matrix. Subsequent analysis confirmed the formation of three aluminate containing phases within the system; C-A-S-H, monocarboaluminate and strätlingite, all of which provide sites for the chemical incorporation of Al ions. It was found that the incorporation of Al^{3+} into the C-S-H phase to form C-A-S-H was not significantly increased in this sample, Al levels within the C-S-H were similar to those observed in standard blended cement systems of a comparable age. Due to these observations, it was proposed that the primary chemical immobilisation potential within this sample was via the mass formation of the Mc and strätlingite phases.

Despite the proposed level of chemical immobilisation of Al via the Mc and strätlingite phases it is estimated the majority of the simulant waste remained physically encapsulated. This was due to the significant quantity of pre-formed waste material remaining largely unreacted within the cement matrix. The pre-treatment process seemed to enable the effective physical encapsulation of the waste in the hydrating binding matrix. It was proposed that this pre-treatment was also likely to be a contributor in the formation of the observed monocarboaluminate.The floc containing systems all showed strong indications for the effective physical encapsulation of the flocs within the C-S-H binding matrix as imaged by the TEM analysis. It was considered that the majority of waste ions would remain within the pre-treated floc waste form as minimal chemical reaction between the floc and cement matrix was observed; because of this the physical encapsulation of the floc should be seen as the primary form of waste treatment.

In these floc systems, a minority of ions however were indicated to be immobilised via chemical mechanisms; immobilisation or sorption within a C-A(F)-S-H phase or within a hydrogarnet phase. Due to its relative stability the substitution of Fe/Al ions within a silicated hydrogarnet was identified however this hydrogarnet phase was only observed as a minor phase so it is not thought that this is the primary immobilisation mechanism. In contrast, the potential for immobilisation in the C-S-H phase is far greater due to its relative quantity and potential for Fe and Al substitution into its chain lengths, in addition to possible sorption. The immobilisation of ions into the C-S-H was investigated, with iron shown to be intimately associated with the C-S-H binding phase via TEM-EDX analysis suggesting a C-A(F)-S-H system, this indicated a level of immobilisation had occurred within the cement binding phase. This evidence supports the potential dual routes to stabilisation for the waste, with significant levels of physical encapsulation observed alongside varied chemical immobilisation processes. The assessment of chemical reactivity and resultant interactions with the encapsulation medium is a major step for any waste treatment process. This project has shown the successful physical encapsulation and at times chemical immobilisation of several simulant waste streams within their relevant matrices. In many cases the waste material directly creates or is later associated with newly formed phases within the cement grouts; generally this is not seen as a problematic development due to the level of stability displayed under optimum storage conditions.

The discussed findings will help to address some of the key weaknesses in knowledge identified during the literature review, particularly regarding improved evidence for waste ion incorporation into hydrated cement phases. This additional knowledge was evident for the floc samples which showed the Fe incorporation into hydrogarnet and C-S-H phases in enhanced detail, similarly the formation of Al containing lathes was well characterised using transmission microscopy techniques. The study has also provided a range of insights into aged samples which been subject to prolonged periods of hydration. Whilst the timescales involved are negligible compared to many radioactive waste decay rates this still provided a valuable insight into the inherent stabilities of the studied wasteforms, due to the longer timescales involved compared to previous literature.

The study into the aged NRVB grout material provided a new insight into its microstructure and hydrated phase formation at various curing temperatures. Increased temperature curing was shown to result in a decreased level of Al substitution in the C-S-H phase. It was also shown that elevated curing temperatures resulted in the decomposition of the formed monocarboaluminate phase, the associated decomposition product hydrogarnet was also identified by XRD. TEM imaging of the microstructure of the NRVB samples found a similar structure to that described in neat OPC and C_3S pastes [8, 168]. A coarse morphology was dominant for the C-S-H phase with alterations to a more fine-fibrillar aspect depending on the local space constraints. Large quantities of C-S-H and unreacted $Ca(OH)_2$ were identified during the examination of the aged NRVB samples. This was of particular interest due to the required chemical sorption capacity and high pH these phases will provide for the NRVB material respectively. The findings therefore support the confidence that the NRVB material is capable of achieving its desired design requirements in the GDF concept. In summary this study has produced additional insights into the hydrated composition of NRVB and the effects of higher temperature curing on the material. This will supplement and build on the existing literature and provide greater understanding of NRVBs containment capacity in service.

As discussed in the context for this study, public acceptance of nuclear energy will rely partly upon the confidence in its capacity to safely and efficiently manage resultant wastes. This project has helped to demonstrate that current waste management solutions are capable of producing stable, low risk wasteforms suitable for long-term storage. Simulant wastes have been shown to be both physically encapsulated and chemically immobilised via a variety of mechanisms, these mechanisms have demonstrated the ability to isolate radionuclides from their immediate environment and then retain them in a stable form.

9.2 Future work

This PhD project has extended the current knowledge into a wide range of blended cement pastes used in the encapsulation of radioactive wastes. However, due to time constraints and experimental limitations questions do still remain which could be addressed by future studies.

The use of ^{29}Si MAS NMR should be applied across the full spectrum of samples, quantitative analysis using NMR would allow for valuable comparisons to be made with non-waste containing pastes. In particular accurate estimation of the binding C-S-H 's composition would be of higher confidence if quantitative NMR was completed.

Potentially large quantities of crystalline Fe-katoite like hydrogarnet phases were identified across the floc containing samples whose composition changed with the regards to the respective floc type. The formation process of these phases was not discussed in this study and would provide an interesting base for future studies. Work by Collier et al [93, 245] has suggested that the phase forms during early hydration in potentially reduced quantities. It would be informative however to assess the potential effects of aging and storage/curing conditions upon the formation of the hydrogarnet phase. Increased temperatures would be of particular interest due to the knowledge of hydrogarnets persisting in hydrothermally treated grouts.

The location of iron within the PFA:OPC + floc systems was intimately associated with the analysed C-S-H phase in all samples. Examination using TEM-EDX did however suggest the upper contents of Al and Fe were beyond that possibly accommodated purely by bridging sites within the silicate chains. To assess if the iron was present via an additional binding mechanism such as sorption or surface precipitation an increased range of experimental techniques could be utilised. One avenue of study could be the continued and expanded use of Mössbauer and Raman spectroscopy into the waste grouts; this would provide additional information into the local chemical environment. The use of these techniques in addition to any NMR is due to experimental difficulties in applying NMR spectroscopy without prior removal of paramagnetic material.

In the case of the provided simulant corroded metal samples a greater level of characterisation of the simulant waste form should be carried out prior to the examination of the waste in its respective encapsulation medium. Studies on the corroded sludge products [80, 81] have shown a high level of variation beyond that of simplistic 'pure' phases such as the brucite examined in this project. Improved characterisation and later design of any simulant corrosion sludges will lead to an improved understanding of any formation processes of new phases within the cement grouts after encapsulation.

References

1. IAEA, *Radioactive waste management objectives*. 2011, Vienna: International Atomic Energy Agency.

2. Ojovan, M.I. and W.E. Lee, *An introduction to nuclear waste immobilisation*. 2005, Elsevier,: Amsterdam ; Boston. p. xviii, 315 p. ill. 25 cm.

3. IAEA, *Radiation, People and the Environment*. 2004, Vienna: International Atomic Energy Agency

4. Wilson, P.D., *The Nuclear Fuel Cycle from Ore to Waste*. Vol. 1. 1996, Oxford: Oxford University Press.

5. Milestone, N.B., *Reactions in cement encapsulated nuclear wastes: need for toolbox of different cement types.* Advances in Applied Ceramics, 2006. **105**(1): p. 13-20.

6. Black, L., P. Purnell, and J. Hill, *Current themes in cement research.* Advances in Applied Ceramics, 2010. **109**(5): p. 253-259.

7. Taylor, H.F.W., *Cement Chemistry*. 2nd ed. 1997, London: Thomas Telford.

8. Richardson, I.G., *The nature of C-S-H in hardened cements.* Cement and Concrete Research, 1999. **29**(8): p. 1131-1147.

9. Richardson, I.G., A.R. Brough, G.W. Groves, and C.M. Dobson, *The charaterization of hardened alkali-activated blast- furnace slag pastes and the nature of the calcium silicate hydrate (C-S-H) phase.* Cement and Concrete Research, 1994. **24**(5): p. 813-829.

10. Richardson, I.G., *The nature of the hydration products in hardened cement pastes.* Cement & Concrete Composites, 2000. **22**(2): p. 97-113.

11. Richardson, I.G., *The calcium silicate hydrates.* Cement and Concrete Research, 2008. **38**(2): p. 137-158.

12. Merlino, S., E. Bonaccorsi, and T. Armbruster, *Tobermorites: Their real structure and order-disorder (OD) character.* American Mineralogist, 1999. **84**: p. 1613-1621.

13. Houston, J.R., R.S. Maxwell, and S.A. Carroll, *Transformation of meta-stable calcium silicate hydrates to tobermorite: reaction kinetics and molecular structure from XRD and NMR spectroscopy.* Geochemical Transactions, 2009. **10**(1): p. 1-14.

14. Biagioni, C., E. Bonaccorsi, S. Merlino, and D. Bersani, *New data on the thermal behavior of 14Å tobermorite.* Cement and Concrete Research, 2013. **49**: p. 48-54.

15. Bonaccorsi, E. and S. Merlino, *The crystal structure of tobermorite 14Å (Plombierite) a C-S-H phase.* Journal of the American Ceramic Society, 2005. **88**(3): p. 505-512.

16. Bonaccorsi, E., S. Merlino, and H.F.W. Taylor, *The crystal structure of jennite,* $Ca_9Si_6O_{18}(OH)_6.8H_2O$. Cement and Concrete Research, 2004. **34**: p. 1481-1488.

17. Gard, J.A., H.F.W. Taylor, G. Cliff, and G.W. Lorimer, *A reexamination of jennite.* American Mineralogist, 1977. **62**: p. 365-368.

18. Taylor, H.F.W., *Proposed structure for calcium silicate hydrate gel.* Journal of the American Ceramic Society, 1986. **69**(6): p. 464-467.

19. Feldman, R.F. and P.J. Sereda, *A new model for hydrated Portland cement and its practical implications.* Engineering Journal, 1970. **53**(8/9): p. 53-59.

20. Daimon, M., S.A. Abo-El-Enein, S. Hosaka, S. Goto, and R. Kondo, *Pore structure of calcium silicate hydrate in hydrated tricalcium silicate.* Journal of the American Ceramic Society, 1977. **60**(3-4): p. 110-114.

21. Taylor, H.F.W., *Nanostructure of C-S-H: Current status.* Advanced Cement Based Materials, 1993. **1**: p. 38-46.

22. Cong, X. and R.J. Kirkpatrick, *^{29}Si MAS NMR study of C-S-H.* Advanced Cement Based Materials, 1996. **3**: p. 144-156.

23. Chen, J.J., J.J. Thomas, H.F.W. Taylor, and H.M. Jennings, *Solubility and structure of calcium silicate hydrate.* Cement and Concrete Research, 2004. **34**(9): p. 1499-1519.

24. Richardson, I.G. and G.W. Groves, *The Incorporation of Minor and Trace-Elements into Calcium Silicate Hydrate (C-S-H) Gel in Hardened Cement Pastes.* Cement and Concrete Research, 1993. **23**(1): p. 131-138.

25. Richardson, I.G. and G.W. Groves, *Models for the composition and structure of calcium silicate hydrate (C-S-H) gel in hardened tricalcium silicate pastes.* Cement and Concrete Research, 1992. **22**(6): p. 1001-1010.

26. Richardson, I.G., *Tobermorite/jennite- and tobermorite/calcium hydroxide-based models for the structure of C-S-H: applicability to hardened pastes of tricalcium silicate, β-dicalcium silicate, Portland cement, and blends of Portland cement with blast-furnace slag, metakaolin, or silica fume.* Cement and Concrete Research, 2004. **34**(9): p. 1733-1777.

27. Grutzeck, M.W., S. Kwan, J.L. Thompson, and A. Benes, *A sorosilicate model for calcium silicate hydrate (C-S-H).* Journal of Materials Science Letters, 1999. **18**: p. 217-220.

28. Brydson, R., I.G. Richardson, D.W. Mccomb, and G.W. Groves, *Parallel Electron-Energy-Loss Spectroscopy Study of Al-Substituted Calcium Silicate Hydrate (C-S-H) Phases Present in Hardened Cement Pastes.* Solid State Communications, 1993. **88**(2): p. 183-187.

29. Nonat, A., *The structure and stoichiometry of C-S-H.* Cement and Concrete Research, 2004. **34**: p. 1521-1528.

30. Jennings, H.M., *A model for the microstructure of calcium silicate hydrate in cement paste.* Cement and Concrete Research, 2000. **30**: p. 101-116.

31. Jennings, H.M., *Refinements to colloid model of C-S-H in cement: CM-II.* Cement and Concrete Research, 2008. **38**: p. 275-289.

32. Constantinides, G. and F.J. Ulm, *The effect of two types of C-S-H on the elasticity of cement-based materials: Results from nanoindentation and micromechanical modeling.* Cement and Concrete Research, 2004. **34**: p. 67-80.

33. Jennings, H.M., *Colloid model of C-S-H and implications to the problem of creep and shrinkage.* Materials and Structures, 2004. **37**: p. 59-70.

34. Pellenq, R.J.M., A. Kushima, R. Shahsavari, K.J. Van Vliet, M.J. Buehler, S. Yip, and F.J. Ulm, *A realistic molecular model of cement hydrates.* Proceedings of the National Academy of Sciences of the United States of America, 2009. **106**(38): p. 16102-16107.

35. Allen, A.J., J.J. Thomas, and H.M. Jennings, *Composition and density of nanoscale calcium-silicate-hydrate in cement.* Nature Materials 2007. **6**: p. 311-316.

36. Shi, C.J. and J.S. Qian, *High performance cementing materials from industrial slags - a review.* Resources Conservation and Recycling, 2000. **29**(3): p. 195-207.

37. Zhou, H.H., X.Q. Wu, Z.Z. Xu, and M.H. Tang, *Kinetic-Study on Hydration of Alkali-Activated Slag.* Cement and Concrete Research, 1993. **23**(6): p. 1253-1258.

38. Haha, M.B., B. Lothenbach, G. Le Saout, and F. Winnefeld, *Influence of slag chemistry on the hydration of alkali-activated blast-furnace slag — Part I: Effect of MgO.* Cement and Concrete Research, 2011. **41**(9): p. 955-963.

39. Haha, M.B., B. Lothenbach, G. Le Saout, and F. Winnefeld, *Influence of slag chemistry on the hydration of alkali-activated blast-furnace slag — Part II: Effect of Al2O3.* Cement and Concrete Research, 2012. **42**(1): p. 74-83.

40. Le Saout, G., M. Ben Haha, F. Winnefeld, and B. Lothenbach, *Hydration Degree of Alkali-Activated Slags: A 29Si NMR Study.* Journal of the American Ceramic Society, 2011. **94**(12): p. 4541-4547.

41. Moranville - Regourd, M., *Cements made from Blastfurnace Slag*, in *Lea's Chemistry of Cement and Concrete*. 2003, Elsevier: Oxford.

42. Hill, J. and J.H. Sharp, *Mineralogy and microstructure of three composite cements with high replacement levels.* 2003.

43. Whittaker, M., M. Zajac, M.B. Haha, F. Bullerjahn, and L. Black, *The role of the alumina content of slag, plus the presence of additional sulfate on the hydration and microstructure of Portland cement-slag blends.* Cement and Concrete Research, 2014. **66**: p. 91-101.

44. Oner, A. and S. Akyuz, *An experimental study on optimum usage of GGBS for the compressive strength of concrete.* Cement & Concrete Composites, 2007. **29**(6): p. 505-514.

45. Escalante García, J.I., L.Y. Gomez, K.K. Johal, M. Mendoza, and J. Mendez, *Reactivity of blast-furnace slag in Portland cement blends hydrated under different conditions.* Cement and Concrete Research, 2001. **31**(10): p. 1403-1409.

46. Matschei, T., B. Lothenbach, and F.P. Glasser, *The AFm phase in Portland cement.* Cement and Concrete Research, 2007. **37**(2): p. 118-130.

47. Lothenbach, B., K. Scrivener, and R.D. Hooton, *Supplementary cementitious materials.* Cement and Concrete Research, 2011. **41**(12): p. 1244-1256.

48. Kolani, B., L. Buffo-Lacarrière, A. Sellier, G. Escadeillas, L. Boutillon, and L. Linger, *Hydration of slag-blended cements.* Cement and Concrete Composites, 2012. **34**(9): p. 1009-1018.

49. Bougara, A., C.J. Lynsdale, and N.B. Milestone, *Reactivity and performance of blastfurnace slags of differing origin.* Cement & Concrete Composites, 2010. **32**(4): p. 319-324.

50. Richardson, I.G. and J.G. Cabrera, *The nature of CSH in model slag-cements.* Cement and Concrete Composites, 2000. **22**: p. 259-299.

51. Richardson, I.G. and G.W. Groves, *Microstructure and Microanalysis of Hardened Cement Pastes Involving Ground Granulated Blast-Furnace Slag.* Journal of Materials Science, 1992. **27**(22): p. 6204-6212.

52. Taylor, R., I.G. Richardson, and R.M.D. Brydson, *Composition and microstructure of 20-year-old ordinary Portland cement–ground granulated blast-furnace slag blends containing 0 to 100% slag.* Cement and Concrete Research, 2010. **40**(7): p. 971-983.

53. Taylor, R., I.G. Richardson, and R.M.D. Brydson, *Nature of C–S–H in 20 year old neat ordinary Portland cement and 10% Portland cement–90% ground granulated blast furnace slag pastes.* Advances in Applied Ceramics, 2007. **106**(6): p. 294-301.

54. Richardson, I.G. and G.W. Groves, *The structure of the calcium silicate hydrate phases present in hardened pastes of white Portland cement blast-furnace slag blends.* Journal of Materials Science, 1997. **32**(18): p. 4793-4802.

55. Richardson, I.G., C.R. Wilding, and M.J. Dickson, *The hydration of blastfurnance slag cements.* Advances in Cement Research 1989. **2**(8): p. 147-157.

56. *British Standards BS3892 Pulverised fuel ash*. 1997. p. 1-16.

57. Watt, J.D. and D.J. Thorne, *Composition and pozzolanic properties of pulverized fuel ashes.* Journal of Applied Chemistry, 1996. **15**: p. 585-604.

58. Halse, Y., P.L. Pratt, J.A. Dalziel, and W.A. Gutteridge, *Development of microstructure and other properties in flyash opc systems.* Cement and Concrete Research, 1984. **14**(4): p. 491-498.

59. Massazza, F., *Pozzolana and pozzolanic cements*, in *Lea's Chemistry of Cement and Concrete*, P. Hewlett, Editor. 2003, Butterworth-Heinemann: New York.

60. Bijen, J. and H. Pietersen, *Mineral admixtures: Reactions, microstructure and macro-properties.* Advances in Cement and Concrete, 1994: p. 292-328.

61. Wang, X.-Y., H.-K. Cho, and H.-S. Lee, *Prediction of temperature distribution in concrete incorporating fly ash or slag using a hydration model.* Composites Part B: Engineering, 2011. **42**(1): p. 27-40.

62. Helmuth, R., *Fly Ash in Cement and Concrete*. 1987, Skokie, Illinois: Portland Cement Association.

63. Sakai, E., S. Miyahara, S. Ohsawa, S.-H. Lee, and M. Daimon, *Hydration of fly ash cement.* Cement and Concrete Research, 2005. **35**(6): p. 1135-1140.

64. Fraay, A.L.A., J.M. Bijen, and Y.M. De Haan, *The reaction of fly ash in concrete. A critical examination.* Cement and Concrete Research, 1989. **19**(2): p. 235-246.

65. Dittrich, S., J. Neubauer, and F. Goetz-Neunhoeffer, *The influence of fly ash on the hydration of OPC within the first 44h—A quantitative in situ XRD and heat flow calorimetry study.* Cement and Concrete Research, 2014. **56**: p. 129-138.

66. Rodger, S.A. and G.W. Groves, *Electron microscopy study of ordinary portland cement and ordinary portland cement-pulverized fuel ash blended pastes.* Journal of the American Ceramic Society, 1989. **72**(6): p. 1037-1039.

67. Girao, A.V., I.G. Richardson, C.B. Porteneuve, and R.M.D. Brydson, *Composition, morphology and nanostructure of C-S-H in white Portland cement-fly ash blends hydrated at 85 degrees C.* Advances in Applied Ceramics, 2007. **106**(6): p. 283-293.

68. Girão, A.V., I.G. Richardson, R. Taylor, and R.M.D. Brydson, *Composition, morphology and nanostructure of C–S–H in 70% white Portland cement–30% fly ash blends hydrated at 55°C.* Cement and Concrete Research, 2010. **40**(9): p. 1350-1359.

69. Pietersen, H., *Application of TEM to characterize fly ash- and slag cements.* Heron, 1999. **44**(4): p. 299-310.

70. Deschner, F., F. Winnefeld, B. Lothenbach, S. Seufert, P. Schwesig, S. Dittrich, F. Goetz-Neunhoeffer, and J. Neubauer, *Hydration of Portland cement with high replacement by siliceous fly ash.* Cement and Concrete Research, 2012. **42**(10): p. 1389-1400.

71. Wilson, P.D., *The Nuclear Fuel Cycle from Ore to Waste.* Vol. 1. 1996, Oxford: Oxford University Press.

72. Wilding, C.R., *The performance of cement-based systems.* Cement and Concrete Research, 1992. **22**(2-3): p. 299-310.

73. DECC/NDA, *The 2010 UK Radioactive Waste Inventory: Main Report*. 2011, NDA.

74. Ojovan, M.I. and W.E. Lee, *An introduction to nuclear waste immobilisation*. 2005, Elsevier,: Amsterdam ; Boston. p. 1 online resource (xviii, 315 p.) ill.

75. Schulz, W.W., E.P. Horwitz, and American Chemical Society. Symposium, *Chemical pretreatment of nuclear waste for disposal*. The language of science. 1994, New York ; London: Plenum Press. viii, 212 p.

76. Sharp, J.H.e.a., *Cementitious systems for encapsulation of intermediate level waste*, in *ICEM: 9th International conference on radioactive waste management and environmental remediation*. 2005: Oxford

77. Utton, C. and I.H. Godfrey, *Review of stability of cemented grouted ion-exchange materials, sludges and flocs*. 2010, NNL Report (09) 10212.

78. Wilding, C.R., *The Performance of Cement Based Systems.* Cement and Concrete Research, 1992. **22**(2-3): p. 299-310.

79. Hill, J. and J.H. Sharp, *The mineralogy and microstructure of three composite cements with high replacement levels.* Cement and Concrete Composites, 2002. **24**: p. 191-199.

80. Parry, S.A., F.R. Livens, and L. O'Brien. *Corroded Magnox sludge and plutonium waste cementation*. in *Goldschmidt 07*. 2007. Cologne.

81. Gregson, C.R., D.T. Goddard, M.J. Sarsfield, and R.J. Taylor, *Combined electron microscopy and vibrational spectroscopy study of corroded Magnox sludge from a legacy spent nuclear fuel storage pond.* Journal of Nuclear Materials, 2011. **412**(1): p. 145-156.

82. Fairhall, G.A. and J.D. Palmer, *Encapsulation of Magnox Swarf in Cement in the United Kingdom.* Cement and Concrete Research, 1992. **22**(2-3): p. 293-298.

83. Setiadi, A., N.B. Milestone, J. Hill, and M. Hayes, *Corrosion of aluminium and magnesium in BFS composite cements.* Advances in Applied Ceramics, 2006. **105**(4): p. 191-196.

84. Collier, N.C. and N.B. Milestone, *The encapsulation of Mg(OH)2 sludge in composite cement.* Cement and Concrete Research, 2010. **40**(3): p. 452-459.

85. Lide, D.R., *CRC handbook of chemistry and physics 92nd ed.*, ed. W.M. Haynes. 2011, London: CRC Press.

86. Utton, C.A., E. Gallucci, J. Hill, and N.B. Milestone, *Interaction between BaCO3 and OPC/BFS composite cements at 20°C and 60°C.* Cement and Concrete Research, 2011. **41**(3): p. 236-243.

87. Palmer, J.D. and G.A. Fairhall, *Properties of Cement Systems Containing Intermediate Level Wastes.* Cement and Concrete Research, 1992. **22**(2-3): p. 325-330.

88. Carmona-Quiroga, P.M. and M.T. Blanco-Varela, *Ettringite decomposition in the presence of barium carbonate.* Cement and Concrete Research, 2013. **52**: p. 140-148.

89. Hussein, O., C. Utton, M. Ojovan, and H. Kinoshita, *The effects of BaSO4 loading on OPC cementing system for encapsulation of BaSO4 scale from oil and gas industry.* Journal of Hazardous Materials, 2013. **261**: p. 11-20.

90. Hildred, K.L., P.S. Townson, G.V. Hutson, and R.A. Williams, *Characterisation of particulates in the BNFL enhanced actinide removal plant.* Powder Technology, 2000. **108**: p. 164-172.

91. Collier, N.C., N.B. Milestone, J. Hill, and I.H. Godfrey, *The disposal of radioactive ferric floc.* Waste Management, 2006. **26**(7): p. 769-775.

92. Collier, N.C., N.B. Milestone, J. Hill, and I.H. Godfrey, *Immobilisation of Fe floc: Part 1, pre-treatment of floc with slaked lime.* Journal of Nuclear Materials, 2009. **393**(1): p. 77-86.

93. Collier, N.C., N.B. Milestone, J. Hill, and I.H. Godfrey, *Immobilisation of Fe floc: Part 2, encapsulation of floc in composite cement.* Journal of Nuclear Materials, 2009. **393**(1): p. 92-101.

94. Faucon, P., P. Le Bescop, F. Adenot, P. Bonville, J.F. Jacquinot, F. Pineau, and B. Felix, *Leaching of cement: Study of the surface layer.* Cement and Concrete Research, 1996. **26**(11): p. 1707-1715.

95. Sugama, T., M. Allan, and J.M. Hill, *Calcium phosphate cements prepared by acid-base reaction.* Journal of the American Ceramic Society, 1992. **75**(8): p. 2076-2087.

96. Swift, P., H. Kinoshita, N.C. Collier, and C.A. Utton, *Phosphate modified calcium aluminate cement for radioactive waste encapsulation.* Advances in Applied Ceramics, 2013. **112**(1): p. 1-8.

97. Kinoshita, H., P. Swift, C. Utton, B. Carro-Mateo, G. Marchand, N. Collier, and N. Milestone, *Corrosion of aluminium metal in OPC- and CAC-based cement matrices.* Cement and Concrete Research, 2013. **50**: p. 11-18.

98. Vance, E.R. and D.S. Perera, *Development of geopolymers for nuclear waste immobilisation*, in *Handbook of Advanced Radioactive Waste Conditioning Technologies*, M. Ojovan, Editor. 2011, Woodhead: Cambridge. p. 207-229.

99. Li, Q., Z.Q. Sun, D.J. Tao, Y. Xu, P.M. Li, H. Cui, and J.P. Zhai, *Immobilization of simulated radionuclide 133Cs(+) by fly ash-based geopolymer.* Journal of Hazardous Materials, 2013. **262**: p. 325-331.

100. Fernandez-Jimenez, A., D.E. Macphee, E.E. Lachowski, and A. Palomo, *Immobilization of cesium in alkaline activated fly ash matrix.* Journal of Nuclear Materials, 2005. **346**(2-3): p. 185-193.

101. Shi, C. and A. Fernández-Jiménez, *Stabilization/solidification of hazardous and radioactive wastes with alkali-activated cements.* Journal of Hazardous Materials, 2006. **137**(3): p. 1656-1663.

102. Rooses, A., D. Lambertin, D. Chartier, and F. Frizon, *Galvanic corrosion of Mg–Zr fuel cladding and steel immobilized in Portland cement and geopolymer at early ages.* Journal of Nuclear Materials, 2013. **435**(1-3): p. 137-140.

103. Rooses, A., P. Steins, A. Dannoux-Papin, D. Lambertin, A. Poulesquen, and F. Frizon, *Encapsulation of Mg-Zr alloy in metakaolin-based geopolymer.* Applied Clay Science, 2013. **73**: p. 86-92.

104. Berger, S., F. Frizon, and C. Joussot-Dubien, *Formulation of caesium based and caesium containing geopolymers.* Advances in Applied Ceramics, 2009. **108**(7): p. 412-417.

105. Kinoshita, H., C. Circhirillo, I. SanMartin, C.A. Utton, P.H.R. Borges, C.J. Lynsdale, and N.B. Milestone, *Carbonation of composite cements with high mineral admixture content used for radioactive waste encapsulation.* Minerals Engineering, 2014. **59**: p. 107-114.

106. Collier, N., *Immobilisation matrices for intermediate level nuclear wastes using sulphate activated BFS/OPC and PFA/OPC composite cements.* Advances in Applied Ceramics, 2010. **109**(5).

107. Nirex, *The Nirex Phased Disposal Concept*. 2003, Nirex Report.

108. Bailey, L.E.F., A.J. Hooper, and M.J. Poole, *Modelling decisions for a cementitious repository for long-lived ILW (TRU)*, in *Engineered Barrier Systems (EBS) in the Safety Case: The Role of Modelling*. 2005, OECD: NEA: La Coruna. p. 139 - 149.

109. Holland, T.R. and D.J. Lee, *Radionuclide getters in cement.* Cement and Concrete Research, 1992. **22**(2-3): p. 247-258.

110. Francis, A.J., R. Cather, and I.G. Crossland, *Development of the Nirex Reference Vault Backfill; Report on Current Status in 1994*. 1997, Nirex Report S97/014.

111. Crossland, I.G. and R. Thetford, *Cracking of the Nirex Reference Vault Backfill: A Review of its Likely Occurrence and Significance*. 2007, Crossland Report CCL/2007/1.

112. Harris, A.W., *An assessment of pH buffering Provided by the Nirex Reference Vault Backfill Within a Radioactive Waste Repository*. 1997, Nirex Report NSS/R323.

113. MacPhee, D.E. and F.P. Glasser, *Immobilisation Science of Cement Systems.* MRS Bulletin, March 1993: p. 66-71.

114. Crossland, I. and S.P. Vines, *Why a cementitious repository?* 2001, Nirex Report N/034.

115. Baston, G.M.N., M.M. Cowper, and T.A. Marshall, *Sorption properties of aged cements.* Mineralogical Magazine, 2012. **76**(8): p. 3411-3423.

116. McCarter, W.J., I. Crossland, and T.M. Chrisp, *Hydration and drying of Nirex Reference Vault Backfill.* Building and Environment, 2004. **39**(2): p. 211-221.

117. McCarter, W.J., T.M. Chrisp, G. Starrs, and E.H. Owens, *Setting, hardening and moisture-loss within a cement-based backfill grout under simulated repository environments.* Measurement, 2012. **45**(3): p. 235-242.

118. Butcher, E.J., J. Borwick, N. Collier, and S.J. Williams, *Long term leachate evolution during flow-through leaching of a vault backfill (NRVB).* Mineralogical Magazine, 2012. **76**(8): p. 3023-3031.

119. Collier, N. and G. Woodhouse, *Results from one year hydrothermal ageing of BFS:OPC, PFA:OPC and NRVB samples*. 2010, NNL.

120. Willcox, D., *Personal Communication*, J.A. Rickerby and I.G. Richardson, Editors. 2012.

121. *British Standard Specification for Ground Granulated Blastfurnace Slag for use with Portland Cement, BS6699* 1992.

122. Collier, N.C., *The encapsulation of iron hydroxide floc in composite cement. PhD Thesis*. 2006, University of Sheffield.

123. Ramachandran, V.S., *Handbook of thermal analysis of construction materials*. 2002, New York: William Andrew Publishing

124. Alarcon-Ruiz, L., G. Platret, E. Massieu, and A. Ehrlacher, *The use of thermal analysis in assessing the effect of temperature on a cement paste.* Cement and Concrete Research, 2005. **35**(3): p. 609-613.

125. Zhou, Q. and F.P. Glasser, *Thermal stability and decomposition mechanciums of ettringite at <120˚C.* Cement and Concrete Research, 2001. **31**: p. 1333-1339.

126. Bhatty, J.I., D. Dollimore, G.A. Gamlen, R.J. Mangabhai, and H. Olmez, *Estimation of calcium hydroxide in OPC, OPC/PFA and OPC/PFA/Polymer modified systems.* Thermochimica Acta, 1986. **106**: p. 115-123.

127. Vedalakshmi, R., A. Sundara Raj, S. Srinivasan, and K. Ganesh Babu, *Quantification of hydrated cement products of blended cements in low and medium strength concrete using TG and DTA technique.* Thermochimica Acta, 2003. **407**(1-2): p. 49-60.

128. Villain, G., M. Thiery, and G. Platret, *Measurement methods of carbonation profiles in concrete: Thermogravimetry, chemical analysis and gammadensimetry.* Cement and Concrete Research, 2007. **37**(8): p. 1182-1192.

129. Klug, H.P. and L.E. Alexander, *X-Ray Diffraction Procedures for Polycrystalline and Amorphous Materials* 1962, New York: John Wiley & Sons.

130. Bowen, D.K. and C.R. Hall, *Microscopy of materials - Modern imaging methods using electron, X-ray and Ion beams*. 1975, London and Basingstoke: The Macmillan Press.

131. Taylor, J.C., *X-ray powder analysis of cements*, in *Structure and Performance of Cements*, J. Bensted and P.D. Barnes, Editors. 2001, Taylor and Francis: London.

132. Apperley, D.C., R.K. Harris, and P. Hodgkinson, *Solid-State NMR: Basic Principles & Practice*. 2012, New York: Momentum Press.

133. MacKenzie, K.J.D. and M.E. Smith, *Multinuclear solid-state NMR of inorganic materials*. Pergamon materials series. 2002, Amsterdam ; London: Pergamon. xix, 727 p.

134. Sanders, J.K.M. and B.K. Hunter, *Modern NMR Spectroscopy: A Guide for Chemists*. 1997, Oxford: Oxford University Press.

135. Richardson, I.G., L. Black, J. Skibsted, and R.J. Kirkpatrick, *Characterisation of cement hydrate phases by TEM, NMR and Raman spectroscopy.* Advances in Cement Research, 2010. **22**(4): p. 233-248.

136. Skibsted, J. and C. Hall, *Characterization of cement minerals, cements and their reaction products at the atomic and nano scale.* Cement and Concrete Research, 2008. **38**(2): p. 205-225.

137. Thomas, G. and M.J. Goringe, *Transmission Electron Microscopy of Materials*. 1979, New York: John Wiley & Sons.

138. Richardson, I.G., *Electron Microscopy of Cements*, in *Structure and Performance of Cement*, P. Barnes and J. Bensted, Editors. 2002, Spon Press: London.

139. Dalgleish, B.J. and K. Ibe, *Thin-Foil Studies of Hydrated Portland-Cement.* Cement and Concrete Research, 1981. **11**(5-6): p. 729-739.

140. Jennings, H.M., B.J. Dalgleish, and P.L. Pratt, *Morphological Developement of Hydrating Tricalcium Silicate as Examined by Electron Microscopy Techniques.* Journal of the American Ceramic Society, 1981. **64**(10): p. 567-572.

141. Lachowski, E.E., K. Mohan, H.F.W. Taylor, and A.E. Moore, *Analytical Electron-Microscopy of Cement Pastes .2. Pastes of Portland Cements and Clinkers.* Journal of the American Ceramic Society, 1980. **63**(7-8): p. 447-452.

142. Loretto, M.H., *Electron Beam Analysis of Materials*. 1994, London: Chapman & Hall.

143. Rossler, C., J. Stark, F. Steiniger, and W. Tichelaar, *Limited-dose electron microscopy reveals the crystallinity of fibrous C-S-H phases.* Journal of the American Ceramic Society, 2006. **89**(2): p. 627-632.

144. Goodhew, P.J., J. Humphreys, and R. Beanland, *Electron Microscopy and Analysis* 3rd ed. 2001, London: Taylor & Francis.

145. Scrivener, K.L., *Backscattered electron imaging of cementitious microstructures: understanding and quantification.* Cement and Concrete Composites, 2004. **26**(8): p. 935-945.

146. Kjellsen, K.O., R.J. Detwiler, and O.E. Gjørv, *Backscattered electron image analysis of cement paste specimens: Specimen preparation and analytical methods.* Cement and Concrete Research, 1991. **21**(2-3): p. 388-390.

147. Roomans, G.M. and A. Dragomir, *X-Ray microanalysis in the scanning electron microscope*, in *Electron Microscopy: Methods and Protocols*, J. Kuo, Editor. 2007, Humana: Totowa.

148. Wong, H.S. and N.R. Buenfeld, *Monte Carlo simulation of electron-solid interactions in cement-based materials.* Cement and Concrete Research, 2006. **36**(6): p. 1076-1082.

149. Sun, J., *Carbonation Kinetics of Cementitious Materials Used in the Geological Disposal of Radioactive Waste. PhD Thesis*. 2010, Department of Chemical Engineering, University College London.

150. Damidot, D., S. Stronach, A. Kindness, M. Atkins, and F.P. Glasser, *Thermodynamic investigation of the $CaO-Al_2O_3-CaCO_3-H_2O$ closed system at 25°C and the influence of Na_2O.* Cement and Concrete Research, 1994. **24**(3): p. 563-572.

151. Bonavetti, V.L., V.F. Rahhal, and E.F. Irassar, *Studies on the carboaluminate formation in limestone filler-blended cements.* Cement and Concrete Research, 2001. **31**: p. 853--859.

152. Lothenbach, B. and F. Winnefeld, *Thermodynamic modelling of the hydration of Portland cement.* Cement and Concrete Research, 2006. **36**(2): p. 209-226.

153. Lothenbach, B., G. Le Saout, E. Gallucci, and K. Scrivener, *Influence of limestone on the hydration of Portland cements.* Cement and Concrete Research, 2008. **38**(6): p. 848-860.

154. Matschei, T., B. Lothenbach, and F.P. Glasser, *Thermodynamic properties of Portland cement hydrates in the system CaO–Al2O3–SiO2–CaSO4–CaCO3–H2O.* Cement and Concrete Research, 2007. **37**(10): p. 1379-1410.

155. Matschei, T. and F.P. Glasser, *Temperature dependence, 0 to 40°C, of the mineralogy of Portland cement paste in the presence of calcium carbonate.* Cement and Concrete Research, 2010. **40**(5): p. 763-777.

156. Schmidt, T., B. Lothenbach, M. Romer, J. Neuenschwander, and K. Scrivener, *Physical and microstructural aspects of sulfate attack on ordinary and limestone blended Portland cements.* Cement and Concrete Research, 2009. **39**(12): p. 1111-1121.

157. Zajac, M., A. Rossberg, G. Le Saout, and B. Lothenbach, *Influence of limestone and anhydrite on the hydration of Portland cements.* Cement and Concrete Composites, 2014. **46**: p. 99-108.

158. Fentiman, C.H., *Hydration of carbo-aluminous cement at different temperatures.* Cement and Concrete Research, 1985. **15**: p. 622-630.

159. Dilnesa, B.Z., B. Lothenbach, G. Renaudin, A. Wichser, and D. Kulik, *Synthesis and characterization of hydrogarnet* $Ca_3(Al_xFe_{1-x})_2(SiO_4)_y(OH)_{4(3-y)}$. Cement and Concrete Research, 2014. **59**(1): p. 96-111.

160. Harris, A.W., K.A. Boult, M.C. Manning, and W.M. Tearle, *Experimental Study of Carbon Dioxide Uptake by NRVB and 3:1 BFS/OPC*. 2003, SERCO ERRA-0453.

161. Harris, A.W., M.C. Manning, and W.M. Tearle, *Carbonation of Nirex Reference Vault Backfill*. 2003, SERCO ERRA-0454.

162. Kakali, G., S. Tsivilis, E. Aggeli, and M. Bati, *Hydration products of* C_3A, C_3S *and Portland cement in the presence of* $CaCO_3$. Cement and Concrete Research, 2000. **30**: p. 1073-1077.

163. Péra, J., S. Husson, and B. Guilhot, *Influence of finely ground limestone on cement hydration.* Cement and Concrete Composites, 1999. **21**: p. 99-105.

164. Taylor, H.F.W. and D.E. Newbury, *An electron microprobe study of a mature cement paste.* Cement and Concrete Research, 1984. **14**: p. 565-573.

165. Famy, C., K.L. Scrivener, and A.K. Crumbie, *What causes differences of C-S-H gel grey levels in backscattered electron images?* Cement and Concrete Research, 2002. **32**: p. 1465-1471.

166. Groves, G.W., P.J. Le Sueur, and W. Sinclair, *Transmission Electron Microscopy and Microanalytical Studies of Ion-Beam-Thinned Sections of Tricalcium Silicate Paste.* Journal of the American Ceramic Society, 1986. **69**(4): p. 353-356.

167. Richardson, I.G. and G.W. Groves, *Microstructure and Microanalysis of Hardened Ordinary Portland-Cement Pastes.* Journal of Materials Science, 1993. **28**(1): p. 265-277.

168. Groves, G.W., A.R. Brough, I.G. Richardson, and C.M. Dobson, *Progressive changes in the structure of hardened C3S cement pastes due to carbonation.* Journal of the American Ceramic Society, 1991. **74**(11): p. 2891-2896.

169. Escalante García, J.I. and J.H. Sharp, *Variation in the composition of C-S-H Gel in Portland cement pastes cured at various temperatures.* Journal of the American Ceramic Society, 1999. **82**(11): p. 3237-3241.

170. Escalante García, J.I. and J.H. Sharp, *Effect of temperature on the hydration of the main clinker phases in portland cements: Part I neat cements.* Cement and Concrete Research, 1998. **28**(9): p. 1245-1257.

171. Gallucci, E., X. Zhang, and K.L. Scrivener, *Effect of temperature on the microstructure of calcium silicate hydrate (C-S-H).* Cement and Concrete Research, 2013. **53**: p. 185-195.

172. Lothenbach, B., F. Winnefeld, C. Alder, E. Wieland, and P. Lunk, *Effect of temperature on the pore solution, microstructure and hydration products of Portland cement pastes.* Cement and Concrete Research, 2007. **37**(4): p. 483-491.

173. Kjellsen, K.O., R.J. Detwiler, and O.E. Gjørv, *Development of microstructures in plain cement pastes hydrated at different temperatures.* Cement and Concrete Research, 1991. **21**: p. 179-189.

174. Scrivener, K.L., *The effect of heat treatment on inner product C-S-H.* Cement and Concrete Research, 1992. **22**: p. 1224-1226.

175. Richardson, I.G. and G.W. Groves, *Models for the composition and structure of calcium silicate hydrate (C-S-H) gel in hardened tricalcium silicate pastes.* Cement and Concrete Research, 1992. **22**: p. 1001-1010.

176. Young, J.F., *Investigations of Calcium Silicate Hydrate structure using Silicon-29 Nuclear Magnetic Resonance Spectroscopy.* Communications of the American Ceramic Society 1988. **71**(3): p. C-118-C-120.

177. Brough, A.R., C.M. Dobson, I.G. Richardson, and G.W. Groves, *In situ solid-state NMR studies of Ca_3SiO_5: hydration at room temperature and at elevated temperatures using ^{29}Si enrichment.* Journal of Materials Science, 1994. **29**: p. 3926-3940.

178. Dent Glasser, L.S., E.E. Lachowski, K. Mohan, and H.F.W. Taylor, *A multi-method study of C_3S hydration.* Cement and Concrete Research, 1978. **8**(6): p. 733-740.

179. Mohan, K. and H.F.W. Taylor, *A trimethylsilylation study of tricalcium silicate pastes.* Cement and Concrete Research, 1982. **12**: p. 25-31.

180. Richardson, I.G., *The nature of C-S-H in hardened cements.* Cement and Concrete Research, 1999. **29**: p. 1131-1147.

181. Richardson, I.G., A.R. Brough, R.M.D. Brydson, G.W. Groves, and C.M. Dobson, *Location of aluminium in substituted calcium silicate hydrate (C-S-H) gels as determined by ^{29}Si and ^{27}Al NMR and EELS.* Journal of the American Ceramic Society, 1993. **76**(9): p. 2285-2288.

182. Andersen, M.D., H.J. Jakobsen, and J. Skibsted, *Incorporation of Aluminum in the Calcium Silicate Hydrate (C-S-H) of Hydrated Portland Cements: A High-Field ^{27}Al and ^{29}Si MAS NMR Investigation.* Inorganic Chemistry, 2003. **42**: p. 2280-2287.

183. Faucon, P., A. Delagrave, J.C. Petit, C. Richet, J.M. Marchand, and H. Zanni, *Aluminum incorporation in Calcium Silicate Hydrates (C-S-H) Depending on their Ca/Si ratio.* Journal of Physical Chemistry B, 1999. **103**: p. 7796-7802.

184. Taylor, H.F.W., *Proposed structure for calcium silicate hydrate gel.* Journal of the American Ceramic Society, 1986. **69**(9): p. 464-467.

185. Skibsted, J., H.J. Jakobsen, and C. Hall, *Quantification of Calcium Silicate Phases in Portland Cements by ^{29}Si MAS NMR Spectroscopy.* Journal of the Chemical Society, Faraday Transactions, 1995. **91**(24): p. 4423-4430.

186. Lippmaa, E., M. Mägi, M. Tarmak, W. Wieker, and A.R. FGrimmer, *A high resolution ^{29}Si NMR study of the hydration of tricalciumsilicate.* Cement and Concrete Research, 1982. **12**(5): p. 597-602.

187. Sevelsted, T.F., D. Herfort, and J. Skibsted, *13C chemical shift anisotropies for carbonate ions in cement minerals and the use of 13C, 27Al and 29Si MAS NMR in studies of Portland cement including limestone additions.* Cement and Concrete Research, 2013. **52**: p. 100-111.

188. Andersen, M.D., H.J. Jakobsen, and J. Skibsted, *A new aluminium-hydrate species in hydrated Portland cements characterized by 27Al and 29Si MAS NMR spectroscopy.* Cement and Concrete Research, 2006. **36**(1): p. 3-17.

189. Le Saout, G., E. Lécolier, A. Rivereau, and H. Zanni, *Chemical structure of cement aged at normal and elevated temperatures and pressures Part I. Class G oilwell cement.* Cement and Concrete Research, 2006. **36**(1): p. 71-78.

190. Skibsted, J., H.J. Jakobsen, and C. Hall, *Quantitative aspects of ^{27}Al MAS NMR of Calcium Aluminoferrites.* Advanced Cement Based Materials, 1998. **7**: p. 57-59.

191. Hidalgo, A., C. Domingo, C. Garcia, S. Petit, C. Andrade, and C. Alonso, *Microstructural changes induced in Portland cement-based materials due to natural and supercritical carbonation.* Journal of Materials Science, 2008. **43**: p. 3101-3111.

192. Baston, G.M.N., M.M. Cowper, and T.A. Marshall, *Sorption of U(VI) onto leached and hydrothermally-aged NRVB*. 2010, NDA RWMD

193. Dumitru, G., T. Vázquez, F. Puertas, and M.T. Blanco-Varela, *Influencia de la adición del $BaCO_3$ sobre la hidratación del cemento portland.* Materiales de Construcctión 1999. **49**(254): p. 43-48.

194. Richardson, I.G., C.R. Wilding, and M.J. Dickson, *The hydration of blast-furnance slag cements.* Advanced Cement Research 1989. **2**: p. 147-157.

195. Bellotto, M., B. Rebours, O. Clause, J. Lynch, D. Bazin, and E. Elkaïm, *A reexamination of hydrotalcite crystal chemistry.* Journal of Physical Chemistry, 1996. **100**(20): p. 8527-8534.

196. Francois, M., G. Renaudin, and O. Evrard, *A Cementitious Compound with Composition 3CaO.Al2O3.CaCO3.11H2O.* Acta Crystallographica Section C, 1998. **54**(9): p. 1214-1217.

197. Kanezaki, E., *Thermal behaviour of the hydrotalcite-like layered structure of Mg and Al-layered double hydroxides with interlayer carbonate by means of in situ powder HTXRD and DTA/TG.* Solid State Ionics, 1998. **106**: p. 279-284.

198. Sato, T. and J.J. Beaudoin, *Effect of nano-CaCO3 on hydration of cement containing supplementary cementitious materials.* Advances in Cement Research, 2011. **23**(1): p. 33-43.

199. Utton, C., E. Gallucci, J. Hill, and N.B. Milestone, *Interactions between $BaCO_3$ and OPC/BFS composite cements at 20˚C and 60˚C*, in *Workshop on Mechanisms and Modelling of Waste/Cement Interactions*. 2008: Le Croisic, France.

200. Li, S., *Carbonation of 20-year-old Blended Cement Pastes*. 2011, School of Civil Engineering, University of Leeds.

201. Evans, N.D.M., *Binding mechanisms of radionuclides to cement.* Cement and Concrete Research, 2008. **38**(4): p. 543-553.

202. Rozov, K., U. Berner, C. Taviot-Gueho, F. Leroux, G. Renaudin, D. Kulik, and L.W. Diamond, *Synthesis and characterization of the LDH hydrotalcite-pyroaurite solid-solution series.* Cement and Concrete Research, 2010. **40**: p. 1248-1254.

203. Poulsen, S.L., V. Kocaba, G. Le Saout, H.J. Jakobsen, K.L. Scrivener, and J. Skibsted, *Improved quantification of alite and belite in anhydrous Portland cements by (29)Si MAS NMR: effects of paramagnetic ions.* Solid State Nucl Magn Reson, 2009. **36**(1): p. 32-44.

204. Schneider, J., M.A. Cincotto, and H. Panepucci, *^{29}Si and ^{27}Al high- resolution NMR charaterization of calcium silicate hydrate phases in activated blast- furnace slag pastes.* Cement and Concrete Research, 2001. **31**: p. 993-1001.

205. Murgier, S., H. Zanni, and D. Gouvenot, *Blast furnace slag cement: a 29Si and 27Al NMR study.* Comptes Rendus Chimie, 2004. **7**(3-4): p. 389-394.

206. Rey, F. and V. Fornés, *Thermal decomposition of hydrotalcites an infrared and nuclear magnetic resonance spectroscopic study.* Journal of the Chemical Society, Faraday Transactions, 1992. **88**(15): p. 2233-2238.

207. Rickerby, J.A., I.G. Richardson, and L. Black, *Characterisation of blended cements incorporating simulant intermediate level nuclear wastes*, in *33rd Cement and Concrete Science Conference* 2013: University of Portsmouth, Portsmouth, UK. .

208. Mesbah, A., C. Cau-dit-Coumes, G. Renaudin, F. Frizon, and F. Leroux, *Uptake of chloride and carbonate ions by calcium monosulfoaluminate hydrate.* Cement and Concrete Research, 2012. **42**(8): p. 1157-1165.

209. Banba, T., J. Matsumoto, and S. Muraoka, *Leaching behaviour of carbon-14 contained in portland cement.* cement and Concrete Research, 1992. **22**(2-3): p. 381-386.

210. Glasser, F.P., *Chemistry of Cement-Solidified Waste Forms*, in *Chemistry and Microstructure of Solidified Waste Forms*, R.D. Spence, Editor. 1992, CRC Press: Boca Raton. p. 1-40.

211. Glasser, F.P., *Application of inorganic cements to the conditioning and immobilisation of radioactive wastes*, in *Handbook of Advanced Radioactive Waste Conditioning Technologies*, M. Ojovan, Editor. 2011, Woodhead: Cambridge. p. 67-135.

212. Batchelor, B., *Overview of waste stabilization with cement.* Waste Management, 2006. **26**(7): p. 689-698.

213. Bone, B.D., L.H. Barnard, D.I. Boardman, P.J. Carey, C.D. Hills, H.M. Jones, C.L. MacLeod, and M. Tyrer, *Review of scientific literature on the use of stabilisation/solidification for the treatment of contaminated soil, solid waste and sludges*. 2004, Environment Agency

214. Castleton, H.F., V. Stovin, S.B.M. Beck, and J.B. Davison, *Green roofs; building energy savings and the potential for retrofit.* Energy and Buildings, 2010. **42**(10): p. 1582-1591.

215. Komarneni, S., E. Breval, and D.M. Roy, *Reactions of some calcium silicates with metal cations.* Cement and Concrete Research, 1988. **18**(2): p. 204-220.

216. Goldschmidt, V.M., *The principles of distribution of chemical elements in minerals and rocks.* Journal of the Chemical Society, 1937: p. 655.

217. Ringwood, A.E., *The influence of electro-negativity.* Geochemica et Cosmochimica Acta 1955. **7**: p. 189-202.

218. Shannon, R.D., *Revised Effective Ionic-Radii and Systematic Studies of Interatomic Distances in Halides and Chalcogenides.* Acta Crystallographica Section A, 1976. **32**(Sep1): p. 751-767.

219. Puertas, F., M.T. Blanco-Varela, and T. Vazquez, *Behaviour of cement mortars containing an industrial waste from aluminium refining - Stability in Ca(OH)(2) solutions.* Cement and Concrete Research, 1999. **29**(10): p. 1673-1680.

220. Rinaldi, R., M. Sacerdoti, and E. Passaglia, *Strätlingite: crystal structure, chemistry, and a reexamination of its polytype vertumnite.* European Journal of Mineralogy, 1990. **2**: p. 841-849.

221. Jia, S. and J.A. Rickerby, *Report on the composition and microstructure of selected ILW encapsulation grouts*. 2012, University of Leeds.

222. Gruskovnjak, A., B. Lothenbach, F. Winnefeld, B. Munch, R. Figi, S.C. Ko, M. Adler, and U. Mader, *Quantification of hydration phases in supersulfated cements: review and new approaches.* Advances in Cement Research, 2011. **23**(6): p. 265-275.

223. Antoni, M., J. Rossen, F. Martirena, and K. Scrivener, *Cement substitution by a combination of metakaolin and limestone.* Cement and Concrete Research, 2012. **42**(12): p. 1579-1589.

224. Renaudin, G., J. Russias, F. Leroux, F. Frizon, and C. Cau-Dit-Coumes, *Structural characterization of C-S-H and C-A-S-H samples-Part I: Long-range order investigated by Rietveld analyses.* Journal of Solid State Chemistry, 2009. **182**(12): p. 3312-3319.

225. Wang, S.-D. and K.L. Scrivener, *29Si and 27Al NMR study of alkali-activated slag.* Cement and Concrete Research, 2003. **33**(5): p. 769-774.

226. Kwan, S., J. La Rosa, and M.W. Grutzeck, *^{29}Si and ^{27}Al MASNMR Study of Strätlingite.* Journal of the American Ceramic Society, 1995. **78**(7): p. 1921-1926.

227. Ghorab, H.Y., E.A. Kishar, and S.H.A. Elfetouh, *Studies on the stability of the calcium sulfoaluminate hydrates. Part II: Effect of alite, lime, and monocarboaluminate hydrate.* Cement and Concrete Research, 1998. **28**(1): p. 53-61.

228. Ipavec, A., R. Gabrovsek, T. Vuk, V. Kaucic, J. Macek, and A. Meden, *Carboaluminate Phases Formation During the Hydration of Calcite-Containing Portland Cement.* Journal of the American Ceramic Society, 2011. **94**(4): p. 1238-1242.

229. Pardal, X., I. Pochard, and A. Nonat, *Experimental study of Si-Al substitution in calcium-silicate-hydrate (C-S-H) prepared under equilibrium conditions.* Cement and Concrete Research, 2009. **39**(8): p. 637-643.

230. Midgley, H.G. and P. Bjaskara Rao, *Formation of strätlingite, $2CaO.SiO_2.Al_2O_3.8H_2O$, in relation to the hydration of high alumina cement.* Cement and Concrete Research, 1978. **8**(2): p. 169-172.

231. Kwan, S., J. La Rosa-Thompson, and M.W. Grutzeck, *Structures and Phase Relations of Aluminum-Substituted Calcium Silicate Hydrate.* Journal of the American Ceramic Society, 1996. **79**(4): p. 967-971.

232. Lodeiro, I.G., A. Fernandez-Jimenez, A. Palomo, and D.E. Macphee, *Effect on fresh C-S-H gels of the simultaneous addition of alkali and aluminium.* Cement and Concrete Research, 2010. **40**(1): p. 27-32.

233. Ding, J., Y. Fu, and J.J. Beaudoin, *Strätlingite formation in high alumina cement - silica fume systems: significance of sodium ions.* Cement and Concrete Research, 1995. **25**(6): p. 1311-1319.

234. Rios, C., C. Williams, and M. Fullen, *Hydrothermal synthesis of hydrogarnet and tobermorite at 175 °C from kaolinite and metakaolinite in the CaO–Al2O3–SiO2–H2O system: A comparative study.* Applied Clay Science, 2009. **43**(2): p. 228-237.

235. Taylor, H.F.W., *Cement Chemistry 2$^{nd\ ed}$*. 1997, London: Thomas Telford.

236. Dweck, J., P.M. Buchler, A.C.V. Coelho, and F.K. Cartledge, *Hydration of a Portland cement blended with calcium carbonate.* Thermochimica Acta, 2000. **346**: p. 105-113.

237. Luke, K. and E. Lachowski, *Internal Composition of 20-Year-Old Fly Ash and Slag-Blended Ordinary Portland Cement Pastes.* Journal of the American Ceramic Society, 2008. **91**(12): p. 4084-4092.

238. Richardson, I.G., S.A. Rodger, and G.W. Groves, *The Microstructure of Ggbfs Opc Hardened Cement Pastes and Some Effects of Leaching.* Scientific Basis for Nuclear Waste Management Xiii, 1990. **176**: p. 63-74.

239. Richardson, I.G. and G.W. Groves, *Models for the Composition and Structure of Calcium Silicate Hydrate (C-S-H) Gel in Hardened Tricalcium Silicate Pastes and the Incorporation of Minor and Trace-Elements into Calcium Silicate Hydrate (C-S-H) Gel in Hardened Cement Pastes - Reply.* Cement and Concrete Research, 1993. **23**(4): p. 999-1000.

240. Brew, D.R.M. and F.P. Glasser, *Synthesis and characterisation of magnesium silicate hydrate gels.* Cement and Concrete Research, 2005. **35**(1): p. 85-98.

241. Morandeau, A., M. Thiéry, and P. Dangla, *Investigation of the carbonation mechanism of CH and C-S-H in terms of kinetics, microstructure changes and moisture properties.* Cement and Concrete Research, 2014. **56**: p. 153-170.

242. Bonen, D. and M.D. Cohen, *Magnesium-Sulfate Attack on Portland-Cement Paste .1. Microstructural Analysis.* Cement and Concrete Research, 1992. **22**(1): p. 169-180.

243. Bonen, D. and M.D. Cohen, *Magnesium-Sulfate Attack on Portland-Cement Paste .2. Chemical and Mineralogical Analyses.* Cement and Concrete Research, 1992. **22**(4): p. 707-718.

244. Cronin, J. and N. Collier, *Corrosion and expansion of grouted Magnox.* Mineralogical Magazine, 2012. **76**(8): p. 2901-2909.

245. Collier, N.C., N.B. Milestone, J. Hill, and I.H. Godfrey, *The disposal of radioactive ferric floc.* Waste Manag, 2006. **26**(7): p. 769-75.

246. Gosselin, C., *Microstructural Developement of Calcium Aluminate Cement Based Systems with and without Supplementary Cementitious Materials. PhD Thesis*. 2009, École Polytechnique Fédérale de Lausanne.

247. Le Saoût, G., E. Lécolier, A. Rivereau, and H. Zanni, *Chemical structure of cement aged at normal and elevated temperatures and pressures, Part II: Low permeability class G oilwell cement.* Cement and Concrete Research, 2006. **36**(3): p. 428-433.

248. Neuville, N., E. Lecolier, G. Aouad, A. Rivereau, and D. Darnidot, *Effect of curing conditions on oilwell cement paste behaviour during leaching: Experimental and modelling approaches.* Comptes Rendus Chimie, 2009. **12**(3-4): p. 511-520.

249. Marsh, B.K. and R.L. Day, *Pozzolanic and cementitious reactions of fly ash in blended cement pastes.* Cement and Concrete Research, 1988. **18**(2): p. 301-310.

250. Pertlik, F., *Bibliography of Hibschite, a Hydrogarnet of Grossular Type.* Geolines, 2003. **15**: p. 113-119.

251. Cohen-Addad, C., P. Ducros, A. Durif-Varambon, E.F. Bertaut, and A. Delapalme, *Détermination de al position des atomes d'hydrogene dans l'hydrogrenat $Al_2O_3(CaO)_3(H_2O)_6$ par résonance magnétique nucléaire et diffraction neutronique.* Journ. Phys. Fr, 1964. **25**: p. 478-483.

252. Basso, R., *Crystal Chemical and Crystallographic Properties of Compounds with Garnet or Hydrogarnet Structure.* Neues Jahrbuch Fur Mineralogie-Monatshefte, 1985(3): p. 108-114.

253. Basso, R. and L. Zefiro, *Fast Prediction of Hydrogarnet Composition.* Neues Jahrbuch Fur Mineralogie-Monatshefte, 1992(6): p. 251-257.

254. Sacerdoti, M. and E. Passaglia, *The Crystal-Structure of Katoite and Implications within the Hydrogrossular Group of Minerals.* Bulletin De Mineralogie, 1985. **108**(1): p. 1-8.

255. Armbruster, T. and G.A. Lager, *Oxygen Disorder and the Hydrogen Position in Garnet-Hydrogarnet Solid-Solutions.* European Journal of Mineralogy, 1989. **1**(3): p. 363-369.

256. Lager, G.A., T. Armbruster, and J. Faber, *Neutron and X-Ray-Diffraction Study of Hydrogarnet $Ca_3Al_2(O4H4)_3$.* American Mineralogist, 1987. **72**(7-8): p. 756-765.

257. Passaglia, E. and R. Rinaldi, *Katoite, a New Member of the Ca3al2(Sio4)3-Ca3al2(Oh)12 Series and a New Nomenclature for the Hydrogrossular Group of Minerals.* Bulletin De Mineralogie, 1984. **107**(5): p. 605-618.

258. Sawada, H., *Electron density study of garnets: Z(3)Al(2)Si(3)O(12) (Z = Mg, Fe, Mn, Ca) and Ca3Fe2Si3O12.* Journal of Solid State Chemistry, 1999. **142**(2): p. 273-278.

259. Prandl, W., *Verfeinerung der Kristallstruktur des Grossulars mit Neutronen- und Roentgenstrahlbeugung.* Zeitschrift fuer Kristallographie, Kristallgeometrie, Kristallphysik, Kristallchemie, 1966. **123**: p. 81-116.

260. Lager, G.A., G.R. Rossman, F.J. Rotella, and A.J. Schultz, *Neutron-Diffraction Structure of a Low-Water Grossular at 20 K.* American Mineralogist, 1987. **72**(7-8): p. 766-768.

261. Lager, G.A., T. Armbruster, F.J. Rotella, and G.R. Rossman, *OH Substitution in Garnets - X-Ray and Neutron-Diffraction, Infrared, and Geometric-Modeling Studies.* American Mineralogist, 1989. **74**(7-8): p. 840-851.

262. Pabst, A., *The crystal structure of plazolite.* American Mineralogist, 1937. **22**: p. 861-868.

263. Ferro, O., E. Galli, G. Papp, S. Quartieri, S. Szakall, and G. Vezzalini, *A new occurrence of katoite and re-examination of the hydrogrossular group.* European Journal of Mineralogy, 2003. **15**(2): p. 419-426.

264. Flint, E.P., H.F. McMurdie, and L.S. Wells, *Hydrothermal and X-ray studies of the garnet-hydrogarnet series and the relationship of the series to hydration products of Portland cement.* Journal of Research of the National Bureau of Standards, 1941. **26**(1): p. 13-33.

265. Quartieri, S., G. Artioli, A. Deriu, P.P. Lottici, and G. Antonioli, *Fe-57-Mossbauer Investigation on Garnets from the Ivrea-Verbano Zone.* Mineralogical Magazine, 1993. **57**(389): p. 671-676.

266. Taylor, H. 1980, ICDD Grant-in-Aid.

267. Cullity, B.D. and S.R. Stock, *Elements of X-ray diffraction*. 3rd ed. 2001, London: Prentice Hall.

268. Kyritsis, K., N. Meller, and C. Hall, *Chemistry and Morphology of Hydrogarnets Formed in Cement-Based CASH Hydroceramics Cured at 200° to 350°C.* Journal of the American Ceramic Society, 2009. **92**(5): p. 1105-1111.

269. Venkateswarlu, K., A.C. Bose, and N. Rameshbabu, *X-ray peak broadening studies of nanocrystalline hydroxyapatite by Williamson-Hall analysis.* Physica B-Condensed Matter, 2010. **405**(20): p. 4256-4261.

270. Bueno-Ferrer, C., S. Parres-Esclapez, D. Lozano-Castello, and A. Bueno-Lopez, *Relationship between surface area and crystal size of pure and doped cerium oxides.* Journal of Rare Earths, 2010. **28**(5): p. 647-653.

271. Williamson, G.K. and W.H. Hall, *X-Ray line broadening from filed aluminium and wolfram.* Acta Metallurgica, 1953. **1**.

272. Zak, A.K., W.H.A. Majid, M.E. Abrishami, and R. Yousefi, *X-ray analysis of ZnO nanoparticles by Williamson-Hall and size-strain plot methods.* Solid State Sciences, 2011. **13**(1): p. 251-256.

273. Burton, A.W., K. Ong, T. Rea, and I.Y. Chan, *On the estimation of average crystallite size of zeolites from the Scherrer equation: A critical evaluation of its application to zeolites with one-dimensional pore systems.* Microporous and Mesoporous Materials, 2009. **117**(1-2): p. 75-90.

274. Jappy, T.G. and F.P. Glasser, *Synthesis and stability of silica-substituted hydro garnet* $Ca_3Al_2Si_{3-x}O_{12-4x}(OH)_{4x}$. Advances in Cement Research, 1991. **4**(13): p. 1-8.

275. Bennett, D.G., D. Read, M. Atkins, and F.P. Glasser, *A Thermodynamic Model for Blended Cements .2. Cement Hydrate Phases, Thermodynamic Values and Modeling Studies.* Journal of Nuclear Materials, 1992. **190**: p. 315-325.

276. Dilnesa, B.Z., E. Wieland, B. Lothenbach, R. Dähn, and K.L. Scrivener, *Fe- containing phases in hydrated cements.* Cement and Concrete Research, 2014. **58**(1): p. 45-55.

277. Dilnesa, B.Z., *Fe-containing hydrates and their fate during cement hydration: thermodynamic data and experimental study*. 2011, École Polytechnique Fédérale de Lausanne.

278. Passaglia, E. and P. Rinaldi, *Katoite, a new member of the* $Ca_3Al_2(SiO_4)_3$-$Ca_3Al_2(OH)_{12}$ *series and a new nomenclature for the hydrogrossular group of minerals.* Bulletin De Mineralogie, 1984. **107**: p. 605-618.

279. Girao, A.V., I.G. Richardson, C.B. Porteneuve, and R.M.D. Brydson, *Composition, morphology and nanostructure of C-S-H in white Portland cement-fly ash blends hydrated at 85°C.* Advances in Applied Ceramics, 2007. **106**(6): p. 283-293.

280. Luke, K., *Pulverised Fuel Ash as a Cement Extender*, in *Structure and Performance of Cements*, J. Bensted and P.D. Barnes, Editors. 2001, Taylor and Francis: London.

281. Rickerby, J.A., I.G. Richardson, and L. Black, *Characterisation of blended cements incorporating simulant intermediate level nuclear wastes*, in *33rd Cement and Concrete Science* 2013: University of Portsmouth, UK.

282. Zhang, Y.M., W. Sun, and H.D. Yan, *Hydration of high-volume fly ash cement pastes.* Cement and Concrete Composites, 2000. **22**(6): p. 445-452.

283. Meller, N., K. Kyritsis, and C. Hall, *The hydrothermal decomposition of calcium monosulfoaluminate 14-hydrate to katoite hydrogarnet and beta-anhydrite: An in-situ synchrotron X-ray diffraction study.* Journal of Solid State Chemistry, 2009. **182**(10): p. 2743-2747.

284. Richardson, I.G., *Model structures for C-(A)-S-H(I).* Acta Crystallographica B, 2014. **B70**: p. 903-923.

285. Faucon, P., T. Charpentier, A. Nonat, and J.C. Petit, *Triple-quantum two-dimensional Al-27 magic angle nuclear magnetic resonance study of the aluminum incorporation in calcium silicate hydrates.* Journal of the American Chemical Society, 1998. **120**(46): p. 12075-12082.

286. Brunet, F., T. Charpentier, C.N. Chao, H. Peycelon, and A. Nonat, *Characterization by solid-state NMR and selective dissolution techniques of anhydrous and hydrated CEM V cement pastes.* Cement and Concrete Research, 2010. **40**: p. 208-219.

287. Duchesne, J. and M.A. Be´rube´, *Effect of supplementary cementing materials on the composition of cement hydration products.* Advanced Cement Based Materials, 1995. **2**(2): p. 43-52.

288. Girao, A.V., I.G. Richardson, R. Taylor, and R.M.D. Brydson, *Composition, morphology and nanostructure of C-S-H in 70% white Portland cement-30% fly ash blends hydrated at 55 degrees C.* Cement and Concrete Research, 2010. **40**(9): p. 1350-1359.

289. Fu, X., Z. Wang, W. Tao, C. Yang, W. Hou, Y. Dong, and X. Wu, *Studies on blended cement with a large amount of fly ash.* Cement and Concrete Research, 2002. **32**(7): p. 1153-1159.

290. Wieland, E., I. Bonhoure, T. Fujita, J. Tits, and A.M. Scheidegger, *Combined wet chemistry and EXAFS studies on the radionuclide immobilisation by cement and calcium silicate hydrates.* Geochimica Et Cosmochimica Acta, 2003. **67**(18): p. A532-A532.

291. Moulin, I., W.E.E. Stone, J. Sanz, J.Y. Bottero, F. Mosnier, and C. Haehnel, *Lead and zinc retention during hydration of tri-calcium silicate: A study by sorption isotherms and (29)Si nuclear magnetic resonance spectroscopy.* Langmuir, 1999. **15**(8): p. 2829-2835.

292. Johnson, C.A., *Cement stabilization of heavy-metal-containing wastes.* Geological Society, London, Special Publications, 2004. **236**(1): p. 595-606.

293. Atkins, M., J. Cowie, F.P. Glasser, T. Jappy, A. Kindness, and C. Pointer, *Assessment of the Performance of Cement-Based Composite-Material for Radioactive-Waste Immobilization.* Scientific Basis for Nuclear Waste Management Xiii, 1990. **176**: p. 117-127.

294. Glasser, F.P. and M. Atkins, *Cements in Radioactive-Waste Disposal.* Mrs Bulletin, 1994. **19**(12): p. 33-38.

295. Gougar, M.L.D., B.E. Scheetz, and D.M. Roy, *Ettringite and C-S-H Portland cement phases for waste ion immobilization: A review.* Waste Management, 1996. **16**(4): p. 295-303.

296. Jantzen, C., A. Johnson, D. Read, and J.A. Stegemann, *Cements in waste management.* Advances in Cement Research, 2010. **22**(4): p. 225-231.

297. Ziegler, F., R. Giere, and C.A. Johnson, *Sorption mechanisms of zinc to calcium silicate hydrate: Sorption and microscopic investigations.* Environmental Science & Technology, 2001. **35**(22): p. 4556-4561.

298. Ziegler, F., A.M. Scheidegger, C.A. Johnson, R. Dahn, and E. Wieland, *Sorption mechanisms of zinc to calcium silicate hydrate: X-ray absorption fine structure (XAFS) investigation.* Environmental Science & Technology, 2001. **35**(7): p. 1550-1555.

299. Bonhoure, I., E. Wieland, A.M. Scheidegger, M. Ochs, and D. Kunz, *EXAFS study of Sn(IV) immobilization by hardened cement paste and calcium silicate hydrates.* Environmental Science & Technology, 2003. **37**(10): p. 2184-2191.

300. Pannaparayil, T., S. Komarneni, E. Breval, D.M. Roy, and L.N. Mulay, *Fe-3+-Substituted Tobermorites - Synthesis and Characterization by Mossbauer-Spectroscopy and Other Techniques.* Materials Research Bulletin, 1985. **20**(12): p. 1393-1400.

301. Atkins, M. and F.P. Glasser, *Application of Portland cement-based materials to radioactive waste immobilization.* Waste Management, 1992. **12**: p. 105-131.

302. Chen, Q.Y., M. Tyrer, C.D. Hills, X.M. Yang, and P. Carey, *Immobilisation of heavy metal in cement-based solidification/stabilisation: A review.* Waste Management, 2009. **29**(1): p. 390-403.

303. Faucon, P., F. Adenot, J.F. Jacquinot, J.C. Petit, R. Cabrillac, and M. Jorda, *Long-term behaviour of cement pastes used for nuclear waste disposal: Review of physico-chemical mechanisms of water degradation.* Cement and Concrete Research, 1998. **28**(6): p. 847-857.

304. Faucon, P., P. LeBescop, F. Adenot, P. Bonville, J.F. Jacquinot, F. Pineau, and B. Felix, *Leaching of cement: Study of the surface layer.* Cement and Concrete Research, 1996. **26**(11): p. 1707-1715.

Appendices

Appendix A – XRD

Calculation of HG unit cell dilation for Fe^{3+} substitution of Al^{3+}, resultant calculation of miscibility gap shown in chapter 8 XRD section.

$Grossular \ \rightarrow Andradite$

$a = 11.84 - 12.06$

$a = 0.22\text{Å}\ for\ 100\%\ Fe\ substitution$

$\Delta a = 0.0022\text{Å}\ at\ \%\ Fe\ substitution$

$Katoite \ \rightarrow C_3FH_6$

$a = 12.57 - 12.74$

$a = 0.17\text{Å}\ for\ 100\%\ Fe\ substitution$

$\Delta a = 0.0017\text{Å}\ at\ \%\ Fe\ substitution$

Therefore the dilation due to Fe is very close between the two end members of the HG group

$For\ C_3AS_3 \ \rightarrow \ C_3AH_6$

$C_3AH_6 \ \ a = 12.57\text{Å}$

Reported miscibility gap limits for this solid solution

$C_3AS_{0.41}H_{5.18} \qquad a = 12.47\text{Å}$ [1]

$C_3AS_{0.84}H_{4.32} \qquad a = 12.37\text{Å}$ [i]

Taking dilation for 12.47 relative to 12.57

$\Delta a = 0.1\text{Å}$

Taking dilation for 12.47 relative to 12.57

$\Delta a = 0.2\text{Å}$

For the C_3AS_3 to C_3AH_6 axis for when Si (*x*) = 0 - 3

---

[1] Dilnesa, B.Z. PhD Thesis, EPFL, 2011.

$\Delta a = 0.243\text{Å}$

Therefore for lower miscibility level (*x*):

$$\frac{0.1}{0.243} = 0.41$$

Therefore for higher miscibility level (*x*):

$$\frac{0.2}{0.243} = 0.82$$

$For\ C_3FS_3\ \rightarrow\ C_3FH_6$

$C_3AS_{0.41}H_{5.18} \qquad a = 12.47\text{Å}$

$C_3FH_6\ a = 12.74\text{Å}$

Reported miscibility gap limits for this solid solution

$C_3FS_{0.95}H_{8.20} \qquad a = 12.5424\text{Å}$ [2]

$C_3FS_{1.52}H_{5.92} \qquad a = 12.4257\text{Å}$ [ii]

Taking dilation for 12.5424 relative to 12.74

$\Delta a = 0.1976\text{Å}$

Taking dilation for 12.4297 relative to 12.74

$\Delta a = 0.3103\text{Å}$

For the C_3FS_3 to C_3FH_6 axis for when Si (*x*) = 0 - 3

$\Delta a = 12.74 - 12.06 = 0.68\ for\ 3x$

$\Delta a = 0.227\text{Å}$

Therefore for lower miscibility level (*x*):

$$\frac{0.1976}{0.227} = 0.87$$

Therefore for higher miscibility level (*x*):

---

[2] Dilnesa, B.Z. PhD Thesis, EPFL, 2011.

$$\frac{0.3103}{0.227} = 1.37$$

Slightly different Si contents calculated due to slightly differing unit cell value for C_3FH_6 used in this study.

Calculation of Scherrer equation for broadening for crystal size:

$$\beta_c = \frac{K\lambda}{D\ cos\theta}$$

Calculation of stress induced broadening:

$$\beta_e = 4e\ tan\theta$$

Then total broadening (not including instrumental):

$$\beta_t = \beta_c + \beta_e^1$$

Therefore:

$$\beta_t = \frac{K\lambda}{D\ cos\theta} + 4e\ tan\theta$$

$$\frac{\beta_t\ cos\theta}{\lambda} = \frac{K}{D} + \frac{4e\ sin\theta}{\lambda}$$

Data for Williamson-Hall plots of the Hydrogarnet phase

Fe floc A Sample 93 - 12 $\lambda = 1.5406$

hkl	2θ breadth	Rads	θ	cosθ	B cosθ/λ	sinθ	2 sinθ/λ
211	0.236	0.00412	8.85	0.9881	0.00264	0.1538	0.1997
220	0.242	0.00422	10.22	0.9841	0.00270	0.1774	0.2303
400	0.265	0.00463	14.51	0.9681	0.00291	0.2505	0.3253
420	0.293	0.00511	16.26	0.9600	0.00318	0.2800	0.3635
422	0.317	0.00553	17.85	0.9519	0.00342	0.3065	0.3979
431	0.255	0.00445	18.59	0.9478	0.00274	0.3188	0.4139
521	0.297	0.00518	20.03	0.9395	0.00316	0.3425	0.4446
611	0.345	0.00602	22.66	0.9228	0.00361	0.3853	0.5001
640	0.382	0.00667	26.70	0.8927	0.00387	0.4506	0.5849
642	0.404	0.00705	27.85	0.8842	0.00405	0.4672	0.6065

Estimated crystallite size=535Å

Strain = 0.23%

Fe floc B Sample 91 - 13

hkl	2θ breadth	Rads	θ	cosθ	B cosθ/λ	sinθ	2 sinθ/λ
211	0.227	0.00396	8.79	0.9883	0.00254	0.1528	0.1984
220	0.250	0.00436	10.15	0.9843	0.00279	0.1762	0.2287
321*	0.178	0.00311	13.55	0.9722	0.00196	0.2343	0.3042
400	0.389	0.00679	14.425	0.9685	0.00427	0.2491	0.3234
420	0.390	0.00681	16.19	0.9603	0.00424	0.2788	0.3619
431	0.359	0.00627	18.49	0.9484	0.00386	0.3171	0.4117
611	0.494	0.00862	22.59	0.9233	0.00517	0.3841	0.4986
642	0.750	0.01309	27.775	0.885	0.00752	0.466	0.605

* Data point sat well outside expected range and was discounted

Estimated crystallite size=4200Å

Strain = 0.53%

Al floc Sample 93 - 001

hkl	2θ breadth	Rads	θ	cosθ	B cosθ/λ	sinθ	2 sinθ/λ
211	0.227	0.00396	8.79	0.9883	0.002542	0.1528	0.1984
220	0.202	0.00353	10.155	0.9843	0.002253	0.1763	0.2289
400	0.283	0.00494	14.425	0.9685	0.003105	0.2491	0.3234
420	0.305	0.00532	16.19	0.9603	0.003318	0.2788	0.3620
422	0.350	0.00611	17.79	0.9522	0.003775	0.3055	0.3966
431	0.297	0.00518	18.85	0.9482	0.003191	0.3176	0.4124
521	0.341	0.00595	19.95	0.9400	0.003612	0.3412	0.4429
611	0.402	0.00702	22.575	0.9234	0.004205	0.3839	0.4984
640	0.487	0.00850	26.7	0.8934	0.004929	0.4493	0.5833
642	0.519	0.00906	27.79	0.8847	0.005203	0.4662	0.6053

Estimated crystallite size=1150Å

Strain = 0.47%

Appendix B – SEM

Fe floc A Sample 93 - 12

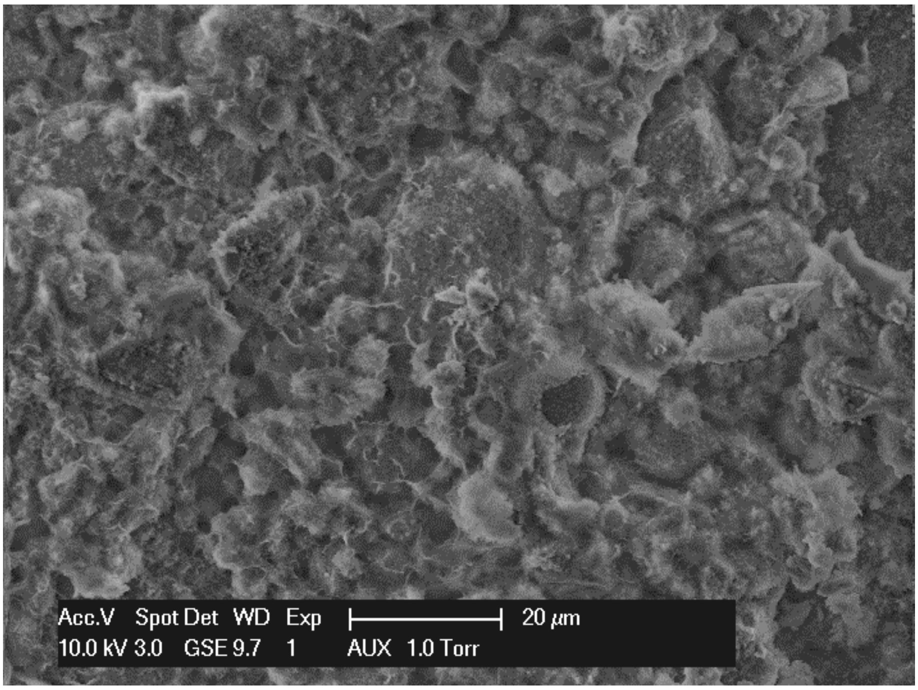

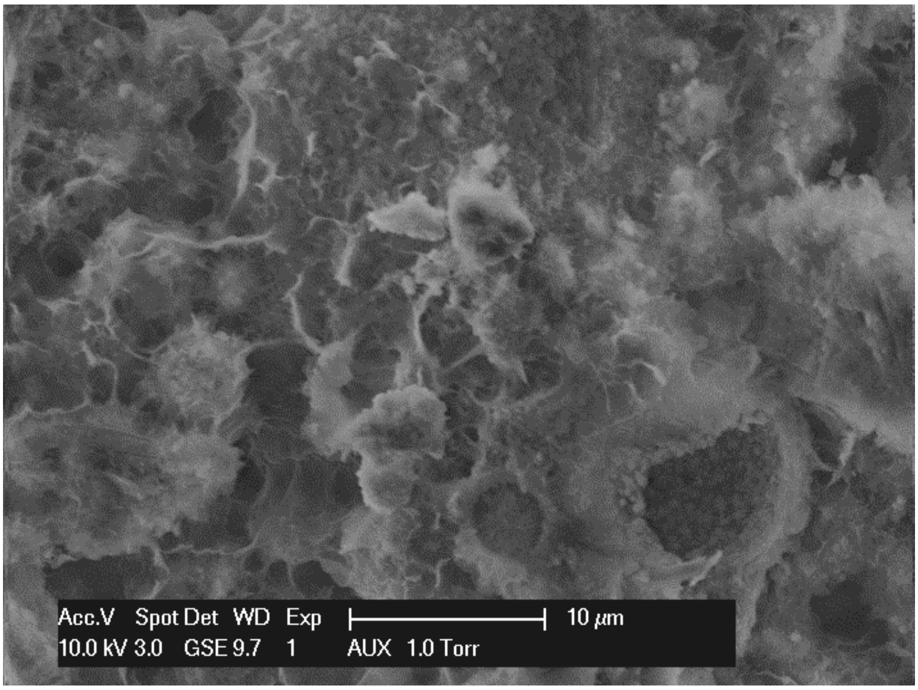

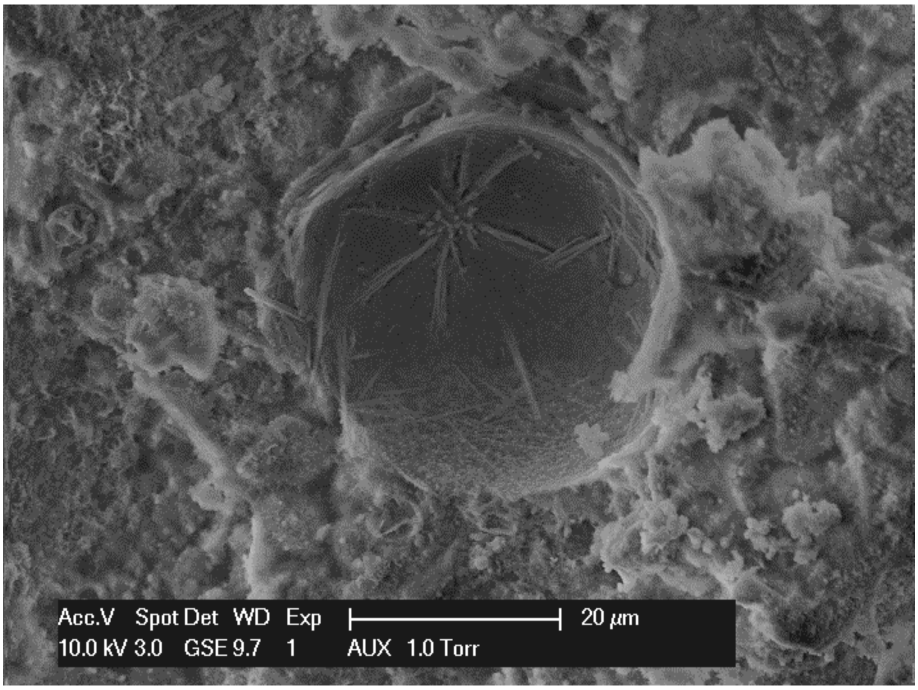
Acc.V Spot Det WD Exp
20 µm
10.0 kV 3.0 GSE 9.7 1 AUX 1.0 Torr

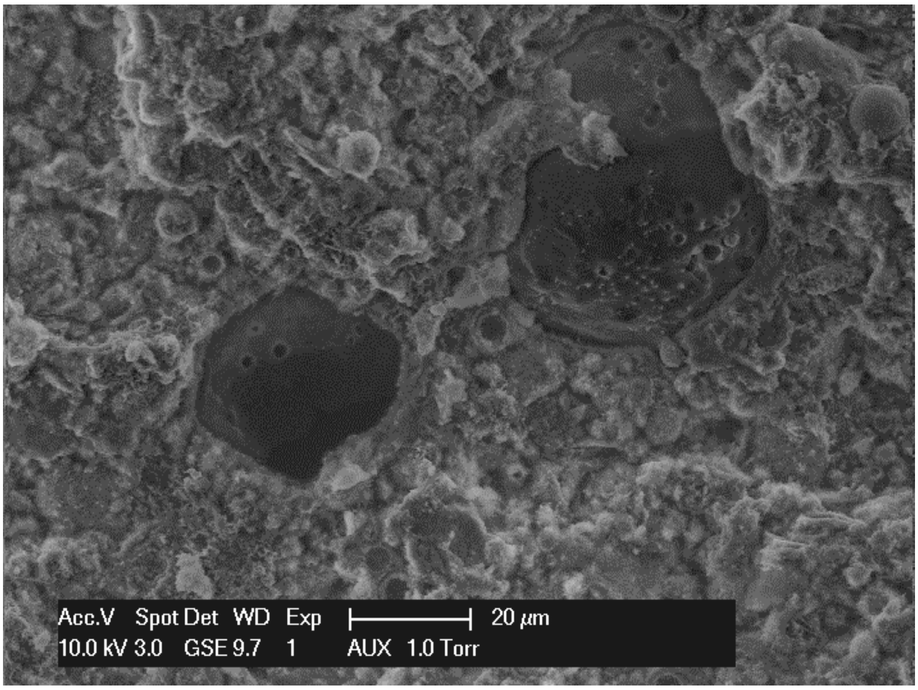
Acc.V Spot Det WD Exp
20 µm
10.0 kV 3.0 GSE 9.7 1 AUX 1.0 Torr

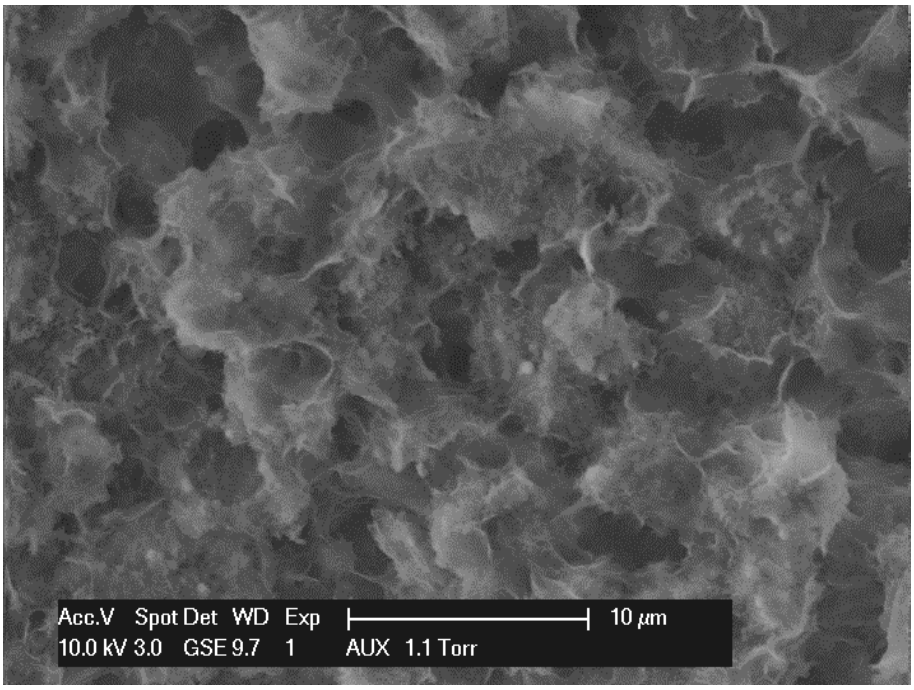
Acc.V Spot Det WD Exp
10 µm
10.0 kV 3.0 GSE 9.7 1 AUX 1.1 Torr

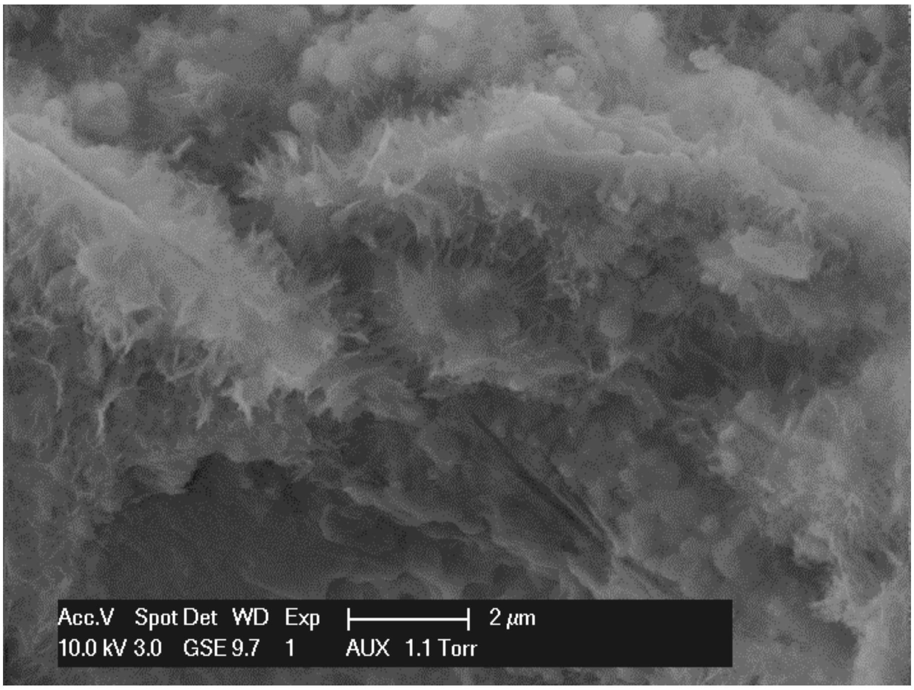
Acc.V Spot Det WD Exp
2 µm
10.0 kV 3.0 GSE 9.7 1 AUX 1.1 Torr

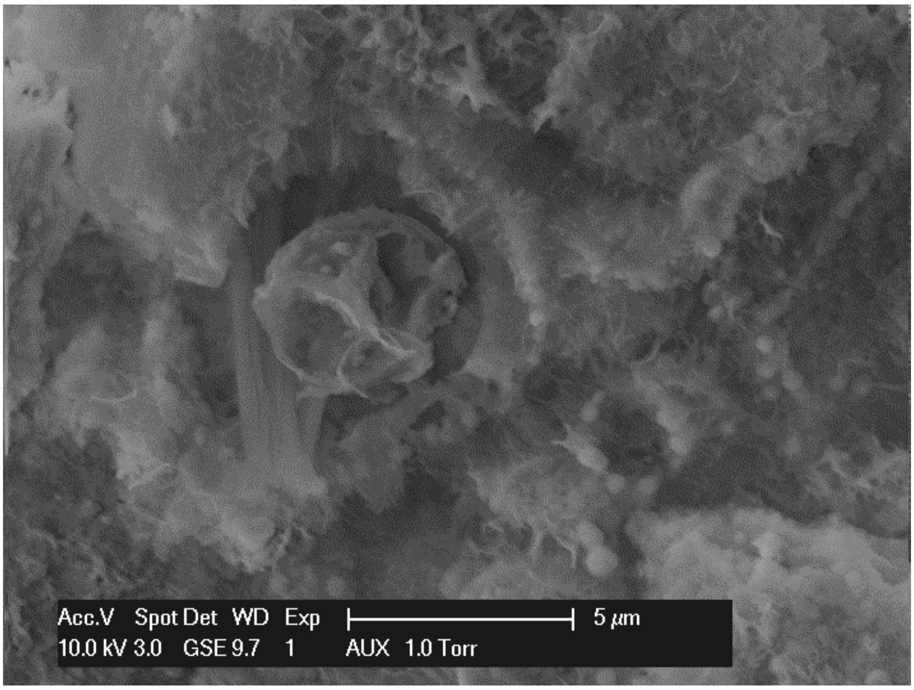
Acc.V Spot Det WD Exp
5 μm
10.0 kV 3.0 GSE 9.7 1 AUX 1.0 Torr

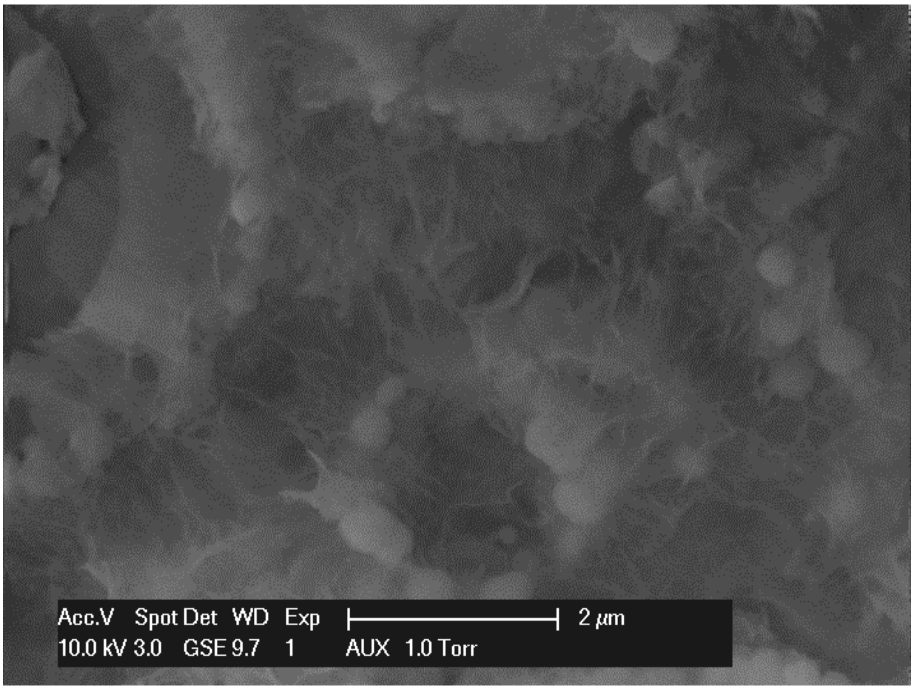
Acc.V Spot Det WD Exp
2 μm
10.0 kV 3.0 GSE 9.7 1 AUX 1.0 Torr

Fe floc B Sample 91 - 13

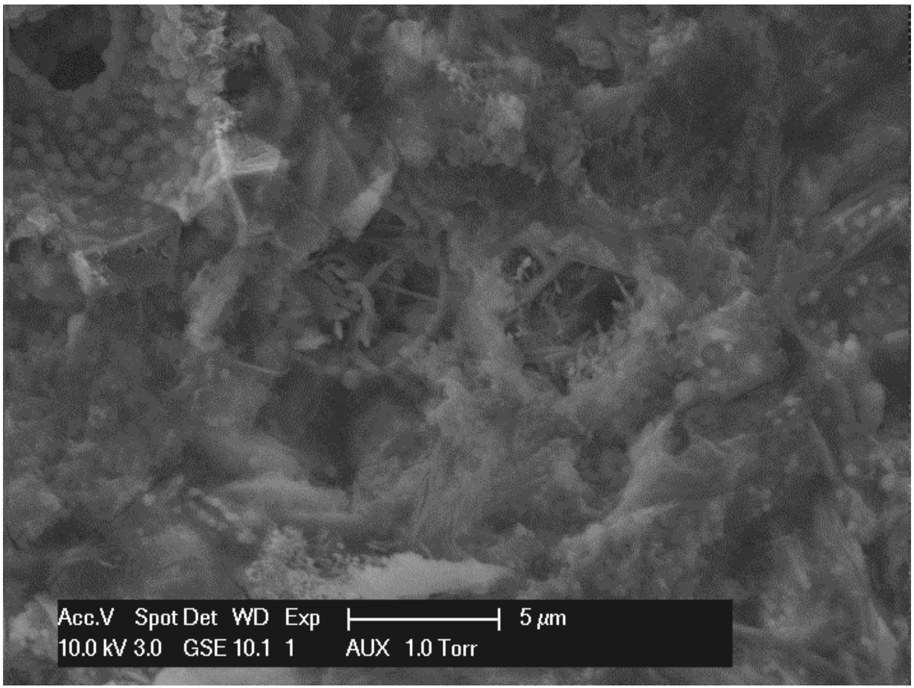

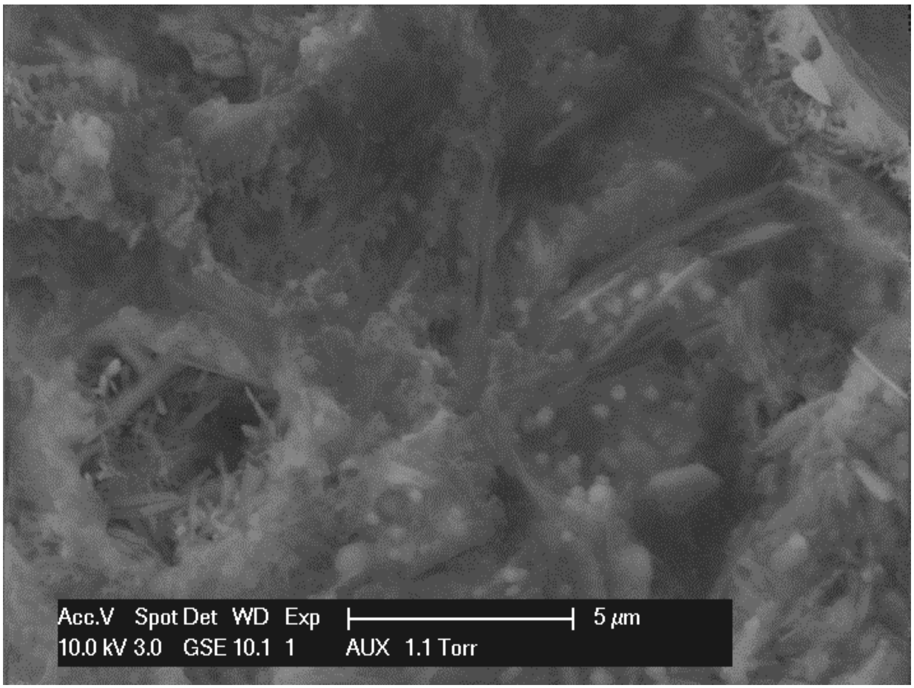
Acc.V Spot Det WD Exp
10.0 kV 3.0 GSE 10.1 1
5 µm
AUX 1.1 Torr

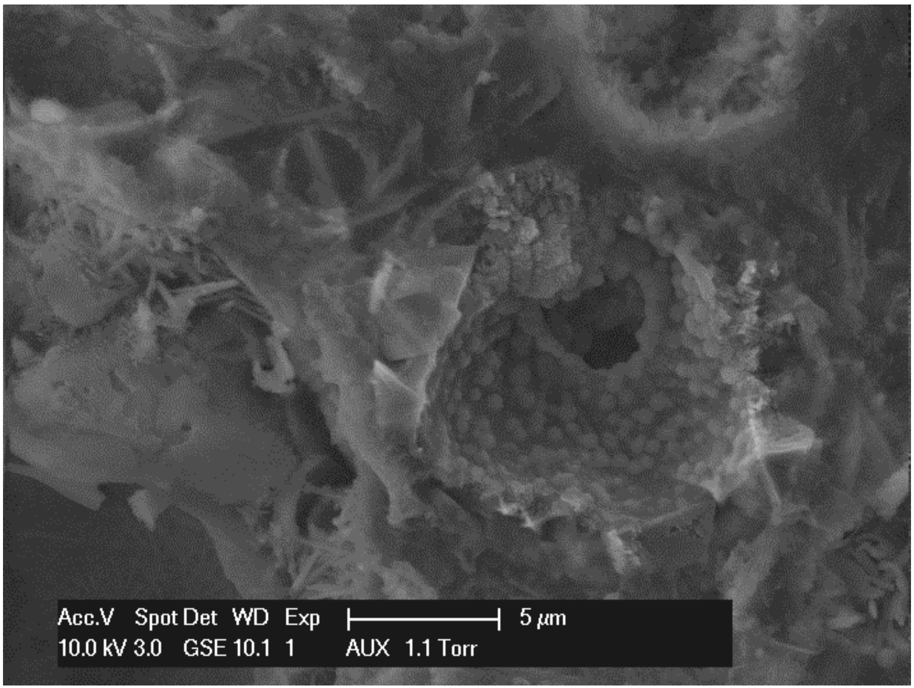
Acc.V Spot Det WD Exp
10.0 kV 3.0 GSE 10.1 1
5 µm
AUX 1.1 Torr

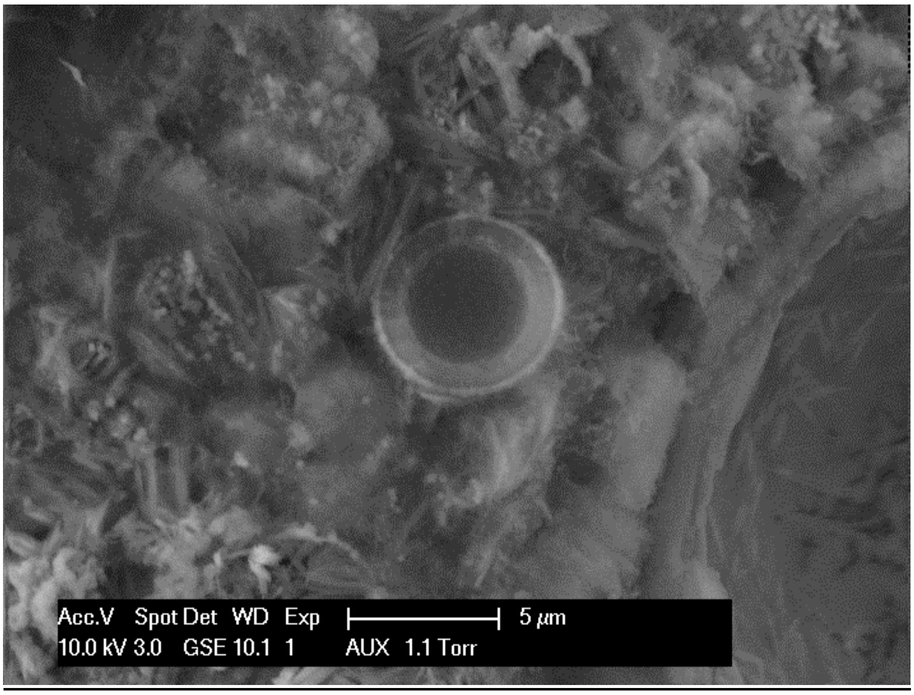
Acc.V Spot Det WD Exp
10.0 kV 3.0 GSE 10.1 1
5 μm
AUX 1.1 Torr

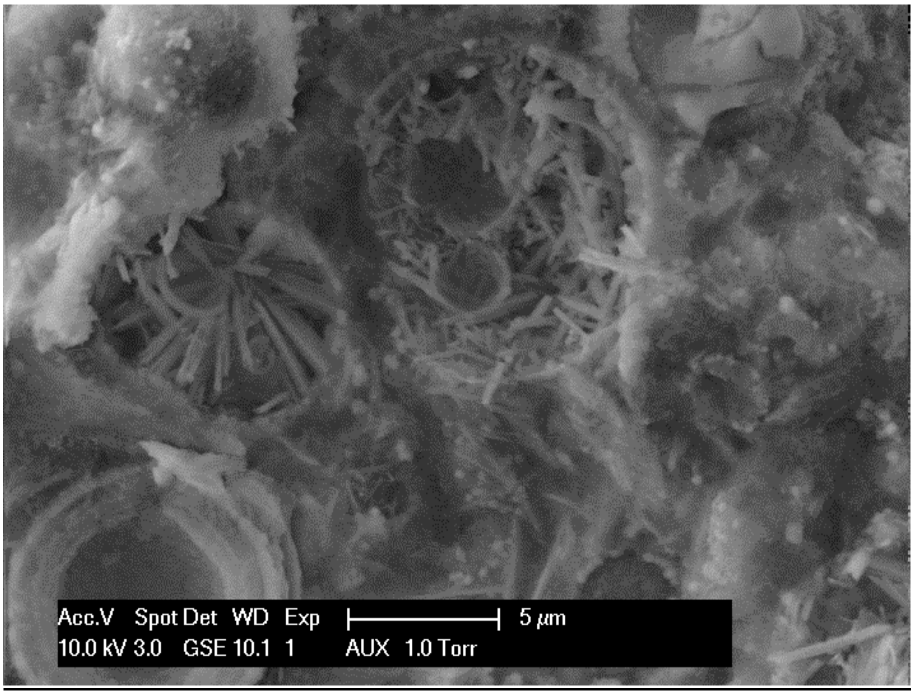
Acc.V Spot Det WD Exp
10.0 kV 3.0 GSE 10.1 1
5 μm
AUX 1.0 Torr

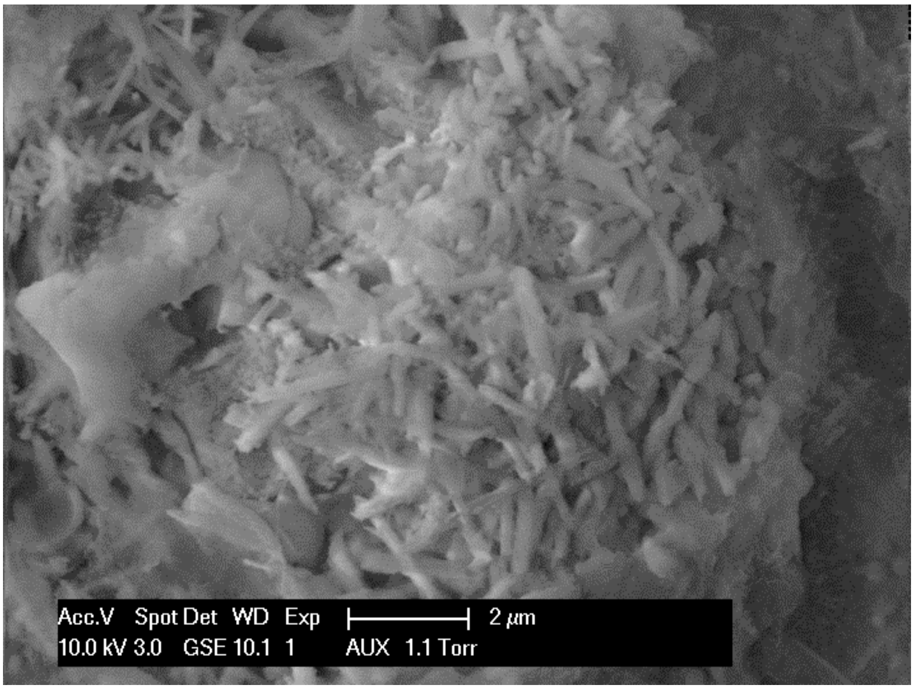
Acc.V Spot Det WD Exp
10.0 kV 3.0 GSE 10.1 1
2 µm
AUX 1.1 Torr

Al floc Sample 93 - 001

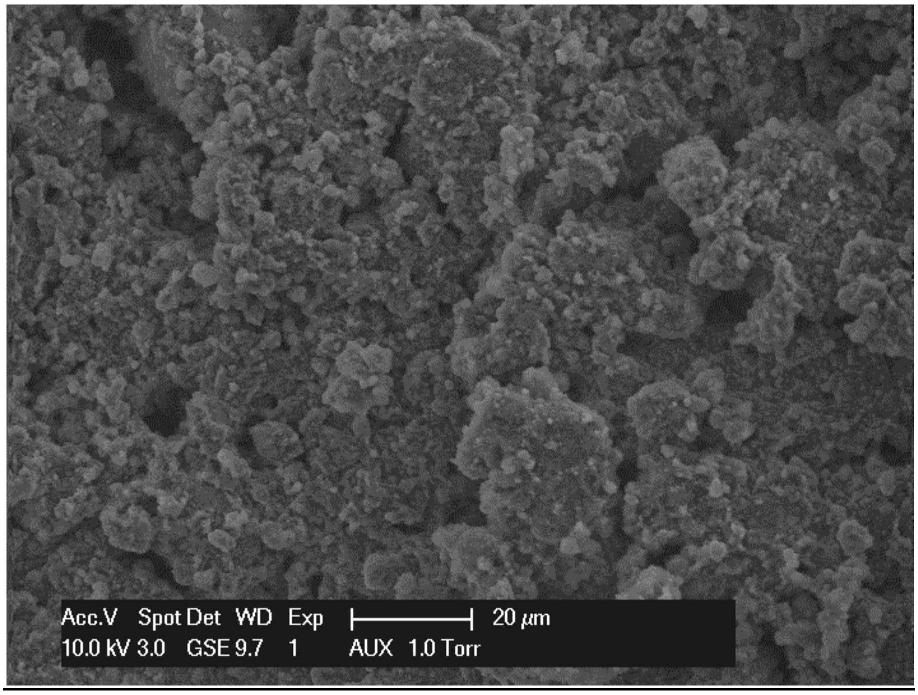

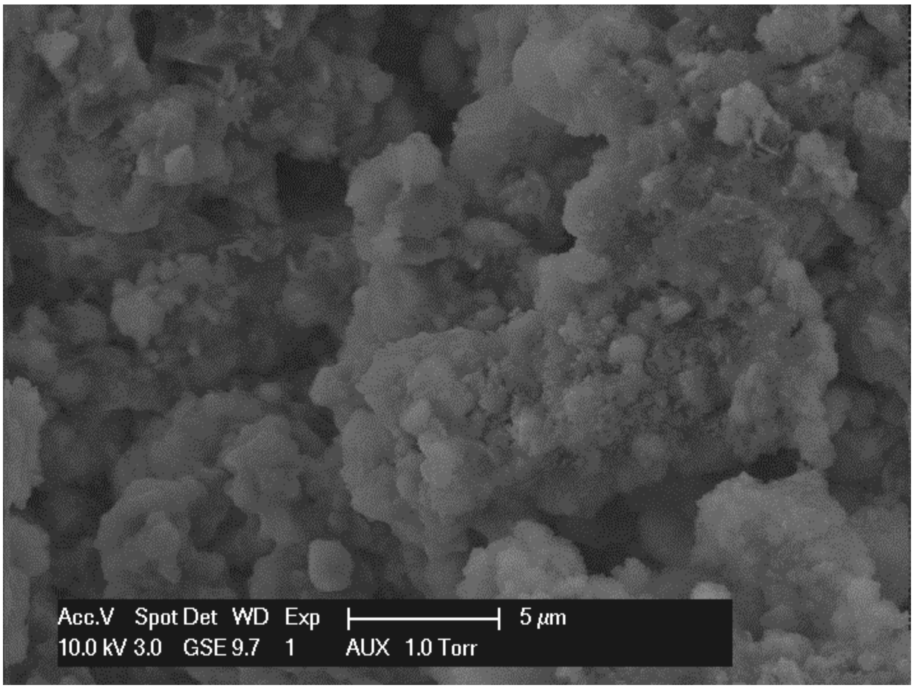

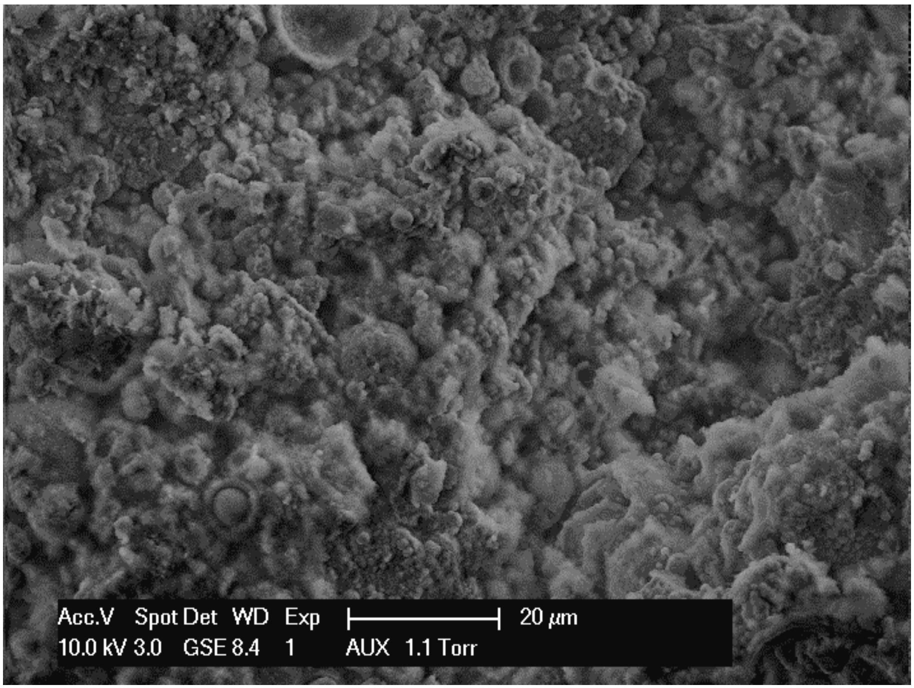
Acc.V Spot Det WD Exp
10.0 kV 3.0 GSE 8.4 1
20 μm
AUX 1.1 Torr

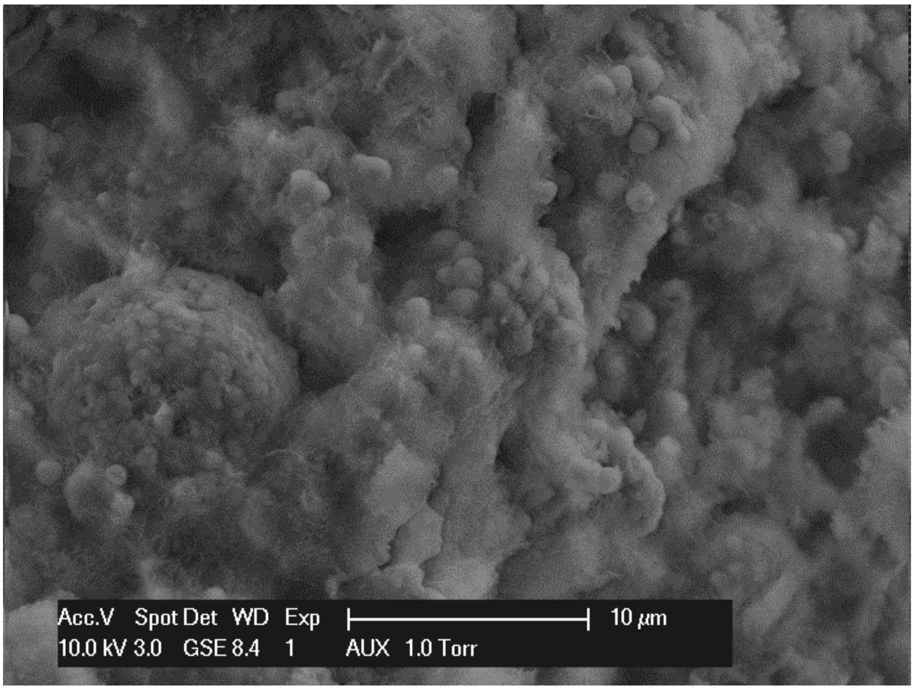
Acc.V Spot Det WD Exp
10.0 kV 3.0 GSE 8.4 1
10 μm
AUX 1.0 Torr

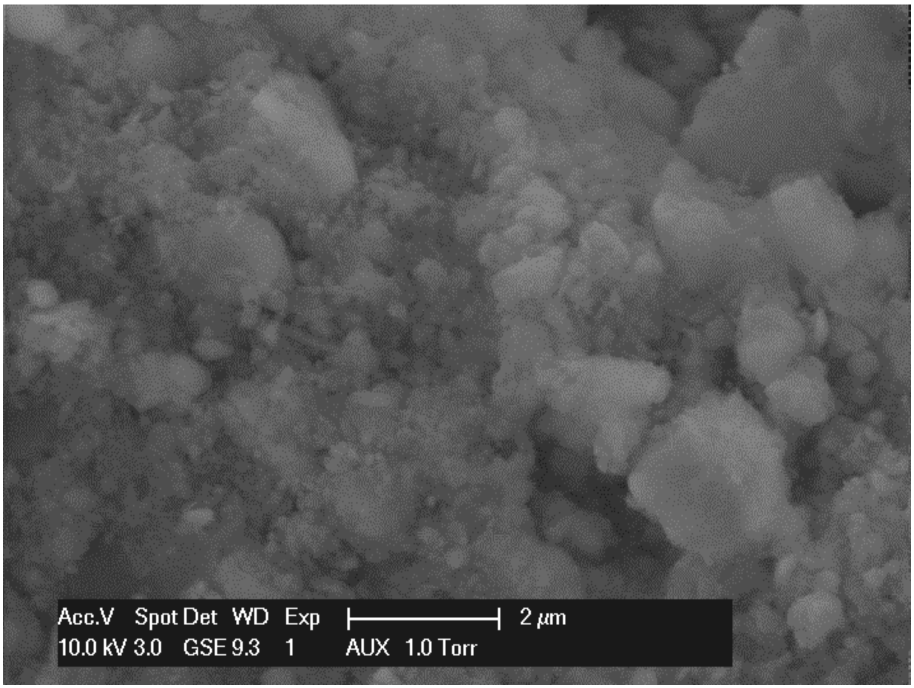
Acc.V Spot Det WD Exp
2 µm
10.0 kV 3.0 GSE 9.3 1
AUX 1.0 Torr

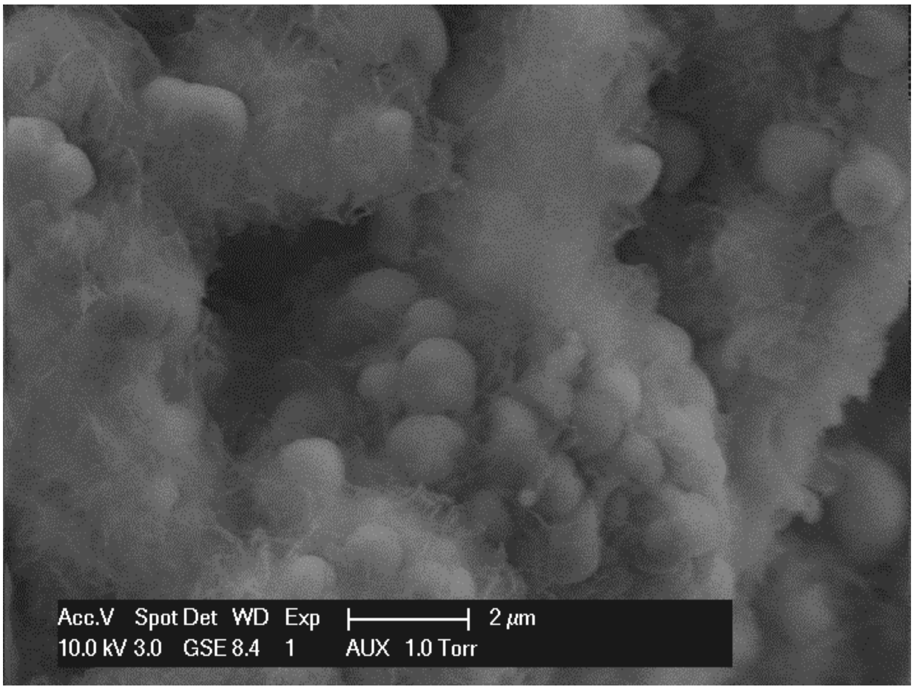
Acc.V Spot Det WD Exp
2 µm
10.0 kV 3.0 GSE 8.4 1
AUX 1.0 Torr

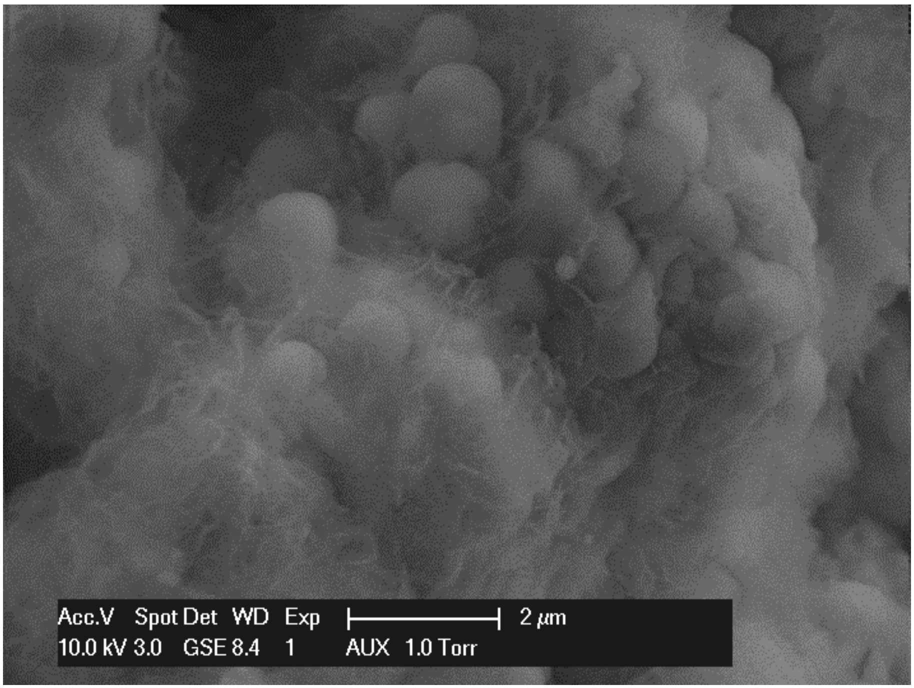
Acc.V Spot Det WD Exp
10.0 kV 3.0 GSE 8.4 1
2 μm
AUX 1.0 Torr

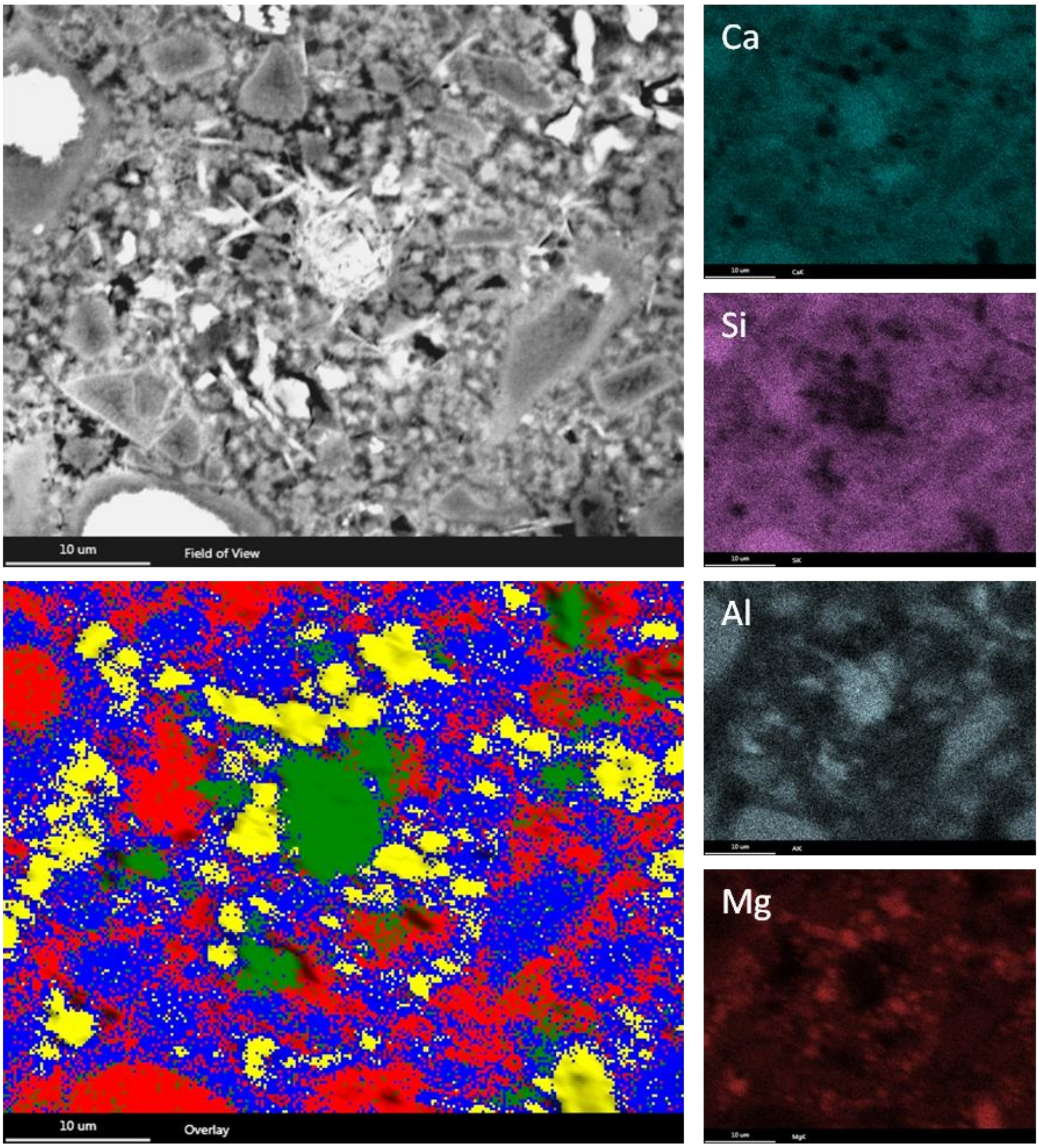

Figure B1 Sample 97-120: ESEM mapping and phase assignment, AFm formations are marked by calcium rich green areas, hydrated phases such as Slag Ip are blue and $Mg(OH)_2$ formations are in yellow.

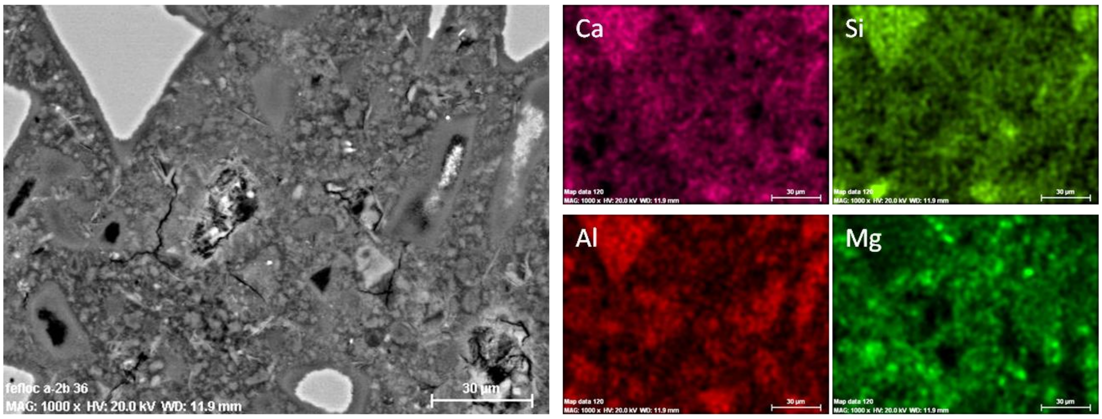

Figure B2 Sample 97-120: FEGSEM mapping

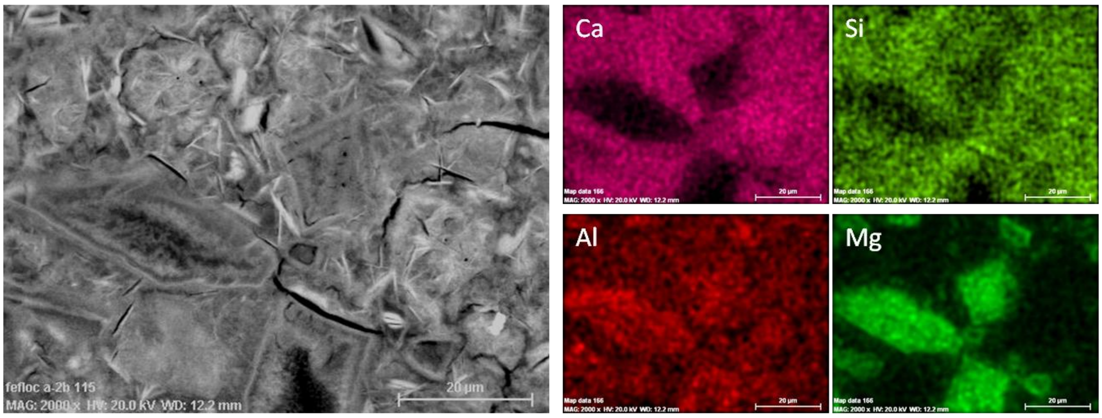

Figure B3 Sample 97-118: FEGSEM mapping

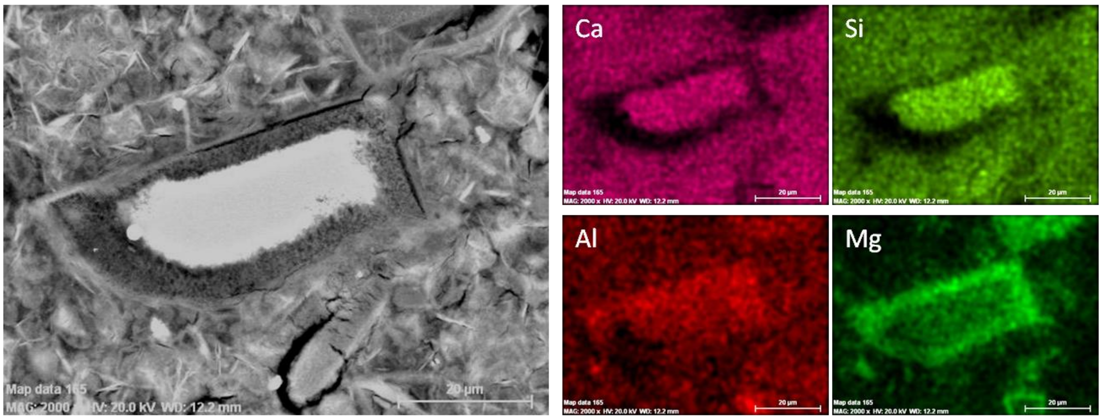

Figure B4 Sample 97-118: FEGSEM mapping

Appendix C – Conference Papers

Characterisation of blended cements incorporating simulant intermediate level nuclear wastes. J.A Rickerby, I.G. Richardson, L. Black. 33rd Cement & Concrete Science Conference, 2013, University of Portsmouth, Portsmouth, UK.

Study of aged composite grout encapsulating iron hydroxide floc. J. Rickerby, I. Richardson. 32nd Cement & Concrete Science Conference, 2012, Queens College Belfast, Belfast, UK.

Composition and Microstructure of a PFA:OPC grout and NRVB Backfill Material for Encapsulation of Intermediate Level Nuclear Waste. J.A Rickerby, I.G. Richardson. 31st Cement & Concrete Science Conference, 2011, Imperial College London, London, UK.